MEASUREMENT OF THE GALACTIC COSMIC RAY ANTIPROTON FLUX FROM 0.25 GEV TO 3.11 GEV WITH THE ISOTOPE MATTER ANTIMATTER EXPERIMENT (IMAX)

Thesis by

Allan Wayne Labrador

In Partial Fulfillment of the Requirements

for the Degree of Doctor of Philosophy

California Institute of Technology

Pasadena, California

1997

(Submitted September 3, 1996)

Acknowledgments

So many wonderful people had a hand in the making of this thesis — and in the education of this young scientist — that a full expression of my gratitude would require almost an entire chapter alone. First and foremost, my thanks go to my research advisor, Dr. Richard Mewaldt, for his guidance and patience through the years of difficult analysis which form the substance of this thesis. Among a multitude of things which I learned, he taught me that clarity of expression must accompany clarity of thought, and the best writing in this thesis is due to his advice. My thanks must also go to Dr. Stephen Schindler, who provided guidance in the development of the IMAX aerogel Cherenkov counters. Without his confident expertise during my first years with the experiment, I might never have believed that IMAX would fly. Dr. Andrew Davis was my closest daily collaborator in the development of our data analysis software and in our approach to our selection criteria, and I also thank him for pruf–redding this thesis.

Thanks must also go to our collaborators. From the Goddard Space Flight Center, Dr. Robert Streitmatter, our IMAX principal investigator, played the part of unofficial research advisor with great warmth shrouded in clouds of pipe tobacco smoke, and my gratitude to him will inevitably exceed any attempt at expression. Dr. John Mitchell effectively supervised our overall operations during the flight campaign, and his cheerful attention to detail will be the stuff of future legend. Dr. Louis Barbier, Dr. John Krizmanic, and especially Dr. Eric Christian provided indispensable analysis and great companionship, in and out of our work.

Thanks also go to Dr. Manfred Simon at the University of Siegen, who is always a warm presence and who raised interesting questions during the calculation of the photoelectron scales. Thanks go to Dr. Olaf Reimer and to Dr. Wolfgang Menn, who were my comrades–in–arms as graduate students. Wolfgang in particular deserves my undying thanks for teaching me, from very far away, how the tracking software worked.

Dr. Steve Stochaj at NMSU has similarly earned thanks for friendship and for advice on a number of relevant and irrelevant (but important) topics. Though I was in the presence of

Dr. Robert Golden for only a few weeks during IMAX integration and flight, I will always remember his kindness, patience, and support. Thanks also to Dr. Ted Bowen for advice in our analysis.

Many thanks to Glen Allbritton, Don Righter, Steve Holder, Clem Hull, Roy Park, and Barbara Kimbell, for doing the kind of hard work that never seems to get enough recognition in print.

Thanks to Dr. José Navarro, who let me use his source code for data acquisition on the Macintosh; his software was indispensable in our aerogel tests. Thanks to Dr. Richard Leske, who was my walking, talking IDL help system, and to Dr. Richard Selesnick, who was an excellent source of knowledge for statistics of small numbers. Debby Kubly used her expert marksmanship to shoot me down occasionally upon entering her office, and I thank her and Frances Spalding for helping give home–like familiarity to Caltech SRL.

My thanks and love go without pause or reservation to my parents, without whom I could not have even dreamed of being a scientist. My love and thanks go to Heather Hsuan Sze, for making the rest of my life something to look forward to.

Finally, I will be forever grateful to the memory of Dr. William M. Fairbank Sr., who gave me my start in physics.

Abstract

The intensities and relative abundances of galactic cosmic ray protons and antiprotons have been measured with the Isotope Matter Antimatter Experiment (IMAX), a balloon–borne magnet spectrometer. The IMAX payload had a successful flight from Lynn Lake, Manitoba, Canada on July 16, 1992. Particles detected by IMAX were identified by mass and charge via the Cherenkov–Rigidity and TOF–Rigidity techniques, with measured rms mass resolution $\leq$0.2 amu for Z=1 particles.

Cosmic ray antiprotons are of interest because they can be produced by the interactions of high energy protons and heavier nuclei with the interstellar medium as well as by more exotic sources. Previous cosmic ray antiproton experiments have reported an excess of antiprotons over that expected solely from cosmic ray interactions.

Analysis of the flight data has yielded 124405 protons and 3 antiprotons in the energy range 0.19–0.97 GeV at the instrument, 140617 protons and 8 antiprotons in the energy range 0.97–2.58 GeV, and 22524 protons and 5 antiprotons in the energy range 2.58–3.08 GeV. These measurements are a statistical improvement over previous antiproton measurements, and they demonstrate improved separation of antiprotons from the more abundant fluxes of protons, electrons, and other cosmic ray species.

When these results are corrected for instrumental and atmospheric background and losses, the ratios at the top of the atmosphere are $\bar{p}/p = 3.21(+3.49, -1.97)\times10^{-5}$ in the energy range 0.25–1.00 GeV, $\bar{p}/p = 5.38(+3.48, -2.45)\times10^{-5}$ in the energy range 1.00-2.61 GeV, and $\bar{p}/p = 2.05(+1.79, -1.15)\times10^{-4}$ in the energy range 2.61–3.11 GeV. The corresponding antiproton intensities, also corrected to the top of the atmosphere, are $2.3(+2.5, -1.4)\times10^{-2}$ $(m^2\ s\ sr\ GeV)^{-1}$, $2.1(+1.4, -1.0)\times10^{-2}$ $(m^2\ s\ sr\ GeV)^{-1}$, and $4.3(+3.7, -2.4)\times10^{-2}$ $(m^2\ s\ sr\ GeV)^{-1}$ for the same energy ranges.

The IMAX antiproton fluxes and antiproton/proton ratios are compared with recent Standard Leaky Box Model (SLBM) calculations of the cosmic ray antiproton abundance. According to this model, cosmic ray antiprotons are secondary cosmic rays arising solely from

the interaction of high energy cosmic rays with the interstellar medium. The effects of solar modulation of protons and antiprotons are also calculated, showing that the antiproton/proton ratio can vary by as much as an order of magnitude over the solar cycle. When solar modulation is taken into account, the IMAX antiproton measurements are found to be consistent with the most recent calculations of the SLBM. No evidence is found in the IMAX data for excess antiprotons arising from the decay of galactic dark matter, which had been suggested as an interpretation of earlier measurements. Furthermore, the consistency of the current results with the SLBM calculations suggests that the mean antiproton lifetime is at least as large as the cosmic ray storage time in the galaxy (~10^7 yr, based on measurements of cosmic ray ^{10}Be). Recent measurements by two other experiments are consistent with this interpretation of the IMAX antiproton results.

Table of Contents

1. Introduction

The study of cosmic ray antimatter should have obvious appeal in a society in which widespread science fiction entertainment has made well–known the concept of antimatter as an exotic form of matter, with the additional benefit that antimatter is known to exist in reality — unlike many other concepts which arise in science fiction. The conceptual appeal of antimatter may even be explained psychologically, with antimatter as a physical counterpart to the psychological concepts of the other, the shadow, or the Rankian double. Those with a modicum of science education beyond science fiction understand further that the study of antimatter is connected to fundamental concepts of physics, such as the creation and annihilation of matter and energy, the balanced production of matter and antimatter in high energy particle interactions, and the apparent imbalance between the abundances of matter and antimatter in the observable universe. The study of cosmic ray antiprotons, in particular, touches on issues of fundamental physics and cosmology, such as the lifetime of the antiproton, but it has its most direct applications to several basic questions of cosmic ray physics.

In 1911, Victor Hess began what would become the first series of balloon–borne cosmic ray experiments (Hess 1912), finding that the ionization rate in an airtight ionization chamber first decreased and then increased with increasing altitude. While the initial decrease in ionization rate was attributed to increasing distance from radioactive material in the ground, Hess inferred that the subsequent increase in rate at higher altitudes could be attributed to an extraterrestrial source of radiation. In later years, Millikan confirmed Hess' results and coined the term "cosmic rays" (Millikan and Cameron 1926).

During the first half of the 20th century, cosmic rays remained the primary source of high energy particles for high energy physics research. With the advent of high energy particle accelerators, the study of cosmic rays evolved from a method of studying high energy physics to being a branch of space physics and astrophysics. Further research has demonstrated that $\geq$98% of cosmic rays are atomic nuclei and that $\leq$2% are electrons and

positrons. Of the nuclear component, ~87% are protons, ~12% are helium nuclei, and the remainder are heavier nuclei.

The study of cosmic rays seeks to answer several questions, among which are the following: How are cosmic rays generated? How are cosmic rays accelerated to high energies? How do they propagate from their sources to the earth, and what happens to them during propagation through the galaxy?

The following general picture of galactic cosmic rays has emerged: Protons can be ejected from stellar surfaces via stellar winds or other mechanisms, or they may originate in the interstellar medium and be swept up by passing shock fronts. Heavier nuclei are formed first by quiescent stellar nucleosynthesis or by explosive nucleosynthesis during supernova explosions before being ejected into space. Based on theoretical studies, experimental evidence from cosmic ray spectral index measurements, and x–ray observations of supernova remnants, the most likely acceleration mechanism for cosmic rays is shock acceleration across supernova shock fronts (e.g. Blandford and Ostriker 1978; Koyama et al. 1995). Propagation of cosmic rays through the galaxy involves interaction with the interstellar medium, including spallation, further acceleration, and energy loss mechanisms. Radioactive nuclei may also be created and undergo decay during propagation, and all cosmic rays have some probability of escape from the galaxy. Cosmic rays are confined to the galaxy by the galactic magnetic field, with high energy cosmic rays having a greater probability of escape than cosmic rays at lower energies.

Galactic cosmic rays which enter our solar system must diffuse through the interplanetary magnetic field. In this process, they undergo solar modulation, by which the particles lose energy through interactions with irregularities in the magnetic fields carried by the solar wind. Particles which reach the Earth must also penetrate the Earth's magnetic field, and those which penetrate further will also interact with the atmosphere.

Galactic propagation of cosmic rays can be described by the following equation:

$$\frac{\partial}{\partial t}N_i(E,t) = Q_i(E,t) + \nabla \bullet \left(D_i \nabla N_i\right) - \frac{\partial}{\partial E}\left(b_i(E)N_i(E)\right) - \nabla \bullet \mathbf{u}N_i(E) \\ -p_i N_i + \frac{v\rho}{m}\sum_{k \geq i}\int \frac{d\sigma_{i,k}\left(E,E'\right)}{dE}N_k\left(E'\right)dE' \qquad (1.1.1)$$

Equation 1.1.1 (from Ginzburg and Syrovatskii 1964) gives the time–dependent behavior of cosmic rays of species i, where $N_i(E,t)$ is the number of particles of species i (e.g. protons), at energy E and time t. The first term on the right side, $Q_i(E,t)$, is the source term for species i. The second term describes diffusion (diffusion coefficient D_i). The third gives energy loss or acceleration, in which the mean rate of energy loss or gain for species i is given by $b_i(E)=dE_i/dt$. Energy losses for a given species can arise from scattering or ionization in the interstellar medium. The term is also important in describing possible reacceleration during propagation (e.g. Simon et al. 1987).

The fourth term describes convection (**u** is the convection velocity). The fifth term yields losses through inelastic collisions, decay and spallation, with

$$p_i=(v\rho/\lambda_i)+(1/\gamma\tau_i) \qquad (1.1.2)$$

Here, the first term gives the loss rate due to interactions (v=velocity, ρ=average density of matter in the cosmic ray propagation region, and λ_i=interaction pathlength). The second term gives the loss rate due to decay with mean lifetime τ_i and Lorentz factor γ.

The final term in Equation 1.1.1 describes feed–down to species i from fragmentation of heavier nuclei, where $\sigma_{i,k}$ is the cross section for producing species i from a nucleus of species k during a collision with a target nucleus, and m is the mass of a target nucleus in the interstellar medium. Generally, Equation 1.1.1 is solved numerically assuming a steady–state solution ($\partial N_i(E,t)/\partial t = 0$).

The most widely used model for cosmic ray propagation in the Galaxy is the Standard Leaky Box Model (SLBM), which is a phenomenological model incorporating the above–named processes after acceleration at the source and prior to solar modulation in the interplanetary medium. In this model, the galaxy is described as a confinement volume (the "box") through which the cosmic rays propagate, and the cosmic rays have some probability of escape from the confinement volume, which gives the box its leakiness. The "Leaky" part of the name arises from how the diffusion term is treated. In this case, the diffusion term is replaced by $-N_i v/d_{esc}$, where d_{esc} is interpreted as an escape length from the confinement volume and v is the velocity of the cosmic ray. (Note that d_{esc} is in units of distance. In practice, escape length is given in units of g/cm^2, such that $\lambda_{esc}=\rho d_{esc}$, where ρ is the average density of the interstellar medium.) Under the SLBM, Equation 1.1.1 can be simplified by neglecting convection and changes in energy and assuming a steady–state condition:

$$v\rho\frac{N_i(E)}{\lambda_{esc}} = Q_i(E) - p_i N_i + \frac{v\rho}{m}\sum_{k\geq i}\sigma_{i,k}N_k(E) \qquad (1.1.3)$$

The SLBM has been used successfully to describe much of the measured spectra and elemental and isotopic ratios of cosmic rays (e.g. Simpson 1983; Gibner 1992). In discussing low energy (< 1 GeV/nuc) cosmic rays and antiprotons, in particular, energy–losses due to inelastic scattering can be restored to Equation 1.1.3 (e.g., Gaisser and Schaefer 1992).

Note that the SLBM is not a physical model. Leakage in the SLBM is assumed to occur throughout the confinement volume, and the physical configuration (disk, halo, and magnetic field) of the galaxy is not explicitly modeled. The diffusion model retains the diffusion term and gives a more physical description of the galaxy, including disk and halo models. (For detailed discussions of diffusion models, see Berezinskii et al. 1990.) However, the SLBM has proved to be very useful for discussions of cosmic ray data, and it is computationally simpler.

Figure 1.1 gives an example of the effectiveness of the SLBM for cosmic ray B/C measurements (Gibner 1992). The boron to carbon ratio is an example of a secondary to primary

cosmic ray ratio. Cosmic rays which arrive unchanged (except possibly in energy) from their sources are called primary cosmic rays. Cosmic rays which are produced during interaction of other cosmic rays with the interstellar medium (or in the atmosphere above the measuring instrument, or in the instrument itself), or by decay of radioactive cosmic rays during propagation, are called secondary cosmic rays. (Cosmic rays which originate in the Sun are called solar energetic particles, while those which originate elsewhere in the galaxy are galactic cosmic rays.)

Regarding B/C measurements: If we assume that cosmic ray sources are stars, then boron is not expected to be present in cosmic ray sources except in minute quantities. On the other hand, carbon is a primary product of stellar nucleosynthesis. Thus, for example, the relative abundances of boron and carbon in the solar system is given by B/C ~ 10^{-6}–10^{-5} (e.g. Anders and Grevesse 1989). On the other hand, cosmic ray measurements yield B/C ~ 0.1–0.3, depending on energy. The relatively large abundance of boron in cosmic rays is thought to be a result of spallation of heavier cosmic rays (such as carbon) during propagation through the interstellar medium. The B/C ratio gives a measure of the amount of material through which the primary cosmic rays pass, and the data in Figure 1.1 implies an energy– or rigidity– dependence to this pathlength, with less matter traversal at higher energies. One possible parametrization for this pathlength, based on B/C data, is given by Equation 1.1.7. (See Section 1.1.) A vastly different pathlength, based on a reacceleration model, is given by Equation 1.1.10 (Section 1.3).

1.1 Cosmic Ray Antiproton Production and Propagation

The study of cosmic ray antiprotons should yield similar information about cosmic ray propagation in the galaxy. In the absence of a source of primary antimatter (e.g. antimatter stars or galaxies), cosmic ray antiprotons will be produced as secondary cosmic rays, primarily through the collision of high energy cosmic ray protons with protons and heavier nuclei in the

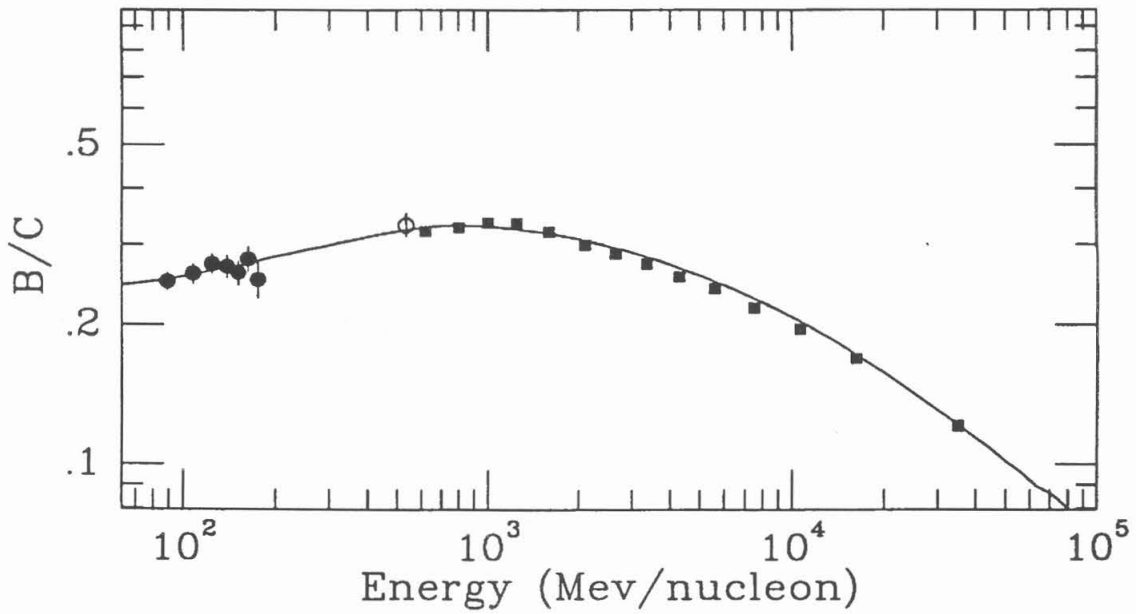

Figure 1.1: Boron to carbon ratio measurements at 1 AU, compared to Leaky Box Model calculations with a rigidity–dependent escape pathlength with a turnover rigidity of 3.5 GV. (For a similar pathlength parametrization, see Equation 1.1.7.) Solar modulation, with a modulation parameter of 450 MV, is included in the calculation. The data are from Krombel and Wiedenbeck (1988, solid circles), Engelmann et al. (1990, solid squares), and Gibner (1992, open circle). Figure taken from Gibner (1992).

interstellar medium. A measurement of the cosmic ray antiproton abundance should yield information on the rate of cosmic ray interactions with the interstellar medium. In principle, such measurements may yield information on whether cosmic ray protons have the same origin and history as heavier cosmic rays, such as C, N, O, and Fe. For example, the abundance of antiprotons, relative to the abundance of protons, may imply a greater pathlength for protons than is implied by the B/C ratio.

Of basic importance are the kinematics of antiproton production. A proton–proton collision in the center of mass frame can produce three protons (p) and one antiproton ($\bar{p}$) *at rest*.

$$p + p \rightarrow p + p + p + \bar{p} \tag{1.1.4}$$

In the center of mass frame, the initial 4–momentum vector has the form

$$\mathbf{p}_{CM,before} = \left(\frac{2E_{CM,before}}{c}, 0, 0, 0 \right) = \left(\frac{2m_p c}{\sqrt{1-\beta_{CM}^2}}, 0, 0, 0 \right) \tag{1.1.5}$$

where β_{CM} is the velocity (though in opposite directions) of the two protons in the center of mass frame, and m_p is the rest mass of the proton. The 4–momentum vector after the collision has the form

$$\mathbf{p}_{CM,after} = \left(\frac{4E_{CM,after}}{c}, 0, 0, 0 \right) = \left(4m_p c, 0, 0, 0 \right) \tag{1.1.6}$$

Equating the invariant intervals yields a threshold kinetic energy for the incident proton, in the lab frame, of $6m_p c^2 \approx 5.6$ GeV and a kinetic energy for the resulting antiproton of $m_p c^2 \approx 0.938$ GeV. In order to produce higher or lower energy antiprotons, the incident proton must have a higher kinetic energy. Figure 1.2 shows some calculations of the relative

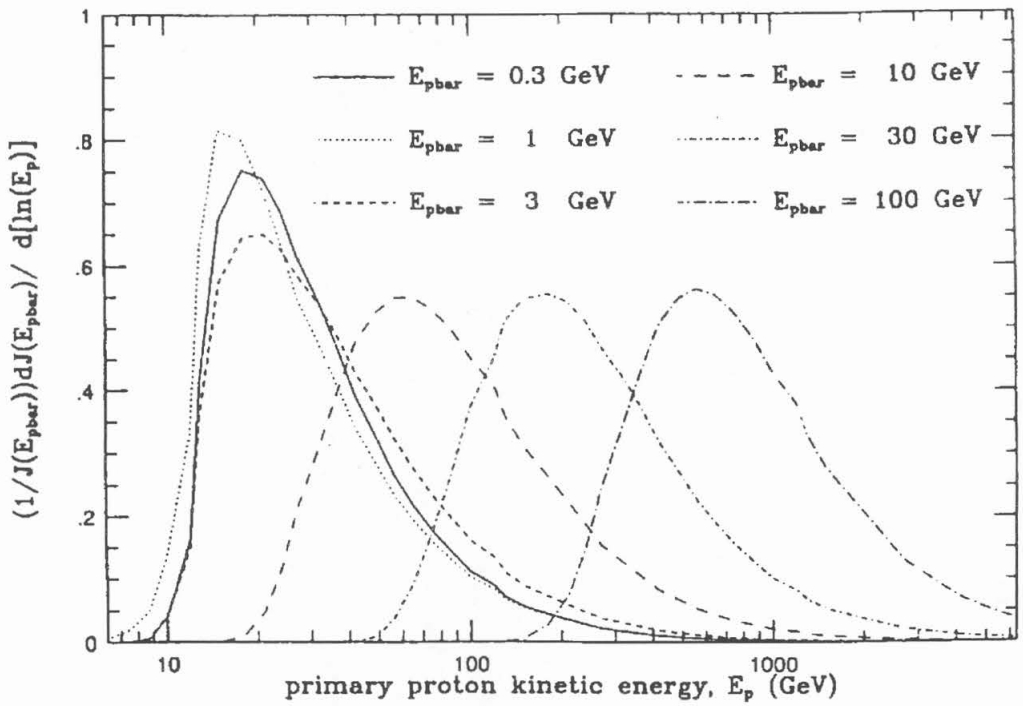

Figure 1.2: Fraction of antiprotons of energy E_{pbar} produced by primary protons of kinetic energy E_p. The threshold for antiproton production (6 GeV) is apparent. Antiprotons with energies below 1 GeV must be produced with large backward momentum in the center of momentum frame and are mostly produced by high energy primary protons. Figure taken from Gaisser and Schaefer (1992).

contributions to antiproton production from cosmic ray protons of various energies (Gaisser and Schaefer 1992).

Production of antineutrons by a similar interaction, with similar kinematics, results in further antiproton production as those antineutrons beta–decay to antiprotons (with the additional production of positrons and electron neutrinos). Antineutrons should be produced in roughly equal numbers as antiprotons, and because the antineutron lifetime is much smaller than the lifetime of cosmic rays in the galaxy, antineutron production effectively doubles the number of antiprotons from direct production alone. (The mean lifetime of a free neutron is about 900 seconds. Cosmic ray ^{10}Be measurements imply that the lifetime of cosmic rays in the galaxy is approximately 10^7 years. See Simpson and Garcia–Muñoz 1988, Lukasiak et al. 1994.)

In addition to antineutron production from proton–proton interactions, any model of cosmic ray antiproton propagation will have to take into account antiproton (and antineutron) production from interactions of heavier cosmic rays with the interstellar medium. Although the kinematics of production for these interactions will not be exactly the same as for proton–proton interactions, the detailed physics of the interactions and their abundances relative to proton–proton interactions are not well–known. Most authors have treated the relative contribution of these interactions as a constant "nuclear enhancement factor" resulting in increases ranging from 20% to 60% beyond production from proton–proton interactions alone. (See Gaisser and Schaefer 1992 for a brief review of the nuclear enhancement factors used by various authors. Further discussion in this section will concentrate on the proton–proton interaction.)

Calculating an interstellar antiproton spectrum involves first obtaining an interstellar proton spectrum, at least for energies above the antiproton production threshold of ~6 GeV. At much higher energies, the effects of solar modulation are minimal, so that current measurements of high energy proton fluxes within the solar system are adequate approximations of the interstellar proton fluxes at high energies. At low energies, the estimated interstellar proton flux must take into account the effects of solar modulation when

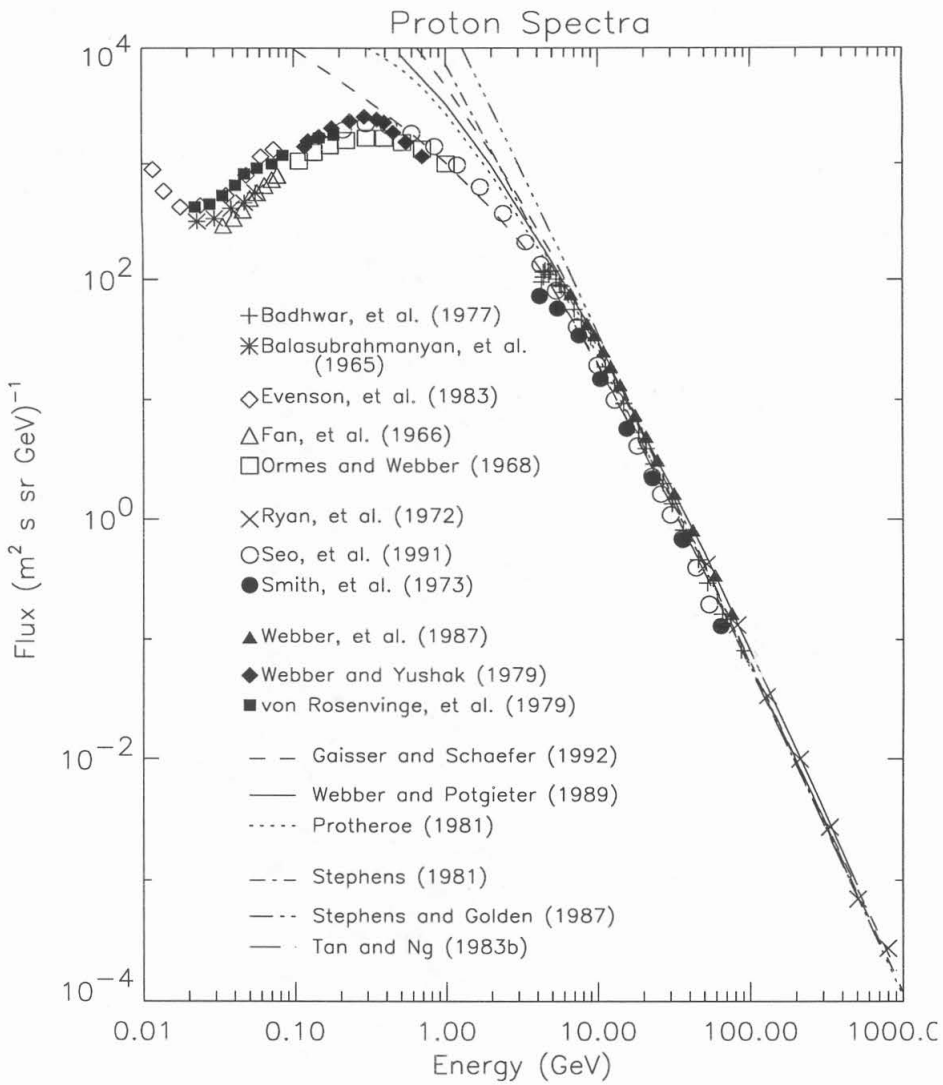

Figure 1.3: Interstellar proton spectra, derived by Gaisser and Schaefer (1992; upper and lower limits), Webber and Potgieter (1989), Protheroe (1981), Stephens (1981), Stephens and Golden (1987), and Tan and Ng (1983b). Also shown are a number of proton flux measurements at 1 AU, made at various times during the solar cycle. The difference between the interstellar spectra and the measurements at low energies is due to solar modulation. (See Section 5.2).

derived from low energy measurements. (See Section 5.2 for more detailed discussion of solar modulation.) Cosmic ray proton flux measurements have yielded an interstellar proton spectral index in the range ~2.5–2.8 at high energies, although most measurements center on ~2.7. See Figure 1.3.

Because of solar modulation effects, the interstellar proton flux at energies below a few GeV is largely unknown. However, protons below 6 GeV will not produce antiprotons, so the shape of the interstellar proton spectrum below 6 GeV will have no effect on the antiproton spectrum. On the other hand, the low energy interstellar proton spectrum will have an affect on the low energy antiproton/proton ratio, as will be discussed later. For now, it is enough to state that measurements of the B/C ratio can be fit with SLBM calculations, using a rigidity dependent pathlength through the galaxy of the form

$$\lambda_{esc} = \begin{cases} 10.8\beta\left(\frac{R_0}{R}\right)^{0.6} & R > R_0 = 4.0GV \\ 10.8\beta & R \leq 4.0GV \end{cases} \qquad (1.1.7)$$

where λ_{esc} is measured in g/cm^2 (Gupta and Webber 1989; Webber and Potgieter 1989). Other investigators have arrived at different pathlength parametrizations, albeit with similar general characteristics (e.g. Garcia–Muñoz et al. 1987; Ormes and Protheroe 1983). The rigidity–dependent decrease at high rigidities is interpreted as escape from confinement by the magnetic fields in the galaxy. Some of these pathlengths are given in Figure 1.4. These pathlengths are also generally consistent, under the SLBM, with measurements of Fe fragment measurements (e.g. Engelmann et al. 1990) and recent measurements of ^{3}He (e.g. Reimer et al. 1995; Davis et al. 1995). If one assumes that protons have the pathlength used by Webber and Potgieter, then a high energy proton spectral index of 2.75 implies a source spectrum index of ~2.15, where the difference arises from the rigidity dependence of the escape pathlength. Such a source spectrum is consistent with calculations of shock acceleration (e.g. Blandford and Ostriker 1978; Bell 1978), which yield source spectra with an index of ~2.

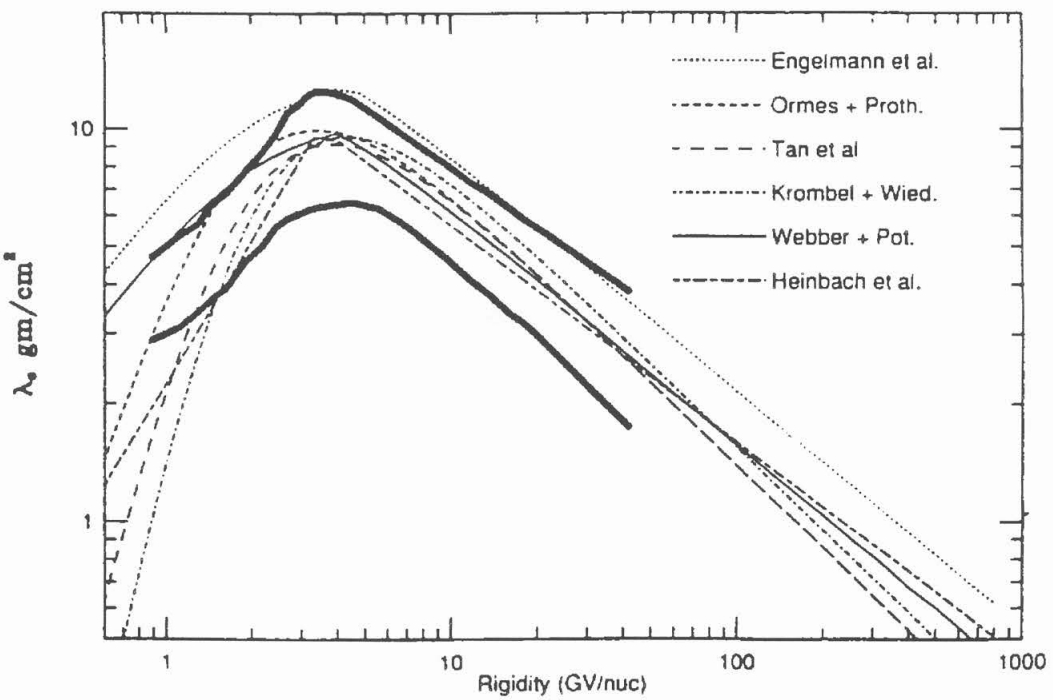

Figure 1.4: Different fits to the escape pathlength, obtained from fits to secondary to primary nuclei (Engelmann et al. 1990; Webber and Potgieter 1989; Ormes and Protheroe 1983; Tan et al. 1987; Krombel and Wiedenbeck 1987; Heinbach and Simon 1990). The bold lines are estimated maximal errors to the pathlength fit given in Garcia–Muñoz et al. (1987). Path lengths roughly agree for rigidities above 3 GV; however, the fits show a large spread below this energy. Figure taken from Gaisser and Schaefer (1992).

The interstellar proton flux and the pathlength contribute to the antiproton production spectrum according to the formula

$$\frac{dN_{\bar{p}}}{dE} = 2\frac{\langle\lambda\rangle}{m_p}\varepsilon \int_{E_{threshold}}^{\infty} \frac{d\sigma_{pp\to\bar{p}}}{dE}\frac{dN_p}{dE_p}dE_p \tag{1.1.8}$$

where $<\lambda>$ is the mean pathlength (at energy E) of protons through the interstellar medium, m_p is the proton mass, the factor of 2 takes into account the antiproton production through antineutron production and beta–decay, and ε is the nuclear enhancement factor mentioned earlier. The first factor in the integral is the differential antiproton production cross–section for proton–proton interactions, and the second factor is the interstellar differential proton spectrum. The integration is taken over energies which can contribute to antiproton production.

The invariant antiproton production cross–section, for protons on proton targets, has been parametrized by Stephens (1981):

$$\begin{aligned} E\frac{d^3\sigma}{dp^3} &= 3.5\exp(-3.1p_\perp)(1-\tilde{x})^{8.5-1.4p_\perp+0.7p_\perp^2} \\ \tilde{x} &= \sqrt{x_{11}^{*2}+m_p^2+p_\perp^2} \end{aligned} \tag{1.1.9}$$

where $p_\perp$ is the transverse momentum of the resulting antiproton, and x_{11}^* is the ratio of the antiproton momentum to the maximum available momentum. Stephens found that this parametrization fits the available data well. (See Figure 1.5.) Other authors have found slightly different numerical constants for their parametrizations, but all show a similar dependence on $\tilde{x}$ and $p_\perp$, resulting in a strong suppression of antiproton production at low energies.

The result of the kinematics of antiproton production in combination with the known characteristics of the high energy cosmic ray proton flux and the SLBM is that the expected antiproton flux should peak around 1–3 GeV and be suppressed at lower and higher energies.

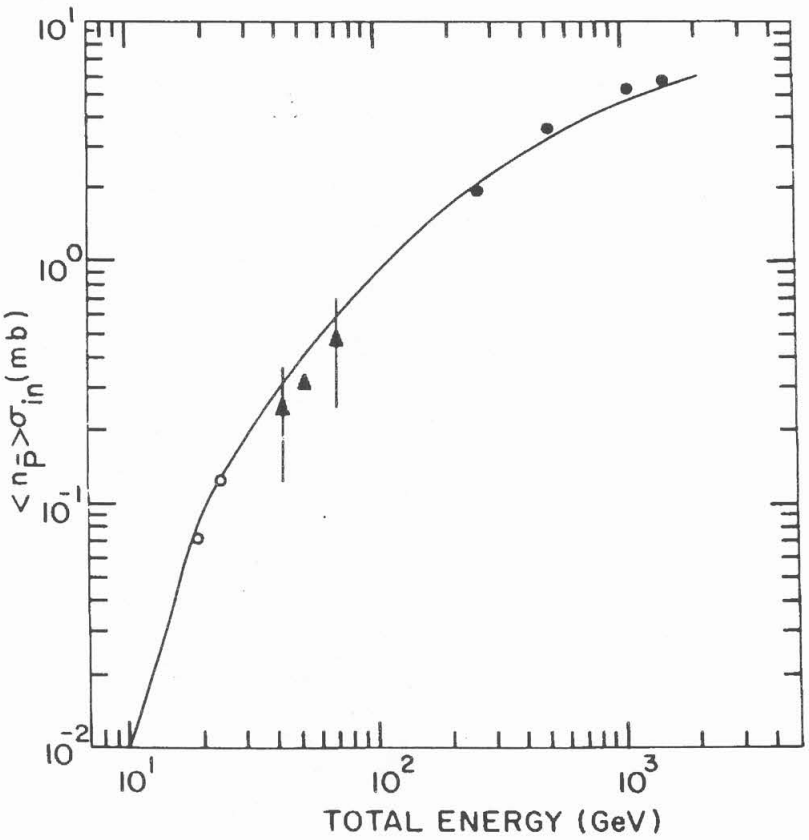

Figure 1.5: Total inclusive cross–section for the production of antiprotons in proton–proton collisions, plotted as a function of proton energy. Figure taken from Stephens (1981).

Early SLBM calculations (e.g. Protheroe 1981) as well as more recent calculations (e.g. Webber and Potgieter 1989; Gaisser and Schaefer 1992) reflect this expectation. (See Figure 1.6.)

Finally, it should be noted that cosmic ray antiproton measurements have implications well beyond cosmic ray physics. Secondary cosmic ray antimatter remains a significant source of detectable, naturally–occurring antimatter, in addition to some products of radioactive decay and interactions in accelerators. Because the abundance of secondary cosmic ray antimatter can be calculated, measurement of cosmic ray antimatter in excess of the expected secondary abundance may indicate other possible sources of antimatter, such as primary antimatter (e.g. antimatter galaxies) or the decay of exotic particles.

1.2 Previous Cosmic Ray Antiproton Measurements

The history of experimental cosmic ray antiproton research is comparatively recent. Although antiprotons were first generated artificially in laboratory experiments in 1955 (Chamberlain et al. 1955), early searches from the 1950's to the 1970's failed to detect convincing evidence for antiprotons in cosmic rays (for a review, see Stephens and Golden 1987). Cosmic ray antiprotons were first detected in the middle to late 1970's by Golden et al. (1979) and Bogomolov et al. (1979). The Golden et al. experiment was a balloon–borne cosmic ray payload, and it employed a magnetic deflection technique (with multiwire proportional counters for trajectory determination) to detect charge sign and rigidity. A gas Cherenkov detector ($\beta_{threshold}$=0.9991) was employed as an anticoincidence counter to discriminate between light negatively–charged particles (electrons, muons, and pions) and heavier negatively–charged particles (assumed to be antiprotons) of the same magnetic rigidity (R=pc/Ze, a measure of momentum over charge). Scintillators were employed to determine charge, and a shower counter identified electrons which would otherwise escape discrimination by the Cherenkov detector. The scintillators and shower counters also provided rough time–of–flight to reject albedo particles.

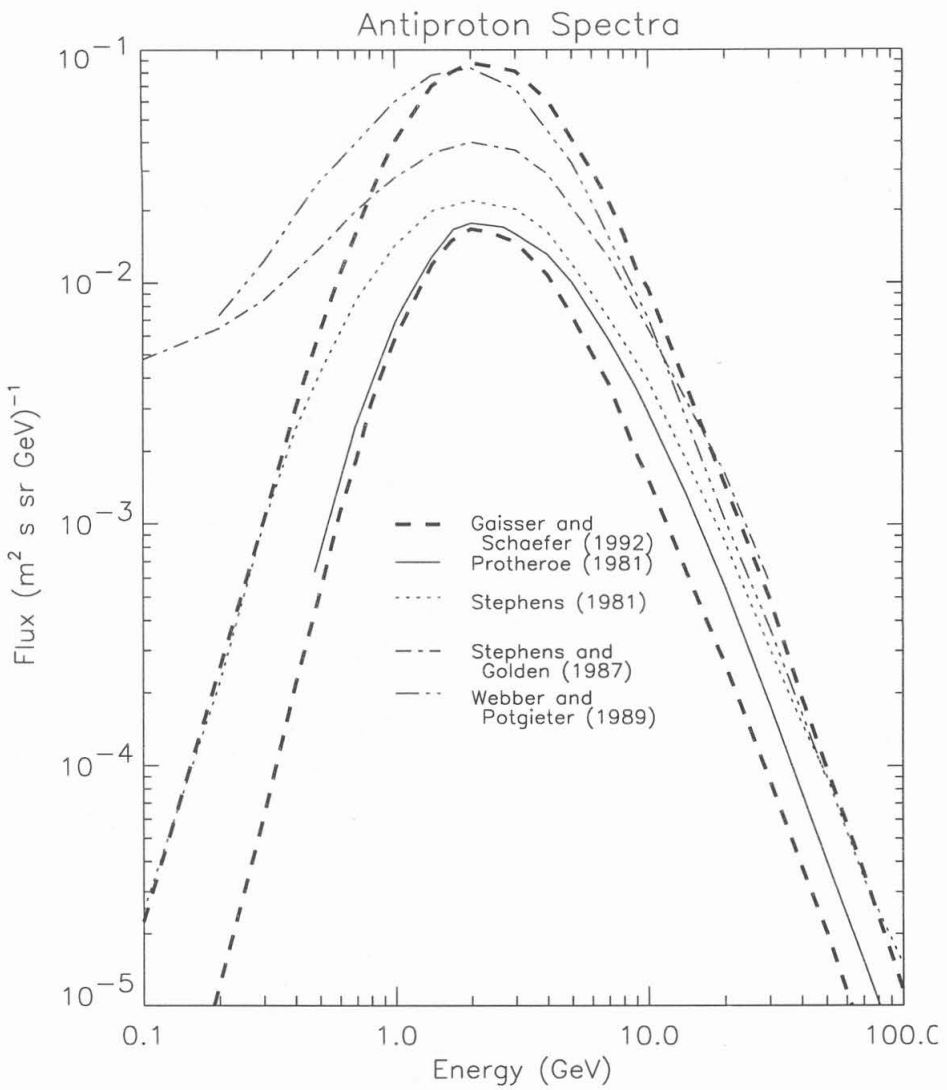

Figure 1.6: Standard Leaky Box interstellar antiproton fluxes, calculated by Protheroe (1981), Stephens (1981), Stephens and Golden (1987), and Webber and Potgieter (1989). The bold dashed lines are the outer limits calculated by Gaisser and Schaefer (1992). The evolution of these models will be discussed in Section 5.1.

The original paper (Golden et al. 1979) reported a total of 46 antiprotons (see Table 1.1), and after making what were claimed to be conservative estimates of atmospheric and instrumental background, they reported an antiproton/proton ratio of $5.2(\pm1.5)\times10^{-4}$ in the energy range of 4.7–11.6 GeV. Subsequent reanalysis in a second paper (Golden et al. 1984), using less conservative estimates of background, yielded a ratio of $6.8(\pm1.7)\times10^{-4}$ in the same energy range. Also in the second paper, the energy range was extended to 4.4–13.4 GeV, and the group reported 56 antiprotons (~41.5 primary plus ~14.5 background) in this range, which yielded a ratio of 6.0×10^{-4} after correction for background.

A significant limitation of the Golden et al. payload is that it did not measure mass. In a magnet spectrometer, one needs a measurement of velocity in addition to a measurement of magnetic rigidity in order to determine mass. The time–of–flight measurement was sufficient only to reject upward–moving particles, and the Cherenkov counter was used only to discriminate between fast– and slow–moving particles of the same magnetic rigidity. Even if the assumption is correct that slow–moving particles of a given magnetic rigidity are antiprotons, limitations on the rejection efficiency of the Cherenkov system and spillover in the deflection (inverse rigidity, 1/R) distribution will yield some ambiguity in the identification of high energy particles. Although rejection efficiency is examined in the Golden et al. papers, a direct mass measurement would have provided added confidence to the identification of antiprotons.

The Bogomolov et al. experiment was a balloon–borne magnet spectrometer experiment employing a permanent magnet, spark chambers for trajectory and charge sign determination, and a collection of scintillators and Cherenkov counters to provide charge determination, light–heavy particle discrimination, and system trigger (Bogomolov et al. 1971). The payload enjoyed a number of successful flights to search for antiprotons during the 1970's and 1980's, and it remains an active experiment in the 1990's.

To date, none of the Bogomolov et al. measurements have been published in the refereed literature, and the available conference papers reporting their measurements are sometimes

unclear regarding the actual number of antiprotons detected, whether or how corrections for atmospheric and instrumental background are applied, and whether some measurements are combined with previous measurements. The Bogomolov et al. experiment first reported 2 "primary" cosmic ray antiprotons in the energy range from 2 to 5 GeV, resulting in a "corrected" antiproton/proton ratio of $6(\pm4)\times10^{-4}$ (Bogomolov et al. 1979). Subsequent flights in 1984 and 1985 resulted in 1 antiproton in the energy range 0.2 to 2.0 GeV and an antiproton/proton ratio of $6\ (+14, -5)\times10^{-5}$ and an antiproton flux of $5\ (+10, -4)\times10^{-2}$ $(m^2\ s\ sr\ GeV)^{-1}$ (Bogomolov et al. 1987). For 2 to 5 GeV, they accumulated additional protons but no new antiprotons from these flights, and by combining these results from those of earlier flights, they reported a new antiproton/proton ratio of $3\ (+4, -2)\times10^{-4}$ in this energy range. (Note that, because the 1984-85 and 1970's flights took place during different times in the solar cycle, combining results in this way is not strictly valid, as will be discussed in Section 5.2.) Finally, flights from 1986 and 1987 were reported to yield 3 "primary" antiprotons in the 2 to 5 GeV range, with a reported antiproton/proton ratio of $2.4\ (+2.4, -1.3)\times10^{-4}$ (Bogomolov et al. 1990). The 1990 results do not appear to have been combined with earlier measurements. Although the language of their papers implies that the results are for primary protons and antiprotons, it is always clear whether or how atmospheric and instrumental background corrections were employed.

A balloon–borne experiment by Buffington et al. (1981) employed an annihilation detection technique, with an upper set of spark chambers to provide initial tracking and a larger, lower set of spark chambers to act as a calorimeter to detect annihilations of antiprotons. Annihilation was identified through detection of interaction products and measurements of their total energies. A set of scintillators provided a trigger, and a Cherenkov counter provided rejection of particles above a preselected threshold velocity. The experiment reported 14 cosmic ray antiprotons in the energy range from 130 to 320 MeV (Buffington et al. 1981). This measurement was analyzed to yield a top–of–the–atmosphere (TOA) antiproton flux of $1.7\ (\pm1.5)\times10^{-1}$ $(m^2\ s\ sr\ GeV)^{-1}$ and an antiproton/proton ratio of $2.2\ (\pm0.6)\times10^{-4}$.

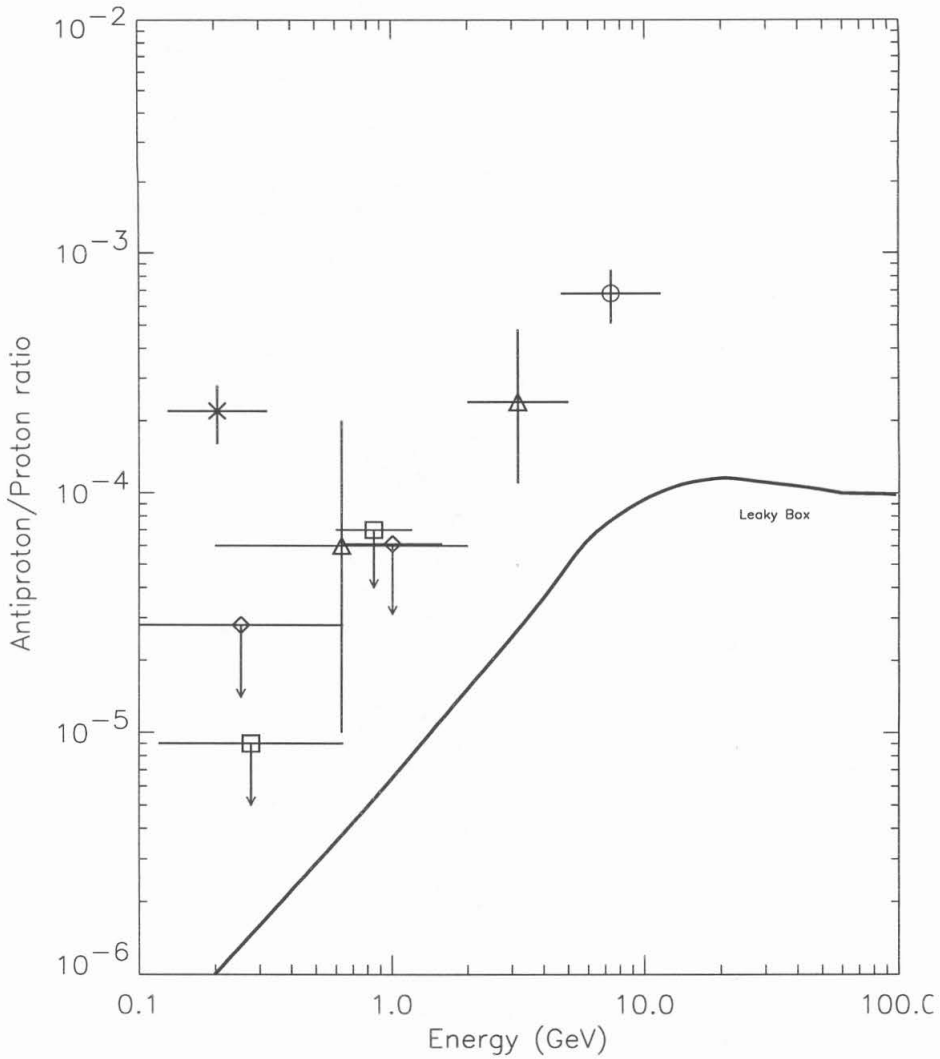

Figure 1.7: Comparison of cosmic ray antiproton/proton ratio measurements made during and before 1987 with the Standard Leaky Box Model calculation by Protheroe (1981). The points are by Golden et al. (1984, open circle), Bogomolov et al. (1987 and 1990, open diamond), Buffington et al. (1981, asterisk), Barwick et al. (1990, open diamond), Stochaj (1990, open square), and Moats et al. (1990, open square).

It is beyond the scope of this thesis to reassess the Buffington et al. selection criteria and results in detail, particularly since other authors have already commented upon the experiment (e.g. Stephens and Golden 1987). The initial candidate antiproton set included ~1500 candidate events, and the reduction to 14 reported antiprotons may imply a certain necessary stringency to the selection criteria. Ultimately, however, ambiguity in identification of annihilation events makes this measurement problematic.

The Golden et al. and Bogomolov et al. measurements proved to be in excess of the antiproton fluxes (and antiproton/proton ratios) predicted by the Standard Leaky Box Model, as it was then formulated (e.g. Protheroe 1981; see Figure 1.7.) The Buffington et al. measurement was in even larger excess of standard theory, particularly given that the 130–320 MeV energy range lies well within the range for which antiproton production is strongly suppressed. These results, especially that of Buffington et al. (1981), sparked ~20 papers with a variety of explanations, some of which will be discussed in the next section.

Two further experiments were flown in 1987 to search further for low energy cosmic ray antiprotons. Both were superconducting magnet spectrometer experiments capable of measuring particle mass. The PBAR experiment employed a drift tube hodoscope for particle trajectory determination (magnetic rigidity measurement), a scintillator time–of–flight system for low–energy velocity measurement, and a water Cherenkov counter for higher velocities (Ahlen et al. 1988; Barwick et al. 1990). The Low Energy AntiProton (LEAP) experiment used a somewhat different configuration, employing multiwire proportional counters for particle trajectory determination, a time–of–flight system, and FC72 as a Cherenkov radiator (Moats et al. 1990; Stochaj 1990). Neither experiment reported the detection of cosmic ray antiprotons; only upper limits to fluxes and antiproton/proton ratios were reported. (The LEAP experiment detected one antiproton, which was attributed to atmospheric background.) These results failed to confirm the Buffington et al. measurements, and there was a subsequent decrease in the theoretical interest in low energy antiprotons. The LEAP and PBAR results, as well as those of the earlier balloon–borne cosmic ray experiments, are reported in Table 1.1.

Table 1.1:

Cosmic Ray Antiproton Measurements from Balloon–Borne Cosmic Ray Experiments Flown During and Before 1987

Energy (GeV)	# Candidate Antiprotons	# Cosmic Ray Antiprotons	Antiproton/Proton Ratio	Antiproton Flux $(m^2\ s\ sr\ GeV)^{-1}$	Flight Year	Reference
4.7 — 11.6	46[1]	36.9	$6.8\ (\pm 1.7)\times 10^{-4}$	not presented	1979	Golden et al. 1979, 1984
2.0 — 5.0	N/A[2]	2	$6\ (\pm 4)\times 10^{-4}$	not presented	1972/74/77	Bogomolov et al. 1979
0.2 — 2.0	1	N/A[3]	$6\ (+14, -5)\times 10^{-5}$	$5\ (+10, -4)\times 10^{-2}$	1984/85	Bogomolov et al. 1987
2.0 — 5.0	N/A[4]	3	$2.4\ (+2.4, -1.3)\times 10^{-4}$	not presented	1986/87	Bogomolov et al. 1990
0.13 — 0.32	14	N/A[5]	$2.2\ (\pm 0.6)\times 10^{-4}$	$1.7\ (\pm 0.5)\times 10^{-1}$	1980	Buffington et al. 1981
0.10 — 0.64	0	0	$\leq 2.8\times 10^{-5}$ (85% CL)	not presented	1987	Barwick et al. 1990
0.64 — 1.58	0	0	$\leq 6.1\times 10^{-5}$ (85% CL)	not presented	1987	Barwick et al. 1990
0.12 — 0.64	1	0	$\leq 4.2\times 10^{-6}$	not presented	1987	Stochaj 1990
0.60 — 1.20	3	(≤3)[6]	$\leq 2.3\times 10^{-4}$ (90% CL)	not presented	1987	Moats et al. 1990

[1]The second paper includes a reanalysis of data reported in the first paper for instrumental and atmospheric background and loss. In the second paper, Golden et al. also extended the energy range to 4.4–13.4 GeV and included a total of 56 antiprotons (41.5 primary), with a top of the atmosphere antiproton/proton ratio of 6.0×10^{-4} after correction for background.

[2]Bogomolov et al. (1979) reported 28 events due to instrumental background (interactions in the instrument) but did not report an estimate for atmospheric background in this energy range. The two antiprotons in the 1979 paper came from the 1974 flight.

[3]It is unclear from this paper what fraction of the measurement is attributed to atmospheric or instrumental background.

[4]The Bogomolov et al. (1990) paper attributed 20 events to instrumental background, and one event was identified as a secondary antiproton.

[5]The number of background events is assumed to be zero. A factor of 1.2 was applied to correct for instrumental attenuation, and another factor of ~1.2 was applied for atmospheric attenuation and background.

[6]As of the writing of the paper (Moats et al. 1990), the three candidates were not yet positively identified as antiprotons. A factor of 1.34 (Bowen and Moats 1986) was applied for antiproton annihilation and absorption in the gondola and atmosphere, and assuming that the 3 candidate antiprotons followed a Poisson distribution, a 90% CL upper limit of 7 antiprotons was derived.

1.3 Other Sources of Cosmic Ray Antiprotons

The three early positive measurements all exhibited antiproton abundances in excess of contemporary theoretical calculations of the Standard Leaky Box Model (SLBM), and a number of alternative models were proposed to explain this excess while maintaining results consistent with standard calculations for other cosmic rays. The alternative models for cosmic ray antiproton abundance can be separated into two general categories: models which are variations on standard cosmic ray propagation models, and models with exotic production mechanisms for antiprotons. (See Stephens and Golden 1987 for a review.) Figure 1.9 gives a comparison of some of these models with the earlier measured antiproton/proton ratios.

The most obvious candidates for the first category of models are variations of the SLBM. Parameters which may change include the escape pathlengths through the galaxy, antiproton production cross sections, the spectrum of high energy interstellar protons needed for antiproton production, and the relative contribution of heavier nuclei to antiproton production. For example, Gaisser and Schaefer (1992) have examined uncertainties in various parameters for the Standard Leaky Box Model, including uncertainties in the interstellar proton spectrum and the relative contributions of heavy nuclei to the antiproton production spectrum, and their calculations have resulted in upper and lower limits to the interstellar antiproton spectrum. (See Figure 1.4.) Also, Stephens and Golden (1987) have noted that the antiproton production cross section parametrization by Tan and Ng (1983a) may underestimate the antiproton production near threshold. Some of these issues will be discussed in Section 4.7.

One modification to the SLBM is the inclusion of reacceleration, a physical process not explicitly included in most calculations of the SLBM. In the SLBM, acceleration is assumed to take place solely at the source. Under the diffusive (or distributed) reacceleration model, acceleration occurs initially at the source, and during propagation through the galaxy, cosmic rays encounter irregularities (e.g. shock fronts) in the galactic magnetic field which can induce further reacceleration. The effect is to increase the energy of primary cosmic rays and induce greater production of antiprotons during galactic propagation, by increasing the abundance of

high energy primary cosmic rays capable of producing antiprotons. The antiprotons and other secondary cosmic rays are also reaccelerated. (See the third term on the right side of Equation 1.1.1. The usual ionization and scattering energy losses also occur via this term, so that reacceleration competes with energy loss.) Simon et al. (1987) found that the addition of reacceleration to the SLBM can as much as triple the antiproton/proton ratio at 10 GeV while depleting the ratio around 1 GeV. (In this case, the calculated antiproton spectrum is shifted and increased at higher energies, while the proton spectrum, adopted from measurements, is left unchanged.) A later calculation used a simple power–law escape length of the form

$$\lambda_{esc} = 103(R[MV])^{-1/3} \tag{1.1.10}$$

(compare with Equation 1.1.5) to improve the fit of the model to the available cosmic ray nuclear data (e.g. B/C) (Heinbach and Simon 1995; Simon and Heinbach 1996). Their result shows an increase, relative to their calculation with the SLBM, of more than 2 orders of magnitude in the low energy (~100 MeV) interstellar antiproton flux. (See Figure 1.8.) On general principles, reacceleration is certainly expected to occur during transport in the galaxy, but its relative contribution remains an open question.

A more radical change to the SLBM is the Closed Galaxy Model (Peters and Westergaard 1977; Protheroe 1981). In this model, cosmic ray leakage from the galaxy does not occur, and all cosmic ray losses occur through decay, energy losses, and other interactions. The model by Peters and Westergaard includes both an inner containment volume (e.g. the spiral arms, which contain the cosmic ray sources) and an outer containment volume (e.g. the halo), and cosmic rays may leak from the inner region to the outer region but not from the outer region to outside of the galaxy. The model can be characterized, in part, by the ratio, K, of the total mass of interstellar gas to the mass of interstellar gas in the inner containment volume. Protheroe (1981) has calculated the cosmic ray antiproton/proton ratio vs. energy for various values of K. Protheroe's calculation shows that the Closed Galaxy Model yields an

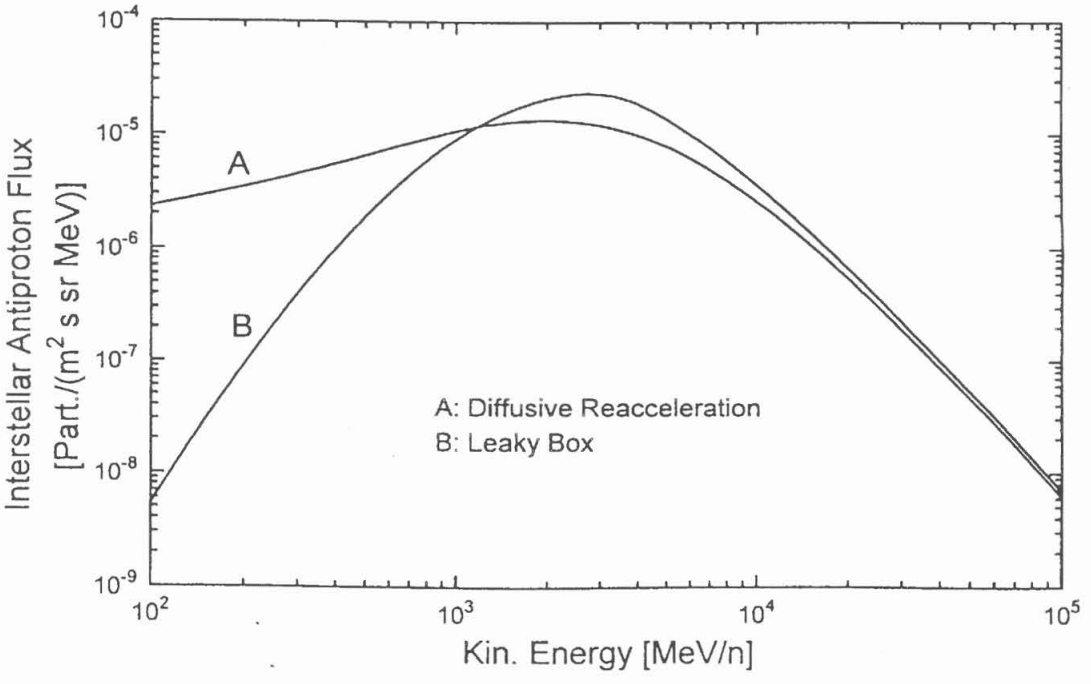

Figure 1.8: Interstellar antiproton flux calculations, comparing the Standard Leaky Box model with a model including diffusive reacceleration. Figure taken from Simon and Heinbach (1996).

antiproton/proton ratio a factor of ~4 higher than that predicted by the SLBM, for energies around a few GeV and higher.

Also among the category of models which yield different propagation histories are those which include shrouded sources of cosmic rays. In a shrouded source model, some fraction of cosmic ray sources are embedded in dense molecular clouds in the galaxy (Cowsik and Gaisser 1981; Tan and Ng 1983b; Lagage and Cesarsky 1985). Cowsik and Gaisser (1981) identify these sources as also being bright gamma ray sources. The models are characterized, in part, by the abundance of shrouded cosmic ray sources relative to other sources, the cosmic ray elemental abundances in these sources relative to those of normal cosmic ray sources, and the additional pathlength which the shrouds present to those cosmic rays which originate therein. The shrouds act as a slab of matter through which some cosmic rays propagate, in addition to the interstellar medium during propagation through the rest of the galaxy. The extra matter traversed by protons and helium nuclei in these clouds would provide added interaction rates for antiproton and positron production and annihilation. Heavy cosmic rays (e.g. C, N, O, and other elements heavier than He) would be broken down by spallation during passage through the clouds, so that the products are light isotopes (e.g. ^{3}He, deuterium, antiprotons, positrons, etc.). Propagation through the galaxy, outside of the shrouded sources, is calculated as with the SLBM. Any heavy cosmic rays which are detected at the Earth would come from non–shrouded sources. It is important to note that the bulk of the heavy cosmic rays in shrouded sources must be broken down to helium isotopes or lighter: Measurements of the (Li+Be+B)/(C+O) ratio imply that the escape pathlength of these nuclei through the galaxy is ~5–10 g/cm^2, depending on energy, and any excess of Li, Be, or B from shrouded sources would skew these measurements. Cowsik and Gaisser (1981) have estimated that, if 10% of all cosmic ray sources are shrouded in 50 g/cm^2 of matter, then the antiproton/proton ratio at 10 GeV increases by about a factor of 3 over the SLBM, while remaining consistent with the observed spectra of heavier cosmic rays. Lagage and Cesarsky (1985) have estimated that, if all cosmic ray sources were shrouded, the mean additional matter needed to explain the Golden et al.

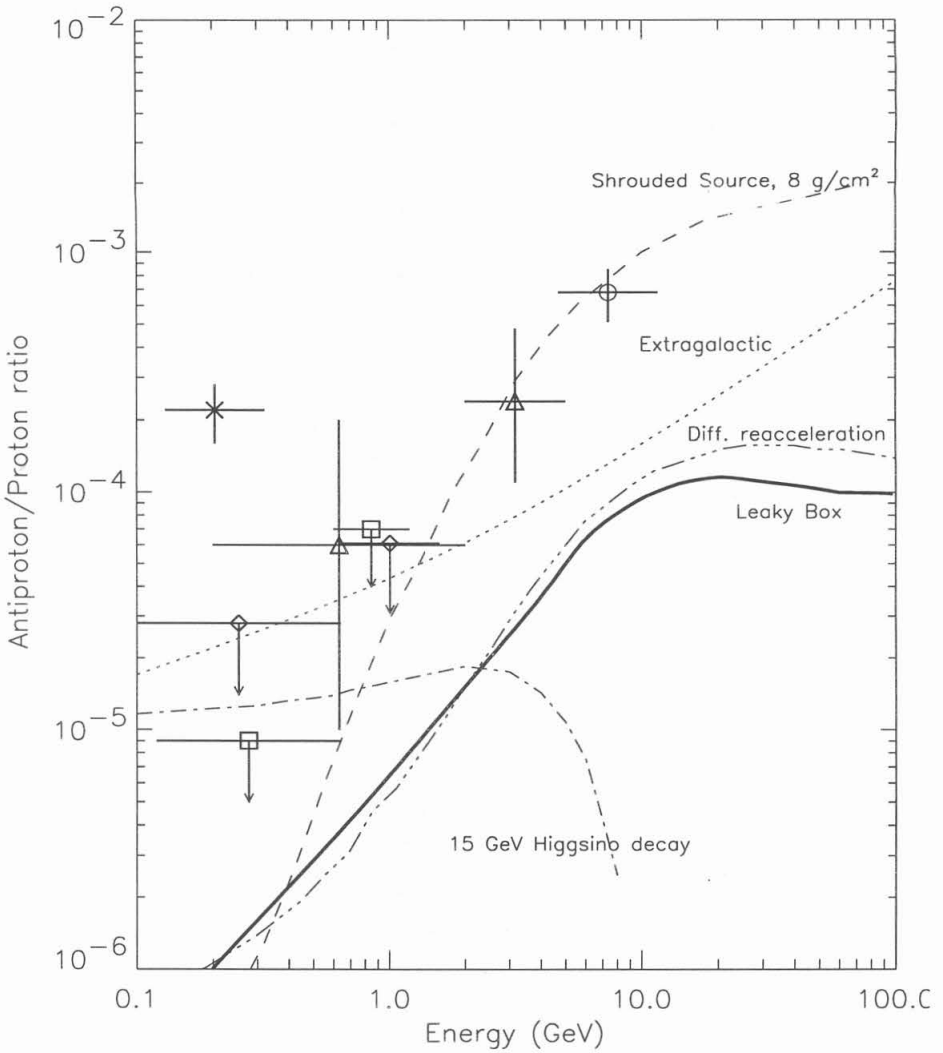

Figure 1.9: Comparison of antiproton/proton ratio measurements (listed in Figure 1.7) with the Standard Leaky Box Model calculation of Protheroe (1981), a dark matter decay calculation of Stecker and Tylka (1989), a Shrouded Source calculation by Lagage and Cesarsky (1985; the ratio is for particles exiting the source and shroud and does not include propagation), an extragalactic source curve with a rigidity dependence of $R^{0.7}$, and a diffusive reacceleration calculation by Simon and Heinbach (1996).

antiproton measurements would be about 7.5 g/cm^2, but such an additional grammage would result in an overproduction of Li, Be, and B and of Fe fragments. They estimate that the minimum grammage needed to eliminate this excess (by breaking up all heavy nuclei) would be about 30 g/cm^2, and the fraction of cosmic ray sources which are shrouded would be ~25%.

In addition to variations of standard cosmic ray propagation models, some authors have proposed "exotic" sources or production mechanisms for antiprotons. Hawking (1974) proposed that black holes may "evaporate" and lose mass by emission of photons or particles, with a black body spectrum characterized by the black hole mass. (Emission of particles can occur via pair production near the event horizon, with one entering the black hole and the other "emitted.") Such black hole evaporation could produce antiprotons, and with an energy spectrum with an index of about -3 (Kiraly et al. 1981), the contribution would be primarily to low energy antiproton abundance. Stephens and Golden (1987) point out that the minimum contribution from black holes needed to explain the early, low energy antiproton measurements conflicts with estimates of the maximum abundance of evaporating black holes from radio astronomy observations.

Another possible primary source of excess antiprotons is bulk antimatter, such as antimatter galaxies. In such an antimatter galaxy, antimatter cosmic rays would propagate as normal matter cosmic rays propagate through our own, and leakage from the antimatter galaxy would presumably be rigidity–dependent as well. In such a case, extragalactic contribution to the antiproton/proton ratio might follow a form of R^{δ}, where $\delta \sim 0.6$–0.7 to reflect rigidity–dependent leakage from other galaxies. An example is given in Figure 1.9, showing how extragalactic sources could contribute to antiproton abundances at higher energies.

It is important to note that both the extragalactic contributions and the black hole evaporation contributions are very uncertain, due to the unknown abundance of extragalactic sources of antimatter in the former and to the unknown abundance of evaporating black holes in the latter.

Finally, it is possible for antiprotons to arise as decay products from exotic, as yet undiscovered elementary particles. Among the more intriguing candidates for exotic particles are dark matter candidates, such as photinos and higgsinos. Calculations following the Buffington et al. (1981) measurements implied that essentially the entire cosmic ray antiproton spectrum up to ~10 GeV, as then measured, could be attributed to dark matter annihilation in the galactic halo (e.g. 15 GeV higgsino annihilation, see Stecker et al. 1985, and Rudaz and Stecker 1988). However, after the reported upper limits by LEAP and PBAR, Stecker and Tylka (1989) calculated that dark matter annihilation contributions to the antiproton abundance could not simultaneously account for the low energy upper limits as well as the high energy abundances of Golden et al. (1984). Instead, they suggested that further low–energy measurements might constrain the contributions due to dark matter annihilation. More recently, Diehl et al. (1995) have calculated possible contributions to cosmic ray antiproton abundance from the decay of supersymmetric dark matter candidates. They calculate the ratio of antiprotons from possible neutralino decays to antiprotons arising from cosmic ray interactions in the galaxy, for a range of neutralino masses and for antiproton energies in the range 100–200 MeV. For solar minimum conditions (see Section 5.2), they find that this ratio approaches ~0.6 for neutralinos of mass ~23 GeV, and the ratio drops rapidly for neutralinos of higher mass, approaching ~0.004 for neutralino masses around 80 GeV.

2. The Isotope Matter Antimatter Experiment

The Isotope Matter Antimatter Experiment (IMAX) payload was a balloon–borne superconducting magnet spectrometer designed to measure the galactic cosmic ray fluxes of protons, antiprotons, deuterium, ^{3}He and ^{4}He . (See Figure 2.1.) It used a combination of multiwire proportional counters (MWPCs) and drift chambers (DCs) to provide particle trajectories and rigidities in a magnetic field, a set of scintillators (two scintillator counters plus time–of–flight paddles) to provide charge determination via dE/dx ($\propto Z^2$) measurement, and a combination of three Cherenkov counters and a time–of–flight (TOF) system to provide velocity measurements. Concurrent measurement of particle rigidity, charge, and velocity yields unambiguous particle identification through mass and charge sign. The useful energy range for mass identification in IMAX extends from ~0.2 GeV/nucleon to ~3.2 GeV/nucleon.

IMAX is a collaboration between the California Institute of Technology (Caltech), the NASA Goddard Space Flight Center (GSFC), New Mexico State University (NMSU), the University of Siegen in Germany, and the Danish Space Research Institute (DSRI). Caltech provided the aerogel Cherenkov counters (C2 and C3) for IMAX, and DSRI provided some aerogel development support. NASA/GSFC provided overall management of IMAX, the time–of–flight system, and the S2 scintillator. The University of Siegen provided the drift chambers. New Mexico State University provided the IMAX payload framework (the NMSU Balloon Borne Magnet Facility), including the magnet and MWPCs, and overall payload support. Each institution was also responsible for calibration and preliminary data analysis relating to the detectors which they provided.

IMAX was designed to provide high resolution measurements in the critical energy range of ~0.2–3.2 GeV/nucleon, which includes the expected peak in the cosmic ray antiproton spectrum at ~2 GeV along with the associated decrease in antiproton intensity and antiproton/proton ratio at lower energy. IMAX has also extended ^{3}He and ^{4}He measurements to much higher energies than previously achieved. The payload detector systems provide multiple redundancy in measurements of rigidity (DC's and MWPCs), velocity (TOF, multiple

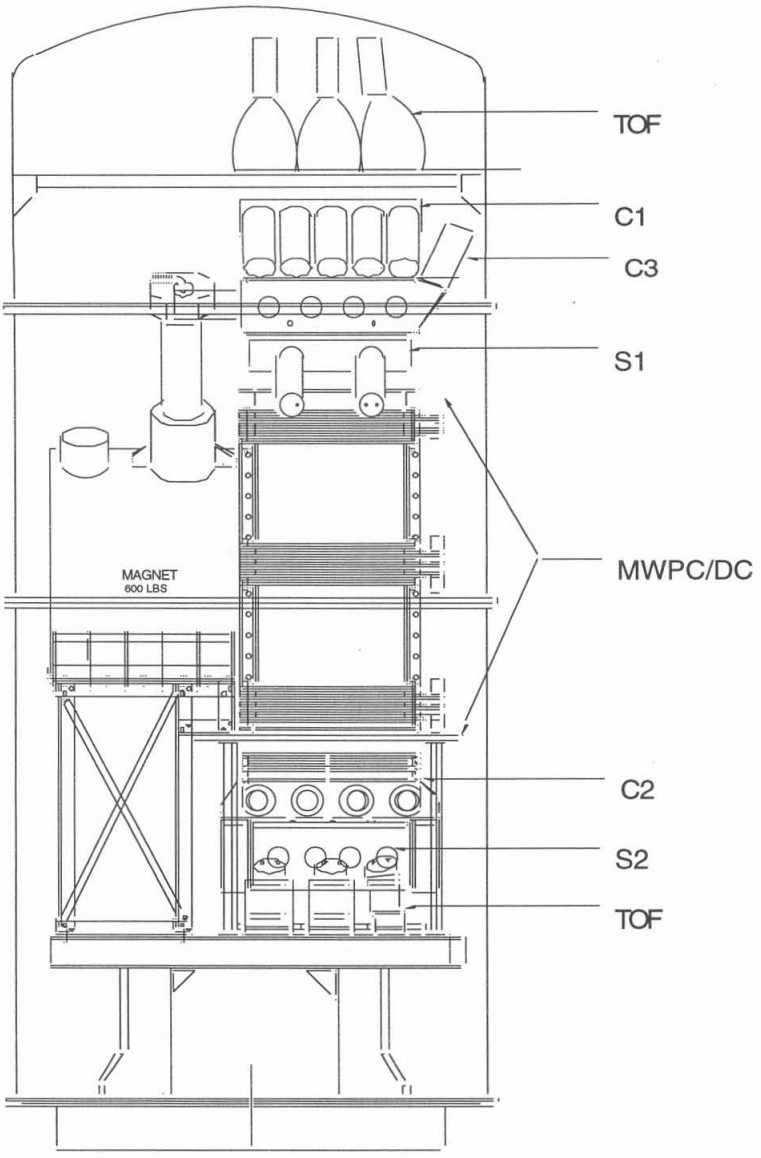

Figure 2.1: Isotope Matter Antimatter Experiment (IMAX) Payload Schematic. The detector systems are the top and bottom time–of–flight (TOF) paddles, the Teflon Cherenkov counter (C1), the two scintillator light integration boxes (S1 and S2), the two aerogel Cherenkov counters (C2 and C3), the drift chambers (DC), and the multiwire proportional counters (MWPC). Schematic courtesy of NMSU.

Cherenkov counters), and charge (four scintillator measurements per event). In combination, these measurements allow for particle identification by mass, via Cherenkov–Rigidity and TOF–Rigidity techniques.

This Chapter will cover descriptions of the IMAX payload and the individual detector systems, up to and including function, calibration, and flight performance. Science data analysis will be presented in Chapter 3.

2.1 Aerogel Cherenkov Counters

The two aerogel Cherenkov counters, designated C2 and C3, provided the primary method for velocity determination for $\beta \geq \sim 0.96$. These counters were developed by Caltech as its primary contribution to the IMAX payload (Labrador et al. 1993).

Each aerogel Cherenkov radiator was mounted on a light integration box constructed of 3/32" thick dip–brazed 6061 aluminum. The dip–brazing technique allowed the boxes to be constructed from a single piece of metal aluminum, folded into the appropriate shape, and the technique has the effect of both light–sealing the box and providing the necessary structural rigidity to the assembly. The boxes themselves were lined with a single thickness of millipore filter paper (0.1 micron pore size, type VCWP), providing a ~93-94% diffuse reflectivity at Cherenkov light wavelengths (i.e. < 400 nm). Millipore paper was chosen rather than barium sulfate paint because the paint tends to outgas solvents which degrade aerogel performance over time (Grove 1989).

The C2 and C3 box interiors were viewed by 14 and 16 photomultiplier tubes (PMTs), respectively. The PMTs were 3 inch diameter Hamamatsu 1848's, which provided the single–photoelectron resolution required for low light yield measurements. (See Section 2.1.1 for photoelectron scales.) They were also chosen because of their short profile, good quantum efficiency, and their dynode construction (box and grid plus mesh), which is relatively insensitive to low magnetic fields. During flight, the PMTs were run at +1500 Volts.

Magnetic shielding for the PMTs was accomplished with multilayer shields composed of steel tubing and high–μ material of different thicknesses customized for each PMT location. The PMTs were recessed at varying depths within their shields to provide for more efficient magnetic shielding; recessing the PMTs lowered measured light yield by ~10% relative to having the PMT faces nearly flush with the box interior surface. The mounting tubes were lined with aluminized mylar, which provides ~90% reflectivity at the wavelengths of interest.

C2 and C3 were designed to allow multiple silica aerogel blocks to be stacked on the tops of the boxes. (See Figures 2.2, 2.3 and 2.4.) Aerogels are of interest as Cherenkov radiators because they are the only solid radiators which can be made in a range of refractive indexes from ~1.01 to 1.25 (e.g. Poelz 1986; Rasmussen 1989). This range of indexes allows aerogel Cherenkov counters to measure particle velocities not easily measured by other Cherenkov radiators. Because they are solids, aerogels offer engineering convenience not available with liquid or gaseous radiators.

The aerogel index of refraction can be controlled during manufacture by controlling the density of the final aerogel. The experimentally–determined index–density relationship is given by the formula

$$n - 1 = 0.21\rho \tag{2.1.1}$$

where ρ is the density in grams per cubic centimeter, and n is the index of refraction (e.g. Henning and Svensson 1981; Poelz and Riethmüller 1982). By the chemical process alone, aerogels can be produced with n = ~1.01 – 1.06. Further sintering of the aerogel (i.e. heating at temperatures above 1000°C) can produce refractive indexes from 1.06 to about 1.25 (Rasmussen 1989). The ability to control the refractive index during manufacture is another feature which makes aerogels so useful in astrophysics and high–energy physics research, as will be discussed later in this section.

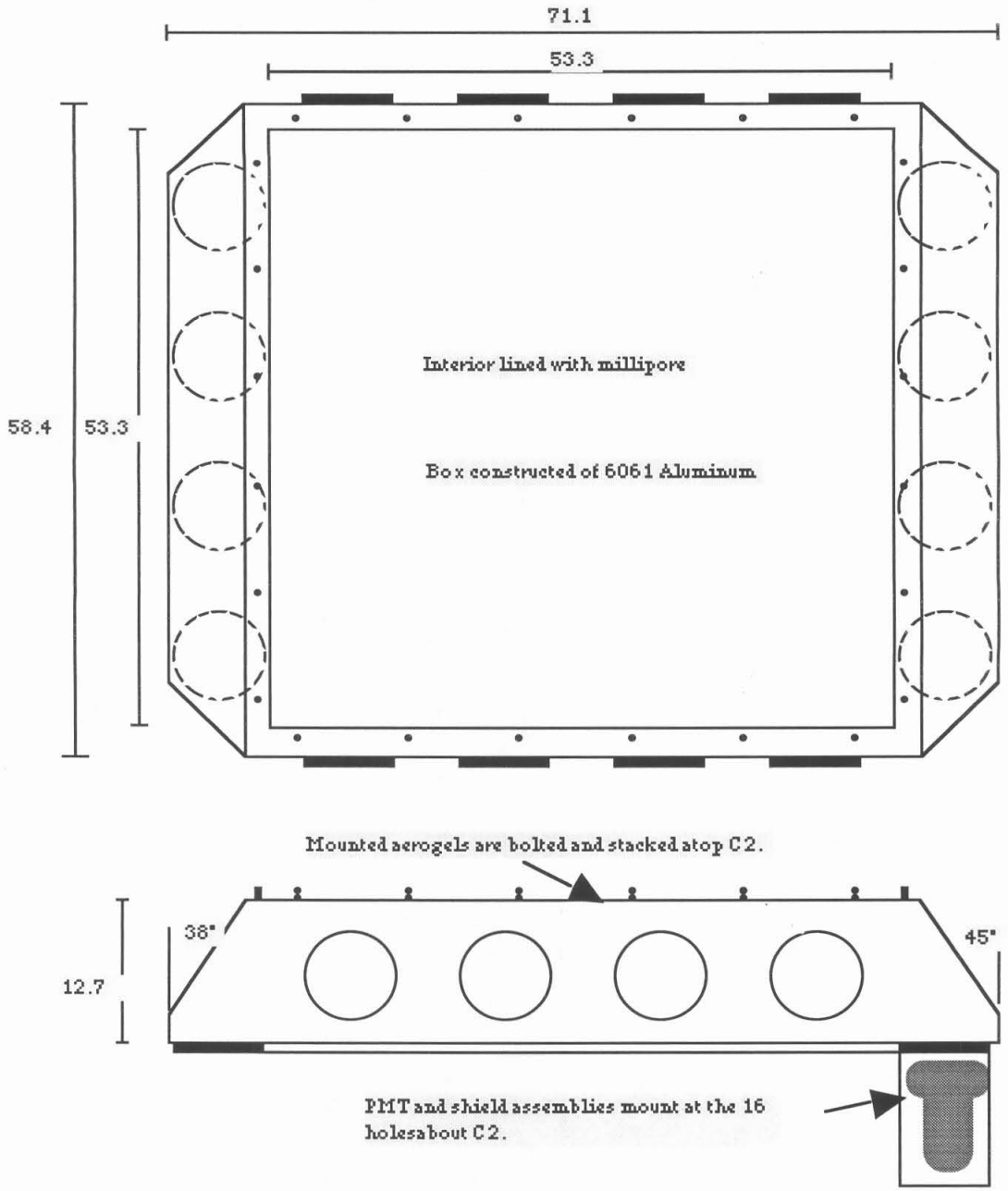

Figure 2.2: IMAX Aerogel Cherenkov Counter C2. Dimensions are in cm.

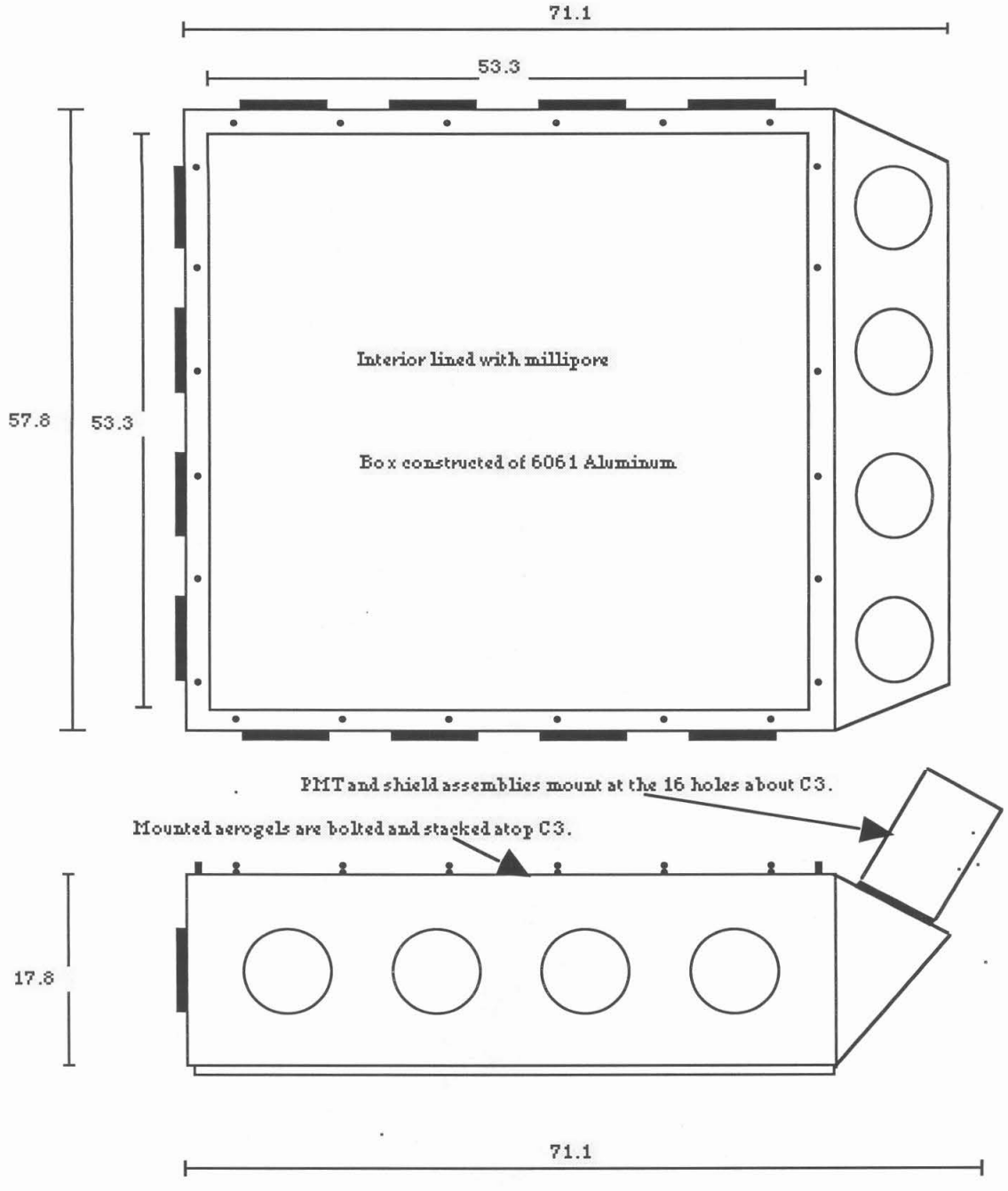

Figure 2.3: IMAX Aerogel Cherenkov Counter C3. Dimensions are in cm.

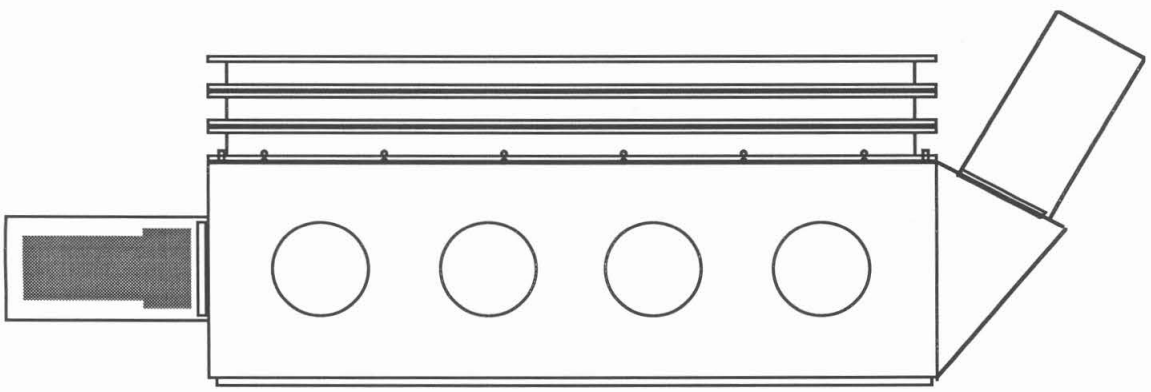

Figure 2.4: IMAX Aerogel Cherenkov Counter C3 with 3 stacked aerogels.

The aerogels used in IMAX were manufactured by the Airglass Company in Sweden. They have a measured refractive index of 1.043±0.002 and approximate total dimensions of 55 cm x 55 cm x 3 cm, considerably larger in area than the 14 cm x 14 cm blocks used in previous balloon-borne instruments (e.g. Rasmussen et al. 1983). Laboratory tests showed that, with our inventory of aerogels prior to the IMAX flight, three stacked aerogels atop each counter were sufficient to meet the performance requirements of the counters. (See Section 2.1.3 an explanation of the C2 and C3 performance requirements and Section 2.1.4 for a description of the index of refraction measurement. Further details concerning the manufacture, mounting, storage, and testing of aerogels for IMAX can be found in Appendix A.)

A charged particle passing through a Cherenkov radiator generates light according to the formula

$$\left(\frac{dE}{dx}\right)_{Cherenkov} = \frac{(Ze)^2}{c^2} \int_{\varepsilon(\omega)>\frac{1}{\beta^2}} \omega\left(1-\frac{1}{\beta^2\varepsilon(\omega)}\right)d\omega \qquad (2.1.2)$$

where dE/dx is the energy (emitted as Cherenkov light) per unit length of radiator traversed, Ze is the charge of the particle, β is the velocity of the particle (in units of c), and $\varepsilon(\omega)$ is the relative electric permittivity (dielectric "constant") of the radiator as a function of the frequency of the emitted light (e.g. Jackson 1975).

In IMAX, the Cherenkov counters are light integration boxes viewed by collections of PMTs, and only a fraction of the Cherenkov photons produced in the radiator are converted to photoelectrons at the PMT photocathodes. It is these resulting photoelectrons (pes) which are actually counted in IMAX data analysis. Therefore, it is simpler to assume integration of Equation 2.1.2, such that

$$L = KZ^2\left(1-\frac{1}{\beta^2 n^2}\right) \qquad (2.1.3)$$

where L is the measured light yield (in photoelectrons), n is the effective index of refraction, and K is a proportionality constant which includes various detector efficiencies. K can be determined experimentally by measuring the light yield of the radiator for Z=1, β=1 particles. In preliminary calibrations, it is sufficient to determine K by making measurements with secondary, relativistic cosmic ray muons generated in the upper atmosphere.

No Cherenkov radiation is produced for $\beta<1/n$. Given a known charge Z (determined from dE/dx measurements) and a positive Cherenkov light yield measurement, velocity may be determined between threshold ($\beta=1/n$) and saturation ($\beta\approx1$). In practice, velocity resolution is greatest in that portion of the Cherenkov light yield curve for which the slope is greatest — typically a limited range just above Cherenkov threshold, as shown in Figure 2.5 The figure also shows that one may select a useful velocity range (or energy range) by choosing a Cherenkov radiator of the appropriate index of refraction. Because aerogels may be manufactured with a range of refractive indices, one may in principle select threshold energies from 0.6 to ~5.7 GeV/nuc (index n from 1.25 to ~1.01).

The uncertainty in the velocity determination is given by

$$\frac{\partial\beta}{\beta} = \frac{n^2\beta^2}{2KZ^2}\partial L \qquad (2.1.4)$$

where, if we assume Poisson statistics, ∂L is roughly the square root of the measured photoelectron light yield of the particle. As will be discussed in later sections, other factors such as knock–on electrons and response variations across the aerogel radiators also contribute to the light yield uncertainty. The contribution of the velocity uncertainty to the mass resolution is proportional to $\partial\beta/\beta$. Clearly, since K is proportional to the "saturation" (Z=1, β=1) light yield of the counter, precise measurement of β requires as large a value of K as possible. The "saturation" light yield will be discussed in greater detail in Section 2.1.2.

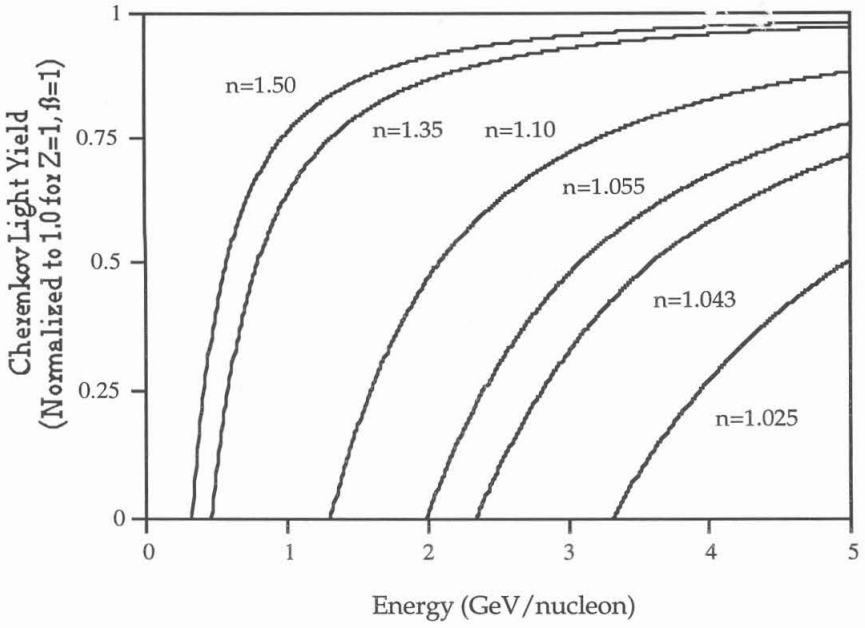

Figure 2.5: Cherenkov Light Yield vs. Energy per nucleon for various indexes of refraction.

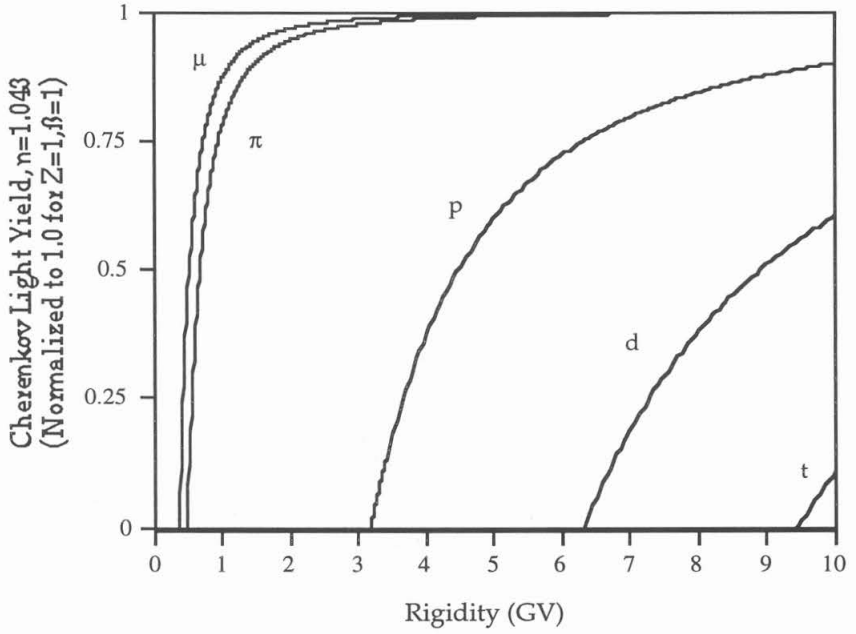

Figure 2.6: Cherenkov Light Yield vs. Rigidity for muons, pions, protons, deuterons, and tritons, for a radiator index of refraction n=1.043.

In addition to velocity determination, the IMAX Cherenkov counters provided discrimination between antiprotons and electrons or mesons of the same rigidity. At velocities below threshold, antiprotons produce no Cherenkov radiation, and the measured light signal is at the noise level. However, for the same magnetic rigidities (see Equation 2.1.10), electrons and negative muons travel above threshold velocity, producing Cherenkov radiation. (See Figure 2.6.) At these velocities, the electrons and negative muons produce Cherenkov light which we expect to follow a Poisson distribution with nonzero mean for each velocity. (There are additional contributions from response map uncertainties and knock–on electrons, but for IMAX, these are expected to be small relative to the Poisson statistics. See Sections 2.1.2 and 2.1.5 for discussions of response maps and knock–on electrons, respectively.) Thus, there is a nonzero probability, arising from statistical fluctuations in light yield, that electrons at saturation velocities (β near 1), but at magnetic rigidities below threshold for antiprotons, may be falsely identified as antiprotons. To minimize this probability, we again require that the saturation light yield be as high as possible. Section 2.1.3 gives a discussion of the aerogel Cherenkov performance requirements for IMAX.

2.1.1 Photoelectron Scales

The 30 C2 and C3 PMTs were pulse height analyzed individually by LeCroy 2249A analog–to–digital converters (ADCs) preceded by LeCroy 612A x10 voltage amplifiers. Because they are charge integrating ADCs, the 2249A inputs were modified with the addition of blocking capacitors, to eliminate voltage offsets from the voltage amplifier outputs. Gate widths for the ADCs were set at 200 ns during flight. (Trigger logic for IMAX is discussed in Section 2.6.)

When a photon strikes the PMT photocathode, a number of electrons are kicked off the photocathode, with the number of electrons dependent on the quantum efficiency of the photocathode material. The total number of electrons increases geometrically by the progress of the electron cascade along the PMT dynodes, and the resulting number of electrons reaching

the PMT output is proportional to the number of initial electrons provided at the photocathode. The Hamamatsu 1848 PMTs were chosen because, among other reasons, the output signals show clearly resolved 0 and 1 photoelectron (pe) peaks.

Figure 2.7 shows sample histograms of light yields from typical PMTs in C2 and C3 for a sample of charged particles passing through the radiator. The horizontal scale is in ADC channels, and the selected events for these histograms had high magnetic rigidities, implying high β and, thus, maximized average Cherenkov light yield in order to resolve higher photoelectron peaks. Marked on the histograms are the 0 pe peak, indicating zero light yield detected by the PMT, and the 1 pe peak, indicating a minimum positive measured light yield by the PMT. (Any given PMT signal is affected in part by the geometry of a particle trajectory through the counter, the location of the PMT relative to the counter geometry, the effects of any residual magnetic field penetrating the PMT magnetic shielding, and the quantum efficiency of the PMT photocathode.)

Note in the Figure that the 0 and 1 pe peaks are clearly resolved from one another. (The 0 pe peak is also referred to as the pedestal.) The width of these peaks arises from a combination of pe statistics and electronic noise in the system. Depending on the resolving power of the individual PMT, the 2 pe peak may also be seen to the right of the 1 pe peak. For single event measurements, it is critical to establish a photoelectron scale for each PMT based on the available light yield data compiled from similar histograms.

In order to fit a photoelectron scale from the light yield histograms, an algorithm combining chi–square minimization and robust estimation was developed to fit the 0, 1, 2, 3, and 4 pe peaks, approximated as Gaussian functions. The final algorithm chosen for fitting the photoelectron scales was a 6–pass, 10–parameter downhill simplex ("amoeba") fit, with limited error–checking (Press et al. 1988).

As can be seen from a typical histogram, only the 0 and 1 pe peaks are well–defined. Therefore, these peaks are fitted individually as full Gaussians (amplitude, centroid, and width), accounting for 6 of the 10 parameters in the fit. The 2 pe peak is usually a slight bump

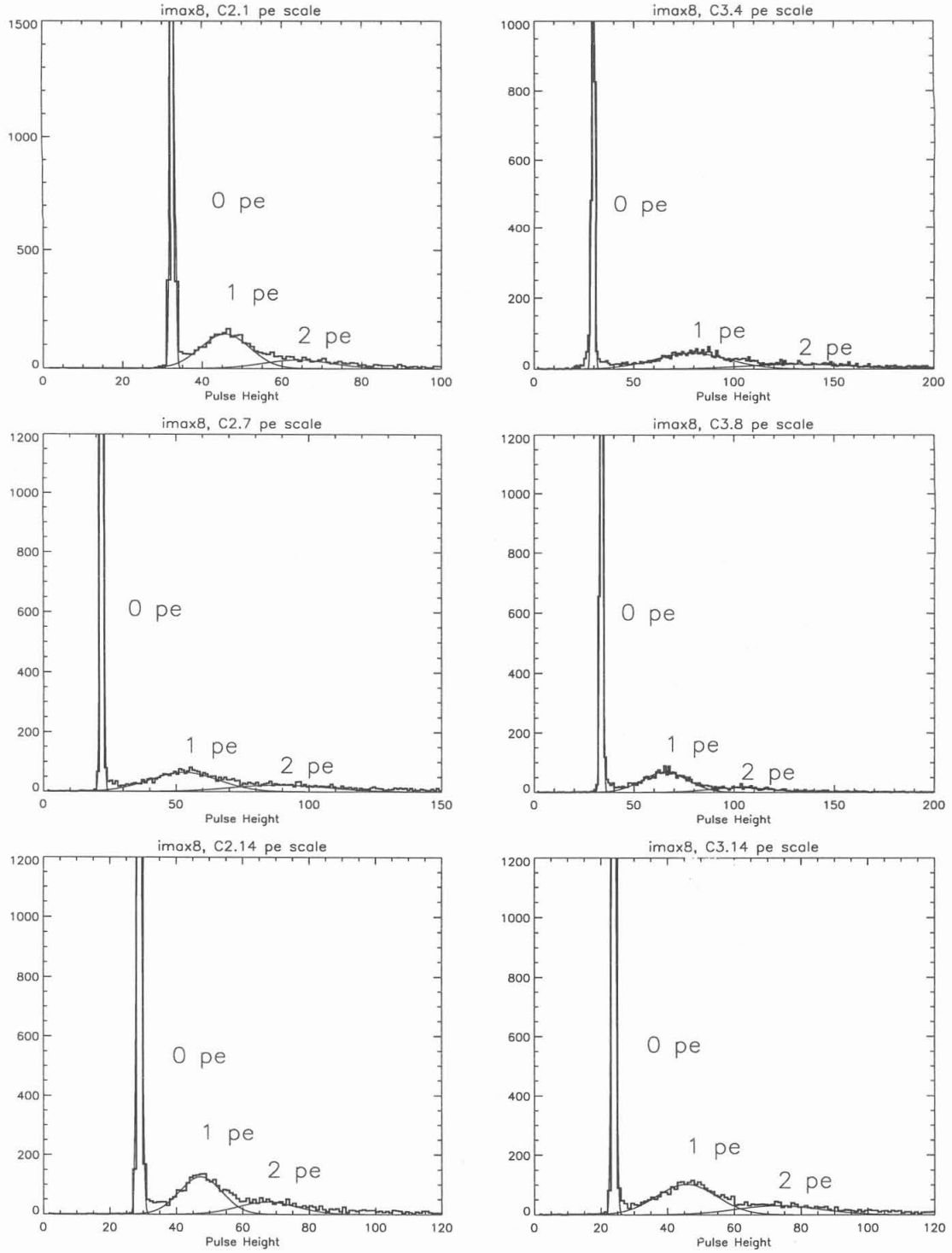

Figure 2.7: Cherenkov light yield histograms for selected PMTs from C2 and C3. One hour of data is included in each histogram. The 0, 1, and 2 pe peak fits are shown.

on the right of the 1 pe peak, and the 3 and 4 pe peaks may be visually indistinguishable from a flat background to the right of the 2 pe peak. The width of the 2 pe peak is scaled from the widths of the 0 and 1 pe peaks, while its amplitude and centroid are fitted as free parameters, accounting for an additional 2 parameters. For the 3 and 4 pe peaks, only the amplitudes are free parameters, accounting for the remaining 2 parameters in the fit, while the centroid locations are scaled from the 1–2 pe peak centroid spacing and the widths are scaled from those of the 0 and 1 pe peaks. As an additional precaution against faulty fitting, the "meniscus" between the 0 and 1 pe peak is excluded from the fit. (See the Figure.)

Implicit in the limited number of fit parameters is the assumption of a piece–wise linearity in the ADC scale: All signals above the 1 pe centroid are assumed linear according to the 1–2 pe peak spacing, while signals below the 1 pe centroid are assumed linear according to the 0–1 pe peak spacing. Attempts to model ADC nonlinearity in greater detail failed because of limited statistics above 2 pes and generally poorer peak resolution above 1 pe. Because the Cherenkov signals of interest are dominated by the 0 and 1 pe peaks, the current photoelectron scales are sufficient for both the antiproton measurements and the isotope measurements.

The fit algorithm involved six passes by the downhill simplex method. Prior to the first pass, the histogram local maxima are located and used to estimate the 0 and 1 pe peak amplitudes and centroids. The initial estimate for the 2, 3, and 4 pe peaks is made assuming complete linearity from the 0 and 1 pe peak centroid approximations. From these estimates, an initial simplex in 10–parameter space is defined, and the downhill simplex algorithm is allowed to find the minimum of $|\chi|$ = |histogram – fitting function| for three passes. The simplex for the second and third passes are defined by the results of the first and second passes, respectively. The fourth pass takes the results of the third pass, generates a smaller simplex, and similarly minimizes $|\chi|$. Finally, the fifth and sixth passes utilize small simplexes and minimizes χ^2. These multiple passes allow the simplex to be kicked out of local minima in the 10–parameter phase space being explored.

Furthermore, after each pass, a separate algorithm examines the results of the previous pass to check for known classes of errors. These errors include cases in which the 3 or 4 pe peak is substituted by the algorithm for the 2 pe peak and in which the 2 pe peak is, therefore, suppressed. Similar errors include the 2 pe peak substituting for the 1 pe peak while the 1 pe peak is suppressed. When any such errors are detected, the simplex is reset, and the previous downhill simplex pass is re–run. When errors are repeated or a threshold number of attempts at a given pass fail, the fit of the given histogram is marked as having failed. To bypass such a failure, it has proven sufficient to add more data to the histogram in order to improve statistics and improve the resolution of the 0, 1, and 2 pe peaks, resulting in a successful fit at the expense of time–resolution in the time–dependence of the photoelectron scales.

The photoelectron scale data used by IMAX data includes only the fitted centroid locations for the 0, 1, and 2 pe peaks. Because the temperature during the IMAX flight (see Figure 2.8) varied widely during the flight, we incorporated rough time–dependence in the photoelectron scales. Changing temperatures could change the gain of a given amplifier or shift the pedestal of a given ADC. Shifts in the 0 pe peak centroid (the pedestal) can be independent of the total signal gain (0–1 and 1–2 pe peak spacing). Figure 2.9 shows such time–dependence for a number of C2 and C3 PMTs. Photoelectron scales were fit in roughly half–hour, one hour, and two hour intervals. If shorter time scale fits failed, they were combined into larger time segments for successful fits. It was found that the photoelectron scales varied slowly enough over the flight that it was unnecessary to fit a detailed function to the time–dependence of the photoelectron scales.

Although the signals represent quantized entities (e.g. 0, 1, and 2 pes), quantization of the measured photoelectron signals was not enforced in the analysis. Keeping the linear scaled photoelectron light yield preserved information such as electronic noise, demonstrated, for example, by the widths of total 0 pe histograms. (See Figure 2.10.) This width and results from random trigger runs and thermal tests put the electronic noise at less than 1 pe.

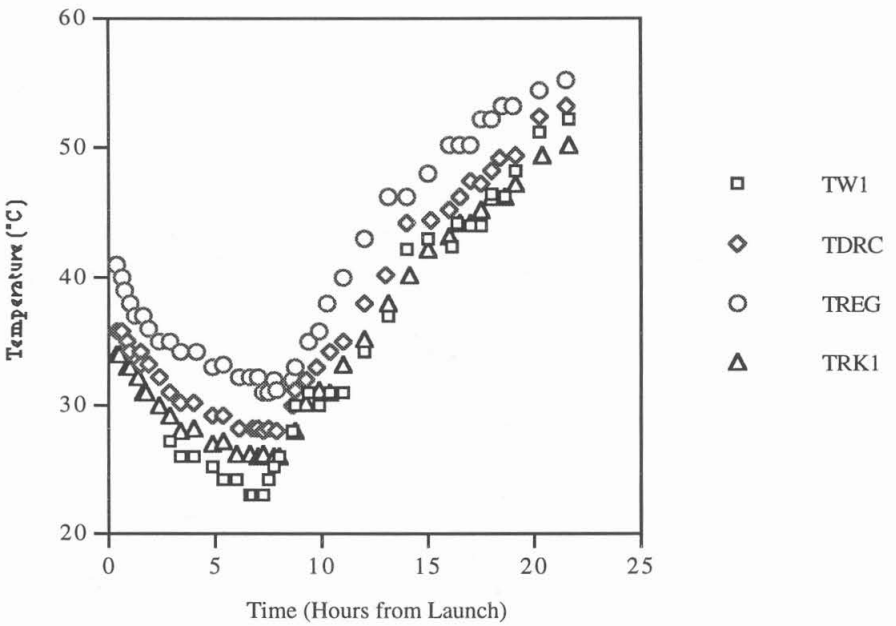

Figure 2.8: Temperature vs. Time in the IMAX Payload during flight. Temperature readings from four locations in the payload are shown. The temperature probes were on the wall near rack 1 (TW1), near the drift chamber electronics crate (TDRC), near the rack 0 regulator (TREG), and near rack 1 (TRK1).

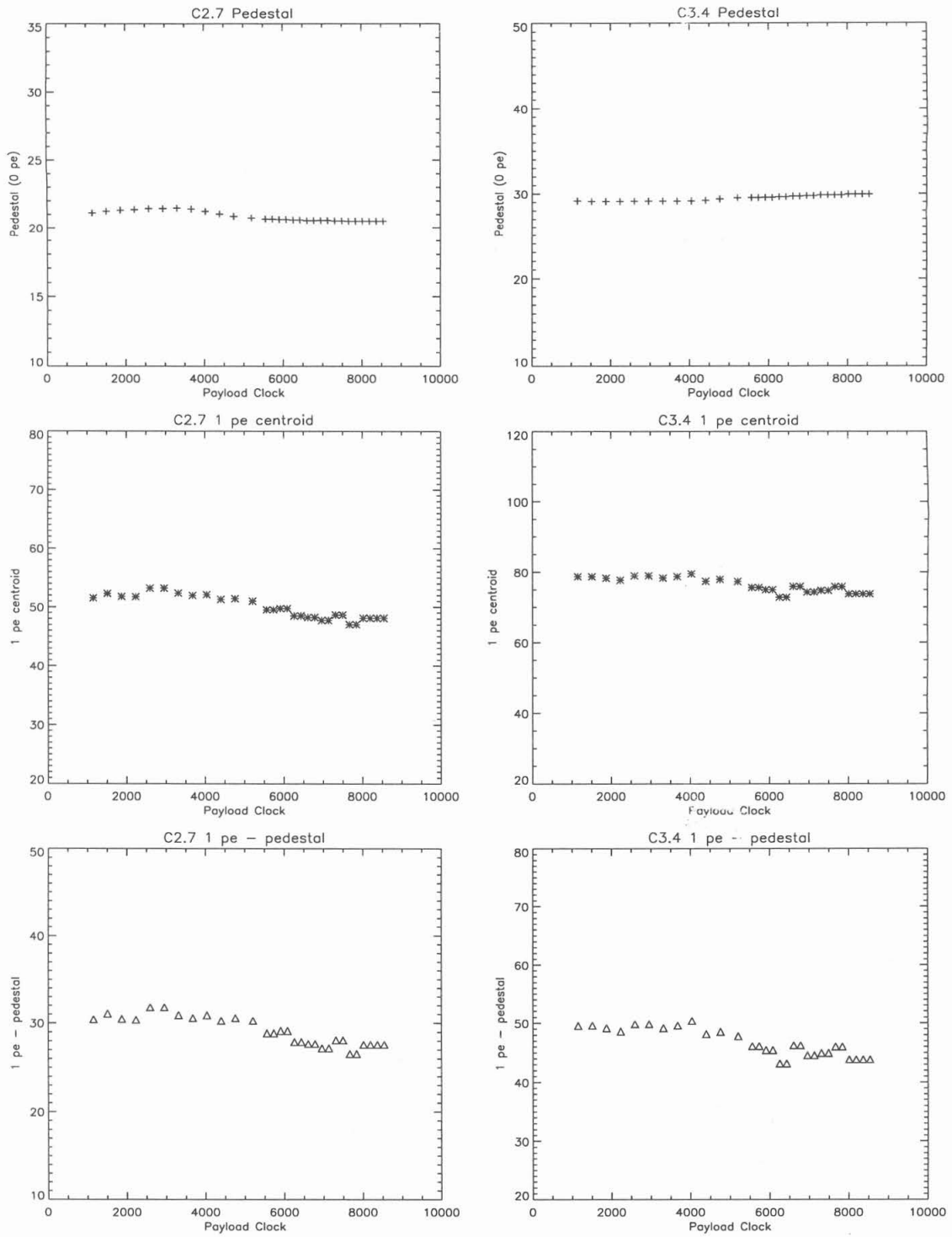

Figure 2.9: Time–dependence of the pe scales for selected C2 and C3 PMTs. The 0 and 1 pe peaks shift in ADC channels, and the 0–1 pe spacing shows changes in gain. Plots are for entire flight.

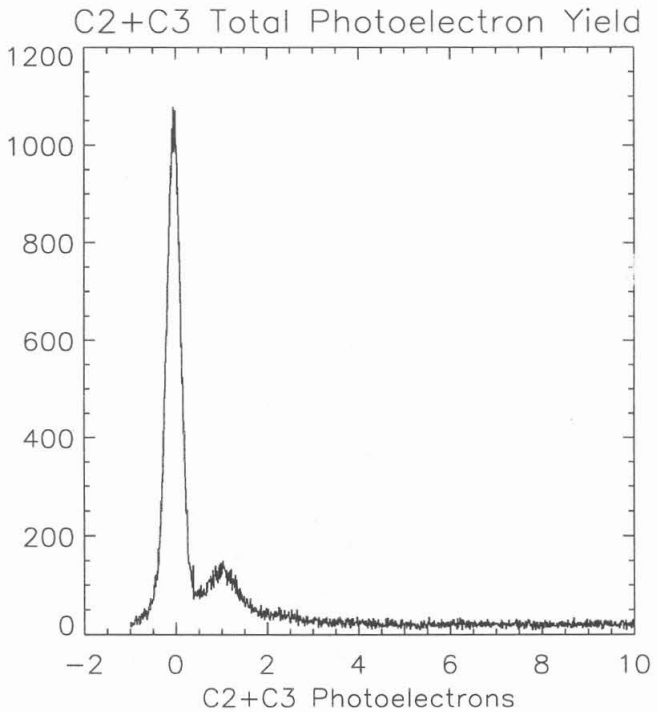

Figure 2.10: Total photoelectron yield (C2+C3), for one hour of sample data at float altitude.

Ultimately, the total photoelectron light yield for a given event was calculated by summing the scaled light yields from the individual PMTs of a given counter:

$$L = \sum_i l_i \tag{2.1.5}$$

where l_i is the photoelectron light yield measured by the i^{th} PMT in the counter, and L is the total photoelectron light yield for the counter. (A "fraction of 0's" method for estimating average light yields is further described in Appendix A.)

2.1.2 Aerogel Response Maps

For any given particle, a simple Cherenkov photoelectron light yield is insufficient to determine the velocity of the particle. For purposes of calibration, what is needed is the light yield for Z=1, β=1 particles. For C2 and C3, this light yield is dependent, to varying degrees, on position–dependent non–uniformities in the aerogel response, the light collection geometry at various points along the counters, and on the angle at which the particle passes through the radiator. (See Section 2.1.6 for a discussion of the effect of trajectory angle.)

Because the Cherenkov counter response can vary with the particle position in the counter, this response must be mapped to determine position dependence. We define Cherenkov response map value, M, to be the Cherenkov light yield, L, at some position in the counter, for a Z=1, β=1 particle. Employing Equation 2.1.3, we get

$$M = K\left(1 - \frac{1}{n^2}\right) \tag{2.1.6}$$

Dividing Equation 2.1.3 by Equation 2.1.6 yields

$$f \equiv \frac{L}{M} = Z^2 \frac{\left(1 - \frac{1}{\beta^2 n^2}\right)}{\left(1 - \frac{1}{n^2}\right)} \tag{2.1.7}$$

where f=L/M is called the normalized Cherenkov light yield. Position dependence is implied for both M and n. (The index map is discussed in Section 2.1.4. See Section 2.1.1 for a description of L. M may be defined similarly by M=L(β=1).)

In terms of measured photoelectron light yields (see Section 2.1.1), we may write f as

$$f \equiv \frac{L}{M} = \frac{\sum_i l_i}{\sum_i \overline{l_i(\beta = 1)}} \tag{2.1.8}$$

where the sum in the numerator is over the PMT measured photoelectron light yields for a given particle or event, and the sum in the denominator is over PMT measured photoelectron light yields averaged individually for β=1.

From Equation 2.1.7, solving for β is straightforward:

$$\beta = \frac{1}{\sqrt{n^2 - \frac{L}{M}\frac{(n^2 - 1)}{Z^2}}} \tag{2.1.9}$$

One may obtain estimated response maps for C2 and C3 by fitting Poisson distributions to the light yield histograms for Z=1, high–rigidity (high β) particles, for various x,y position bins in the counters. However, for IMAX, another method allows more events to be employed per mapping bin, yielding greater statistical precision. The magnetic rigidity for a charged particle is defined as

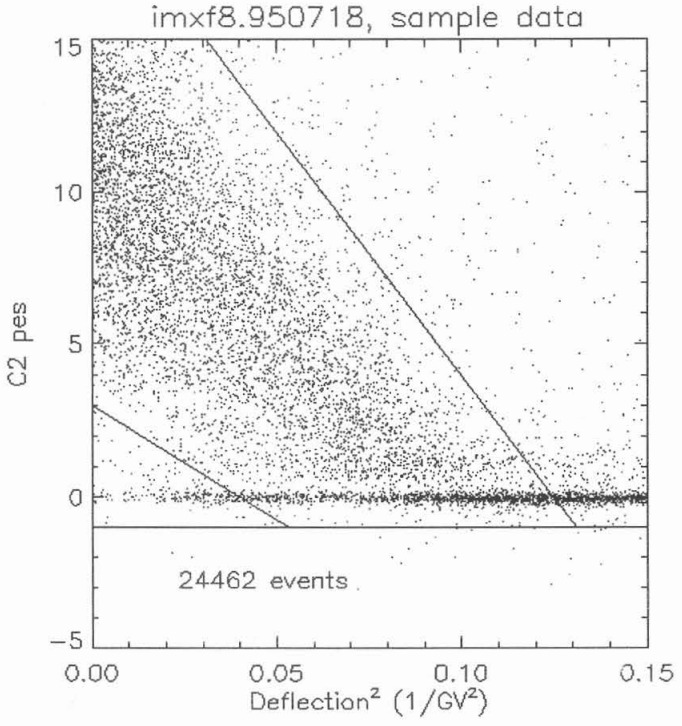

Figure 2.11: Cherenkov light yield vs. deflection^2 for a 20x20 cm^2 bin in C2, for a sample of protons from flight data. Also shown are first iteration limits imposed for mapping Cherenkov response and index of refraction.

$$R = \frac{pc}{Ze} = \frac{mc^2}{Ze}\frac{\beta}{\sqrt{1-\beta^2}} \tag{2.1.10}$$

Using this expression and Equation 2.1.3, we may rewrite the Cherenkov photoelectron light yield in terms of magnetic rigidity, rather than β:

$$L = KZ^2\left(1-\frac{1}{n^2}\right)-\frac{K}{n^2}\left(\frac{mc^2}{e}\right)^2\frac{1}{R^2} \tag{2.1.11}$$

The quantity 1/R is defined as the deflection of the particle. By this equation, L is linear in the square of the deflection. At high rigidity, L converges to MZ^2. For a given species of particle of mass m, Z=1, and a range of deflections, a linear fit of L vs. $1/R^2$ should yield the response map value M as the y–intercept. Furthermore, as will be discussed in Section 2.1.4, this fit will provide an estimate of the index of refraction, n.

In order to generate response maps for C2 and C3 from flight data, selection was made for protons, which represent the vast majority of the useful flight events. Selection criteria for protons and antiprotons are described in Chapter 3. Figure 2.11 shows a sample plot of L vs. $1/R^2$ for one 20 cm x 20 cm mapping bin from C2. The dark band of points represents proton data. Upper and lower limits shown on the figure were established in order to reduce the effects of below–threshold protons, deuterons, electrons on the linear fit. Furthermore, an absolute lower limit of -1 pe was chosen for each counter, with a cross–check that the other counter had at least 3 pes. This cross–check was selected to allow a small fraction of near threshold events to be included in the fit, in order to improve determination of the refractive index maps; see Section 2.1.4. The cross–check had minimal effect on response map determination. Several linear fits were attempted, including linear regression and robust estimation. At any given rigidity, the Cherenkov light yield distribution approximates a Poisson distribution. While a

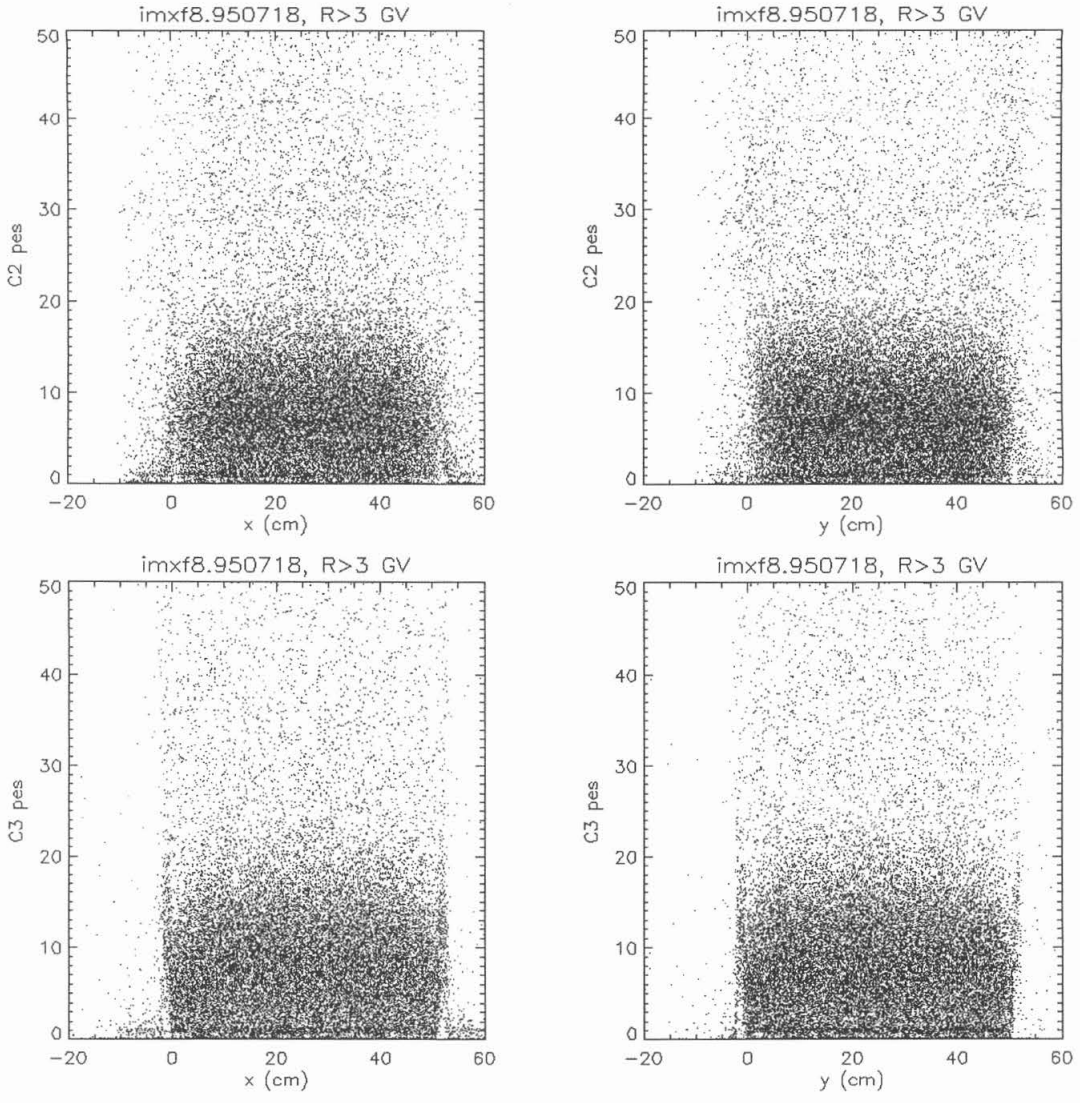

Figure 2.12: C2 and C3 light yield vs. x and y coordinates. Sylgard 184 spikes are evident at the edges of the counters.

robust estimation linear fit is less susceptible to outlier points than a linear regression, the robust estimation tends to fit to the median which, in a Poisson distribution, is lower than the mean, μ. A linear regression yields results closer to the mean. Therefore, the final mapping algorithm was a two–step iteration, with the first step being a robust estimation of the line using the initial limits described earlier. In the second iteration, tighter upper and lower limits were imposed to eliminate outliers, based on the robust estimation fit, and a linear regression was applied for the final fit.

Once the response mapping method was chosen, mapping bin size and counter active areas had to be chosen. Figure 2.12 shows photoelectron light yield vs. x and photoelectron light yield vs. y in the counters. Of special note are the large spikes in light yield at the edges of the counters. In laboratory tests, it was found that the Sylgard 184 which is used as the aerogel potting material (see Appendix A) produces Cherenkov or scintillation light. In order to reduce mixing Cherenkov light from the aerogels with light from the Sylgard 184, the C2 and C3 active areas were chosen to lie safely within the boundaries defined by the Sylgard 184 signal. The active areas for C2 and C3 are defined in Table 2.1.1.

Table 2.1.1: C2 and C3 Active Areas, in Drift Chamber Coordinates

	x (cm)	y (cm)
C2	$1.0 \leq x \leq 50.0$	$3.0 \leq y \leq 49.0$
C3	$0.0 \leq x \leq 50.0$	$0.0 \leq y \leq 50.0$

Bin sizes were chosen to be 4.9 cm x 4.6 cm for C2 and 5.0 cm x 5.0 cm for C3. Larger bin sizes reduced mapping resolution needed toward the edges, while much smaller bin sizes were less meaningful for ~9 cm of aerogel vertical thickness. Figures 2.13 and 2.14 show the aerogel response maps used for this analysis; the numerical values per bin are given in Table 2.1.2. Bilinear interpolation was used to provide smoothing in the use of the response maps, and at

Table 2.1.2: C2 and C3 Flight Response Maps (960619)

Units are in Photoelectrons (pes)

C2	map								
8.2±0.18	9.3±0.13	9.9±0.12	9.9±0.12	10.1±0.12	10.0±0.12	9.9±0.13	9.6±0.11	9.0±0.13	8.0±0.18
8.2±0.12	9.5±0.09	9.9±0.09	10.4±0.09	10.4±0.09	10.4±0.09	10.3±0.09	9.7±0.09	9.4±0.09	8.3±0.13
8.6±0.13	9.7±0.09	10.2±0.08	10.5±0.09	10.5±0.08	10.5±0.08	10.5±0.08	10.3±0.09	9.7±0.09	9.1±0.13
8.5±0.12	10.1±0.09	10.6±0.09	10.8±0.08	10.7±0.08	10.7±0.08	10.3±0.08	10.4±0.09	10.0±0.09	9.2±0.12
8.9±0.14	10.2±0.09	10.7±0.08	11.1±0.08	10.7±0.08	10.8±0.08	10.7±0.09	10.7±0.09	10.2±0.09	9.2±0.12
9.3±0.13	10.6±0.09	10.8±0.08	11.0±0.08	11.1±0.08	11.1±0.08	11.0±0.08	11.0±0.08	10.4±0.09	9.2±0.12
9.4±0.12	10.8±0.09	11.0±0.08	11.1±0.08	10.9±0.08	11.2±0.08	10.9±0.08	11.1±0.09	10.6±0.09	9.8±0.13
9.6±0.13	10.9±0.09	11.2±0.08	11.2±0.08	11.4±0.08	11.2±0.08	11.2±0.09	11.1±0.09	10.8±0.09	9.4±0.12
9.8±0.14	11.0±0.09	11.3±0.08	11.4±0.08	11.4±0.09	11.3±0.09	11.4±0.09	11.1±0.09	11.1±0.10	10.0±0.13
9.9±0.17	11.1±0.11	11.2±0.10	11.2±0.10	11.1±0.10	11.1±0.11	11.3±0.11	11.1±0.11	10.9±0.12	10.1±0.16

C3	map								
9.0±0.13	10.0±0.11	10.5±0.12	10.5±0.12	10.7±0.12	10.7±0.12	10.5±0.12	10.6±0.12	10.1±0.13	9.1±0.13
9.8±0.12	11.1±0.11	11.6±0.10	11.8±0.10	11.8±0.10	11.9±0.10	11.9±0.11	11.8±0.12	11.2±0.11	10.0±0.13
10.0±0.12	11.7±0.10	12.3±0.11	12.4±0.10	12.4±0.10	12.4±0.11	12.5±0.11	12.4±0.11	11.9±0.11	10.2±0.12
10.2±0.11	11.9±0.11	12.2±0.11	12.3±0.10	12.6±0.10	12.5±0.11	12.5±0.10	12.6±0.11	12.0±0.11	10.4±0.12
10.1±0.10	12.1±0.10	12.5±0.10	12.7±0.10	12.5±0.10	12.7±0.10	12.6±0.10	12.4±0.10	12.1±0.10	10.5±0.11
10.1±0.10	12.0±0.10	12.4±0.10	12.5±0.09	12.9±0.10	12.8±0.10	12.8±0.10	12.6±0.10	12.6±0.11	10.8±0.11
10.1±0.10	12.0±0.10	12.4±0.10	12.5±0.10	12.7±0.10	12.7±0.10	12.8±0.10	12.7±0.11	12.2±0.11	10.8±0.11
9.9±0.11	11.8±0.10	12.5±0.10	12.4±0.10	12.6±0.10	12.6±0.10	12.7±0.10	12.5±0.11	12.0±0.11	10.7±0.11
9.7±0.10	11.4±0.10	11.8±0.10	11.9±0.10	11.9±0.10	12.1±0.10	12.0±0.11	11.8±0.10	11.7±0.11	10.5±0.11
8.9±0.10	10.0±0.10	10.2±0.10	10.5±0.10	10.4±0.10	10.4±0.10	10.4±0.11	10.2±0.11	10.2±0.12	9.4±0.11

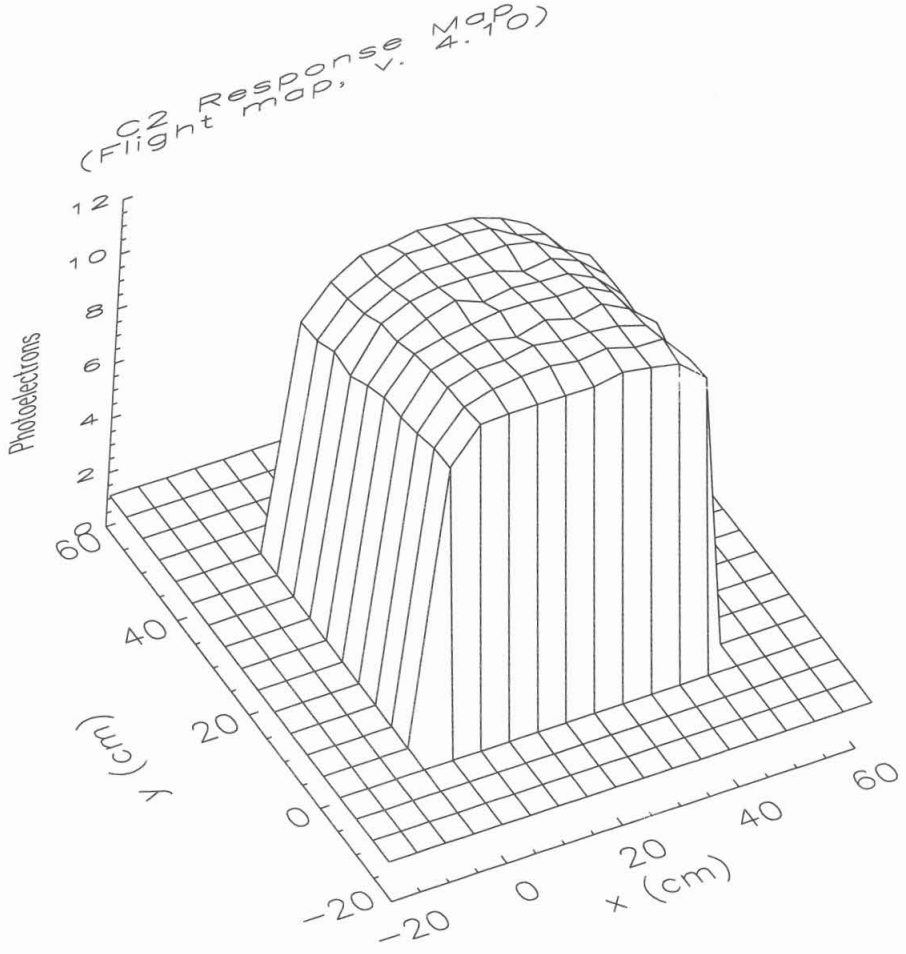

Figure 2.13: C2 Response Map. The coordinates are defined by the tracking system.

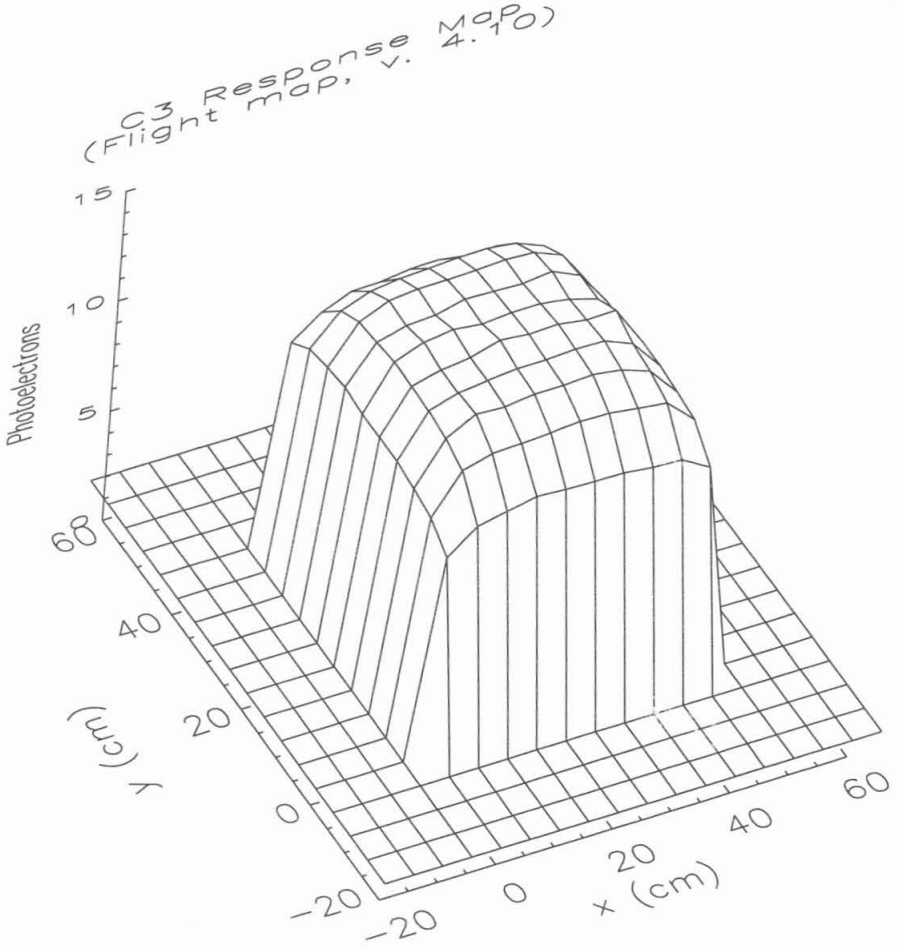

Figure 2.14: C3 Response Map.

the edges, *bilinear* extrapolation was implemented with the two mapping bins adjacent to a given map edge. An important characteristic of the response maps is the remarkable flatness over most of the total active areas.

2.1.3 C2 and C3 Performance Requirements and Characteristics

In the absence of other detectors, the aerogel Cherenkov detectors had to provide excellent discrimination between Z=1, $\beta \approx 1$ particles (e.g. electrons) and Z=1, $\beta \leq 1$ particles (e.g. protons) at the same magnetic rigidity. A sufficiently strong discrimination factor would reduce false antiproton background to levels well below the reported antiproton/proton ratios in the energy range covered by IMAX. Additional discrimination was provided by the time–of–flight system, which is discussed in Section 2.3, and the spectrometer.

For comparison, the electron flux, at the top of the atmosphere, is on the order of 10 $(m^2 \text{ s sr GeV})^{-1}$ at the rigidities of interest for IMAX (Golden et al. 1994; Clem et al. 1995). The expected antiproton flux is ≤ 0.03 $(m^2 \text{ s sr GeV})^{-1}$, and the expected proton flux is ~1000 $(m^2 \text{ s sr GeV})^{-1}$. Assume that the Cherenkov light yield distribution for a monoenergetic set of Z=1 particles follows a Poisson distribution

$$p(x,\mu) = \frac{\mu^x}{x!} e^{-\mu} \tag{2.1.12}$$

In this case, the average theoretical light yield for a particle in this distribution is μ, and $p(x,\mu)$ gives the probability that the measured light yield fluctuates to x. The probability that the light yield will fluctuate below some threshold x_0 is given by

$$\begin{aligned} p(\leq x_0,\mu) &= \int_0^{x_0} p(x,\mu)dx = e^{-\mu} \int_0^{x_0} \frac{\mu^x}{x!} dx \\ &\approx e^{-\mu} \sum_{x=0}^{x_0} \frac{\mu^x}{x!} \end{aligned} \tag{2.1.13}$$

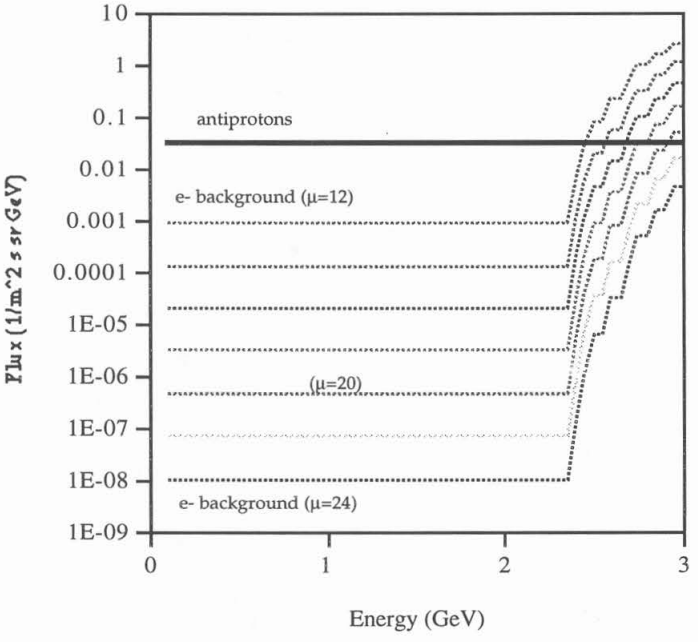

Figure 2.15: Calculation of electron background in the antiproton flux measurement for varying Cherenkov response levels (μ). The Cherenkov response levels, as shown, range from 12 pes to 24 pes in 2 pe steps.

Since *photoelectrons* are quantized, the summation form of Equation 2.1.13 is an adequate approximation. A series of calculations employing this equation shows that, for $x_0 \leq 1.5$ pes, a $Z=1$, $\beta=1$ light yield of $\mu \geq \sim 20$ pes yields an electron background which is approximately 10^{-5} that of the expected antiproton flux. (See Figure 2.15.) The combined light yield of C2 and C3 almost always exceeds this light yield. (See Table 2.1.2.)

2.1.4 Determination of Aerogel Index of Refraction

The Cherenkov response mapping algorithm described in Section 2.1.2 can also be used to determine the index of refraction of the aerogels to limited precision. In this case, the x–intercept of Equation 2.1.11 can be used to calculate the index. Specifically, one obtains a linear fit of Cherenkov light yield (L) vs. the square of deflection (or $1/R^2$) to proton data, and the x–intercept yields a threshold deflection or rigidity. From Equation 2.1.10, a threshold velocity, $\beta_{threshold}$, arises from the threshold rigidity, and the index of refraction is calculated as $n=1/\beta_{threshold}$.

In practice, the precision of the technique is limited by characteristics of the data set. Again, because protons comprised the vast majority of useable events in the flight data, the same protons used for response map determination were also used for the final index maps. Of the protons used in this mapping, ~50% had squared deflections less than 0.025 GV^{-2}, and ~79% had squared deflections less than 0.05 GV^{-2}. Because the squared deflection at threshold is approximately 0.1 GV^{-2}, the bias of the data toward low deflections and away from threshold deflection make this method less precise for determining index. A competing and opposite effect arises from fluctuations due to knock–on electrons (see Section 2.1.5) produced by protons near threshold, which can apply a strong upward bias to the apparent index of refraction. A linear fit may be well–determined from data near zero deflection, avoiding or reducing the effects of knock–on electrons from near–threshold events..

One selection criterion was chosen to help improve index determination: For any given mapping event, light yield as low as -1 pe were allowed for one counter, as long as the opposite

counter had light yield above 3 pes for the same event. The intended effect was to allow for the inclusion of near–threshold events whose light yields in one counter may fluctuate down to zero, increasing the contribution of near–threshold events to the linear fits.

The aerogels were originally assumed to have index of 1.055, based on the manufacturer's chemical stoichiometry during the manufacturing process. (See Appendix A.) Preliminary maps of the index of refraction used muons detected at ground level as the mapping particles, and these maps implied an average index of refraction of ~1.043. Application of this index mapping method to the Teflon Cherenkov counter, C1, yielded the expected index of refraction of ~1.36, consistent with the nominal value of n=1.355 (Gibner 1992) and demonstrating the usefulness of this technique.

Final maps of the C2 and C3 aerogel indexes of refraction yielded indexes of n=1.0453±(0.0009, 0.0010) at the centers of the aerogels, where the mapping statistics are best. The first uncertainty is measure the scatter of the bin values, and the second is a measure of the average statistical uncertainty for the individual bins. Over the active areas of the counters, these maps show indexes which can vary to as low as 1.033 and as high as 1.055. However, most of these variations occur toward the edges of the counters, where the number of mapping events is low and the resulting statistical uncertainties in index can be as high as ±0.1. Thus, it cannot be determined whether the variations arise from real variations in index, from limitations of the mapping method and the mapping statistics, or from other systematic effects. Therefore, while the technique is useful for mapping counter response (which is expected to have real variations, due to counter geometry), it is not very useful for mapping index of refraction in this case.

Instead, the L vs. $1/R^2$ technique is best used to determine an average, effective index of refraction. When the index is determined for the entire active areas, and not just for individual mapping bins, the average index is n=1.0451±0.0001. The uncertainty is statistical, from the fits. In an attempt to reduce the effect of knock–on electrons, robust estimation linear fits were applied to the data, yielding similar results, albeit with larger uncertainties.

There are other methods of verifying the index of refraction from the data. Proton mass histograms, from the Cherenkov–Rigidity technique (see Section 3.7), imply an index of refraction of ~1.041–1.043. Comparison of IMAX helium data with IMAX Monte Carlo simulation implies an index of refraction of ~1.042±0.002 (Davis 1994). IMAX Monte Carlo simulation for protons shows that the mapping technique may overestimate the index of refraction by as much as 0.002 to 0.006, depending on the statistics of the L vs. $1/R^2$ data. The overestimation is due largely to fluctuations of knock–on electrons from near threshold protons. A simulation of the proton mapping data shows that a measured index of ~1.045 is consistent with an actual index of refraction of 1.043.

Therefore, an average index of refraction of n=1.043 was employed in this analysis, with a residual uncertainty of ±0.002 implied by Monte Carlo simulations compared with IMAX helium data (Davis 1994). An error of 0.001 in index of refraction corresponds to an error in threshold of ~40 MeV. The threshold energy is ~2.4 GeV, and because errors in cosmic ray antiproton data are dominated by antiproton counting statistics, such an error in index is not significant in this analysis.

2.1.5 Knock–on Electron Contributions

An incident particle of charge Z and velocity $\beta_{incident}$ (or Lorentz factor $\gamma_{incident}$) passing through matter will liberate electrons, and the maximum energy that can be transferred to one of these knock–on electrons is $E_{max}=m_ec^2(\gamma_{incident}-1)$. If the incident particle is passing through a Cherenkov radiator, some of these knock–on electrons may have sufficient velocity to produce Cherenkov light, adding to fluctuations in the photoelectron yield and possibly producing Cherenkov light even if the incident, primary particle travels through the radiator at velocity below Cherenkov threshold.

The average Cherenkov light yield, K, from knock–on electrons due to passage of a primary, charged particle is a product of the average number of above–threshold knock–on electrons, N, and the average light yield, <Y>, of these electrons:

$$K(Z,E,\theta) = \sum_{T} N_T(Z,E,\theta)\langle Y(E,\theta,E',x')\rangle \tag{2.1.14}$$

where Z, E, and θ are the charge, energy, and angle of incidence for the primary particle. The sum is taken over the various materials within and directly above the Cherenkov radiator.

The number of knock–on electrons is given by

$$N_T(Z,E,\theta) = \int_{x_{T1}}^{x_{T2}} \int_{E_{T1}}^{E_{T2}} \phi_T(Z,E,E')dE'\,dx' \tag{2.1.15}$$

where the integrals are taken over electron energy and the thickness of the materials through which the primary particle passes, and ϕ_T contains information concerning the charge and mass numbers of the target materials (Lezniak 1976). The Cherenkov light yields of these electrons is given by

$$Y(E,\theta,E',x') = \int_{E'}^{E_2} \frac{dC}{dx}(Z=1,E'')\frac{dx}{dE}(E'')dE'' \tag{2.1.16}$$

where the energy integration is taken over the energy range of the knock–on electrons, dC/dx gives the Cherenkov light yield (see Equation 2.1.2), and dE/dx accounts for energy loss of electrons in the radiator.

Lezniak (1976) developed a calculation for Cherenkov contribution from knock–on electrons in a non–equilibrium population. In equilibrium, the production of knock–on electrons in a radiator is balanced by losses of electrons due to energy losses. Grove and Mewaldt (1992) extended the treatment of Lezniak to equilibrium populations of knock–on electrons, and they developed expressions for K, N_T, and Y appropriate for use in numerical simulations. The numerical treatment of Grove and Mewaldt was employed for IMAX analysis.

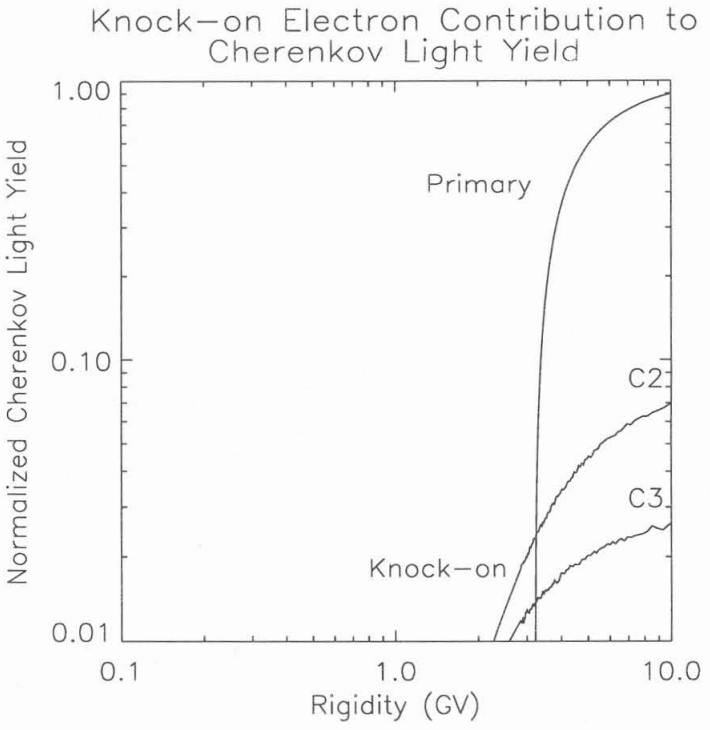

Figure 2.16: Cherenkov light yield vs. Rigidity for protons, broken down into primary and knock–on contributions for C2 and C3. The lower knock–on contribution is for C3, primarily from knock–on electrons produced in the material above the counter. C2 is closer to the magnet, and knock–on electrons produced in the material above C2 have a greater probability of being swept out by the magnetic field. However, knock–on electrons produced within the C2 aerogel spend more time within the radiator (due to the magnetic field).

The knock–on electron simulation for IMAX assumes an aerogel index of refraction of 1.043. In addition to the 9 cm thickness of aerogel (~1.84 g/cm^2), the simulation assumes 4 g/cm^2 of additional material over C3 (primarily Teflon from C1) and 0.1 g/cm^2 over C2. Because C2 is close to the magnet, the magnetic field sweeps out most knock–on electrons produced in material above C2.

Figure 2.16 shows the Cherenkov contribution from knock–on electrons, relative to the saturation light yield (Z=1, β=1) for a primary particle, for both C2 and C3. Corrections for average knock–on contributions can be applied versus measured light yields, because there is a one–to–one correspondence, on average, between measured light yield and primary light yield, neglecting photoelectron fluctuations. As will be discussed in Chapter 3, the normalized and uncorrected Cherenkov light yield (C2+C3) selected for Cherenkov–Rigidity analysis is 0.16 to 0.36, corresponding to a proton energy range of 2.64 – 3.12 GeV assuming n=1.043. When corrected for knock–on contribution, the energy range becomes 2.58 – 3.08 GeV at the spectrometer, or 2.61–3.11 GeV at the top of the atmosphere.

2.1.6 Secant(θ) Corrections

In the absence of light absorption, the primary Cherenkov light yield of a particle passing at incident angle θ relative to the flat, parallel surfaces of the radiator would be proportional to $L_0\sec(\theta)$, where L_0 is the primary light yield at normal incidence and the $\sec(\theta)$ accounts for increased path length. However, measurements of Cherenkov light yield for various thicknesses of aerogels indicates significant reabsorption of Cherenkov light by the radiator (Labrador et al. 1993; see also Appendix A).

A fit to Cherenkov light yield vs. radiator thickness takes the form

$$L(t) = K\lambda\left(1-\frac{1}{n^2}\right)\left(1-e^{-t/\lambda}\right) \qquad (2.1.17)$$

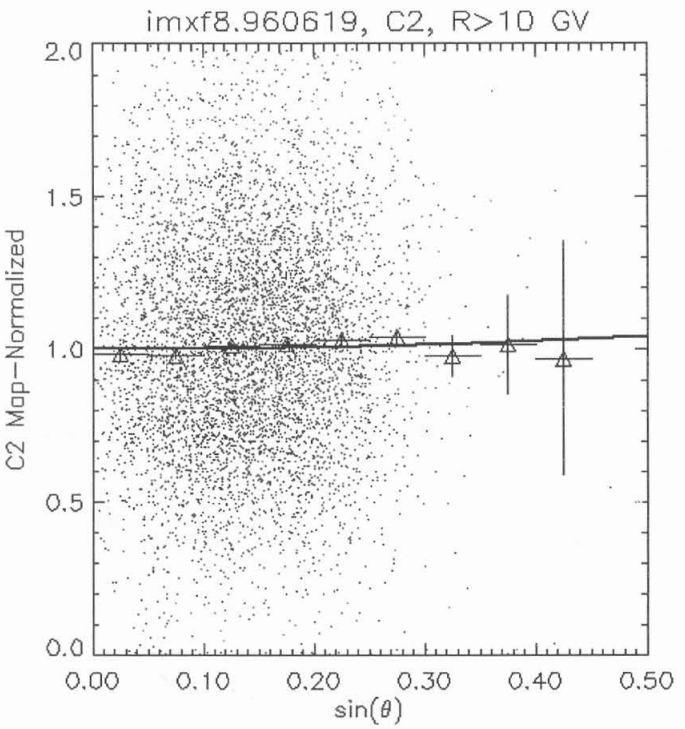

Figure 2.17: Normalized Cherenkov light yield for C2 vs. sin(θ), where θ is the incident angle. Events are selected with magnetic rigidity greater than 10 GV, and binned measurements are also given, with error bars reflecting uncertainties in the mean values. Also shown is the expected change as a function of angle (solid line). Average angle of incidence is ~8°.

where t is the thickness of the radiator and λ is the effective absorption length of the radiator. For the IMAX aerogels, $\lambda \approx 4.7$ cm. Because of significant light reabsorption, the sec(θ) correction is properly applied to t rather than directly to L(t). With typical angles of incidence for IMAX events, the sec(θ) correction for the IMAX Cherenkov counters yields up to a ~1% correction in light yield. The calculation is demonstrated in the following Equation.

$$\frac{L(t\sec\theta)}{L(t)} = \frac{1-\exp\left(-(t\sec\theta)/\lambda\right)}{1-\exp\left(-t/\lambda\right)} \approx \frac{1-0.1350}{1-0.1474} = 1.0145 \qquad (2.1.18)$$

where $\lambda = 4.7$ cm, t = 9 cm, and $\theta = 17.5°$. However, ~95% of all events in IMAX have angles of incidence less than 17.5°; the mean angle of incidence is ~8°. (See Figure 2.17.) Photoelectron statistical fluctuations account for ~25-27% of the uncertainties at saturation (Z=1, β=1), and the relative photoelectron fluctuations are much larger near threshold. These fluctuations are the major contributor to uncertainties in Cherenkov signal. Therefore, the sec(θ) corrections may be neglected in this analysis.

2.2 Tracking Systems

Several characteristics were required of the tracking systems used to measure magnetic rigidity. First, the ionization medium had to produce low drift velocities for the liberated electrons, so that the effects of the magnetic field on tracking precision would be reduced. The magnetic fields in the vicinity of the tracking system varied from 0.15 to 2.2 Tesla in IMAX.

Second, the tracking system had to produce excellent position resolution, which would reduce measurement uncertainties in rigidity and increase the maximum detectable rigidity (MDR). As shown in Section 2.7, a high MDR results in improved mass resolution, which is critical for light isotope measurements. Of course, improved mass resolution for isotopes is also reflected in improved mass resolution for protons and antiprotons. Further, and more critically,

a *high MDR (or low* uncertainty in rigidity) reduces the probability of deflection spillover of high rigidity (low deflection) protons toward negative rigidities (deflections).

The contribution of position resolution to maximum detectable rigidity can be understood in a constant magnetic field approximation (treatment taken from Rossi 1952). Consider a particle of charge q and velocity v passing through a region of uniform magnetic field B and thickness l. (See Figure 2.18.) The classical equation of motion through the magnetic field region is

$$m\frac{v^2}{r} = q\frac{v}{c}B \tag{2.2.1}$$

where r is the radius of curvature of the circular trajectory in the magnetic field. The maximum distance between a chord on a circle and the arc segment defined by that chord is called the sagitta — s in Figure 2.18. The sagitta can be related geometrically to the radius of curvature by

$$(r-s)^2 + \left(\frac{l}{2}\right)^2 = r^2 \tag{2.2.2}$$

For r>>s,

$$r \approx \frac{l^2}{8s} \tag{2.2.3}$$

Magnetic rigidity R can be defined as momentum divided by charge, and it can be extracted from the equation of motion as

$$R = \frac{mvc}{q} = Br \qquad \left(\text{relativistically, } R = \frac{pc}{q} = \frac{mc^2}{q}\frac{\beta}{\sqrt{1-\beta^2}}\right) \tag{2.2.4}$$

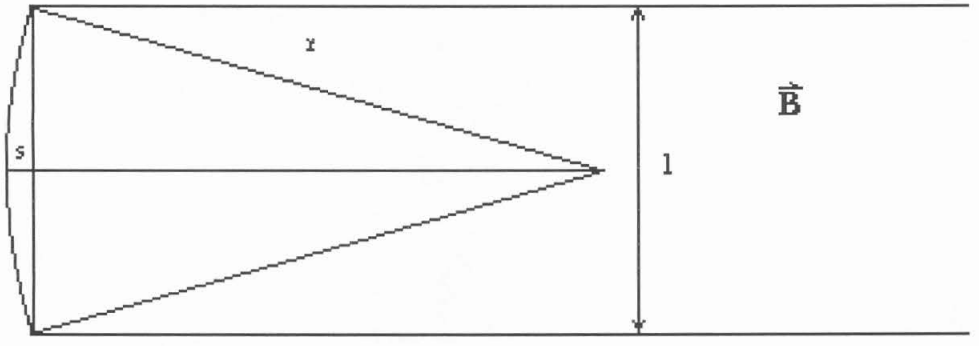

Figure 2.18: Circular trajectory of a charged particle through a region of constant magnetic field **B** and height l. The magnetic field is perpendicular to the page. The radius of curvature, r, and sagitta, s, are marked.

where one can see that rigidity is proportional to the product of magnetic field strength and trajectory radius of curvature. Typically, the radius of curvature is measured in cm, the magnetic field is given in gauss, and the rigidity is measured in volts. Thus, another form for Equation 2.2.4 would be R = 300 Br, where the factor of 300 comes from the conversion from gauss cm to volts.

If the magnetic field is well–defined (e.g. constant in this example, or via a field map in IMAX), then the uncertainty in the magnetic rigidity arises primarily from uncertainties in the determination of the trajectory radius of curvature:

$$dR = Bdr \tag{2.2.5}$$

Next, assume that the particle enters the magnetic field region on a near vertical trajectory and at high magnetic rigidity, such that its trajectory is approximately straight. At sufficiently high magnetic rigidity, corresponding to large radius of curvature and small sagitta, the effective sagitta measured by the tracking system will approach the position resolution of that tracking system, or in other words, the effective sagitta will be as small as the precision with which the sagitta can be measured. This result can be expressed as the maximum radius of curvature which can be measured by the tracking system, or

$$r_{max} \approx \frac{l^2}{8\sigma_s} \tag{2.2.6}$$

where σ_s measures the position resolution at the middle point (e.g. $\sigma_s \leftrightarrow \sigma_x$), and $r_{max} >> s$. In practice, the effective sagitta includes contributions not only from position resolution but also from the effects of multiple scattering on the track–fitting algorithm. In this ideal case, the maximum detectable rigidity (MDR) is related to position resolution by

$$MDR = Br_{max} = B\frac{l^2}{8\sigma_s} \tag{2.2.7}$$

and the relative uncertainty in measured magnetic rigidity is given stepwise by

$$\begin{aligned}\frac{dR}{R} &= \frac{dr}{r} = \frac{\sigma_s}{s} \\ &= \frac{r}{r_{max}} = \frac{R}{MDR}\end{aligned} \tag{2.2.8}$$

Finally, in the case of a nonhomogeneous magnetic field, a factor of Bl in Equation 2.2.7 should be replaced with the path integral $\int B_{\perp} dl$, where $B_{\perp}$ is the field component perpendicular to the path element dl. The contribution of MDR to mass resolution will be treated in Section 2.7.

2.2.1 Drift Chambers

The drift chambers (DCs) provide the primary method for determining particle trajectories and measuring particle magnetic rigidities in IMAX. The drift chambers were developed and constructed by the IMAX collaborators at the University in Siegen in Germany (Hof et al. 1993; Menn et al. 1993). The following discussion is abstracted in part from the two papers as well as from numerous discussions, faxes, and e–mail exchanges with the Siegen collaborators.

IMAX contained two drift chambers placed above and below the central axis of the IMAX magnet coil. Each drift chamber was a box made of 1 cm thick epoxy–composite walls, with interior dimensions of 47 cm x 47 cm x 35 cm. The ionizing gas was CO_2 at 99.995% purity or better. Within each box were 6 layers of drift cells in the x–direction (primary bending direction in the magnetic field), arranged in 3 double–layers, and 2 layers of drift cells in the y–direction, arranged in 2 double–layers. (See Figure 2.19.)

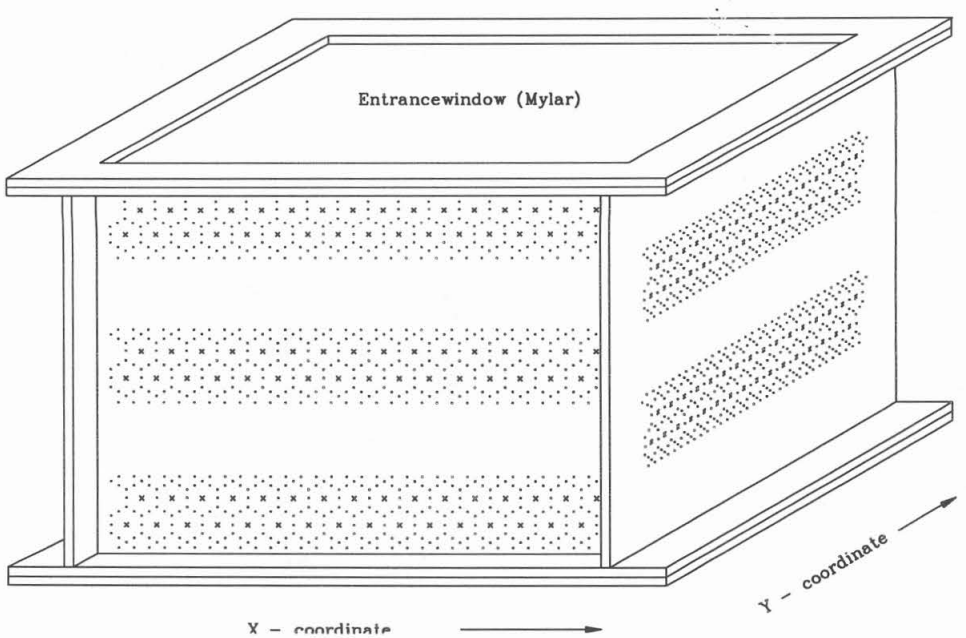

Figure 2.19: Drift Chamber (DC) diagram, showing the double–layer arrangements of hexagonal drift cells. Figure is courtesy of the University of Siegen (Hof et al. 1994).

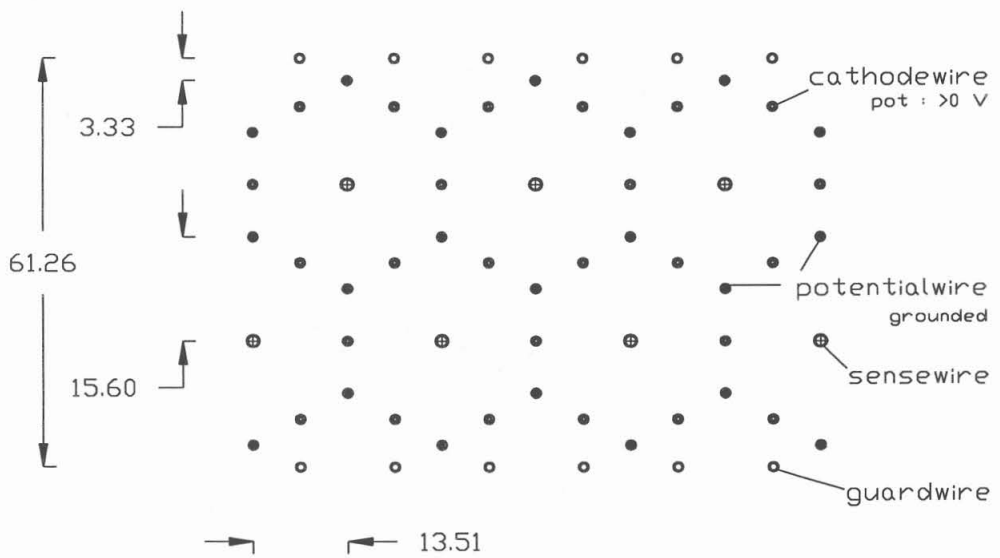

Figure 2.20: Close–up diagram of DC hexagonal drift cell structure. Dimensions are in mm. Figure is courtesy of the University of Siegen (Hof et al. 1994).

Each drift cell layer was an array of drift cells formed by a 2.7 cm wide hexagonal arrangement of electric–field shaping wires. (See Figure 2.20.) The central anode ("sense wire" 30μm diameter tungsten, gold–plated) in each drift cell was kept at +4600 volts. The cathode wires (100 μm diameter tungsten, gold–plated) were run at +500 volts, and the potential wires were grounded. The result of this arrangement of voltages was a cylindrically symmetric electric potential configuration concentric with the sense wire. Because the electron drift velocities in CO_2 are sufficiently low that the magnetic Lorentz force on them is negligible, electrons liberated by an ionizing particle within a drift cell proceed in a nearly straight line from the point of ionization to the sense wire.

Between adjacent x– and y–layers, additional guard wires with a potential of +1100 volts were used to reduce electric field distortions caused by adjacent layers.

In the two drift chambers in IMAX, there were 320 sense wires. A particle passing through the IMAX payload and generating a system trigger (see Section 2.6) might also liberate electrons in a given drift cell. Electrons liberated by the particle would proceed directly to the sense wire. Signals from these sense wires were read by a system of LeCroy 4290 TDCs via LeCroy 2735 amplifier/discriminators, employing leading–edge discrimination. The 4290's were run in Common Stop Mode, with the sense wire signals providing the TDC start signal. The system trigger was delayed by 3.75 μs and gave the common stop signal for the TDCs. The drift–time is the difference between the start–to–stop time and the 3.75 μs delay. During data analysis, a drift–time to position relationship (DPR) was then applied to the measured drift–time for each drift cell signal, resulting in a cylindrical locus of points about the sense wire in which the ionization point was located. The DPRs were obtained initially for each drift cell with calibration data from ground–level muon data with the payload magnet turned off, so that the particle trajectories were known to be straight (within uncertainties due to multiple scattering). The straight tracks also provided alignment data for the DCs and multiwire proportional counters. The DPRs were further refined with high rigidity flight data, divided into time periods during the flight in order to provide time–dependent

calibration of the DPRs. In particular, because the electric potentials do not present an absolutely cylindrical geometry, some angle corrections to the DPRs had to be applied, particularly for particle trajectories near the outer edges of the drift cells. Calibration with flight data also provided time–dependence to the angle corrections.

Because each double–layer was composed of two hexagonal cell layers laterally offset from each other by half a cell width, a single particle may produce ionization in single cells in adjacent layers, providing partial resolution of left–right ambiguity relative to the sense wire of a given drift cell. Further analysis incorporating the track–fitting algorithm and data from the rest of the tracking layers further resolved any position ambiguity in a given layer. These additional ambiguities arise from tracks passing very near a given sense wire or at the very edge of a drift cell. (See Figure 2.21 for a sample track.)

Position resolution — the precision to which an x– or y–position can be determined for any given layer in the DC's — is defined in IMAX as the distribution width of the residual difference between measured and fitted positions,

$$\sigma_x = \text{width}\left(\left(x_{\text{fitted}} - x_{\text{measured}}\right)\sqrt{\frac{NGx}{NGx-5}} \right) \tag{2.2.9}$$

where NGx is the number of measured positions (used in the fit) in the x–position, and the square root factor sets a minimum condition for fits. See Section 3.1 for a description of the tracking algorithm. For the IMAX DC's, position resolution is related to the precision with which the DPR is known. Generally, resolution is impaired close to and far from the sense wire in any given drift cell. For IMAX DC's, the position resolution was better than 100 μm for > 70% of the axial distance from a sense wire. The characteristic DC MDR was 175 GV for protons, obtained from the peak in histograms of the uncertainty in deflection. (See Section 3.1.1, Figure 3.4.) Note that, because the IMAX magnetic field was inhomogeneous, there was a strong position dependence to the MDR. For the DC alone, the MDR was as high as 340 GV for protons passing within 20 cm of the magnet, and it dropped to ~50 GV for protons approaching no closer

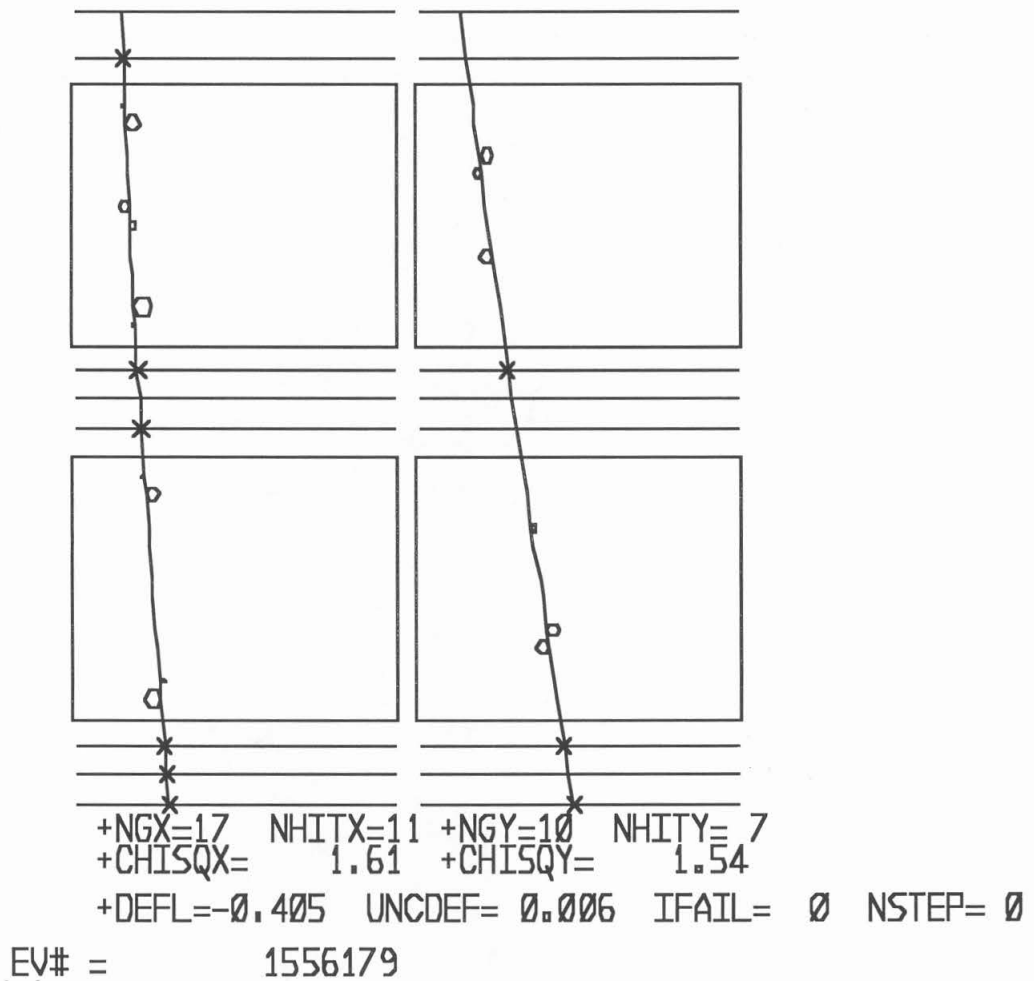

Figure 2.21: Sample trajectory through the IMAX tracking systems.

than 55 cm from the magnet (Hof et al. 1994). (An analytical approximation for the MDR is given in Section 2.7.1.)

2.2.2 Multiwire Proportional Counters

The secondary system for determining particle trajectories and magnetic rigidities was the system of multiwire proportional counters (MWPC), provided by the Particle Astrophysics Laboratory at New Mexico State University (PAL–NMSU) as part of the Balloon–Borne Magnet Facility (BBMF) which served as the overall IMAX payload. The MWPCs are described in full detail in Golden et al. 1990, from which the following discussion is largely extracted.

For IMAX, each MWPC chamber was a 50 cm x 50 cm inner area G10 frame upon which were arranged parallel arrays of anode wires at 2 mm lateral spacing. The anode plane is typically run at +4700 volts with respect to the grounded cathode plane, which is itself composed of a similar layer of wires running in the perpendicular direction and vertically offset by 6 mm (Lacy and Lindsey 1974). Mylar windows isolate the wires from air outside the chambers, and the interior of the chambers was filled with "magic gas" (a mixture of isobutane, freon, and argon) chosen as the ionization medium. (See Figure 2.22, taken from Stochaj 1990.)

When a charged particle passes through the chamber, it ionizes the gas and liberates electrons, which travel along the electric field induced by the potential to the anode wires. A cascade of ionization occurs near the anode wires as the electrons are further accelerated. Electrons which reach the anode wires are drawn off by a capacitor, leaving a distribution of positive ions near the anode wires which induces a negative image charge on the cathode plane. The cathode wire signals are transferred to a delay line, each end of which is read by fast TDCs. The sum of the timing signals is a constant, useful for accepting only "clean" events, and the difference in the timing signals yields a lateral position along the axis perpendicular to the cathode wires. The MWPCs employed by IMAX yielded 200–250 μm position resolution

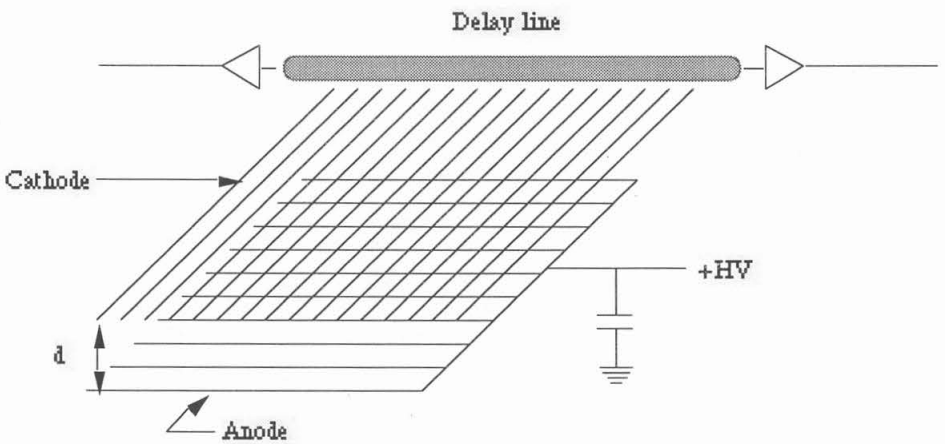

Figure 2.22: Schematic of MWPC, taken from Stochaj (1990).

in the direction perpendicular to the cathode wires and depending on position relative to the payload magnetic field.

There were 8 x–layers (the bending direction in the magnetic field) and 4 y–layers in the MWPC system, distributed directly above, below, and between the two drift chambers. Three MWPC x–layers were placed directly below the bottom DC, three were between the DCs, and two were directly above the top DC. There were two y–layers directly below the bottom DC, one y–layer between the DCs, and one above the top DC. The MWPCs were not employed separately from the DCs in the IMAX analysis, although in the LEAP experiments, the MWPC system provided an MDR of ~67 GV (Stochaj 1990). In IMAX, the MWPCs provided tracking data to supplement the DC tracking data, and the characteristic MDR for the combined systems was ~200 GV for protons.

2.3 Time of Flight System

To measure velocities below Cherenkov threshold, a time–of–flight (TOF) system was developed by the IMAX collaborators at the Goddard Space Flight Center (GSFC). The following discussion is abstracted from Mitchell et al. 1993b as well as from numerous discussions and direct interaction with the GSFC collaborators.

The TOF system was composed of an array of 3 co–planar scintillator paddles at the top of the IMAX payload and another array of 3 co–planar scintillator paddles at the bottom of the payload. The scintillator paddles were 60 cm x 20 cm x 1 cm Bicron BC–420 plastic scintillator paddles, with one top TOF paddle limited by payload geometry to ~53 cm in length. The TOF paddles were wrapped in black, light absorbing paper to absorb any light which left the paddles at positions other than the ends.

Each paddle was viewed by two Hamamatsu R2083 PMTs, one on each end and run at -2700 to -3000 Volts during flight. The PMTs were coupled to the paddles by light pipes made of acrylic plastic capable of transmitting ultraviolet light, and the PMTs were mounted within steel magnetic shielding tubes. Payload geometry as well as magnetic field configuration

required that the light pipes be bent at varying angles. The vertical pathlength through the TOF system was 2.5 meters. The TOF paddles also acted as scintillator counters, for dE/dx measurement, with the PMT signals sent to LeCroy 2249A ADCs. Timing signals were sent to LeCroy 2229 (Mod 400) time–to–digital converters (TDCs), and thresholds were set with LeCroy 2213 discriminators at 15 mV. The pulses for minimum ionizing particles were generally above 100 mV (Mitchell et al. 1993b).

The function of the TOF system is conceptually simple. A charged particle passes through a top TOF paddle and generates a start signal for a time–to–digital converter (TDC). When the particle passes through a bottom TOF paddle, a stop signal is sent to the TDC, which then generates a total flight time, t_{flight}. The tracking system can be used to calculate a total flight path, d, from top to bottom, which yields a velocity $v=d/t_{flight}$.

In practice, the TOF calculation is more complicated. A given TOF paddle is viewed by two PMTs, each of which generates a signal to be sent to the TDCs. Scintillation photons generated at a given position within the TOF paddle must travel to either end of the paddle in order to be detected by a PMT. The position at which the photons are generated and the effective velocities at which they travel will affect the relative timing of the signals between the two PMTs.

Suppose a TOF paddle is laid out in an "East–West" direction. If we look at the timing of a signal in the "East" side of a TOF paddle, we expect the timing equation to have the form

$$T_{East} = T_0 + \frac{x}{v_{eff}} + A\frac{1}{\sqrt{PH}} + C_{East} \qquad (2.3.1)$$

where T_{East} is the time at which the signal arrives at that PMT (as measured by the TDC), T_0 is the time at which the particle actually hits the paddle, x is the distance (in the East-West direction) between the PMT and the point at which the particle hit the paddle, v_{eff} is the effective velocity of light in the paddle along the East-West direction, and PH is the pulse height (amplitude) of the PMT signal. C_{East} is a constant containing electronic offsets, and A is

an *amplitude correction* factor. The equation relates the actual time the particle hit the paddle (T_0) to the time the PMT detected the signal (T_{East}). The second term on the right takes into account the time the scintillation signal had to travel to the PMT. The third term takes into account the effect which the signal amplitude has on the timing signal; larger signals produce shorter threshold rise–times. The exact form for this term is somewhat uncertain, with a 1/PH dependence being another possibility, but the form in Equation 2.3.1 has proved sufficient for this analysis because the relative contribution due to the pulse height is much smaller than the position correction.

The same particle would produce a signal at the "West" end of the paddle governed by the timing equation

$$T_{West} = T_0 + \frac{L - x}{v_{eff}} + A\frac{1}{\sqrt{PH'}} + C_{West} \tag{2.3.2}$$

where L is the length of the paddle, and PH' is the PMT pulse height seen at the west end of the paddle. Taking the average between the two timing signals yields

$$\frac{1}{2}\left(T_{East} + T_{West}\right) = T_0 + \frac{A}{2}\left(\frac{1}{\sqrt{PH}} + \frac{1}{\sqrt{PH'}}\right) + \frac{1}{2}\frac{L}{v_{eff}} + \frac{1}{2}\left(C_{East} - C_{West}\right) \tag{2.3.3}$$

Taking the difference between the two timing signals yields

$$T_{East} - T_{West} = \frac{2}{v_{eff}}x + A\left(\frac{1}{\sqrt{PH}} - \frac{1}{\sqrt{PH'}}\right) - \frac{L}{v_{eff}} + \left(C_{East} - C_{West}\right) \tag{2.3.4}$$

Note that, in Equation 2.3.3, the position dependence has disappeared. Equation 2.3.3 may be used to get the effective time signal from a given paddle. The constants may be fitted with Equation 2.3.4, given measurements of position (from tracking), PMT pulse heights, and timing from the individual paddles.

If we apply Equation 2.3.3 to a top TOF paddle and a bottom TOF paddle, we may take a difference in the sums to obtain

$$\frac{1}{2}\left(T_{East}^{Bottom}+T_{West}^{Bottom}\right)-\frac{1}{2}\left(T_{East}^{Top}+T_{West}^{Top}\right)=\left(T_{0}^{Bottom}-T_{0}^{Top}\right)$$
$$+\frac{A^{Bottom}}{2}\left(\frac{1}{\sqrt{PH^{Bottom}}}+\frac{1}{\sqrt{(PH')^{Bottom}}}\right) \qquad (2.3.5)$$
$$-\frac{A^{Top}}{2}\left(\frac{1}{\sqrt{PH^{Top}}}+\frac{1}{\sqrt{(PH')^{Top}}}\right)+constants$$

The constants include the paddle length terms as well as the electronic offsets. Equation 2.3.5 may be rearranged to give

$$\left(T_{0}^{Bottom}-T_{0}^{Top}\right)+constants=\frac{1}{2}\left(T_{East}^{Bottom}+T_{West}^{Bottom}\right)-\frac{1}{2}\left(T_{East}^{Top}+T_{West}^{Top}\right)$$
$$-\frac{1}{2}A^{Bottom}\left(\frac{1}{\sqrt{PH^{Bottom}}}+\frac{1}{\sqrt{(PH')^{Bottom}}}\right) \qquad (2.3.6)$$
$$+\frac{1}{2}A^{Top}\left(\frac{1}{\sqrt{PH^{Top}}}+\frac{1}{\sqrt{(PH')^{Top}}}\right)$$

The first term on the left side of Equation 2.3.6 is the flight time of a charged particle from the top to the bottom TOF paddle. Constants for each paddle have been fitted separately, and histograms of Equation 2.3.6 for flight data show a time resolution of 130 ps for protons and 105 ps for helium (Mitchell et al. 1993b) With a vertical flight path of 2.5 m, corresponding to a vertical flight time of ~8300 ps, this result is equivalent to better than 1.6% time resolution.

Finally, the TOF paddles may be used as scintillator detectors; see Section 2.4 below. As with the S1 and S2 scintillator counters, the TOF paddle responses have been mapped with minimum ionizing particles from flight data, and the useable active areas are defined in Table 2.3.1. The ~0.5 cm gaps between adjacent paddles represent the physical gaps between the

paddles plus additional margins to reduce the contributions from particles at oblique incidence hitting adjacent paddles.

Table 2.3.1: TOF Paddle Active Areas, in DC Coordinates

	x (cm)	y (cm)
Top TOF Paddle 1	$-7.5 \le x \le 58.5$	$-6.99 + 0.00467\,x \le y \le 13.01 + 0.00467\,x$
Top TOF Paddle 2	$-7.5 \le x \le 58.5$	$13.41 + 0.00467\,x \le y \le 33.41 + 0.00467\,x$
Top TOF Paddle 3	$-5.0 \le x \le 55.0$	$34.14 + 0.01133\,x \le y \le 54.14 + 0.01133\,x$
Bottom TOF Paddle 1	$-4.0 \le x \le 56.0$	$-4.88 - 0.00667\,x \le y \le 15.12 - 0.00667\,x$
Bottom TOF Paddle 2	$-4.0 \le x \le 56.0$	$15.52 - 0.00667\,x \le y \le 35.52 - 0.00667\,x$
Bottom TOF Paddle 3	$-4.0 \le x \le 56.0$	$35.8 \le y \le 55.8$

2.4 Scintillator Counters

IMAX contained a number of scintillator counters for charge determination via dE/dx measurement. These counters included the top and bottom TOF paddles as well as two independent scintillator counters S1 and S2 (Mitchell et al. 1993a). The TOF paddles are described in Section 2.3.

Both S1 and S2 are light integration boxes. S1 (provided by NMSU) contained a 51 cm x 51 cm x 1 cm Bicron BC–400 plastic scintillator. The box is viewed by 4 Hamamatsu R1307 PMTs, gathered into two pairs which are separately pulse–height analyzed with LeCroy 2249A ADCs gated at 200 ns. S2 (provided by GSFC) contained a 55 cm x 49 cm x 1.8 cm Bicron BC–408 plastic scintillator. The S2 box is viewed by 12 Hamamatsu R2409–01 PMTs, all separately pulse–height analyzed with LeCroy 2249A ADCs gated at 125 ns.

When a charged particle passes through a scintillator, it deposits energy according to the Bethe–Bloch formula:

$$\frac{dE}{dx} = -\frac{Z^2 e^4 N_e}{4\pi\varepsilon_0 m_e c^2 \beta^2}\left[\ln\left(\frac{2\gamma^2 m_e c^2 \beta^2}{\bar{I}}\right) - \beta^2\right] \qquad (2.4.1)$$

where Z, β, and γ are the charge, velocity, and Lorentz factor of the incident particle, and N_e I are the electron number density and average ionization potential for the target medium. In a scintillator, the charged particle transfers some of its energy to electrons, exciting them to higher energy states, which then transition to the ground state and release energy via fluorescence. (In plastic or organic scintillators, the excitation states are molecular; in inorganic scintillators like NaI, the states are associated with the electronic lattice of the crystal.) Thus, measured light yield will be proportional to energy deposited and to the square of the charge of the incident particle.

The scintillation efficiency is defined as the fraction of deposited energy which is converted to light. Of the organic scintillators, anthracene has the highest scintillation efficiency, and most plastics have efficiencies over 50% of that of anthracene (Knoll 1989). Plastics, however, have the advantage of being inexpensive, easy to manufacture, and easy to handle, particularly in the large sizes required for astrophysics experiments. In IMAX, all that is required is that the detectors detect the passage of charged particles and have good charge resolution in the Z=1 to 2 range. A rule of thumb for plastic scintillators is that they yield one photon per 100 eV of energy loss in the scintillator (Montanet et al. 1994), and with ~1–10 MeV energy loss per IMAX scintillator, detection efficiency will approach 100%.

The IMAX scintillator responses were mapped with minimum–ionizing particles. Charge separation for IMAX data analysis is described in Section 3.2. The S1 and S2 active areas are defined in Table 2.4.1.

Table 2.4.1: S1 and S2 Active Areas, in Drift Chamber Coordinates

	x (cm)	y (cm)
S1	$0.0 \le x \le 50.0$	$0.0 \le y \le 50.0$
S2	$1.05 \le x \le 50.17$	$0.98 \le y \le 50.35$

2.5 Magnet

Given a measure of charge, the momentum of a particle may be determined by a measure of magnetic rigidity:

$$R = \frac{pc}{Ze} = \frac{mc^2}{Ze}\frac{\beta}{\sqrt{1-\beta^2}} \tag{2.1.10}$$

Classically, the magnetic rigidity is proportional to the product of the magnetic field and the radius of curvature of the particle trajectory — $R \propto Br$. Therefore, to measure momentum (or magnetic rigidity) for charged particles in a spectrometer experiment, a magnet must be employed in conjunction with the tracking system.

IMAX used the superconducting magnet in the NASA Balloon Borne Magnet Facility (BBMF) operated by the Particle Astrophysics Laboratory at New Mexico State University (PAL–NMSU) (Golden et al. 1978, 1991). The magnet is made of copper–clad 54 filament niobium–titanium wire, wound through 11161 turns in a coil with an outer diameter of 24 inches, 5 inches radial thickness, and 3 inches axial thickness. The normal flight current is 120 Amps, which results in a magnetic field between 0.1 and 2.1 Tesla in the drift chambers and up to ~2.5 Tesla in the region of the central multiwire proportional counters (Hof et al. 1994). (See Figure 2.23.)

2.6 Trigger Logic

In order for the IMAX payload to register passage of a particle, an event must satisfy a set of trigger criteria. A schematic of the trigger logic is shown in Figure 2.24. The minimum criterion for a system trigger was a four–fold coincidence of PMT signals from two top TOF PMTs and two bottom TOF PMTs. This basic criterion was the minimum needed to assure that a particle triggered both ends of a TOF paddle at the top and a TOF paddle at the bottom. Further selection criteria, described in Chapter 3, eliminate accidental triggers from the

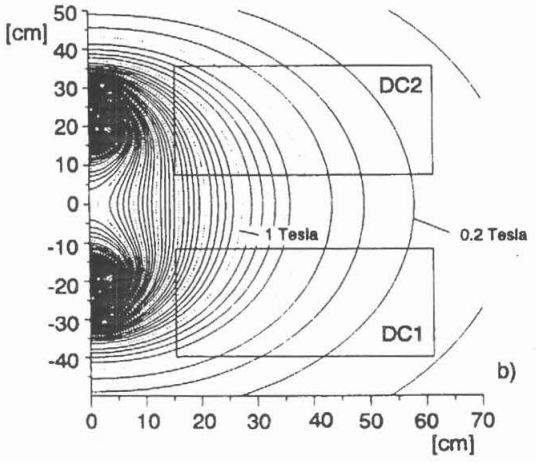

Figure 2.23: Magnetic field map for IMAX, showing the relative positions of the drift chambers. Figure taken from Hof et al. 1994.

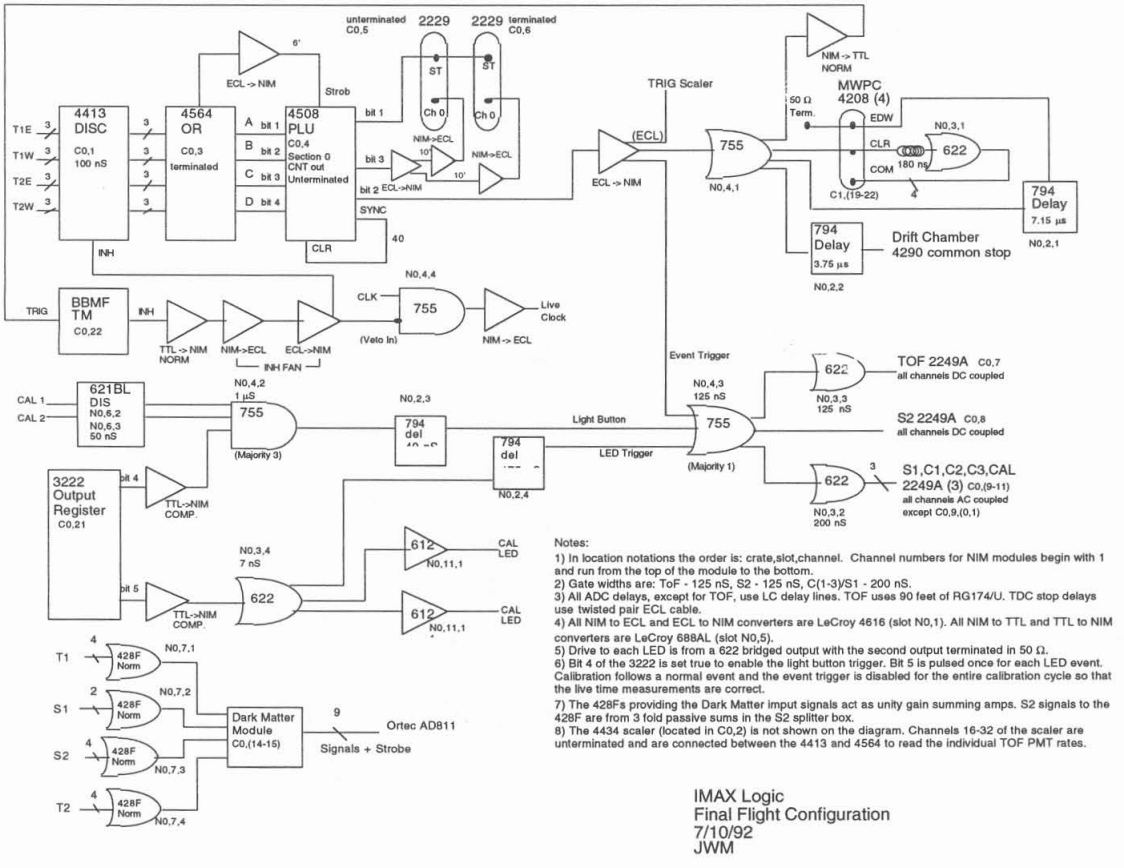

Figure 2.24: IMAX Trigger logic schematic, courtesy of J.W. Mitchell, GSFC. Though included on this schematic, the light button and LED calibration systems were not used in this analysis.

analysis. The rest of the discussion in this section derives heavily from discussions with and documents from Dr. J. W. Mitchell at GSFC.

To achieve this trigger condition, the TOF PMT signals were passed through a LeCroy 4413 discriminator module, with ECL outputs (true = -1.6 V, false = -0.8 V, set at 100 ns width) to signal the passing of the threshold voltage signal, which could be controlled via Camac during flight. The logic outputs were then passed in four gangs of three, representing the East and West banks of the top and bottom TOF paddles, to a LeCroy 4564 OR logic unit. The OR outputs (also ECL logic levels) were passed in four separate bits to a LeCroy 4508 Programmable Lookup Unit, which yielded the system trigger. This system trigger was converted from ECL to NIM (true = ~-600 mV to -1.6 V, false = +~100 mV, into 50Ω).

The system trigger produced gates, via Phillips 755 multiplicity logic units and LeCroy 622 NIM logic modules, for the various LeCroy 2249A ADCs used for the TOF, S1, S2, C2, and C3 PMT pulse heights. For the TOF ADCs, the gate widths were set at 125 ns, and for S1, C2, and C3, the gate widths were 200 ns.

The DC sense wires were separately triggered using LeCroy 2735DC amplifier discriminators, using leading edge discrimination at a fixed threshold. The sense wire signals provided the start signals for LeCroy 4290DC TDCs, running in Common Stop mode. The system trigger was sent through a 3.75 μs delay to the TDCs to produce the common stop signal, and the drift–time for each cell was the difference between 3.75 μs and the start–to–stop time.

2.7 Mass Determination and Resolution

While various aspects of the IMAX payload performance can be treated with Monte Carlo simulations (e.g. Section 2.8), its performance as a mass spectrometer and as a momentum spectrometer may be approximated analytically, using the constant–field approximation discussed in Section 2.2. The results discussed in this section employ a version of a calculation by Streitmatter (1992), with additional information obtained via Monte Carlo simulations

(Davis 1994). It is important to keep in mind that the results of this calculation are limited by the use of the constant–field approximation.

From the expression for rigidity, we may solve for mass in terms of measured rigidity R, velocity β, and charge Z:

$$m = \frac{ZeR}{c^2}\frac{\sqrt{1-\beta^2}}{\beta} \tag{2.7.1}$$

The uncertainty in mass takes on the form

$$\sigma_m^2 = \left(\frac{\partial m}{\partial R}\right)^2 \sigma_R^2 + \left(\frac{\partial m}{\partial \beta}\right)^2 \sigma_\beta^2 + 2\left(\frac{\partial m}{\partial R}\right)\left(\frac{\partial m}{\partial \beta}\right)\sigma_{\beta,R}^2 + \ldots \tag{2.7.2}$$

where the first two terms give the major contributions from uncertainty in rigidity and the uncertainty in velocity, and the third term gives the uncertainty associated with correlations between rigidity and velocity measurements. The charge is assumed to be known to arbitrary precision (e.g. Z=1, 2, ...). Figure 2.25 shows the estimated mass uncertainties, total and broken down by component, for protons in IMAX, along with the measured mass uncertainties. The rest of this section describes the contributions in further detail.

2.7.1 Contributions from Rigidity Measurement

From Equation 2.2.8 and Equation 2.7.1, we can see that the rigidity contribution is given by

$$\left(\frac{\partial m}{\partial R}\right)^2 \sigma_R^2 = \left(\frac{m}{R}\right)^2 \sigma_R^2 = m^2\left(\frac{R}{MDR}\right)^2 \tag{2.7.3}$$

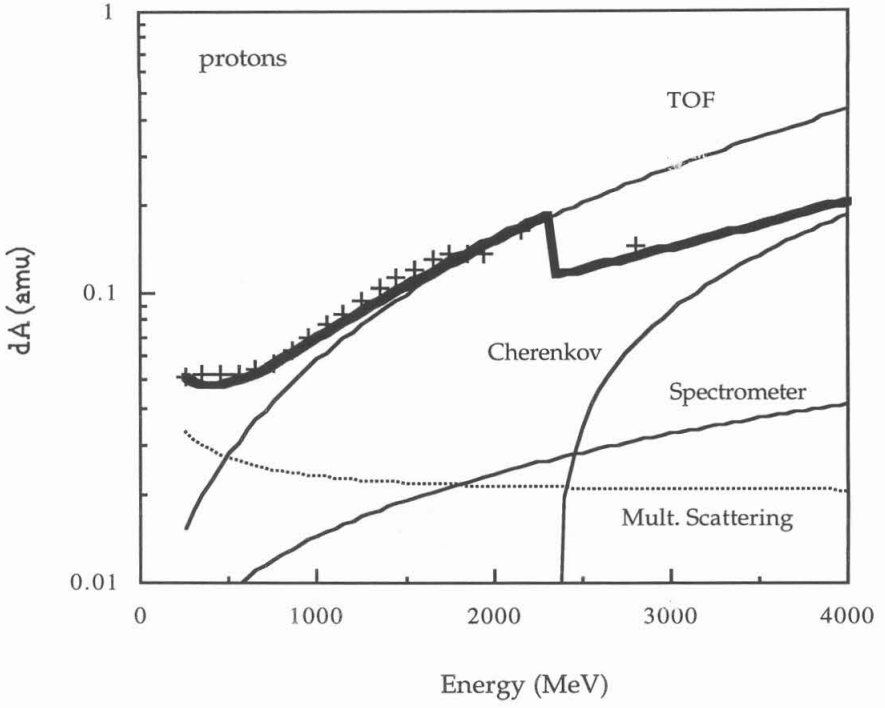

Figure 2.25: Approximate proton mass resolution (in amu) vs. kinetic energy. Separate contributions from spectrometer position resolution, multiple scattering, time–of–flight, and Cherenkov measurements are noted. The bold line shows the total mass resolution, and the crosses (+) show the measured mass resolution.

In the Cherenkov energy range (E>~2.4 GeV), the total mass uncertainty includes the "spill–in" contribution calculated from the Monte Carlo simulation and described in Section 2.7.2. However, the solid line marked "Cherenkov" includes only the primary width calculated analytically from Equation 2.7.19.

The multiple scattering curve is calculated from Equation 2.7.14, but the total mass uncertainty curve, at low energies, multiplies the multiple scattering curve by the "deterioration factor" described in Section 2.7.1.

where MDR has been defined (Section 2.2) as the maximum detectable rigidity of a tracking system. Thus, the relative size of the rigidity contribution to mass uncertainty is

$$\left|\left(\frac{\sigma_m}{m}\right)\right|_R = \frac{R}{MDR} \tag{2.7.4}$$

The MDR contains contributions from the tracking resolution of the spectrometer as well as from multiple scattering effects. As is discussed in Section 2.2, the MDR is the quantity which characterizes the spectrometer resolution. From Equation 2.2.7, we have

$$MDR = \frac{300 l \int B_\perp dl}{8\sigma_s} \tag{2.7.5}$$

where the equation has been expanded, for the purposes of this calculation, to the form for a nonhomogeneous magnetic field. The σ_S is the uncertainty in measuring the sagitta of the track, l is the height of the magnetic field region, $B_\perp$ is the magnetic field component perpendicular to the path element dl, and 300 converts gauss–cm (from the path integral) to volts.

The contribution of tracking system configuration (i.e. the positions of the measuring planes) and position resolution to overall rigidity resolution has been treated, in detail, by Gluckstern (1963) and Blum and Rolandi (1993), for the case of an idealized tracking system with all position measurements taking place entirely within a homogeneous magnetic field. Streitmatter (1970) has given a similar treatment for the case in which some position measurements also take place outside of the magnetic field region, and that treatment is summarized and employed below.

If the magnetic field region is characterized by a half–height of h (see Figure 2.18, l=2h), then a charged particle trajectory through the magnetic field region can be approximated by a quadratic:

$$x = a + bz + cz^2 \tag{2.7.6}$$

where x is the "bending" direction, z is the "vertical" direction, and 2c=1/r where r is the radius of curvature of the track. If we set the origin of the coordinate system (z=0) in the middle of the magnetic field region, then the particle trajectory outside of the field region will be a straight line of the form

$$x = (b \pm 2ch)z + a - ch^2 \tag{2.7.7}$$

where the boundaries of the magnetic field region are given by z=±h.

If measurements of a particle trajectory are made inside and outside of the magnetic field region, then the measurement errors — defined as the difference between the position measurements and the fitted positions — may be summed in quadrature to give

$$\sum (\Delta x)^2 = \sum_i \left(x_i - a - bz_i + ch\left(h - 2|z_i|\right)\right)^2 + \sum_n \left(x_j - a - bz_j + cx_j^2\right)^2 \tag{2.7.8}$$

where the sum over i is taken over measurements outside of the magnetic field region, and the sum over j is taken over measurements inside the magnetic field region. A least squares treatment minimizes $\sum (\Delta x)^2$ with respect to a, b, and c, and under the approximation that the position measurements are symmetric about the origin, Streitmatter (1970) obtains a solution for c of the form

$$c = \frac{\sum_i x_i\left(\xi_i - \overline{\xi}\right)}{N\left[\overline{\xi^2} - \left(\overline{\xi}\right)^2\right]} \tag{2.7.9}$$

where the sum over i is taken over all position measurements, N is the number of position measurements, and

$$\xi_i = \begin{cases} x_i^2 & \text{in field region} \\ h\left(2|x_i| - h\right) & \text{outside field region} \end{cases} \tag{2.7.10}$$

If the position measurement uncertainties are a constant σ_x, then the variance of c will be given by

$$\sigma_c^2 = \sigma_x^2 \frac{\sum_i \left(\xi_i - \bar{\xi}\right)^2}{N^2\left[\overline{\xi^2} - \left(\bar{\xi}\right)^2\right]^2} \tag{2.7.11}$$

From Equation 2.2.6 and c=1/r, we can calculate the uncertainty in the sagitta as

$$\sigma_s = \frac{l^2}{8}\frac{\sigma_r}{r^2} = \frac{l^2}{4}\sqrt{\sigma_c^2} \tag{2.7.12}$$

From the IMAX data, the average number of x-position measurements employed to fit a particle trajectory is NGx~18. (See Figure 3.1.) Therefore, for this calculation, we simulate all 12 DC x–planes plus two MWPC planes above, below, and between the DCs (i.e. 12 DC planes and 6 MWPC planes). If we assume symmetry about the center of the magnetic field region, then these measuring planes have vertical positions given by z_i = ±(3.86, 9.55, 11.89, 22.47, 24.81, 35.39, 37.73, 43.56, 49.67) cm. The spectrometer pathlength is then 2x49.67 = ~100 cm.

The characteristic position resolution is σ_x=100 μm for Z=1 particles in the DCs, and characteristic path integral is found experimentally to be $\int B_\perp dl$=~3.2x10^5 gauss–cm, from the top to the bottom of the tracking system. Because we are dealing with a constant field approximation, this path integral serves as a loose upper limit to that which can be used in these calculations. The other remaining parameter is the half–height, h, of the magnetic field

region. (See Figure 2.18; h=l/2.) The value of h contributes to the calculation of the spectrometer variance factor, defining which measurement planes are inside the magnetic field region. (See Equation 2.7.10.) A brute–force search of possible fits to the spectrometer data yields a large array of values for $\int B_{\perp} dl$ and h. Not all of the solutions are physically reasonable, e.g. some solutions include values of h greater than 50 cm, implying a constant field region which completely spans the spectrometer. One solution which is consistent with the spectrometer configuration and magnetic field map is given by $\int B_{\perp} dl$ = ~1.4x10^5 gauss–cm and h = ~23 cm.

Figure 2.26 compares the calculated contribution to proton mass resolution from the spectrometer to the actual measured contribution from the spectrometer data. The simulated values use the calculations and parameters described above. The measurements implement the average uncertainty, $\sigma_{deflection}$, in measured deflection vs. energy, with the substitution of MDR = $1/\sigma_{deflection}$ in Equation 2.7.4. (See Section 3.1.1 for a description of the $\sigma_{deflection}$ distribution. The spectrometer mass resolution at 4 GeV implies an average MDR of 114 GV.)

The average scattering angle for multiple Coulomb scatters in a plane is given by

$$\theta_{ms} = \frac{13.6 \quad MeV}{\beta cp} Z \sqrt{\frac{x}{X_0}} \left[1 + 0.038 \ln\left(\frac{x}{X_0} \right) \right] \tag{2.7.13}$$

where momentum, velocity, and charge are for the incident particle, and x/X_0 is the pathlength through the scattering medium, in units of radiation length (Montanet et al. 1994). Multiple scattering contributes an additional uncertainty to the sagitta, and given position measurements inside and outside of the magnetic field region, the effective sagitta uncertainty due to multiple scattering takes the form

$$\sigma_{s,ms} = \frac{1}{4\sqrt{3}} x \theta_{ms} \frac{1}{(z_N - z_1)/h - 1} \tag{2.7.14}$$

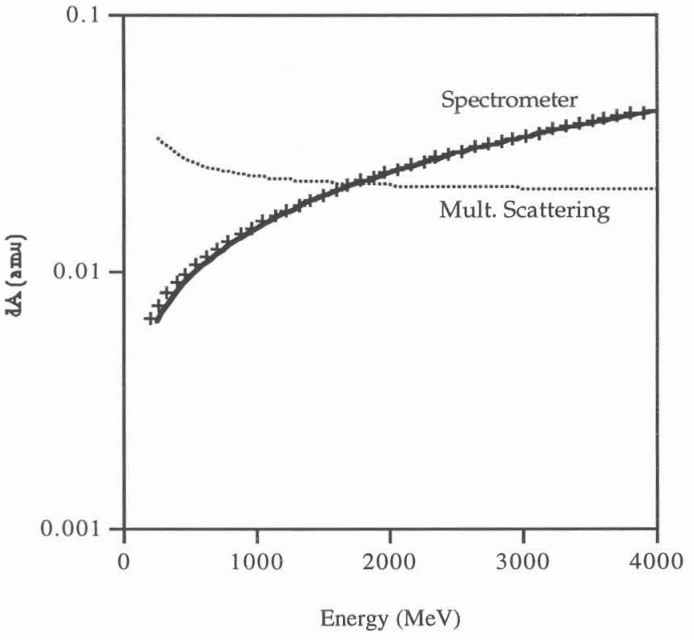

Figure 2.26: Mass resolution contributions from the spectrometer configuration and multiple scattering. The crosses (+) are the measured mass resolution contributions, obtained from $\sigma_{deflection}$ measurements. (See Section 3.1.1.)

For this calculation, X_0=18310 cm for CO_2 gas and take the contributions from the DC wires and mylar to be negligible, and we substitute x = ~100 cm (between the top and bottom measurement planes). The energy dependent contributions to mass uncertainty are shown in Figures 2.25 and 2.26. For protons at 4 GeV, the rms scattering angle is ~0.2 mrad, corresponding to $\sigma_{s,ms}$=~10 μm and effective MDR contribution of ~234 GV from multiple scattering.

Note that, although the position measurements are expected to be contaminated by multiple scattering, the spectrometer contributions shown in Figure 2.26 follow the pure spectrometer contribution without multiple scattering. Reimer (1994) has suggested that, because the track–fitting algorithm (see Section 3.1) does not include explicit corrections for scattering effects, the resulting $\sigma_{deflection}$ values are artificially low at low energies. For example, as a particle passes from the top of the tracking system to the bottom, multiple scattering progressively contaminates the position measurements so that, in principle, the bottom position measurements have larger uncertainties (due to the addition of scattering) than do the top position measurements. However, the track–fitting algorithm fits the trajectories to the position measurements via a least–squares approach in which all available position measurements are weighted equally for a given track. The resulting χ^2 values will be artificially low for those trajectories which are strongly affected by multiple scattering (i.e. at low energies), effectively giving a "best fit" to bottom position measurements which do not warrant such fits.

Thus, Reimer has implemented an energy–dependent "$\sigma_{deflection}$ multiple scattering deterioration factor" in Monte Carlo simulations, to fit helium data. This deterioration factor increases the estimated uncertainty in deflection at lower energies, resulting in a lower MDR or a larger mass uncertainty. For the present calculation, a constant deterioration factor of 1.4 applied to the multiple scattering contribution is sufficient to model the low–energy roll–off shown in Figure 2.25.

The MDRs from multiple scattering (including the deterioration factor) and position resolution combine in inverse quadrature to give total MDR=117 GV. Although the

characteristic MDR for the spectrometer has been defined at ~200 GV, the average MDR (defined as $1/\sigma_{deflection}$) for Z=1 particles accepted into the IMAX data analysis is ~115 GV. (As is discussed in Section 3.1.1, the characteristic MDR is calculated from the peak of the $\sigma_{deflection}$ distribution, while the average MDR is calculated from the average of the $\sigma_{deflection}$ distribution.) Based on a comparison of these calculations with the measured $\sigma_{deflection}$ distribution and the low energy mass resolution, we conclude that the spectrometer performance is well–simulated in terms of spectrometer configuration and multiple scattering.

2.7.2 Contributions from Velocity Measurement

The contribution to mass uncertainty from velocity measurement takes on slightly different form, depending on whether the velocity measurement is from the TOF or from the Cherenkov counters. In general,

$$\left(\frac{\partial m}{\partial \beta}\right)^2 \sigma_\beta^2 = \left(\frac{m}{\beta(1-\beta^2)}\right)^2 \sigma_\beta^2 \tag{2.7.15}$$

The relative size of the velocity contribution to mass uncertainty is

$$\left|\left(\frac{\sigma_m}{m}\right)\right|_\beta = \left|\frac{\sigma_\beta}{\beta(1-\beta^2)}\right| = \left|\gamma^2 \frac{\sigma_\beta}{\beta}\right| \tag{2.7.16}$$

For the TOF system, the velocity is pathlength over flight time

$$v = \frac{d}{t_{TOF}} = \beta_{TOF} c \tag{2.7.17}$$

If one assumes that the pathlength is known to arbitrary precision, then the mass uncertainty due to TOF uncertainty is given by

$$\left|\left(\frac{\sigma_m}{m}\right)\right|_{TOF} = \left|\gamma^2 \frac{c}{d}\beta_{TOF}\sigma_{TOF}\right| \tag{2.7.18}$$

where σ_{TOF} is the timing resolution. The TOF contribution for a timing resolution of 130 ps over a flight path of 2.5 m is shown for protons in Figure 2.25. (For helium, the timing resolution is ~100 ps.) Uncertainties in tracking will yield uncertainties in flight path length, and such uncertainties also contribute to uncertainty in β_{TOF} and would correspond to the third term of Equation 2.7.2. However, in practice, this contribution is much less than that due to timing, and it is folded into the timing resolution.

From the discussion in Section 2.1.2, the relative velocity uncertainty from the Cherenkov counters is given by

$$\frac{\partial\beta}{\beta} \leftrightarrow \left(\frac{\sigma_\beta}{\beta}\right)_{Cherenkov} = \frac{n^2\beta^2}{2Z^2}\left(1-\frac{1}{n^2}\right)\frac{\sigma_L}{M} \tag{2.7.19}$$

where σ_L is the uncertainty in photoelectron light yield, and M is the response map value. The pure Cherenkov contribution in Figure 2.25 is given for 24 pes(=11+13 pes) saturation light yield (Z=1, β=1) and n=1.043. The uncertainty in photoelectron light yield is Poisson only, and Equation 2.7.19 gives the mass uncertainty contribution due to Cherenkov fluctuations away from theoretical value.

However, Equation 2.7.19 does not include mass uncertainty contributions from "spill–in" fluctuations, by which Cherenkov light yields from particles at energies below a given energy range fluctuate up and into the corresponding Cherenkov light yield range. Similarly, particles at energies above the given energy range may have Cherenkov light fluctuating down and into the corresponding Cherenkov light yield range. While such contributions are difficult

to calculate analytically, they can be calculated via Monte Carlo simulation. Such a simulation (Davis 1994) shows that "spill–in" and knock–on electron (Section 2.1.5) contributions can be described adequately by a constant 0.13 amu contribution, for energies between threshold and 4 GeV. Response map variations are also included in the Monte Carlo simulation.

The actual mass resolution for protons is given in Figure 2.25 and in Figure 3.18, which shows the mass histograms for Z=1 particles in IMAX data for three energy bins, discussed in Chapter 3. The mass uncertainties given in Figure 3.18 are 0.06, 0.14, and 0.14 amu, following the general behavior given in Figure 2.25. Deviations from the calculations given in this section arise from a number of factors — e.g. the nonuniformity of the actual magnetic field, and the inclusion of particle MDRs as low as 50 GV. However, as is shown in Figure 2.25, the calculations adequately describe the actual behavior of the instrument.

2.8 Other IMAX Simulations

Several computer simulations were run to estimate various characteristics of the payload performance. An analytic simulation of the spectrometer performance has been described in detail in Section 2.7. The results of other simulations, as applied to this analysis, are described in the appropriate sections of this thesis, as noted below.

At the University of Siegen (Menn 1995), a simulation of particle trajectories through the payload geometry was run in order to estimate the deflection–dependent geometry factor of the payload. (See Section 4.2.1.) At the Goddard Space Flight Center, a GEANT simulation was run to examine particle interactions in the material below the bottom time–of–flight paddle (Krizmanic 1995). In particular, the GEANT simulation was employed to estimate the fraction of antiproton annihilations below the bottom TOF which would cause rejection of the events via backscatters. (See Section 4.3.2.)

At Caltech, a simulation was employed to examine the performance of the aerogel Cherenkov counters (Davis 1994). The simulation includes Monte Carlo code for simulating knock–on electron contributions to the aerogel Cherenkov response (Grove and Mewaldt 1992; see Section 2.1.5). The thickness of the aerogel radiator, its composition, and its index of refraction are entered as parameters for the simulation. The simulation also includes distributions for deflection and the uncertainty in deflection from the spectrometer data (Section 3.1), maps of aerogel Cherenkov response (Section 2.1.2), and PMT dynode statistics. The simulation allows selection of charge, mass, energy range, and spectral shape for the incident particles. Residual uncertainties in index, response, and time–of–flight may also be simulated, as Gaussian deviates. Finally, any or all of these contributions may be turned off during the simulation. (Reimer (1994) employed a similar simulation at the University of Siegen, although the focus of that simulation was on the tracking system performance.)

The results of this Monte Carlo simulation are given in the knock–on correction data (Section 2.1.5) and in the estimation of the index of refraction (Section 2.1.4). The simulation shows a maximum knock–on contribution in C3 of ~3% of the saturation ($Z=1$, $\beta=1$) light yield, and for C2, the maximum knock–on contribution is ~8% of the saturation yield. The simulation also shows that the method of determining the aerogel index of refraction, discussed in Section 2.1.4, tends to overestimate the actual index of refraction by ~0.002 to 0.006.

2.9 Flight

The IMAX payload was launched from Lynn Lake, Manitoba, Canada (56.5° North Latitude, 101° West Longitude) at ~9:35 PM (~2.6 hours UT) on 16 July 1992. The payload reached float altitude after ~7 hours and stayed at float altitude for ~15.27 hours. At float altitude, IMAX recorded 3.19×10^6 trigger events, corresponding to ~14.78 hours of float duration, with a ~1/2 hour period lost during telemetry.

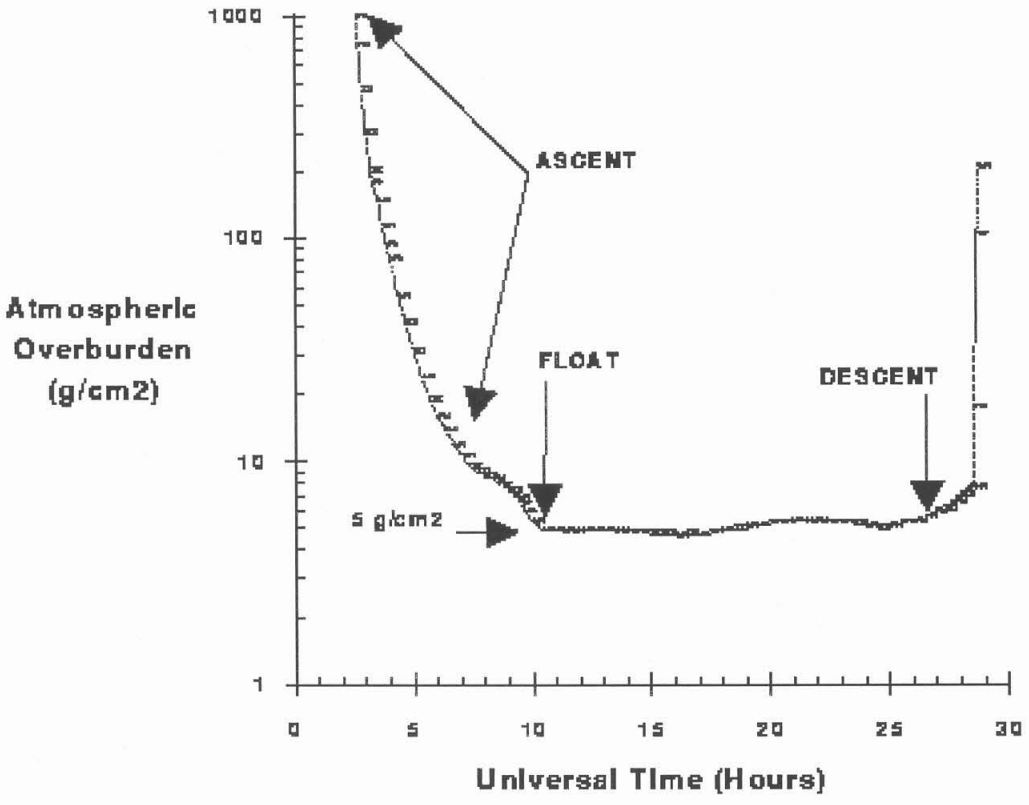

Figure 2.27: IMAX flight profile, as residual atmosphere (column density) vs. time. Figure taken from McGuire 1994. The current analysis spans the region from the beginning of float altitude to approximately one hour prior to the beginning of descent. Note that the long ascent makes available proton fluxes vs. atmospheric overburden for future calculations.

3. Flight Data Analysis

Once software was in place to process the raw flight data, selection criteria (or "cuts") were developed to identify antiprotons and protons. The initial selection criteria involved selection for particles with single, well–determined trajectories through the tracking system and the rest of the payload. Further selection criteria involved charge selection for Z=1 particles and velocity selection for the various energy bins involved in the TOF–Rigidity and Cherenkov–Rigidity techniques. The remaining selection criteria eliminated particles with anomalous data characteristics, usually attributed to system noise, to additional particles passing through the counter geometry without being detected by the tracking system, or to nuclear and electromagnetic interactions that resulted in anomalous signals. Correlations between redundant measurements within IMAX also contributed to elimination of anomalous events. All selection criteria were applied equally to positive and negative rigidity particles, so as not to bias the measurement for or against antiprotons, relative to protons. The selection criteria are listed in Table 3.1 and are described in further detail, along with algorithm descriptions, in later sections of this chapter.

The processing and analysis software and selection criteria evolved over many months from late–1992 to mid–1995. Details of various algorithms and selection criteria are described elsewhere in this thesis. Analysis of IMAX flight data was executed independently at the collaborating institutions, and results were compared and evaluated in order to provide cross–checks of software versions and selection criteria, as well as to investigate effects arising from machine–dependent differences in mathematical precision. (The present analysis derives from work done mainly at Caltech and at the University of Siegen. Caltech ran software on a variety of Sun Sparcstations running Unix, and the University of Siegen ran software on VAXes running VMS.) Evolution of selection criteria followed a loose–to–tight history: An original set of loose selection criteria evolved by addition of more criteria or the tightening of existing criteria in order to eliminate clearly anomalous events.

Table 3.1: Selection Criteria Summary

Tracking Selection Criteria	Fittable track (IFAIL = 0) # x wires used for fit = 11 — 20 # y wires used for fit = 7 — 12 # DC x layers greater than 4 cm off <= 2 # DC y layers greater than 4 cm off <= 2 $\chi^2_x \leq 4, \chi^2_y \leq 4, \sigma_{\text{deflection}} \leq 0.02$
Counter Active Areas	Top and Bottom TOF, S1, S2, C2, C3 (areas defined in Chapter 2)
Charge Selection Criteria	Scintillator dE/dx vs. $1/\beta^2_{TOF}$
Velocity Selection, TOF–Rigidity	β_{TOF} binned, and C2+C3 MN < 0.16
Velocity Selection, Cherenkov–Rigidity	C2+C3 MN = 0.16 — 0.36, and $\beta_{TOF} > 0.93$
Error Signals	Telemetry CHKSUM, TOF Error Flag, Cherenkov PMT > 5 pe flag
Correlation Cuts	C2 vs. C3, TOF vs. Cherenkov, Upper DC vs. Lower DC

Overall, IMAX data analysis at Caltech evolved into a three stage process, to allow for rapid reanalysis after changes in tracking software, other analysis software, and/or selection criteria. In the first stage, raw data files are processed into "fitted" data files, in which particle trajectories are fitted by the HYBMOM software (Section 3.1). Those events which do not meet the minimal track–fitting criteria are discarded and do not enter any further analysis, except in the efficiency calculations which are described in Section 4.2. This first stage of analysis is the most time–consuming single stage, taking as many as 3–5 days on a single, networked Sun Sparc–20. If the HYBMOM software is changed, this stage and the two subsequent stages must be re–run. The basic data format and software framework provided by PAL–NMSU, along with U. of Siegen's HYBMOM software, are used for this stage.

In the second stage of analysis, the fitted data files are processed further to calculate quantities like mapped and normalized detector responses, which are not calculated in the first stage. This stage also produces ASCII formatted files, containing column data of selected IMAX data elements, which can be read and analyzed by commercial software packages like

Research Systems' IDL. If the IMAX data processing software changes (other than the HYBMOM package), this stage and the third stage must be re–run.

In the third stage, the final selection criteria are applied to the fitted and processed data from the first two stages. This stage also counts protons and antiprotons. If selection criteria change at this point, only this stage must be re–run.

Float altitude data consists of 3.19×10^6 trigger events, starting at ~7 hours after launch and lasting ~16 hours, of which ~14.78 hours are used in this analysis. A total of 443836 events passed all of the basic selection criteria described in this chapter. The selection criteria are described in Sections 3.1 through 3.6. However, because of the large array of numbers which arise from the this selection set, a detailed summary of the selection results is also given in Section 3.6, with the resulting raw numbers of protons and antiprotons arising from this analysis given in Section 3.7.

3.1 Track Fitting — The HYBMOM Software

The HYBMOM tracking software for fitting particle trajectories through the drift chambers (DCs) and multiwire proportional counters (MWPCs) was provided to the IMAX Collaboration by the University of Siegen, building on software originally developed by PAL–NMSU for use with the MWPCs alone. The fitting algorithm and the tracking system performance are described by Golden et al. (1991) and Hof et al. (1994). The HYBMOM software package consists of approximately 6000 lines of FORTRAN source code, and it is beyond the scope of this thesis to describe the algorithm in absolute detail. Nevertheless, a summary description is in order, based on Golden et al. (1991), extensive discussions with the IMAX collaborators at the University of Siegen, and examination of the source code.

In order to fit a particle trajectory and obtain its magnetic rigidity, the track–fitting software first reads the raw drift chamber (DC) data. As described in Section 2.2, the raw DC data consists of drift time data from the TDCs for each drift cell in which a signal was detected. Then, time–dependent drift–time–to–position relations (DPR) are applied to each

hit cell to convert the measured drift times to positions within the cells. The measured positions are used to provide an initial, linear fit trajectory, as an initial guess.

The initial, linear fit is used to initialize the state vector for the particle. When fitting a particle trajectory, the state vector for that particle is defined as

$$\alpha = \left(x_1, y_1, \left(\frac{dx}{dz}\right)_1, \left(\frac{dy}{dz}\right)_1, \frac{1}{R} \right) \tag{3.1.1}$$

where the first two elements (x_1, y_1) give a single, measured reference position within the tracking system in the horizontal plane, and the z–axis is vertical to the MWPC and DC planes. The second two elements $\left((dx/dz)_1, (dy/dz)_1\right)$ give the change in x,y with respect to vertical displacement at the reference position, and the last element is the magnetic deflection (inverse rigidity). In the case of IMAX data analysis, the state vector is initialized so that the initial reference position is the fitted position at the bottom MWPC layer, the slopes $\left((dx/dz)_1, (dy/dz)_1\right)$ are taken from the linear fit, and the magnetic deflection is initialized at 0.005 GV^{-1}.

Once the state vector is initialized, the HYBMOM software revises the state vector via the iterative least–squares method of Solmitz and Burkhardt, which is described in full by Golden et al. (1991). The Solmitz and Burkhardt algorithm obtains a fit by minimizing the second order Taylor expansion of

$$\chi^2 = \sum_i \left[\left(\frac{x_{i,\text{fitted}} - x_{i,\text{measured}}}{\sigma_{i,x}} \right)^2 + \left(\frac{y_{i,\text{fitted}} - y_{i,\text{measured}}}{\sigma_{i,y}} \right)^2 \right] \tag{3.1.2}$$

with respect to the state vector. The fitted positions are obtained via stepwise integration from the reference position through the nonuniform magnetic field, with the trajectory defined by the state vector and the magnetic field map. The value of χ^2 is a measure of the difference between the measured position and the fitted positions.

The second order Taylor series expansion of χ^2 takes the form

$$\chi^2(\alpha) = \chi^2(\alpha_0) + \left[\sum_j \left(\frac{d\chi^2}{d\alpha_j} \right)_{\alpha_0} \Delta\alpha_j + \frac{1}{2} \sum_{jk} \left(\frac{d^2\chi^2}{d\alpha_j d\alpha_k} \right)_{\alpha_0} \Delta\alpha_j \Delta\alpha_k \right] \tag{3.1.3}$$

The solution for the state vector is found by minimizing χ^2 with respect to the elements of the state vector, and it takes the form

$$\alpha = \mathbf{Z}^{-1}\mathbf{V} + \alpha_0 \tag{3.1.4}$$

where

$$(\mathbf{Z})_{jk} \equiv \left(\frac{\partial^2\chi^2}{\partial\alpha_j \partial\alpha_k} \right)_{\alpha_0} \text{ and } (\mathbf{V})_l \equiv \left(\frac{\partial\chi^2}{\partial\alpha_l} \right)_{\alpha_0} \tag{3.1.5}$$

(The definition of $(\mathbf{V})_l$ as given in Golden et al. (1991) appears to be a typographical error.) The state vector is calculated iteratively via Equation 3.1.4, with the substitution $\alpha_0 \rightarrow \alpha$ at each step, and as implemented, the iterations are stopped once the elements of α change by less than 10 μm, 0.1 mrad, and 1/300 GV^{-1}, respectively.

Once the state vector has converged to a solution, the software implements angle corrections to correct for deviations from cylindrical symmetry of the electric fields within the drift cells and to refine the measured positions. If any measured DC positions are more than 4 cm off the fitted track — implying a scatter event, a drift cell misfire, or a second particle — then those DC positions are eliminated from further fits. Then, available MWPC positions are added, and the state vector is further revised via the Solmitz and Burkhardt algorithm. Finally, if possible, separate state vectors — and separate measures of magnetic rigidity, or deflection — are obtained for the two drift chambers.

There are a number of defined failure modes for the fitting algorithm for the hybrid (DC+MWPC) tracking system. The fit fails if the Solmitz and Burkhardt algorithm fails to converge within ten iterations, if the number of available measured positions is less than 4 in the x–axis and 3 in the y–axis, if the effective sagitta (see Section 2.2) for the track is greater than 20 cm, or if there are errors in decoding the raw DC data. The efficiency of the tracking detector and track–fitting algorithm is discussed in Section 4.2.3.

3.1.1 Tracking Quality Selection Criteria

If the HYBMOM software (Section 3.1) is able to fit a basic track with the available raw tracking data, it sets a flag called IFAIL to 0, and the fit results are returned. Otherwise, if IFAIL≠0, a fitted track is not available, and the event is rejected from all subsequent analysis. Of the 3.19×10^6 trigger events at float altitude in our data set, 1652075 (or ~52%) passed the IFAIL cut.

As is noted in Section 3.1, the IFAIL=0 condition requires a minimum of 4 available x–positions and 3 available y–positions in the initial tracking data, and of the available positions, a minimum of 4 x–positions and 3 y–positions must be incorporated into the preliminary and final fitted tracks. For example, if 6 x–positions are available for a given event, the algorithm may drop 2 x–positions and still be able to return a fitted track (IFAIL=0).

Thus, the primary cause of IFAIL≠0 conditions is that, in the final fit iteration, less than 4 x–positions and 3 y–positions remain in the fit; approximately 34.4% of all trigger events fail to yield a fitted track for this reason. This condition could be caused simple out–of–geometry events, by hard scatters, or by multiple particles (coincidence events, knock–on electrons, etc.) which would cause large numbers of position measurements to be dropped from the fit. About 5.6% of events fail a similar condition in the MWPC system in the absence of useful DC position information, and another 3.5% of events fail this condition when there are insufficient available positions for the initial fit iteration. Some 2.5% of events fail because

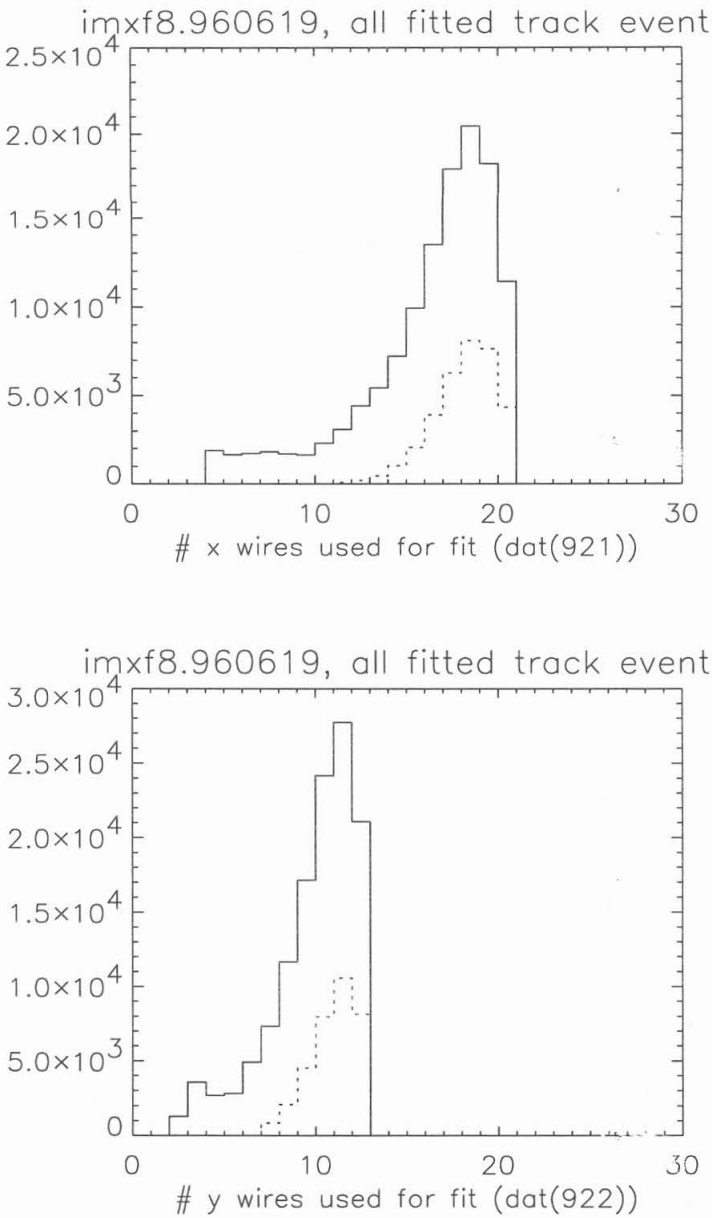

Figure 3.1: Sample histograms of the number of x– and y–positions (NGx and NGy) used for the final track–fitting iteration. The solid histograms give NGx and NGy for a sample of events which passed the basic track–fitting requirements (IFAIL=0). The dashed histograms give NGx and NGy for the corresponding events which pass all cuts in this chapter.

the iterations fail to converge to a solution, and the remaining failure conditions arise from sundry failures in the fit algorithm which do not make up more than 1% (each).

The IFAIL=0 condition reflects a minimum set of track–fitting criteria (see Section 3.1) not necessarily sufficient to ensure that the fitted track is a useful approximation of the path that a single particle actually took. There are instances in which the available tracking data fits the minimum criteria to establish convergence via the Solmitz and Burkhardt algorithm but also in which the data is insufficient to determine whether a scattering interaction occurred and, hence, that the results of the track–fitting may be in error. For example, an event which only meets the minimum 4 x–position requirement — implying an average of 2 x–measurements above and below the magnet — can, in principle, describe a smoothly curved trajectory through all 4 points, or it can describe a straight line (very high magnetic rigidity, R) passing through the top 2 x–positions, followed by a hard scatter and then a straight line through the bottom 2 x–positions. In the latter case, the 4 x–positions may be fitted by a smooth trajectory associated with some magnetic rigidity R, but that rigidity would not necessarily reflect the actual rigidity of the particle. By requiring more x–measurements, we increase the probability of discriminating between smooth tracks and tracks with scatters, and we increase the likelihood that the magnetic rigidities arising from the trajectory fits are accurate. Thus, IMAX data analysis includes stricter set of tracking quality cuts for well–determined particle trajectories, which in turn results in better mass resolution than is given solely by the minimal IFAIL=0 criterion.

For the antiproton and proton analysis, the stricter selection set required that at least 11 x–positions (NGx) and 7 y–positions (NGy) must be incorporated into the fitted track. Sample histograms of NGx and NGy are shown in Figure 3.1, for a sample of events preselected by the IFAIL=0 criterion only, as well as for events passing all cuts in this chapter. Of the 1652075 fitted track events (IFAIL=0), 1416819 events (86%) passed the NGx≥11 cut, and 1357537 events (82%) passed the NGy≥7 cut.

However, it is more interesting to compare the results of these cuts with events preselected by all other cuts in this chapter. For example, 443836 events pass all cuts described in this chapter, and 448148 events pass all cuts independent of the NGx≥11 cut. Thus, the "relative selection percentage" for NGx≥11 is 443836/448148 = 0.99, or 99%. Similarly, for NGy≥7, the relative selection percentage is 443836/466864 = 0.95, or 95%. The reason that the relative selection percentages are higher than the percentages compared with the IFAIL=0 selection set is that the IFAIL=0 selection, taken alone, still allows for the selection of anomalous events which may be out–of–geometry, which may be noisy, which may include scatters, etc., as described above. Preselection of events by the other cuts described in this chapter reduces the incidence of anomalous or out–of–geometry events and, in effect, reduces the fraction of events which would fail the NGx≥11 cut. Note that a summary of all of the cut statistics will be given in Section 3.6.

As described earlier in Section 3.1, for certain events, the HYBMOM algorithm drops individual position measurements when some available positions are inconsistent with well–fitted tracks determined by a good set of other available positions. While the offset from the track may be a result of failure of the HYBMOM algorithm, the position anomaly may also be caused by spontaneous discharge near a given DC sense wire, scattering of the particle, knock–on electrons in or passing through the tracking system, out–of–total–geometry coincidence particles, or even voltage spikes in the tracking system electronics. Figure 3.2 shows histograms, from a flight data sample preselected for IFAIL=0, of the number of planes giving positions (in x and y) 4 cm or more off the best fitted tracks. The vast majority of the events show no planes more than 4 cm off the tracks, but the IMAX antiproton and proton selection set allowed for as many as two planes to be 4 cm off the fitted tracks. Of the 1652075 fitted track (IFAIL=0) events, 1507486 events (91%) had two or fewer x–planes with positions more than 4 cm off the fitted tracks, and 1532692 events (93%) passed the same cut for the y–axis. The relative selection percentages are 99% for both cuts.

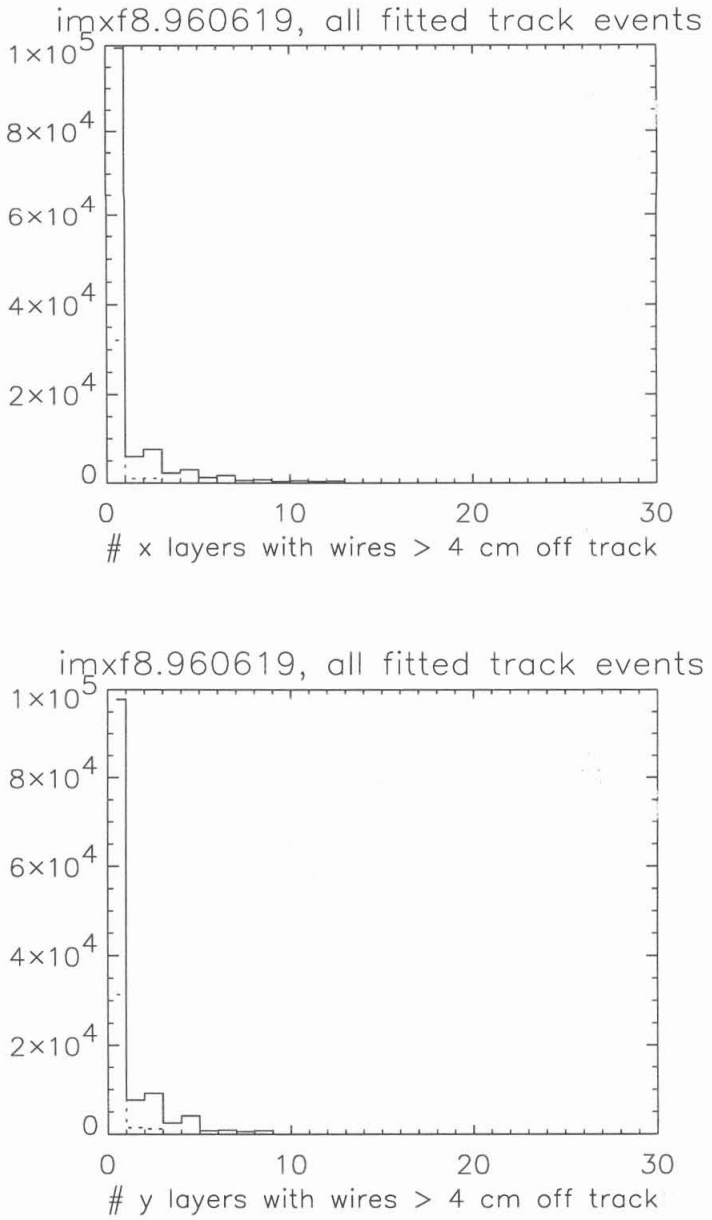

Figure 3.2: Sample histograms of the number of x– and y–positions (NGx and NGy) dropped from the final track–fitting iteration. The solid histograms are given for a sample of events which passed the basic track–fitting requirements (IFAIL=0), and the dashed histograms correspond to events which pass all cuts in this chapter.

Next, χ^2 "goodness–of–fit" quantities were calculated for both the x– and y–positions. For a given position measurement at a given tracking system plane, the χ value, relative to the fitted track, is given by

$$\chi_x = \frac{\left(x_{\text{fitted}} - x_{\text{measured}}\right)}{\sigma_x} \tag{3.1.6}$$

where x_{measured} is the measured x–position at the tracking system plane, x_{fitted} is the x–position at that plane for the fitted track, and σ_x is the position resolution for that plane. The position resolution for a given plane is calculated as the distribution width of the residual difference between measured and fitted positions at that plane:

$$\sigma_x = \text{width}\left(\left(x_{\text{fitted}} - x_{\text{measured}}\right)\sqrt{\frac{NGx}{NGx-5}} \right) \tag{3.1.7}$$

where NGx is the total number of x–measurements used in the fit. The χ^2 for the x–measurements is calculated as the sum of the individual χ^2's for the planes. Similar quantities are calculated for the y–positions. (The -5 term (in NGx-5) comes from the 5 elements of the state vector: The number of degrees of freedom in the fit is given by the number of points that go into the fit minus the 5 elements which define the particle trajectory.) Figure 3.3 shows χ^2 for the x– and y–positions, and selection was made for $\chi^2 \leq 4$ for both x and y. Of the 1652075 fitted tracks (IFAIL=0), 1409556 events (85%) passed the χ^2 cut for x, and 1400607 events (85%) passed the χ^2 cut for y. The relative selection percentages were 96% and 93% for x and y, respectively, with the lower y percentage reflecting the lower precision in determining the y–position fits, which in turn arises from fewer available y–measurements.

Finally, the uncertainty in positions propagates through the calculation of deflection to yield an uncertainty in the fitted deflection is given by $\sigma_{\text{def}} = \left(\mathbf{Z}^{-1}\right)_{5,5}$, where the $\mathbf{Z}$ matrix is defined in Equation 3.1.5. Figure 3.4 shows a histogram of $\sigma_{\text{deflection}}$ for a sample of float

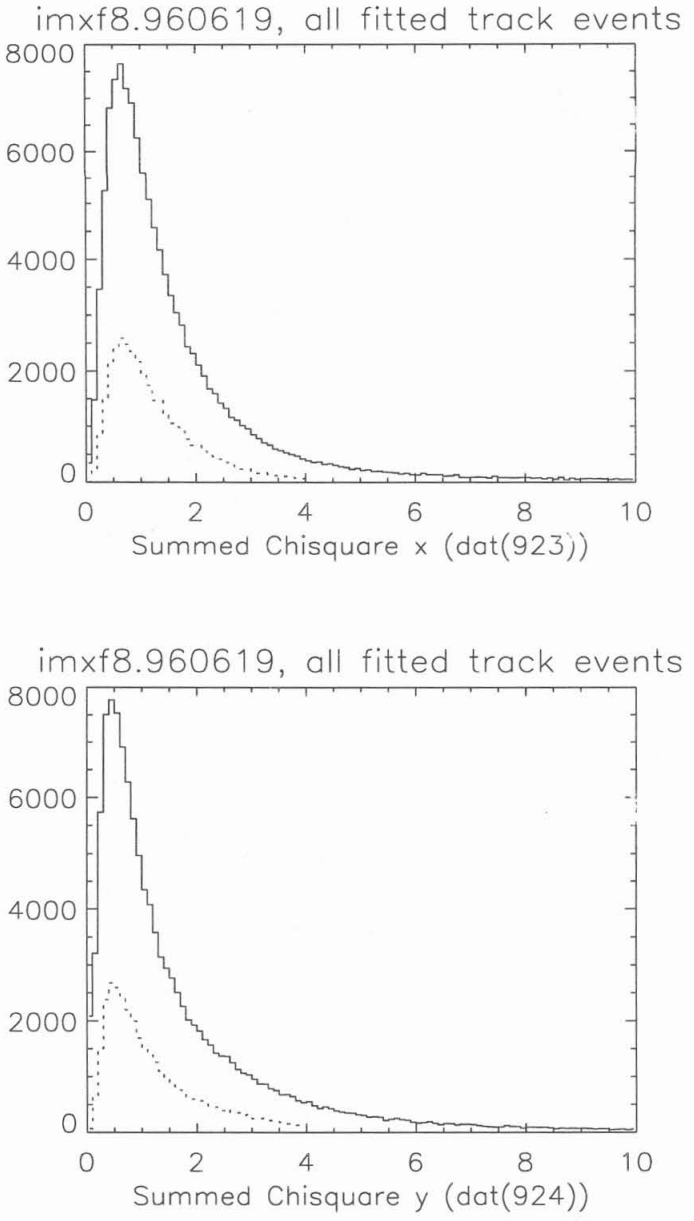

Figure 3.3: Sample histograms of track χ^2 distributions from the final track–fitting iteration. The solid histograms are given for a sample of events which passed the basic track–fitting requirements (IFAIL=0), and the dashed histograms correspond to events which pass all cuts in this chapter.

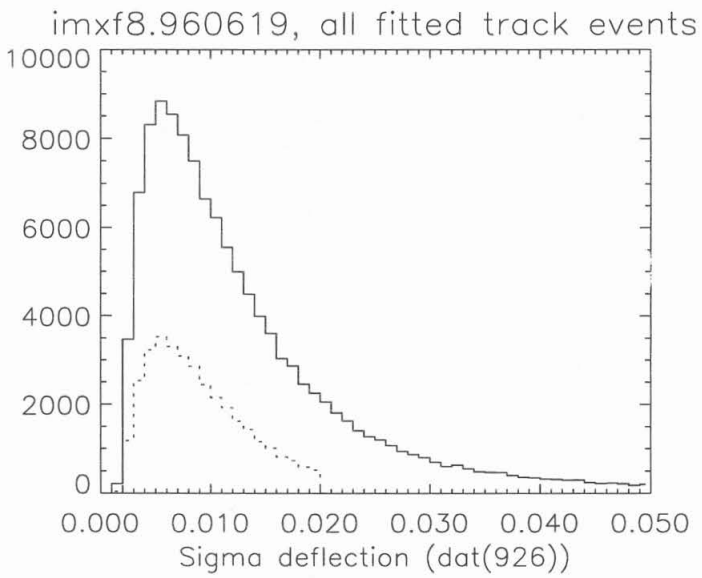

Figure 3.4: Sample histogram of the $\sigma_{deflection}$ distribution from the final track–fitting iteration. Units are GV^{-1}. The solid histogram is given for a sample of events which passed the basic track–fitting requirements (IFAIL=0), and the dashed histogram corresponds to events which pass all cuts in this chapter. The peaks at ~0.05 GV^{-1} imply a characteristic maximum detectable rigidity (MDR) of 200 GV. The average of the dashed histogram distribution (~0.0087 GV^{-1}) corresponds to an average MDR of ~115 GV.

data events preselected for IFAIL=0. The peak in the distribution at ~0.005 GV^{-1} demonstrates that the IMAX tracking system has a characteristic maximum detectable rigidity of 200 GV. The average of the distribution accepted for analysis is 0.0087 GV^{-1}, or an average MDR of ~115 GV. For analysis of flight data, the limit was $\sigma_{deflection}<0.02$ GV^{-1}, implying a maximum detectable rigidity as low as 50 GV for the events allowed into the analysis. Of the 1652075 fitted track (IFAIL=0) events, 1296404 events (78%) passed the $\sigma_{deflection}$ cut, with a relative selection percentage of 92%.

Finally, of the 1652075 fitted track (IFAIL=0) events, 876317 events passed all of the tracking quality cuts. A detailed summary of the results of these and all other selection criteria described in this chapter will be given in Section 3.6.

3.1.2 Tracking System Correlation Cuts

With separate upper and lower DCs, one may enforce rough correlation between the individual DCs and the combined DC+MWPC ("hybrid") measurements. Figure 3.5 shows, for a one–hour sample of float data, histograms of the differences between the hybrid deflection and the upper DC deflection, the hybrid deflection and the lower DC deflection, and the deflections from the upper and lower DCs — all relative to the measurement uncertainty of the hybrid system. A correlation cut applied to this data would remove the effects of scatters, within limitations imposed by the measurement precision. Given the smaller number of fit–points for the individual DCs, the width of the histograms is due largely to the measurements from the individual DCs, and loose limits of ±80 were selected in each histogram. Of the 1652075 fitted track (IFAIL=0) events, 1453386 events (88%) passed the Total vs. Upper deflection cut, 1419237 events (86%) passed the Total vs. Lower deflection cut, and 1364114 events (82%) passed the Upper vs. Lower deflection cut. When applying these cuts individually to events preselected by all other cuts described in this chapter, the relative selection percentages for the cuts are 99.9%, 99.9%, and 99.5%. It is these relative selection percentages which are reflected in Figure 3.5. The higher relative selection percentages arise

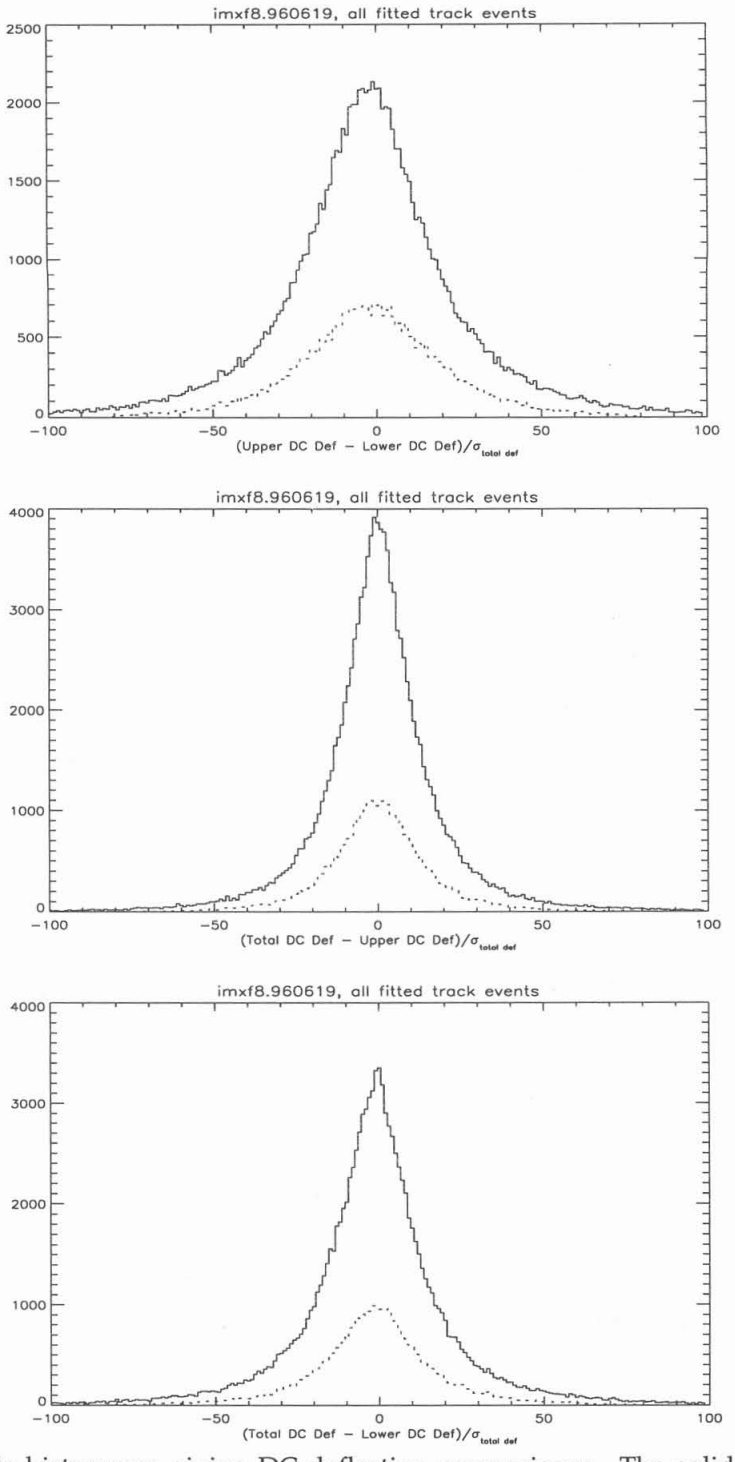

Figure 3.5: Sample histograms giving DC deflection comparisons. The solid histograms are given for a sample of events which passed the basic track–fitting requirements (IFAIL=0), and the dashed histograms correspond to events which pass all cuts in this chapter.

primarily from the tracking quality selection criteria described in Section 3.1.1, which ensure that there are enough position measurements to define trajectories relatively well in the individual DCs.

Another rough cut may be applied to the charge signs indicated by the two DCs relative to the hybrid measurement. Given the limited precision of the individual DC measurements, it is not uncommon for the individual DCs to show different charge signs near zero deflection. However, it is also possible for the DCs to show the same charge signs individually, while yielding an opposite charge sign when combined (with the MWPCs) in the hybrid measurement. Such events usually indicate only a minimal availability of individual tracking position measurements. Of the 1652075 fitted track (IFAIL=0) events, 1599794 events (97%) passed this cut, and compared to all other cuts in this chapter, the relative selection percentage is 98.9%.

A detailed summary of the results of these and all other selection criteria described in this chapter will be given in Section 3.6.

3.1.3 Active Area Cuts

Trajectories obtained from the HYBMOM algorithm can be step–wise integrated through the magnetic field of IMAX to the z–positions of the various counters in IMAX. It is possible for signals to arise in a given counter even if the particle trajectory does not intersect with the detector medium. For example, knock–on electrons from the primary particle may enter a detector, or a second primary particle, coincident with the first but out of the tracking system geometry, may also intersect with the detector. Therefore, cuts were applied to ensure that the selected trajectories projected into the counter active areas, defined in Chapter 2. The results of these active area cuts are given in Table 3.2, with the counters listed from the top to the bottom of the IMAX payload.

The fourth column gives the percentage of events passing all other cuts (e.g. active area cuts from the other counters, plus all other cuts described in this chapter) which also pass the

given active area cut. Thus, for example, 448487 events pass all cuts described in this chapter independent of the Top TOF active area cut, and 443836 of these events also pass the Top TOF active area cut, yielding a relative efficiency of 98.9% for the Top TOF active area cut. Thus, the 100% relative efficiency of the S1 active area cut implies that its active area is larger than the area in S1 defined by trajectories passing through all other active areas.

Table 3.2: Active Area Cut Summary

Counter	# of fitted track events in active area (%)	# events passing all other cuts	Relative Selection Percentage
Top TOF	1396025 (84.5%)	448487	98.9
C3	1332066 (80.6%)	444701	99.8
S1	1528127 (92.5%)	443836	100
C2	1427094 (86.4%)	444701	99.8
S2	1355534 (82.1%)	451415	98.3
Bottom TOF	1384912 (83.8%)	447955	99.1

3.2 Charge Selection Criteria

From the Bethe–Bloch equation (Equation 2.4.1), we can see that the scintillator light yield can take the form

$$\frac{dE}{dx} \propto Z^2\left[A - \frac{A}{\beta^2}\ln\left(B\beta^2\right)\right] \tag{3.2.1}$$

where A and B are constants. Thus, for nonrelativistic β, the scintillator light yields are approximately linear with respect to $1/\beta^2$ for any given charge Z. Figure 3.6 shows plots of scintillator signals vs. $1/\beta^2_{TOF}$ for the various scintillators, where the velocity is measured by the time–of–flight system. Because the velocity is measured as the average velocity through the payload, the plots show some curvature due to energy loss for low energy particles, so that the TOF velocity overestimates actual the velocity of low energy particles in the bottom half

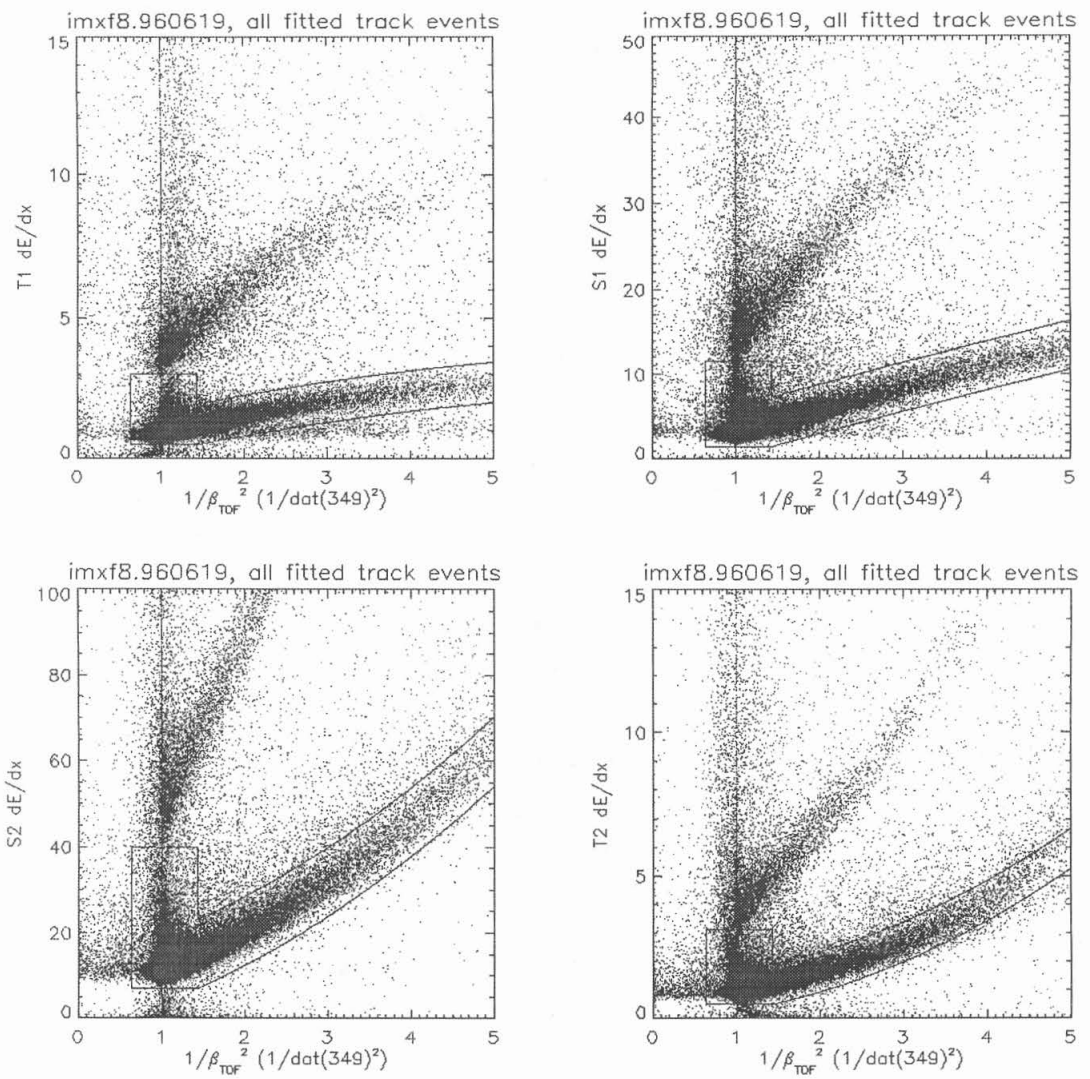

Figure 3.6(a–d): Sample plots of dE/dx (arbitrary scales) vs. $1/\beta^2_{TOF}$ for the IMAX scintillators. The Z=1 selection regions are outlined.

of the payload and slightly underestimates in the upper half. (See Appendix B for a description of energy losses through the atmosphere and instrument.) Nevertheless, separation of Z=1 from Z=2 particles is clear and straightforward. The Z=1 charge selection regions, also shown, were obtained from quadratic fits to dE/dx vs. $1/\beta^2_{TOF}$.

Of the 1652075 fitted track (IFAIL=0) events, 1197084 events (72%) pass the Top TOF Z=1 cut, 1285813 events (78%) pass the S1 Z=1 cut, 1154053 events (70%) pass the S2 Z=1 cut, and 1163606 events (70%) pass the Bottom TOF Z=1 cut. However, the events eliminated by these cuts include Z≥2 events, multiple particle events, etc.

A more interesting set of statistics will be a comparison of the events which pass all cuts described in this chapter relative to the number of events which pass all other cuts independent of any given charge cut. That is, for any given scintillator, we select all Z=1 events from the other scintillators, with further selection for good tracks, active area cuts, etc., and then we find the number of events eliminated by the remaining Z=1 cut. Thus, for example, 453280 events pass all other cuts in this chapter plus the S1, S2, and bottom TOF Z=1 charge cuts, and when the Top TOF Z=1 charge cut is added, 443836 events pass the total selection criteria set, implying a relative Z=1 selection percentage of ~97.9% for the Top TOF paddle. Similarly, the relative Z=1 selection percentages for S1, S2, and the Bottom TOF are 99.0%, 99.1%, and 97.9%, respectively. The relative selection percentages are higher than the percentages compared with IFAIL=0 alone because of the correlation between charge cuts; the IFAIL=0 cut imposes no charge selection. Note that, by definition, these relative selection percentages ignore Z=2 events.

A detailed summary of the results of these and all other selection criteria described in this chapter will be given in Section 3.6.

3.3 Aerogel Cherenkov Analysis

In order to provide maximum velocity resolution and discrimination between particles of various masses, signals from C2 and C3 must be combined and normalized to 1 for Z=1, β=1

particles. (See Section 2.1.2.) Intuitively, one might wish to combine the light yields of the two counters in much the same way that the single PMT light yields are summed for the single counters (see Section 2.1.3), e.g.

$$f_{2+3} \equiv \frac{L_{2+3}}{M_{2+3}} = \frac{L_2 + L_3}{M_2 + M_3} = \frac{\sum_i l_{2,i} + \sum_i l_{3,i}}{\sum_i \overline{l_{2,i}(\beta = 1)} + \sum_i \overline{l_{3,i}(\beta = 1)}} \tag{3.3.1}$$

where Equation 3.3.1 generalizes the fractional light yield, f, for a single counter (Equation 2.1.8) to a form appropriate for two counters — in this case, C2 and C3.

However, it may be argued that the single–counter form is not applicable for two counters, because fluctuations in light yields for separate counters are not correlated, while the individual PMTs in a single counter look at the same light production fluctuations. Therefore, a maximum likelihood approach, taking into account separate fluctuations between counters, is called for.

Assume a single particle of some velocity β passes through two Cherenkov counters, with minimal mapping corrections and with light yield fluctuations dominated by Poisson statistics. Assume the theoretical (i.e. non–fluctuated) light yield in each counter will be μ_2 and μ_3 photoelectrons, while the measured (i.e. fluctuated) light yields are L_2 and L_3, respectively. The probability that two counters, of theoretical light yields μ_2 and μ_3, give measured light yields of L_2 and L_3 photoelectrons is given by

$$P_2 P_3 = \frac{\mu_2^{L_2} e^{-\mu_2}}{L_2!} \frac{\mu_3^{L_3} e^{-\mu_3}}{L_3!} \tag{3.3.2}$$

In principle, we expect that the theoretical, map–normalized light yields between the two counters to be approximately equal, except for small energy losses between counters, differences in index, etc. Thus,

$$\overline{f_2} = \overline{f_3} \text{ or } \mu_2 = \frac{M_2}{M_3}\mu_3 \text{ (since } \overline{f_2} \equiv \frac{\mu_2}{M_2},\ \overline{f_3} \equiv \frac{\mu_3}{M_3}) \tag{3.3.3}$$

Substituting $\mu_2 = \frac{M_2}{M_3}\mu_3$ into Equation 3.3.2 gives

$$P_2P_3 = \frac{\left(\frac{M_2}{M_3}\mu_3\right)^{L_2} e^{-\frac{M_2}{M_3}\mu_3}}{L_2!} \frac{\mu_3^{L_3} e^{-\mu_3}}{L_3!} \tag{3.3.4}$$

Maximizing this expression with respect to μ3 yields

$$\mu_3 = \frac{L_2 + L_3}{1 + \frac{M_2}{M_3}} \tag{3.3.5}$$

Dividing through by M3 yields

$$\overline{f_3} \equiv \frac{\mu_3}{M_3} = \frac{L_2 + L_3}{M_2 + M_3} \tag{3.3.6}$$

in which the first part is the expression for the theoretical map–normalized light yield in C3, given measured map–normalized light yields f2 and f3. Note that f3 is not necessarily equal to $\overline{f_3}$.

However, because we expect the theoretical map–normalized light yields in the two counters to be equal (see Equation 3.3.3), it follows that the non–fluctuated, theoretical combined map–normalized light yield will be equal to the single counter, theoretical values:

$$\overline{f_{2+3}} = \overline{f_2} = \overline{f_3} = \frac{L_2 + L_3}{M_2 + M_3} \tag{3.3.7}$$

Thus, given fluctuated measurements from C2 and C3, the most likely normalized light yield implied by the separate measurements is equal to the map–normalized value calculated from an expression which assumes that the two separate counters may be taken as one large counter.

3.3.1 Aerogel Cherenkov Signal Selection Criteria

Unlike the tracking selection criteria, which all events must pass in order to be considered, some primary aerogel Cherenkov selection criteria change in accordance with the energy range being analyzed. Thus, as will be described in Section 3.7, particles in the TOF–Rigidity energy range (< 2.6 GeV) will have $\overline{f_{2+3}}$ ("C2+C3 Map–Norm") < 0.16, and in the Cherenkov–Rigidity range will have $\overline{f_{2+3}}$ = 0.16 to 0.36.

As described in Section 4.2.1 (Geometry Factor), single particle events must include tracks which pass through the C2 and C3 active areas defined in Table 2.1.1, and cuts for events projected into the active areas are summarized in Section 3.1.3. Furthermore, no single C2 or C3 PMT is allowed to measure more than 5 pes for a given event; such events are assumed to include particles hitting PMT photocathodes. Even for single Z=1, β=1 particles, the average light yield for single PMTs will be ~1 pe per PMT, and assuming Poisson statistics, ~95% of Z=1, β=1 particles will have no PMTs measuring more than 5 pes in a single counter. For slower particles with average light yields at ~0.5 pes per PMT, >99% of these particles will have no PMTs measuring more than 5 pes.

Of the 1652075 fitted track (IFAIL=0) events, 1528233 events (92.5%) had no PMTs with light yields above 5 pes in C2, and 1502242 events (90.1%) passed the same cut for C3. When compared with all other cuts described in this chapter, the relative selection percentages for these "5 pe" cuts are 98.6 % for C2 and 98.8% for C3. Also, of the 450245 events which passed all other cuts independent of the C2 5 pe cut, 443836 events (98.6%) also passed the C2 5 pe cut.

Similarly, 449456 events passed all other cuts independent of the C3 5 pe cut, implying a 98.8% relative efficiency for this cut. A detailed summary of the results of these and all other selection criteria described in this chapter will be given in Section 3.7.

3.3.2 C2–C3 Correlation

The availability of two aerogel Cherenkov counters of similar characteristics allows for correlation between the two counters. As with the derivation of an expression for combining the map–normalized light yields of the two counters (C2+C3 Map–Normalized; see Section 3.3), a Poisson statistical approach may be employed to establish a correlation cut. One caveat to this cut is that Poisson fluctuations at relatively low light yields force this cut to be extremely loose, because the Poisson fluctuations in the two counters are uncorrelated and are large relative to the theoretical (non–fluctuated) signals.

By combining Equations 3.3.4, 3.3.6, and 3.3.7, we find the correlation probability, P_2P_3, may be rewritten as

$$P_2P_3 = \left(M_2\overline{f_{2+3}}\right)^{L_2}\frac{e^{-L_2}}{L_2!}\left(M_3\overline{f_{2+3}}\right)^{L_3}\frac{e^{-L_3}}{L_3!} \tag{3.3.8}$$

where the notation for this expression is as given in Section 3.3. This expression gives the probability that C2 and C3 will yield L_2 and L_3 fluctuated photoelectrons, respectively, for a given particle (and response map values of M_2 and M_3) with a theoretical, non–fluctuated, map–normalized light yield $\overline{f_{2+3}}$. Figure 3.7 shows a plot of P_2P_3 vs. $\overline{f_{2+3}}$ for a one–hour sample of float data.

Because the range of values for P_2P_3 changes rapidly with $\overline{f_{2+3}}$ in the region of interest for IMAX, it is more convenient to calculate the correlation probability relative to its maximum value. Clearly, P_2P_3 is maximized for $f_2=f_3=\overline{f_{2+3}}$, so

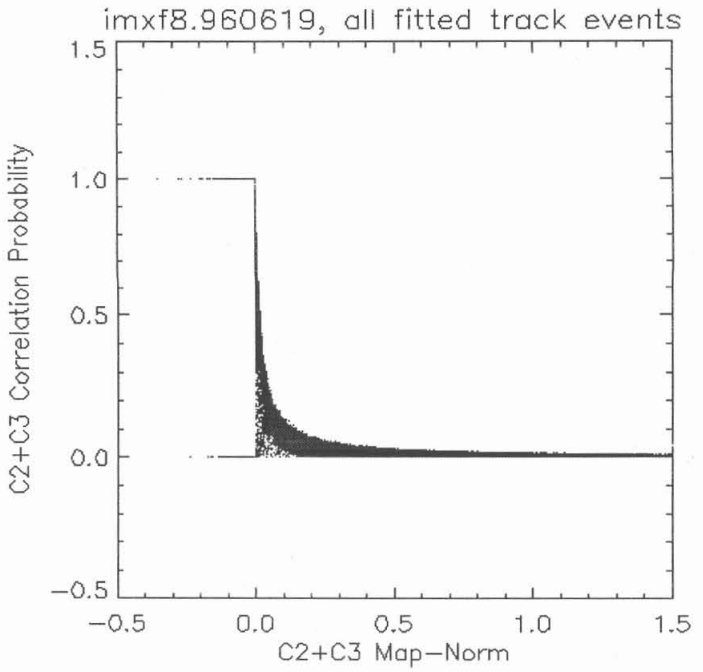

Figure 3.7: C2, C3 correlation probability vs. C2+C3 Map–Normalized.

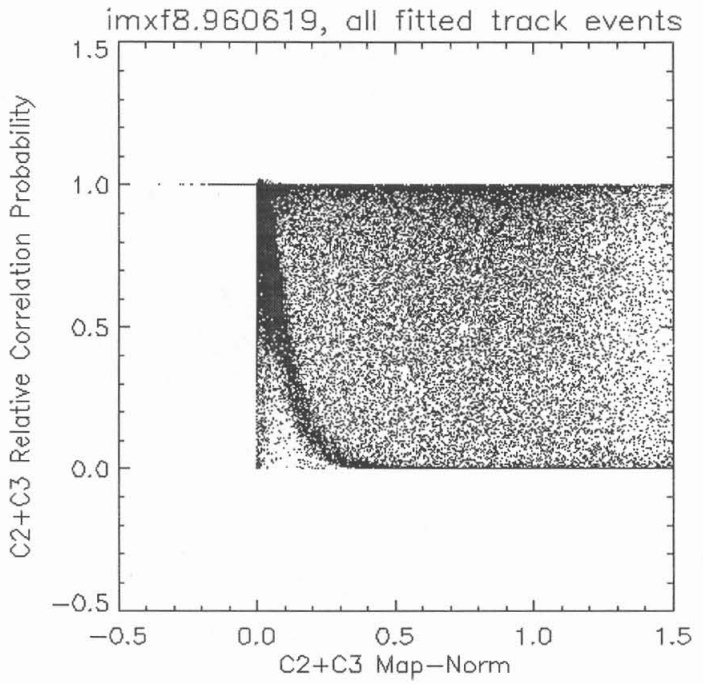

Figure 3.8: C2, C3 relative correlation probability vs. C2+C3 Map–Normalized.

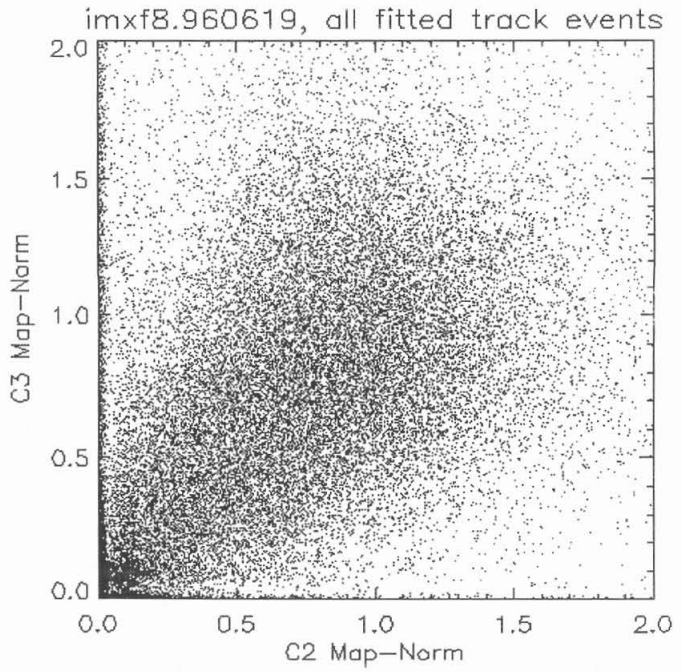

(a)

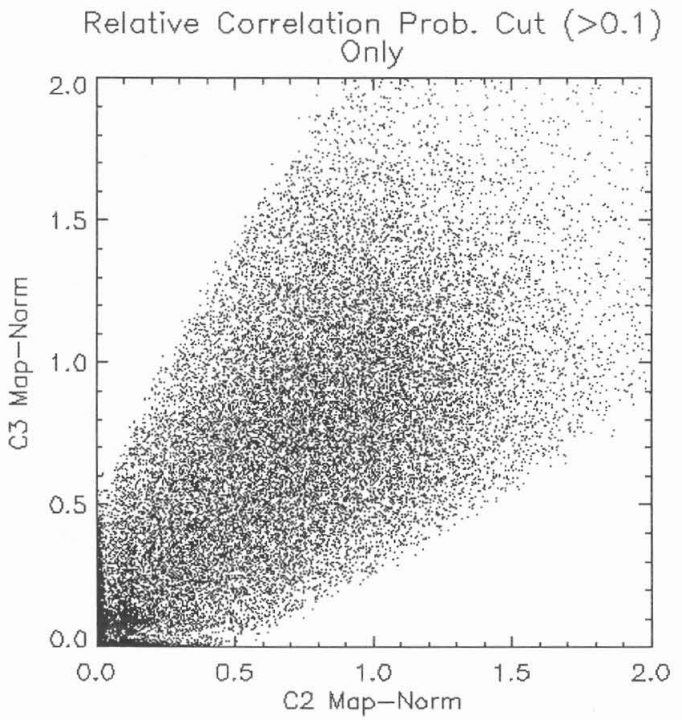

(b)

Figure 3.9 (a,b): The effect of the C2,C3 relative correlation probability cut, shown as C3 Map–Normalized vs. C2 Map–Normalized (a) without and (b) with the cut.

$$\max(P_2P_3) = \frac{\left(\overline{f_{2+3}}M_2\right)^{\overline{f_{2+3}}M_2}\left(\overline{f_{2+3}}M_3\right)^{\overline{f_{2+3}}M_3}}{\left(\overline{f_{2+3}}M_2\right)!\left(\overline{f_{2+3}}M_3\right)!}e^{-\overline{f_{2+3}}(M_2+M_3)} \tag{3.3.9}$$

and

$$\frac{P_2P_3}{\max(P_2P_3)} = \frac{\left[\overline{f_{2+3}}M_2\right]!\left[\overline{f_{2+3}}M_3\right]!}{L_2!L_3!}\left[\overline{f_{2+3}}M_2\right]^{\overline{f_{2+3}}M_2}\left[\overline{f_{2+3}}M_3\right]^{\overline{f_{2+3}}M_3} \tag{3.3.10}$$

Figure 3.8 shows the relative correlation probability vs. $\overline{f_{2+3}}$. Note that this expression fails for negative values of L_2 and L_3, so that, in practice, a cut to the relative correlation probability is applied only to events with positive aerogel Cherenkov light yields. Figure 3.9 shows the effect, on a plot of C2 Map–Normalized (f_2) vs. C3 Map–Normalized (f_3), of setting a lower limit of 0.1 to the relative correlation probability. Of the 1652075 fitted track (IFAIL=0) events, 1645534 events (99.6%) passed this cut, with a relative selection percentage of ~99.9% compared to all other cuts described in this chapter.

3.4 Time of Flight Selection Criteria

Analysis for time–of–flight (TOF) data makes use not only of the TOF ADC (scintillation pulse height) and TDC data but also of tracking data, by stepwise integration of the flight path length through the payload magnetic field from the top TOF paddles to the bottom TOF paddles. With the measured flight time (t, see Section 2.3) and the integrated flight path (d), calculation of velocity is straightforward (v=d/t).

There are a number of basic failure modes defined for TOF analysis, most of which concern coincidence between ADC and TDC signals from the two ends of any given TOF paddle. The basic TOF error flag is designed to eliminate all but well–defined, single particle events passing through the TOF paddles. TOF analysis fails if the payload system triggers without registering signals in the top and/or bottom TDCs, or if more than one EAST-West pair of TDCs

registers signals (implying multiple particles). Further, in either the top or bottom TOF, an East paddle may register a TDC signal, while a West TDC from a different paddle may register a signal. Finally, consistency between ADC and TDC signal pairs is also checked for. If any of these conditions is true, the event fails TOF analysis. Of the 1652075 fitted track (IFAIL=0) events, 1513402 events (91.6%) passed the basic TOF analysis.

From Equation 2.3.4, one may use TDC signals from opposite ends of a given TOF paddle to obtain an approximate x–position at which a particle hit the paddle. Given possible light yield fluctuations, this position measurement is not expected to have a precision as good as that from the tracking system, but a correlation cut can still be applied. If the x–position in a given paddle, as implied by the TDCs, is more than 5 cm off the x–position determined by the tracking system, the event is rejected. Such events may arise from errors in the TDC data, large light yield fluctuations in the TOF system, or scattering of particles not detected by the tracking system (e.g. scattering events occurring outside of the tracking detectors). See Figure 3.10. Of the 1652075 fitted track (IFAIL=0) events, 1167697 events (70.7%) passed this cut, with a relative selection percentage (compared to all other cuts) of 97.1%.

Finally, if the trajectory from the tracking system does not pass through the accepted x– and y– boundaries for the TOF paddles (see Table 2.3.1), the particle is rejected. Such events may arise from scatters, multiple particles triggering the system with only one particle detected by the tracking system, or from particles hitting the "seam" between two paddles at high enough incidence to trigger the TOF yet have trajectories lying between paddles. The results of the TOF active area cuts are given in Section 3.1.3.

3.5 TOF–Cherenkov Correlation

Although the TOF velocity resolution is significantly reduced at the velocity range covered by the aerogel Cherenkov detectors ($\beta \geq \sim 0.95$), there is sufficient TOF velocity resolution up to this region to allow for a rough correlation cut between the two types of velocity measurement. Figure 3.11 shows a cross–plot of $1/\beta^2_{TOF}$ vs. C2+C3 Map–Normalized for one hour

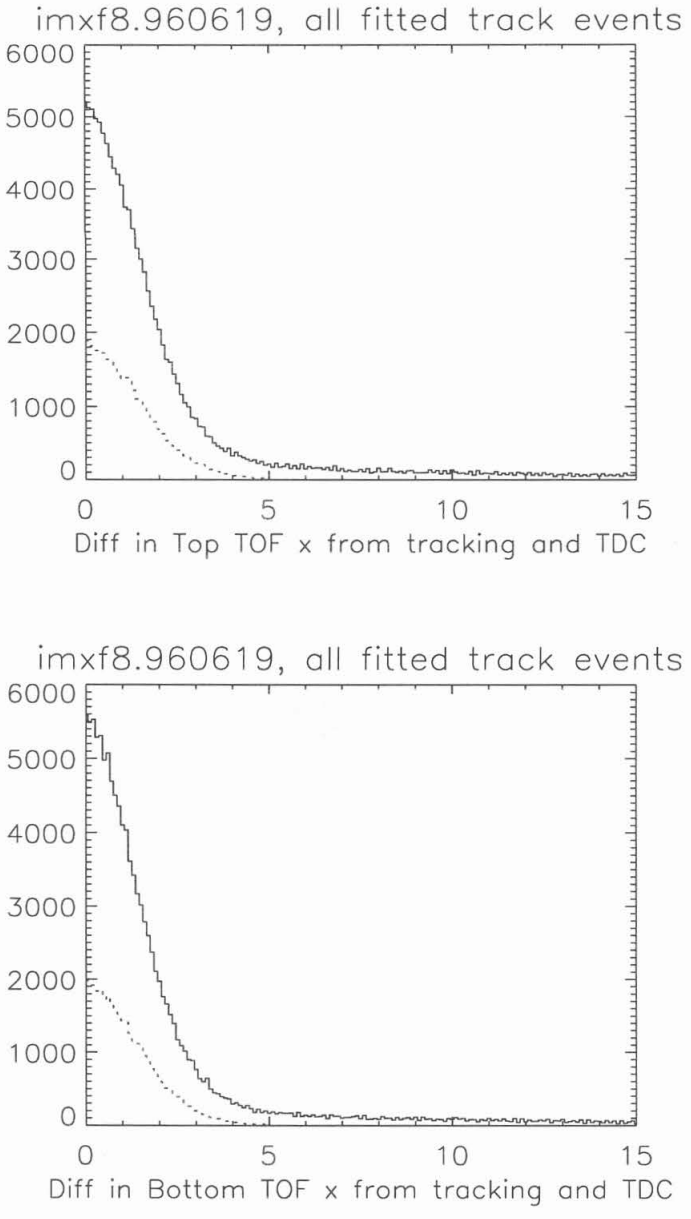

Figure 3.10: Histograms comparing x–positions in the TOF paddles calculated from tracking and x–positions calculated with the TOF TDC data.

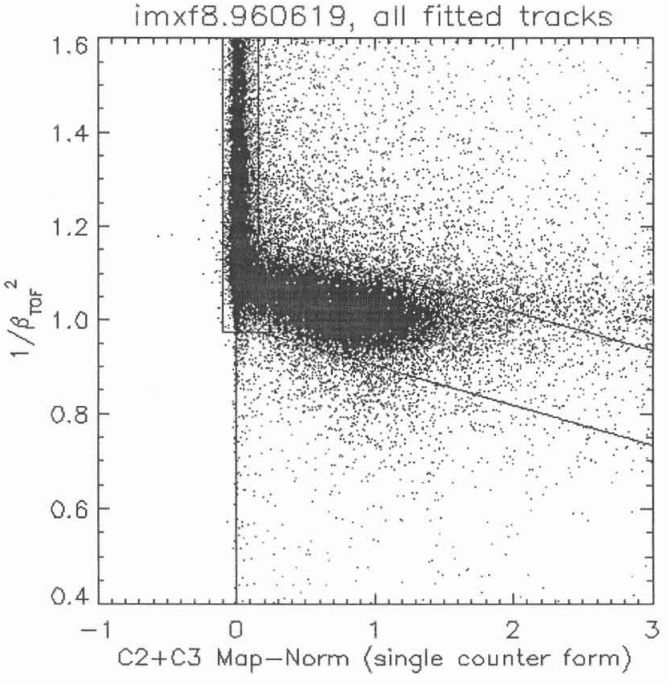

Figure 3.11: Sample data plot of $1/\beta^2_{TOF}$ vs. C2+C3 Map–Normalized, for fitted track events (IFAIL=0).

of flight data. Also shown on the figure are the limits applied for the TOF–Cherenkov correlation selection criterion.

This selection criterion has several purposes, the most general of which is to eliminate anomalous signals in either velocity measurement which are not otherwise eliminated by other cuts (see Sections 2.1.5, 3.4, and 3.3.2). At velocities below Cherenkov threshold, it eliminates particles which have large knock–on fluctuations not already eliminated by the C2–C3 correlation cut. Above threshold, it eliminates events with false or anomalous β_{TOF}, possibly arising from faulty track fits.

Of the 1652075 fitted track (IFAIL=0) events, 1423080 events (86%) pass this selection criterion, with a relative selection percentage of ~98.7% relative to all other cuts. A detailed summary of the results of this and all other selection criteria described in this chapter will be given in Section 3.6.

3.6 Selection Criteria Statistics Summary

Table 3.3 lists all of the selection criteria discussed earlier in this chapter (except the IFAIL cut discussed in Section 3.1.1) roughly in the order in which they were developed during IMAX data analysis. Because most of the selection criteria depend on the existence of a fitted track, the percentages in the table (discussed below) are calculated relative to the 1652075 events which pass the IFAIL=0 cut. Cuts 2 through 8 are the tracking quality selection criteria discussed in Section 3.1.1, and cuts 9 through 14 are the cuts to ensure that selected particles pass through the counter active areas, as discussed in Section 3.1.3. Cuts 15 and 20 are the TOF TDC and TOF error flag cuts described in Section 3.4. Cuts 16 through 19 are the Z=1 selection cuts using the scintillator counters described in Section 3.2. Cuts 21 and 22 eliminate events with anomalously high individual PMT signals in C2 and C3 discussed in Section 3.3.1. Cut 23 is the TOF–Cherenkov correlation cut described in Section 3.5. Cuts 24 through 27 are the tests for correlation between the individual DC measurements discussed in Section 3.1.2. Finally, cut 28 is the C2 vs. C3 relative correlation probability cut described in Section 3.6.

Table 3.3: Selection Criteria Results for the IMAX Flight Data Set

(See text for a description of the numbers.)

#	Selection Criterion	Individual	%	Running	%	Preselected	%
1	Telemetry Checksum	1652023	~100	1652023	~100	443845	~100
2	# x layers > 4 cm (≤2)	1507486	91.2	1507435	91.2	447592	99.2
3	# y layers > 4 cm (≤2)	1532692	92.8	1476042	89.3	446725	99.4
4	# good x planes (NGx≥11)	1416819	85.8	1319170	79.8	448148	99.0
5	# good y planes (NGy≥7)	1357537	82.2	1187179	71.9	466864	95.1
6	Tracking $\chi^2_x \leq 4$	1409556	85.3	1089654	66.0	464351	95.6
7	Tracking $\chi^2_y \leq 4$	1400007	84.7	996161	60.3	479680	92.5
8	$\sigma_{deflection} \leq 0.02 GV^{-1}$	1296404	78.5	876317	53.0	481523	92.2
9	C2 Active Area	1427094	86.4	812373	49.2	444701	99.8
10	C3 Active Area	1332066	80.6	705849	42.7	472021	94.0
11	S1 Active Area	1528127	92.5	705848	42.7	443836	100.0
12	S2 Active Area	1355534	82.1	674468	40.8	451415	98.3
13	Top TOF Active Area	1396025	84.5	662364	40.1	448487	99.0
14	Bottom TOF Active Area	1384912	83.8	650063	39.3	447955	99.1
15	TOF TDC vs. tracking	1167697	70.7	591041	35.8	457236	97.1
16	Z=1, S1 dE/dx vs. $1/\beta^2_{TOF}$	1285813	77.8	529676	32.1	448224	99.0
17	Z=1, S2 dE/dx vs. $1/\beta^2_{TOF}$	1154053	69.9	519260	31.4	447669	99.1
18	Z=1, T1 dE/dx vs. $1/\beta^2_{TOF}$	1197084	72.5	505566	30.6	453280	97.9
19	Z=1, T2 dE/dx vs. $1/\beta^2_{TOF}$	1163606	70.4	492540	29.8	453297	97.9
20	TOF Error Flag	1513402	91.6	492540	29.8	443836	100.0
21	Drop C2 with PMTs > 5 pe	1528233	92.5	484074	29.3	450245	98.6
22	Drop C3 with PMTs > 5 pe	1502242	90.9	476107	28.8	449456	98.7
23	TOF-Cherenkov Correlation	1423080	86.1	469724	28.4	449820	98.7
24	Total vs. Upper Deflection	1453386	88.0	461682	27.9	444194	99.9
25	Total vs. Lower Deflection	1419237	85.9	451636	27.3	444513	99.8
26	Upper vs. Lower Deflection	1364114	82.6	449295	27.2	446175	99.5
27	Deflection Sign Check	1599794	96.8	444204	26.9	448926	98.9
28	C2 vs. C3 correlation	1645534	99.6	443836	26.9	444204	99.9

Selection criteria for defining energy bins are discussed in Section 3.7

The only cut not discussed elsewhere (cut 1) is the telemetry checksum cut, to ensure the quality of the data for individual events in the data files. Generally, flight data for IMAX was divided into files covering approximately half–hour to one hour intervals during the flight, and most of these files were "cleaned" of events with poor telemetry. However, given limited disk space and large data files, some cleaned files were lost or corrupted, and the corresponding original raw files were used instead. Of the 1652075 events which yielded fitted tracks (IFAIL=0), only 52 events had bad checksums, as shown in Table 3.3.

With 28 selection criteria beyond the IFAIL=0 cut, the software set 28 flags per event in order to determine which selection criteria a given event may have passed, and in order to be accepted in the final data set, an event had to pass all selection criteria. The "Flagged" columns of Table 3.3 list the total number of fitted track events (IFAIL=0) which passed the individual cuts. The flagged percentage is calculated relative to the total number of fitted track events. Thus, for example, of the 1652075 fitted track events, 1427094 events had tracks passing through the C2 active area defined in Chapter 2. The events passing this cut represented 86.4% of the fitted track events. As shown in Table 3.3, the deepest cuts were two of the Z=1 charge cuts, although these cuts tended to include Z=2 events which may have been otherwise valid events for the ^{3}He and ^{4}He analysis.

However, these selection criteria do not exist by themselves, and the software could also maintain running counts of events passing selection criteria, in the order in which they were applied. These numbers are given in the "Running" columns of Table 3.3. Thus, for example, of the 876317 events which passed the IFAIL=0 cut, the telemetry checksum (cut 1), and the tracking quality cuts (cuts 2 through 8), 812373 events also passed through the C2 active areas. This number represents 49.2% of the fitted track events. The advantage of this approach is that it demonstrates how the successive application of selection criteria whittle down the original 1652075 fitted track events to 443836 events, or 26.9% of the original. See Figure 3.12. It is interesting to note, from Table 3.3, that the tracking quality cuts and the C2

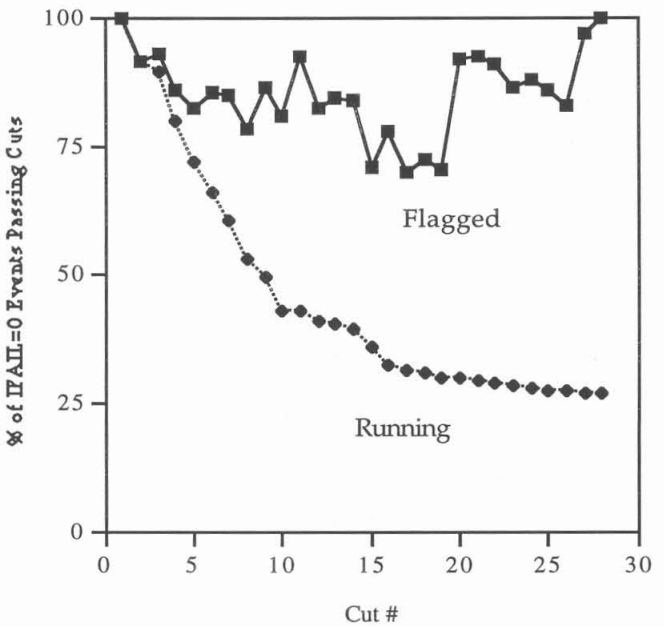

Figure 3.12: Effect of selection criteria, shown as percentage of fitted–track (IFAIL=0) events passing cuts vs. cut #. (See Table 3.3.) The passing percentage is shown for individual cuts ("Flagged") as well as a running percentage.

and C3 active area cuts, taken alone, are sufficient to define a counter geometry which passes well within the S1 active area (see cut 11). A caveat to this approach is that one should not assume that the earlier cuts are necessarily "stronger" than later cuts — the earlier cuts simply have far more "bad" events available to be eliminated.

Finally, it may be assumed that, with the elimination of any single selection criterion, events passing the remaining selection criteria will still yield a largely clean set of events. This idea can be illustrated by considering the four Z=1 selection criteria — any three scintillators should be sufficient to select Z=1 events, with concurrent application of the three selection criteria also acting as correlation cuts between them. Thus, we may define a "relative selection percentage" for the fourth Z=1 charge cut as the fraction of events passing the first three charge cuts which also pass the fourth.

Similarly, we may define the relative selection percentages for any of the cuts in Table 3.3 as the fraction of events passing all other cuts which also pass the given cut. For example, 443836 events pass all of the selection criteria, while 447955 events pass all of the cuts if the Bottom TOF Active Area cut (#14) is neglected. Thus, the relative selection percentage for cut 14 is 99.1%.

The intrinsic efficiency of a detector is the ratio of the number of particles detected to the number of particles which impinge upon the detector active area. Similarly, one may define an intrinsic efficiency for a selection criterion as the ratio of the number of events which meet the criterion to the number of events presented to the cut. Thus, the relative selection percentage discussed above may also be called the relative selection efficiency.

However, because the set of preselected events defined by all other selection criteria may not represent all events presented to the given selection criterion, the resulting relative selection efficiency will not necessarily be identical to the absolute intrinsic efficiency. For example, particles passing through the instrument during deadtime (see Section 4.2.2) will not be detected in IMAX data at all, and such particles will contribute to correlations in efficiency. As will be noted in Section 4.2.3, given relative efficiencies of two detectors or selection criteria,

it is still necessary to know beforehand the absolute efficiency of one detector in order to determine the absolute efficiency of the other. Section 4.2.3 will cover relative and absolute efficiencies in more detail.

The scintillators represent counters for which the absolute intrinsic efficiency can be estimated extremely well. The general rule of thumb for plastic scintillators is that they yield one photon per 100 eV of ionization energy loss in the plastic (Montanet et al. 1994; Yuan and Wu (eds.) 1961). For the IMAX plastic scintillators, the mean energy loss is on the order of 2–20 MeV per g/cm^2 of scintillator thickness, and with scintillators on the order of 1–2 g/cm^2 thick, enough scintillation photons (~10^4–10^5) will be produced per charged particle to result in an absolute intrinsic efficiency approaching 100%, which matches the calculated relative selection efficiencies given in Table 3.3 for the scintillators to within a few percent. Deviations from 100% represent inefficiency primarily in the selection criteria (see Figure 3.6), rather than in the detector itself.

Given that preselected events counted in Table 3.3 are, in effect, preselected by at least two scintillators with near 100% efficiency, the relative selection efficiencies may be assumed to be fair approximations of the intrinsic selection efficiencies of the cuts, to within a few percent. Taking the product of the efficiencies in Table 3.3, we find a total intrinsic efficiency for the selection criteria of ~58.8%±9.5%. The uncertainty is calculated from an average estimated uncertainty of 3% for each relative selection efficiency. Note that this efficiency does not include the livetime fraction of ~74% and telemetry efficiency of ~92.8% (see Section 4.2).

Note, however, that the relative selection efficiency of the IFAIL=0 cut has been left out of this calculation, implying that the 58.8% total intrinsic efficiency is an upper limit. The IFAIL=0 efficiency is a measure of the ability of the HYBMOM software (Section 3.1) and the tracking system (Section 2.2) to meet the minimum conditions to return a fitted track. In principle, we would calculate the relative selection efficiency of this cut with events preselected by the cuts listed in Table 3.3, but as has been noted previously, many of these cuts

cannot be defined for events which do not already pass IFAIL=0. Therefore, a modified approach, plus a more detailed discussion of efficiencies (including energy dependence), will be given in Section 4.2.3. The method described in Section 4.2.3 implicitly includes the IFAIL=0 efficiency, and the resulting efficiency of ~51-52% is consistent with the selection efficiency analysis obtained in this Section.

3.6.1 Background Estimates

The selection criteria described in this Chapter are the final criteria used to select events for further analysis in Chapters 4 and 5. During the development of the selection criteria, the individual criteria were varied, with the effects examined relative to the distributions of the quantities being cut. The general criterion for selecting cuts was to allow as many events as possible while attempting to eliminate as many background events as possible. As can be seen in the relative selection efficiencies in Table 3.3 (Preselected column), no selection criterion eliminated more than ~8% of the events which passed all other selection criteria.

The most likely behavior of the selection criteria is that, given a mostly clean data set preselected by all but one selection criterion, the remaining selection criterion eliminates most but not all of the background while simultaneously eliminating some small fraction of the clean events. There is no good method of absolutely determining eliminated background vs. eliminated signal without some prior knowledge of background, but estimates of background can be obtained via Monte Carlo simulation and by examining selection criteria and varying them.

This subsection summarizes estimates of possible background events which pass the selection criteria. With 28 selection criteria discussed earlier in this Chapter, plus energy bin selection described in Section 3.7, it is impractical to describe the effects of varying all of the cuts in detail. Systematics for the highest and lowest energy bin edges — those energy bin edges most susceptible to background contamination — are discussed in Sections 3.7.1 and 3.7.2.

Variations in some selection criteria may be discussed briefly: The counter active area cuts (cuts 9–14) define the instrument geometry factor (Section 4.2.1) and were not explicitly chosen to eliminate background events. That is, while these cuts ensure that single trajectories pass through all counters, they were not chosen explicitly to distinguish, say, antiproton events from hard scatter events. Any modification to the active area cuts will simply redefine the rigidity–dependent geometry factor.

The charge selection criteria (cuts 16–19; Section 3.2) have individual relative selection percentages around ~98–99%. As is noted in Sections 2.4 and 4.2.3, the scintillator counters have an absolute detection efficiency approaching 100%. With the four charge selection criteria applied simultaneously in four–fold coincidence, background contamination in the charge selection data (mostly multiple particles passing through one or more detector) should be eliminated by these cuts with near 100% efficiency. The result is that the four charge selection criteria select single Z=1 particles with ~94% efficiency, and the ~6% overall inefficiency comes mainly from eliminating 1-2% of events from the upper regions of the scintillator Landau distributions for one or more detectors.

Because particle identification proceeds from mass, charge, and charge sign, it should be apparent from the discussion of mass resolution in Section 2.7 that background contamination is strongly dominated by Cherenkov light yield in the Cherenkov–Rigidity range. Because this background strongly affects the choice of energy bins, it is discussed quantitatively and in detail in Section 3.7.1. That result, from IMAX Monte Carlo simulations, is that light particle Cherenkov fluctuation accounts for ~0.5 false antiprotons and very roughly (i.e. to within an order of magnitude) the same number of false protons in the Cherenkov energy range chosen for the antiproton analysis. For the antiproton/proton ratio, the false proton background is negligible.

Background in the TOF–Rigidity range is dominated by the TOF resolution (see Figure 2.25) above 1 GeV, but background in this energy range is also reduced by Cherenkov selection criteria. The primary source of such background is expected to be light particles (see Figures 3.13, 3.14, and 3.15), with both the Cherenkov light yield fluctuating below threshold and the

β_{TOF} measurement fluctuating downward. The IMAX Monte Carlo simulation shows that light particle Cherenkov and TOF fluctuations account for a background of ≤0.008 false antiprotons and approximately the same number of false protons in this energy range. This contribution to background is negligible. Below 1 GeV, the background due to Cherenkov and TOF fluctuation is similarly negligible.

3.6.2 Background from Deflection Spillover

The remaining selection criteria most susceptible to background effects are those associated with the tracking system (described in detail in Section 3.1.1). The primary source of background contamination is expected to be scattering in the tracking system, resulting in spillover in magnetic deflection distributions and misidentification of a particle as an antiproton. Figure 3.15, discussed in detail in Section 3.7, shows Cherenkov light yield vs. magnetic deflection for all flight events passing all cuts described previously in this Chapter. It is apparent from the Figure that, at high velocities (high Cherenkov light yield) and near zero deflection (high magnetic rigidity), events from the positive charge side can spill over into the negative charge side. At lower velocities, only one event (at deflection = ~-0.05 GV^{-1}) appears to be a spillover event, with its apparent mass at >3 amu. This event is attributed to deflection spillover.

The $\sigma_{deflection}$ cut, in the presence of all other selection criteria, has the effect of reducing contamination due to deflection spillover. One may examine the deflection and associated $\sigma_{deflection}$ distributions (see Figure 3.4) to estimate the probability that a particle at one measured deflection may have an actual deflection offset from the measured deflection by $\sigma_{deflection}$. In the absence of a $\sigma_{deflection}$ cut, an estimated upper limit of ~1 in 10^4 protons in the Cherenkov–Rigidity range has sufficiently large $\sigma_{deflection}$ to be misidentified as an antiproton, and examination of the data implies that the actual number is much smaller (see below). With the $\sigma_{deflection}$ cut imposed, such background is negligible at all energy ranges chosen for this analysis.

Menn (1994) has carried out the definitive exploration of variations on the NGx, NGy, χ^2 (x and y), and $\sigma_{deflection}$ selection criteria for IMAX, by examining events individually to determine whether new events passed by loosening cuts may be actual antiprotons or attributed to deflection spillover. Menn (1994) found that the NGx and NGy cuts could be moderately loosened (e.g. to 8 and 6 lower limits, respectively) with the addition of perhaps one antiproton candidate but approximately quadrupling of spillover. However, this spillover results in "high mass" background which does not apparently contaminate the antiproton results. When the NGx and NGy cuts are loosened radically (e.g. to 4 and 3), one more antiproton candidate may be apparent, but at this level, deflection spillover begins to contaminate the antiproton results, primarily at high velocities.

Menn's examination of the χ^2 cut shows similar contamination from spillover. By loosening the χ^2 upper limits to $\chi^2<6$ (and keeping the original NGx and NGy cuts), one more antiproton candidate may be accepted, with no serious increase in spillover background. When the limit is set at $\chi^2<10$, the number of antiproton candidates increases strongly (from 16 at $\chi^2<4$ to ≥ 23 at $\chi^2<10$), but the spillover seriously contaminates the antiproton results.

Menn's conclusion was that spillover contamination is negligible with the current tracking quality selection criteria. Were such spillover to exist, it would likely show up as high mass events. The selection criteria could be varied slightly (e.g. ±1 in NGx and NGy) with only a few percent change in proton fluxes. Thus, the current tracking quality selection criteria are probably conservative — with possibly reduced detection efficiency for real antiproton and proton events but very strong rejection of background.

3.7 The Antiproton Candidate Events

The selection criteria described in the preceding sections were designed to extract clean, Z=1 data with good mass resolution from the raw flight data. Of the 3.19×10^6 events in the IMAX data from float altitude, 1652075 yielded fitted tracks (IFAIL=0) through the spectrometer, and of these, 449345 events passed all of the selection criteria.

With this data set, particle identification via the TOF–Rigidity and Cherenkov–Rigidity methods may be employed. Figure 3.13 shows a plot of β_{TOF} vs. magnetic rigidity, as measured by the hybrid tracking system, for the resulting Z=1 data set. Positive charges are on the right side of the plot, and negative charges are on the left. The presence of particles at $\beta>1$ indicates the loss of TOF resolution at high velocities, not the presence of faster–than–light particles. Protons, deuterium, and tritium (resulting from atmospheric production) are clearly visible on the right side of the plot. Along the top are electrons, muons, and pions — which travel at much higher velocities than protons at the same rigidities — as well as those heavier particles at the high velocities for which the TOF resolution is reduced. Antiproton candidate events are marked as bold, filled circles on the left of the plot, including some which exist in the region of poor TOF resolution.

These higher energy antiproton candidates may be extracted from the background with the application of a cut to the aerogel Cherenkov data. If one sets an effective threshold light yield for the combined (C2+C3) aerogel Cherenkov, map–normalized signal ($\overline{f_{2+3}}$ from Section 3.3) at 0.36 (corresponding to an energy of ~3.1 GeV for n=1.043; see Section 2.1.2), one can eliminate from the data set nucleonic particles which travel at energies above ~3.1 GeV (or velocities above β~0.97) as well as mesons and electrons. The selection of this Cherenkov limit will be discussed in detail in Section 3.7.1, but in summary, the 0.36 upper limit was chosen by examining the region where antiprotons are not expected to have a nonzero Cherenkov signal and by setting the limit to exclude all electrons and light mesons which would have Cherenkov signal near saturation. The effect of this cut is shown in Figure 3.14, which shows the same β_{TOF} vs. rigidity data, with the aerogel Cherenkov threshold limit imposed. Most of the highest velocity particles have been removed, and the high energy antiproton candidate events are revealed.

Figure 3.15 shows the "Bowen plot" for the Z=1 data — the signed square root of C2+C3 Map–normalized data vs. hybrid deflection. This method of plotting Cherenkov—Rigidity data was recommended by T. Bowen of the University of Arizona. It has the advantage of

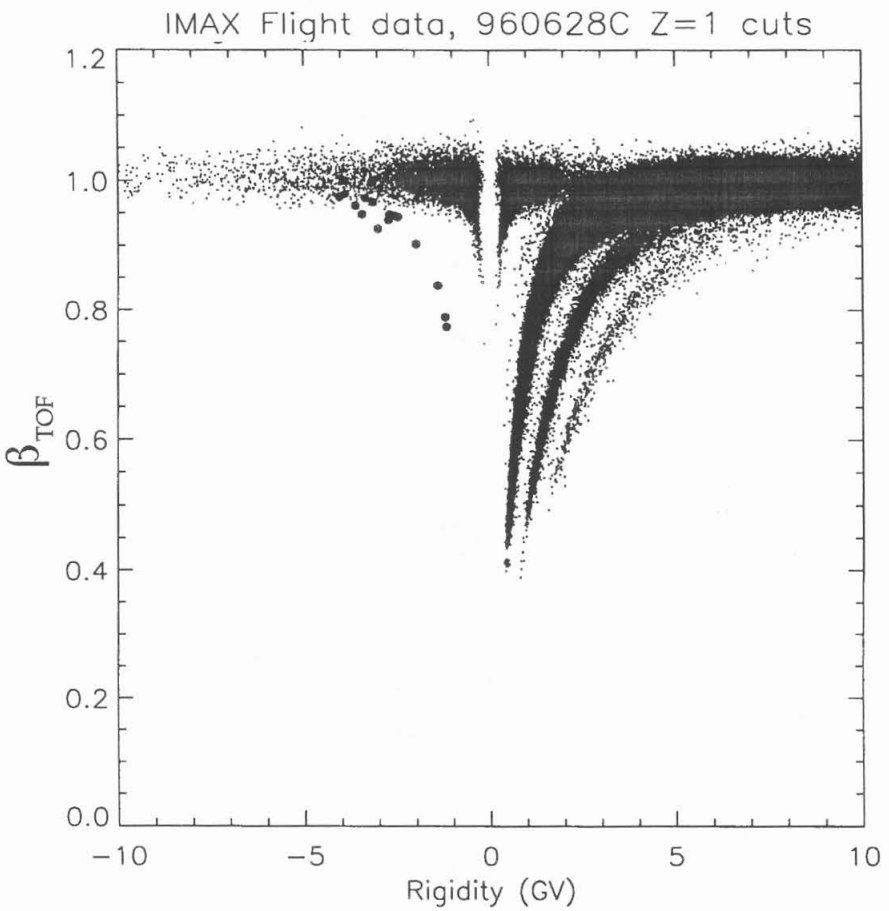

Figure 3.13: β_{TOF} vs. magnetic rigidity for all flight data events passing all of the cuts described in this Chapter, except those cuts used to define energy bins.

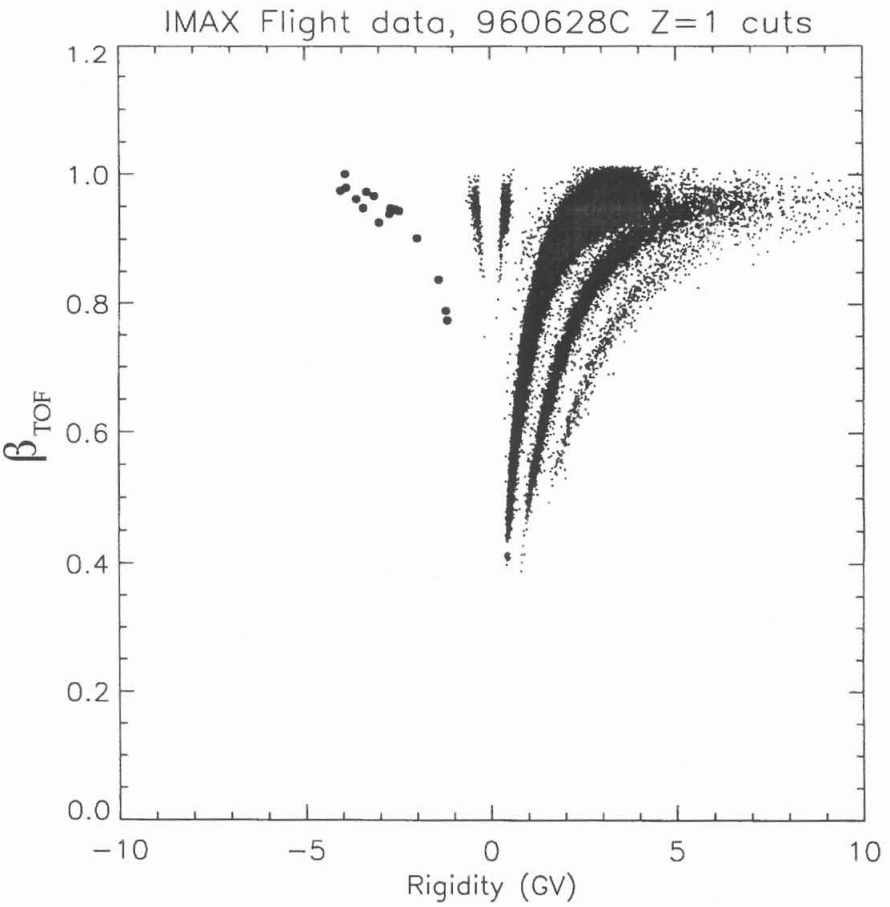

Figure 3.14: β_{TOF} vs. magnetic rigidity for all flight data events passing all of the cuts employed in Figure 3.13, with an additional Cherenkov limit of C2+C3 Map–Normalized < 0.36 imposed on the data.

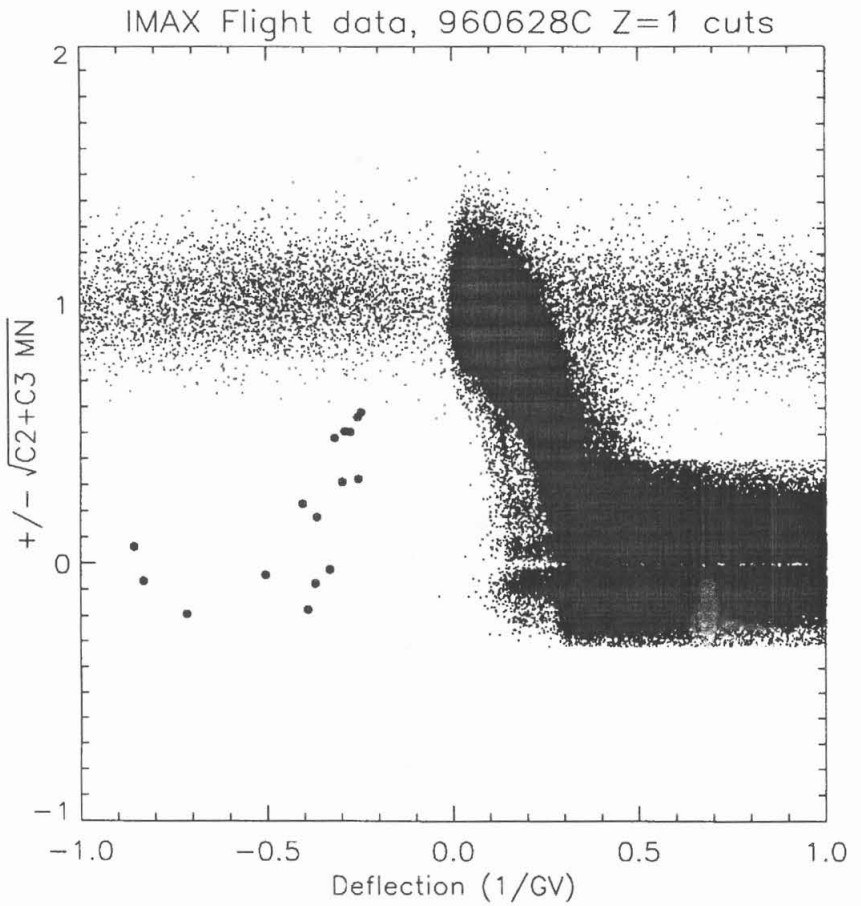

Figure 3.15: Signed square root of C2+C3 Map–normalized data vs. hybrid deflection ("Bowen plot") for all flight data events passing all of the cuts described in this Chapter, except those cuts used to define energy bins.

showing high–rigidity, high–energy data toward the center of the plot, with uncertainties in each axis remaining constant, to lowest order. Particles (mostly protons) with velocities below $\beta \sim 1/n$ ($n \sim 1.043$, see Section 2.1.4) are shown in the band at $\sqrt{\overline{f_{2+3}}} \approx 0.0$ on the right side of the plot. Upon close inspection, the below–threshold protons appear as two strong bands of particles in the Figure. The two bands of below–threshold protons correspond to a light yield of 0 pe, split and "evacuated" from the $\sqrt{\overline{f_{2+3}}} \approx 0.0$ region by the square root operation. A 1 pe band of protons may also be seen in the Figure. Particles (electrons, light mesons) at saturation ($\beta \sim 1$) appear as the light band of points at the top of the plot. Protons are clearly indicated as the dark band and curve, and deuterons are in evidence to the left of the proton curve above threshold. Below–threshold antiprotons from Figure 3.14 are shown, as are above–threshold antiprotons. The straight edges in the proton bands are a result of the TOF–Cherenkov correlation cut described in Section 3.5.

3.7.1 Cherenkov–Rigidity Antiprotons

Selection of energy ranges may proceed from these plots, with the Cherenkov–Rigidity energy range being defined by Figure 3.15. The highest energy range for antiproton measurement can be obtained by setting an upper limit of $\overline{f_{2+3}}$=0.36, which corresponds to an upper limit of 0.6 on the Figure. This upper limit was chosen to eliminate electrons and light mesons at saturation in the deflection range (< -0.5 GV^{-1}) within which antiprotons do not travel cannot produce Cherenkov light, and we expect this limit to eliminate electrons and light mesons at deflections above -0.5 GV^{-1}. The effect of changing this upper limit will be discussed at the end of this subsection.

Setting a lower Cherenkov limit takes into consideration the converse situation — to eliminate from consideration those particles which travel below threshold velocity, e.g. protons (and deuterons) at deflections above 0.5 GV^{-1}. Figure 3.15 employs the TOF–Cherenkov correlation cut (Section 3.5), which implicitly includes the lower Cherenkov limit. Instead, we may examine the photoelectron (pe) histogram in Figure 2.10. As was noted in Section 2.1.1,

electronic noise (from random trigger runs) was less than 1 pe. We may set this noise level conservatively at 1 pe. Knock–on electrons (Section 2.5) produced by below–threshold protons may contribute another 1–2 pes (Figure 2.16). Therefore, a conservative threshold would be set between 3 and 4 pes, and assuming 24 pes at saturation, we round the threshold to $\sqrt{\overline{f_{2+3}}} \approx 0.4$ on Figure 3.15. (This threshold corresponds to ~3.84 pes.) Based on pe histograms of below threshold rigidity protons, this threshold setting eliminates >99.5% of below–threshold particles.

Between these two limits, the IMAX flight data yield 5 candidate antiproton events.

The upper Cherenkov limit is strongly susceptible to background – in this case, background arising from Cherenkov signal fluctuation for light particles. As can be seen in Figure 3.15, electrons and light mesons yield a band of Cherenkov signals near saturation over a wide range of magnetic deflections. As was discussed above, the Cherenkov signal upper limit of $\overline{f_{2+3}}$=0.36 was selected to eliminate signals from electrons and light mesons, but the light particle signal fluctuations are large enough that some background contamination must be accounted for. With a Cherenkov signal range of $\overline{f_{2+3}}$=0.16–0.36, the IMAX Monte Carlo simulation and the flight data imply that ~0.5 antiproton candidates in this range may actually be a result of Cherenkov fluctuation downward from saturation. (See Sections 2.8 and 4.3.)

Figure 3.16 shows the estimated number of background events obtained by raising or lowering the Cherenkov upper limit. Lowering the upper limit to 0.30 (for a range of $\overline{f_{2+3}}$=0.16–0.30) reduces the background to ~0.1 false antiprotons, while subsequently reducing the number of candidate antiprotons to 3. Raising the upper limit to 0.40 raises the background significantly to ~2.6 false antiprotons, while increasing the number of candidate antiprotons to 7 — an increase which is offset by the expected increase in background. Thus, it is not possible to distinguish with certainty whether the two additional antiproton candidates (those two points nearest the 5 bold Cherenkov–Rigidity antiproton points on Figure 3.15) are actual antiprotons or are fluctuated light particles. The results of changing the Cherenkov signal

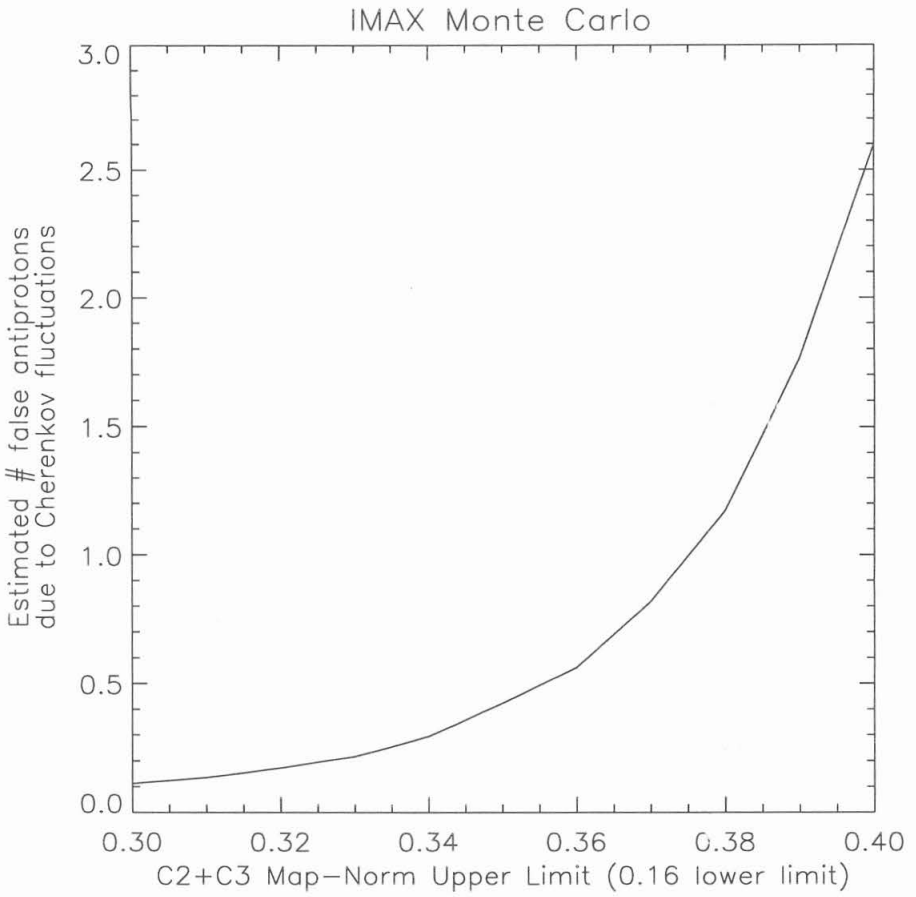

Figure 3.16: IMAX Monte Carlo simulation results showing the estimated number of false antiprotons due to Cherenkov signal fluctuations of light particles down into the Cherenkov signal range with a lower limit of $\overline{f_{2+3}}$=0.16 and an upper limit given by the x–axis of the plot. The false antiproton background increases strongly as the upper limit is increased above 0.36.

upper limit are summarized in Table 3.4 for antiproton candidates, expected background events, and protons.

Table 3.4: Effect of Changing the $\overline{f_{2+3}}$ Upper Limit

$\overline{f_{2+3}}$ upper limit	# Antiproton Candidates	Expected Background Events	# Protons	Antiproton/proton ratio (detected at Instrument)
0.30	3	0.1	15528	$1.87(+1.89,-1.07)\times10^{-4}$
0.36	5	0.5	22524	$2.00(+1.51,-0.97)\times10^{-4}$
0.40	7	2.6	27199	$1.62(+1.39,-0.95)\times10^{-4}$

Note that the antiproton/proton ratios in Table 3.4 are the ratios of events detected by the instrument and are not corrected for background or losses in the instrument or atmosphere other than the Cherenkov fluctuation discussed here. The increase in background of 2.1 false antiprotons (corresponding to shifting the $\overline{f_{2+3}}$ upper limit from 0.36 to 0.40) is greater than the corresponding increase of 2 antiproton candidates, but the difference is attributed to low counting statistics. The choices shown in Table 3.4 all result in consistent antiproton/proton ratios that differ by much less than their associated statistical uncertainties. Thus, our results are not sensitive to variations in this cut, and an upper limit of 0.36 yields adequate signal with significantly less noise than a higher limit.

Furthermore, Figure 3.17 shows the mass histograms (rather, mass times charge) for the Cherenkov–Rigidity data, for the varying upper Cherenkov limits. While upper limits of $\overline{f_{2+3}}$ at 0.30 and 0.36 yield acceptably clean mass histograms — with the 3 and 5 (respectively) antiproton candidates well–resolved from all other events — raising the upper limit to $\overline{f_{2+3}}$=0.40 clearly increases the background. In addition to the two additional antiproton candidates accepted by the new upper limit, there are additional events at mass ~0.5 amu and ~2.7 amu. From the IMAX Monte Carlo, the "heavier" event can be interpreted as a fluctuated

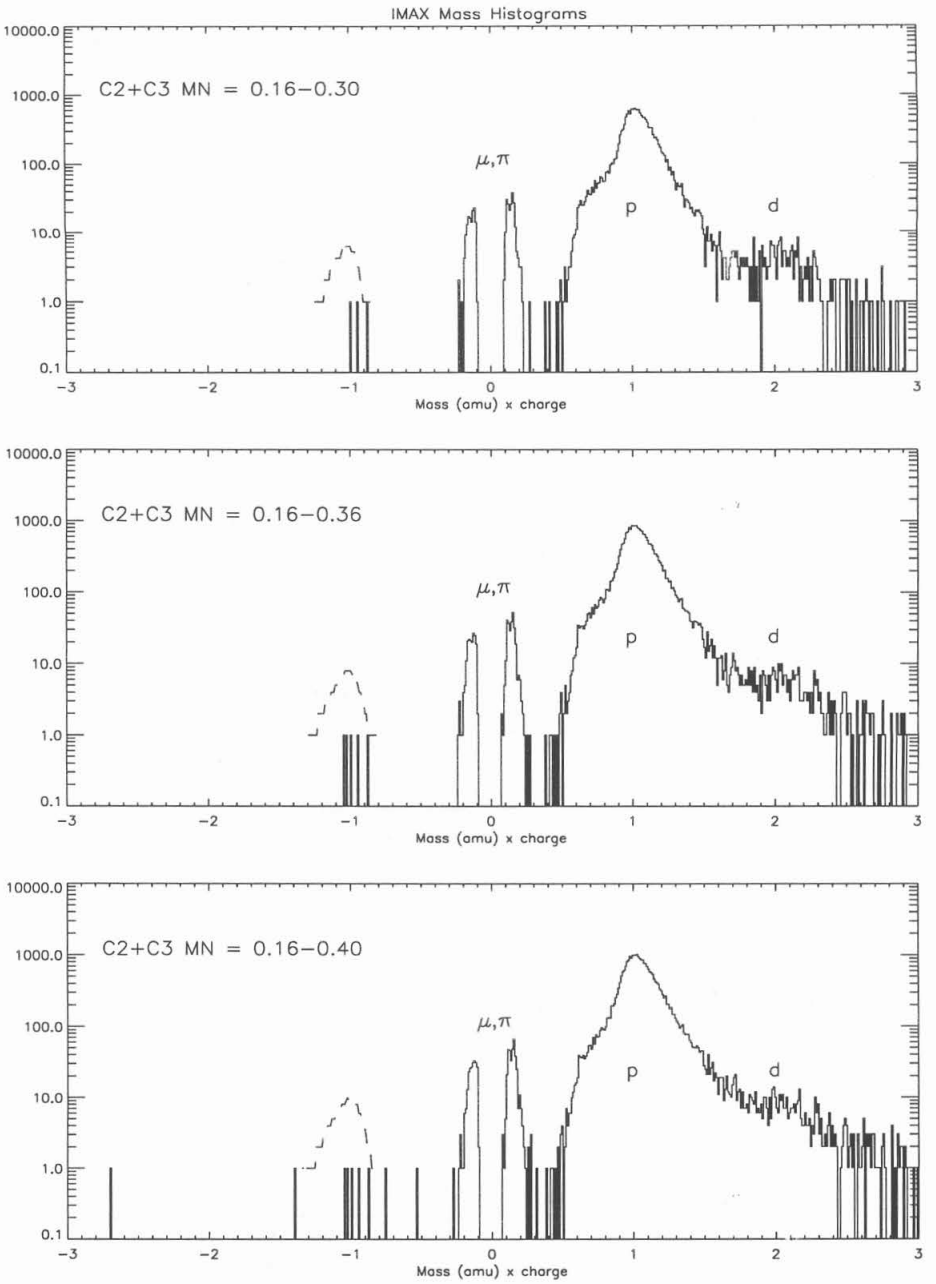

Figure 3.17: IMAX Cherenkov–Rigidity mass histograms obtained by varying the $\overline{f_{2+3}}$ upper limit. With looser limits (bottom) more background contaminates the mass histogram, and with tighter limits (top), more antiproton candidates are eliminated.

light particle, and the lighter event can be either a kaon or a lighter fluctuated meson or electron.

A note on kaons: The final mass histograms for the IMAX data are given in Figure 3.18. There is evidence for approximately 15 K^+ particles in the lowest energy range, but there is no strong evidence for K^- events in any of the energy ranges. Kaon production cross section measurements show that the K^+ production cross sections are larger than the K^- cross sections by at least an order of magnitude (e.g. Pantuev et al. 1995), which is consistent with no K^- in the IMAX mass histograms.

Thus, the Cherenkov signal range is selected as $\overline{f_{2+3}}$=0.16–0.36, and the resulting Cherenkov—Rigidity energy range is then defined as ~2.58–3.08 GeV at the instrument (or 2.61–3.11 GeV at the top of the atmosphere), after corrections for knock–on electron contributions. (See Equation 2.1.9 and Section 2.1.5.)

Finally, Figure 3.15 (the "Bowen plot") gives a visible measure of the effect of deflection spillover, discussed in Section 3.6.2. Near Cherenkov saturation (C2+C3 MN = 1) and near zero deflection, there is some apparent spillover of protons (and other positively charged particles) toward the negative deflection side, but such spillover extends to only ~-0.05 GV^{-1}. There is no evidence in the Figure of deflection spillover reaching the high energy antiproton range (e.g. to deflections around -0.3 GV^{-1}).

3.7.2 TOF–Rigidity Antiprotons

From Figure 3.14, a lower energy range may be similarly defined for the TOF–Rigidity range. The lowest energy limit must take into account energy losses in the instrument and atmosphere. (See Appendix B.) A particular worry is that an antiproton which slows and stops in the material just below the bottom TOF may annihilate and send secondary, annihilation products upward into the IMAX detectors, contaminating what might be an otherwise–clean antiproton measurement (Section 4.3). Almost all protons or antiprotons with 220 MeV at the top of the atmosphere will penetrate through the atmosphere and the bottom

of the IMAX detector stack and gondola; at energies below 220 MeV, the instrument stops increasing numbers of particles, raising the probability of backscatter contamination. By setting a lower limit of 250 MeV at the top of the atmosphere (corresponding to ~188 MeV or β~0.55 at the spectrometer), we accept for analysis only those protons and antiprotons which pass entirely through the bottom of the IMAX gondola.

Finally, a middle energy limit is set arbitrarily at 1.00 GeV (at the top of the atmosphere), in order to divide the TOF–Rigidity range and obtain some energy–dependence information. The upper limit of this energy range is defined by the 2.61 GeV (top of the atmosphere) Cherenkov lower limit described in Section 3.7.2. The IMAX Monte Carlo simulation shows that light particle Cherenkov and TOF fluctuation accounts for a background of $\leq$0.008 false antiprotons and approximately the same number of false protons in this energy range. Below 1 GeV, the background due to Cherenkov and TOF fluctuation is negligible.

The final energy ranges at the top of the atmosphere are 0.25–1.00 GeV, 1.00–2.61 GeV, and 2.61–3.11 GeV.

3.7.3 IMAX Mass Histogram

Figure 3.18 shows mass histograms (rather, mass times charge) calculated from the Z=1 data set with the three selected energy ranges. There are clearly 3, 8, and 5 antiproton candidates in the 0.25–1.0 GeV, 1.0–2.61 GeV, and 2.61–3.11 GeV energy ranges. Proton counts are obtained by dividing the three major energy ranges into energy bins of roughly 0.1 GeV in width. Mass averages and uncertainties (widths, calculated as standard deviations) are calculated for the separate mass histograms from these sub–bins, and protons were summed from all events within $\pm 3\sigma$ of the centroid and then summed for all of the sub–bins within the major energy bins. The mass resolutions are calculated as standard deviations and not as Gaussian distribution widths, and they vary from ~0.06 amu at the lowest energies to ~0.14 at Cherenkov energies. As shown in Figure 3.18, the antiproton candidates all lie within $\pm 3\sigma$ of the centroid defined by a mirror image of the proton peak onto the negative rigidity side of the plot. (All

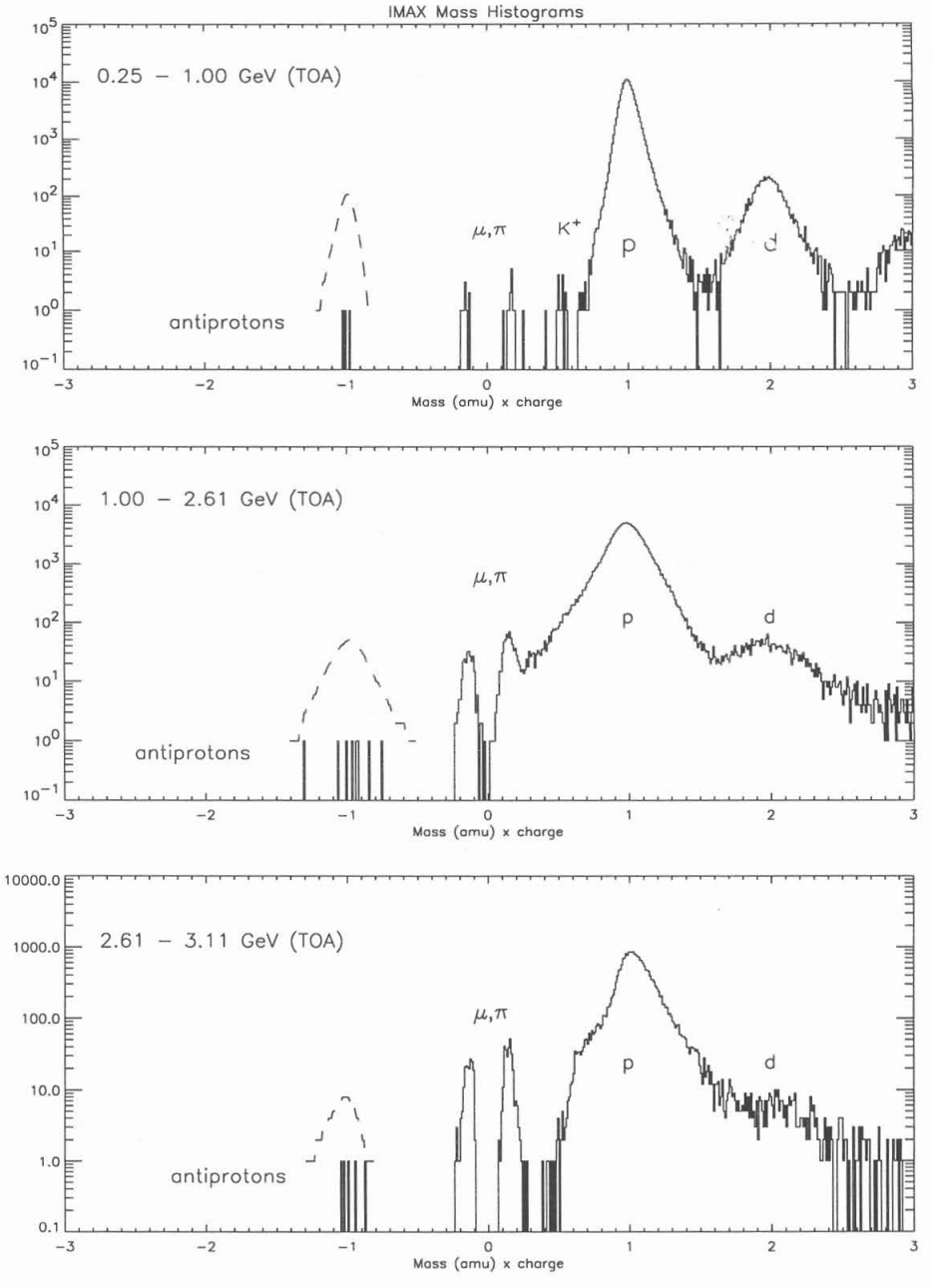

Figure 3.18: IMAX mass histograms, binned by mass (amu) x charge (Z). Proton and deuterium peaks are marked, as are the antiproton candidate events. The dashed lines show where the mirror–image proton peaks would be located.

but one lie within ±2σ of the centroid, and that one outlier is at ~2.1σ.) The strong clustering of antiproton events near 1 amu in mass, and the separation of these clusters from the muon/pion peaks, is evidence that background contamination is negligible. (Background contamination would be expected to be broadly distributed.)

The raw results are shown in Table 3.4. Corrections for instrumental and atmospheric background and losses are described in Chapter 4. Detailed listings of antiproton data are given in Appendix C. Finally, the proton spectrum measured by IMAX (Figure 4.6) is consistent to within ~20% of the results of previous proton spectrum measurements (e.g. Figure 1.3) at the energies discussed in this analysis.

Table 3.4:

Summary of Raw IMAX Antiproton and Proton Data,

Prior to Corrections for Instrumental and Atmospheric Background

Energy at Spectrometer (GeV)	Energy at Top of Atmosphere	# Antiprotons	# Protons
0.188 – 0.967	0.25 – 1.00	3	124405
0.967 – 2.58	1.00 –2.61	8	140617
2.58 – 3.08	2.61 – 3.11	5	22524

3.7.4 Summary of Background Estimates

The total intrinsic detection efficiency for selection criteria described earlier in this Chapter is estimated at 58.8±9.5% (Section 3.6), not including IFAIL=0 selection, livetime, or telemetry efficiency. The actual detection efficiency for particles is expected to be slightly lower, once the IFAIL=0 selection efficiency is included (e.g. total efficiency of 51–52%; Section 4.6.2).

The two most likely sources of false antiproton background are expected to be particle misidentification as antiprotons due to fluctuations in velocity measurement and in deflection measurements. The IMAX Monte Carlo simulation (Section 2.8) shows that the expected background due to velocity fluctuations will be ~0.5 antiprotons in the Cherenkov–Rigidity range, with negligible background in the TOF–Rigidity range (Sections 3.6 and 3.7). Background due to deflection spillover (e.g. from multiple scattering or hard scattering) has been shown to be small with detailed examination of the current selection criteria and in the energy ranges selected for this analysis (e.g. Figure 3.15; Section 3.6.2; Menn 1994).

The final IMAX mass histograms (Figure 3.18) give further evidence that background contamination in the antiproton measurement is small. The IMAX mass histograms show tight clustering of the antiproton events around 1 amu mass, whereas significant background contamination of the antiproton events should be accompanied by background at measured masses other than near 1 amu. For example, background due to velocity errors would result in a broad spectrum of masses of negatively charged particles. Such background is evident in the sample mass histogram in Figure 3.17, in which the Cherenkov signal upper limit is significantly increased, but it is not evident in Figure 3.18, which contains the data selected by the final selection criteria. Further, background due to deflection spillover would be most prevalent at large masses, and any contamination of the antiproton results would have to result from larger spillover than is allowed by the current selection criteria.

Background from instrumental and atmospheric production of secondary protons and antiprotons will be discussed in detail in Chapter 4. However, instrumental production of secondary protons and antiprotons typically results in multiple particle production (e.g. proton–antiproton pairs), and with net forward momentum required for such production, such multiple particles will be detected and rejected by the instrument and selection criteria. Thus, background from instrumental production can be neglected.

4. Results at the Top of the Atmosphere

The raw measurements of proton and antiproton counts presented at the end of Chapter 3 are not directly comparable to measurements presented by other experiments, nor are they comparable to calculations for cosmic ray intensities in the interstellar medium or at the top of the atmosphere (at 1 AU from the sun). The raw results must be corrected for instrumental efficiencies and instrumental and atmospheric background in order to arrive at ratios and spectra at the top of the atmosphere (TOA) , and the corrected results must also be understood in relation to the solar cycle (Chapter 5).

4.1 Geomagnetic Cutoff

Particles with very low magnetic rigidity cannot cross geomagnetic field lines. The result is that, at low latitudes, particles must have very high magnetic rigidity to reach the top of the atmosphere, while at the highest latitudes, where the geomagnetic field lines are open to interplanetary space, only the lowest rigidity particles (e.g. those with rigidities below a few tenths of a GV) fail to reach the top of the atmosphere.

IMAX was launched from Lynn Lake, Manitoba, Canada, (~56°N Latitude) and it flew almost due west to land near Peace River, Alberta. From tables by Shea and Smart (1983), the vertical cutoff rigidity is between 0.3 and 0.4 GV at Lynn Lake, and it rises to approximately 0.6 GV near Peace River. Since these cutoff rigidities correspond to energies below 176 MeV/nuc at the top of the atmosphere (and much lower for most of the flight), geomagnetic cutoff effects can be neglected in this analysis.

4.2 Efficiencies

The selection criteria discussed in Chapter 3 eliminate broad classes of events: multiple particle events (which our analysis is incapable of analyzing as separate particles), false trigger events, events with large electronic or statistical fluctuations in detector signals, and events which may have included significant particle interactions within the instrument

(e.g. scatters, spallation, annihilations, etc.). While the selection criteria were chosen to provide clean data sets of real, single particle events for analysis of proton and antiproton data, a side effect of these cuts may be to eliminate from consideration single or multiple particle events which might otherwise contribute to particle fluxes of interest. For example, a single proton may pass through the payload and produce good signals in all of the detector systems and yet not trigger enough DC or MWPC planes to provide a fitted track. (See Section 3.1.) Alternatively, a single particle may experience a fluctuation in the aerogel Cherenkov light yield that, while reasonable, may place it beyond the acceptable limits for the TOF–Cherenkov correlation cut.

The following subsections and Section 4.3 describe the various detector efficiencies and correction factors needed to calculate antiproton/proton ratios and antiproton fluxes at the top of the atmosphere.

4.2.1 Geometry Factor

The geometry factor, or acceptance, is a measure of the solid angle and area through which an instrument detects particles. Detector active areas and the relative positions of the detectors contribute to the geometry factor. Also, the IMAX magnetic field bends particle trajectories more for low rigidities than for high rigidities, reducing the geometry factor at low rigidities.

Ideally, the geometry factor, $A\Omega$, is the integral of $dAd\Omega$ taken over the instrument active areas and detector solid angle. In practice, the IMAX geometry factor was calculated via Monte Carlo simulations at the University of Siegen (Menn 1995), taking into account the IMAX magnetic fields and the detector active areas used in the selection criteria. The following equations for the geometry factor were taken from fits to the simulation results:

$$\begin{aligned} A\Omega^{+} &= 142.43804 + 0.2196D - 1.08398D^{2} - 1.93706D^{3} + 0.28719D^{4} \\ A\Omega^{-} &= 142.79468 - 2.33186D + 0.98585D^{2} - 2.65302D^{3} + 0.36588D^{4} \end{aligned} \tag{4.2.1}$$

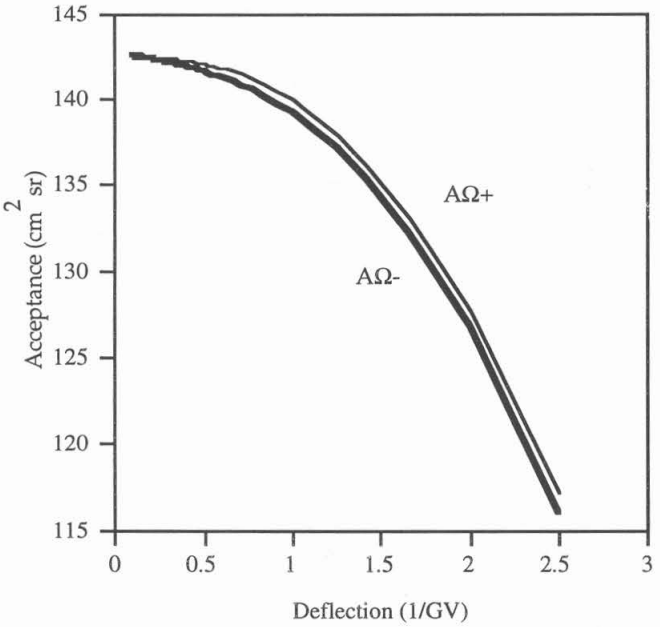

Figure 4.1: Geometry factor (acceptance, cm^2 sr) vs. deflection (GV^{-1}) as calculated via Monte Carlo simulation (Menn 1995). The negative charge form (AΩ-) is used in the antiproton analysis, and the positive charge form is used in the proton analysis (Figure 4.6).

where $A\Omega^+$ and $A\Omega^-$ are the fitted geometry factors, in cm^2 sr, from Monte Carlo simulations of positive and negative charged particles, and D is the deflection, in GV^{-1}. (See Figure 4.1.) The differences between the two fits averages less than 1 cm^2 sr at the deflections of interest, within statistical differences in the two simulations. The form for negative values is applied in the antiproton analysis, while the positive form was applied to protons.

4.2.2 Livetime

Any calculation of cosmic ray flux in an instrument must take into account the instrument dead time, or that fraction of exposure time during which the instrument is unable to register the passage of particles. For IMAX, the livetime fraction (or 1 – deadtime fraction) is calculated with the use of two on–board clocks. The free–running, or real, clock runs without interruption (until reset to zero), while the live clock runs freely until a system trigger indicates the passage of a particle. (See Section 2.6 for a description of trigger logic on IMAX.) At trigger, the live clock is stopped until all of the detector readings (ADCs, TDCs, etc.) have been completed for the event. The livetime fraction is the ratio of the live clock counts to the free–running clock counts.

An examination of the clock data shows a livetime fraction of ~74% for IMAX at float altitude. (See Figure 4.2.) This livetime remains fairly constant over float duration.

4.2.3 Instrumental Detection Efficiencies

Any single particle which passes through the payload geometry will contribute to the actual flux of that particle species through the payload, but it may not necessarily be detected by all of the detectors or pass all of the selection criteria. The absolute intrinsic detection efficiency of IMAX is defined here as the fraction of real particles passing completely through the payload which are detected and which pass all of the selection criteria.

A note on nomenclature: Some textbooks (e.g. Knoll 1989) define the absolute efficiency of a detector as the ratio of the number of pulses recorded by the detector to the number of

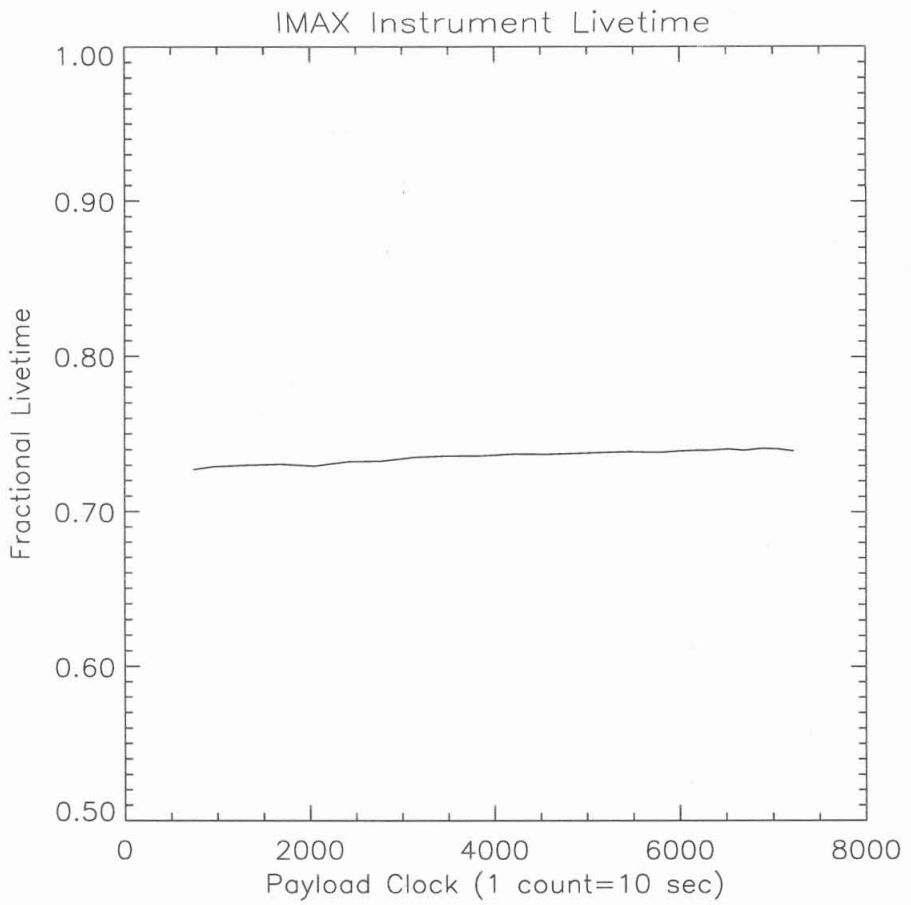

Figure 4.2: Fractional livetime vs. payload clock, taken over the duration at float altitude.

radiation quanta emitted by a source, and the intrinsic efficiency of a detector is defined as the ratio of the number of the number of pulses to the number of quanta incident on the detector. However, in order to simplify the discussion, this section will assume that all detection efficiencies are intrinsic. Relative efficiency for a detector is defined as the fraction of particles detected by the detector which are preselected by another detector, while absolute efficiency is defined with respect to all particles incident on the detector, not just those preselected by another detector.

In the absence of external particle detectors of known detection efficiency and short of a detailed Monte Carlo simulation — which, in practice, would exceed the complexity of the data analysis software itself — it is impossible to determine precisely the absolute detection efficiency of IMAX. Instead, one may calculate the relative detection efficiency of one detector system relative to particles preselected by another detector system within IMAX. The calculation of relative efficiencies of two detectors, A and B, may be described with reference to a matrix I whose elements I_{ab} are defined by the following Table:

Table 4.1: Generalized Detection Efficiency Matrix

	Not Detected by B	**Detected by B**
Not Detected by A	I_{00}=# particles not detected by either	I_{01}=# particles detected by B only
Detected by A	I_{10}=# particles detected by A only	I_{11}=# particles detected by A and B

In this formulation, let I be the total number of particles which pass through both A and B, such that

$$I = \sum_{a,b=0}^{1} I_{ab} \tag{4.2.2}$$

and the absolute efficiency, E_A, of detector A will be given by

$$E_A = \frac{1}{I}\sum_{b=0}^{1} I_{1b} = \frac{I_{10} + I_{11}}{I} \tag{4.2.3}$$

The efficiency of detector A relative to particles preselected by detector B will be given by

$$R_{A;B} = \frac{I_{11}}{I_{01} + I_{11}} \tag{4.2.4}$$

Similar expressions can be obtained for the absolute and relative detection efficiencies of detector B. A little algebra will show that

$$\frac{E_A}{E_B} = \frac{R_{A;B}}{R_{B;A}} \tag{4.2.5}$$

Equation 4.2.5 shows that the absolute efficiency of detector A can be known if the relative efficiencies are measured and if the absolute efficiency of some reference detector B is known. In the absence of an absolute efficiency for B, examination of Table 4.1 shows that $R_{A;B}$ is a good approximation of E_A if the detection of particles by A and B is not strongly correlated. Some correlation might exist if, for example, A and B were identical particle detectors or if A and B relied on the same detector physics and thus had similar energy–dependent efficiency. The difficulty lies in estimating I_{00}.

In the absence of calibration at an accelerator, IMAX detector efficiency has been analyzed with relative efficiency measurements, and some correlation necessarily arises because of the reliance on the system trigger (Section 2.6) to signal particle passage through the detector. Some particles may not be detected by the system trigger, which would yield an uncertainty in estimating I_{00}, but in practice, this particular inefficiency is assumed to be accounted for by the livetime (Section 4.2.2).

Hof et al. (1994) state that the detection efficiency for a single drift cell approaches 100%, but this efficiency is relative to trigger events and does not take into account the effects of the fitting algorithm. The definitive analysis for IMAX detection efficiency for protons was carried out at the University of Siegen, and all subsequent efficiency analyses were made relative to the Siegen analysis. The detection efficiency for the tracking software using drift chambers only was calculated with the following conditions: >8 good measurements (registered planes) in the x–axis, >5 good measurements in the y–axis, chi-square < 4 in the x– and y–axes, and less than 3 planes in the x– and y–axes (each) with positions greater than 4 cm off the fitted track (Menn 1994, 1995).

The reference ("B") detector was defined by events which trigger only the middle top and bottom TOF paddles and whose TDC signals place the events within the middle (x=10–40 cm) of the paddles (Menn 1994). The scintillator signals are also selected for Z=1 events via charge histograms, and as a check against out–of–geometry events (e.g. two particles separately triggering the TOF paddles), selection is made for 4 MWPC x–axis measurements within the x=10–40 cm range, and 2 MWPC y-axis measurements are made within the y=13–33 cm range. The MWPC x– and y–measurements are raw position measurements, not fitted track positions. For the TOF scintillators, the mean energy loss is on the order of 2–20 MeV per g/cm^2 of scintillator thickness. With scintillators ~1 g/cm^2 thick and one photon per 100 eV of ionization energy loss, enough scintillation photons (~10^4–10^5) will be produced per charged particle that the absolute efficiency of this reference system will approach 100% (E_B~1), and by extension, that the relative efficiency also approaches 1. Therefore, the efficiency of the drift chambers and fitting algorithm relative to events preselected by the reference system is assumed to be a good approximation of the absolute detection efficiency of the DCs plus fitting algorithm. From here, the detection efficiency of the entire IMAX system (all detectors, plus selection criteria) may be calculated relative to the efficiency of the DC+cuts system described above. These measures of efficiency do not take into account effects which affect both equally — such as livetime and telemetry efficiency.

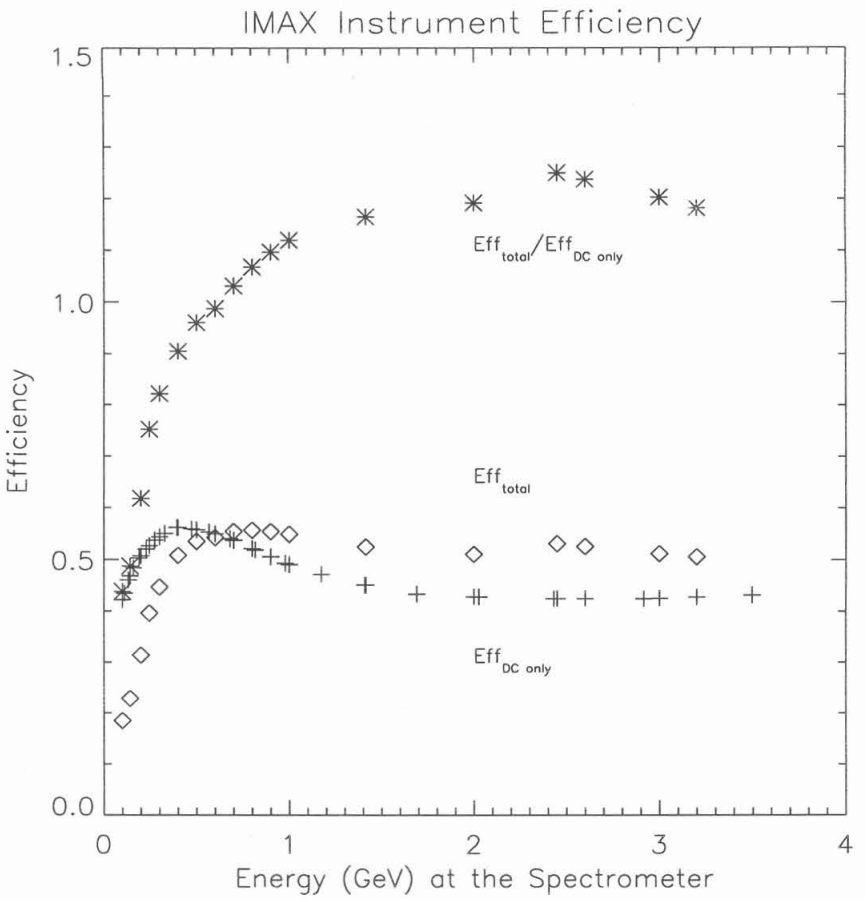

Figure 4.3: Efficiencies vs. Energy (GeV) at the spectrometer. Shown are measurements for the DC–only system ($Eff_{DC\ only}$), for the total selection set (Eff_{total}) described in Chapter 3, and for their ratio. These efficiencies do not include fractional livetime or telemetry efficiency.

The results of the efficiency measurement are shown in Figure 4.3. Included in the Siegen calculations were the energy–dependent DC–efficiency (measured relative to the reference detector described above), the 74% livetime, a 92.8% telemetry efficiency, and an energy dependent charge–selection efficiency which averages ~93%. The Figure excludes livetime and telemetry efficiency, in order to give the efficiency of the selection criteria. The telemetry efficiency comes from a measure of the number of incomplete science (event) data frames in the raw data. While charge–selection efficiency could, in principle, be calculated from a Monte Carlo simulation, it was calculated for IMAX from the experimental data, in keeping with the experimental determination of efficiency for the DCs. The charge–selection efficiency is calculated from the number of events which pass Z=1 cuts for all four scintillators relative to the number of events which pass Z=1 cuts for at least three scintillators. The charge–selection cuts used by Siegen are looser than those used in the present analysis (Section 3.2), but final fluxes are normalized to the Siegen fluxes, implicitly taking into account the differences in charge selection.

The features of the Siegen detection efficiency curve (Figure 4.3) can be attributed to a number of factors. At low energies (e.g. below 300 MeV), multiple scattering decreases the effectiveness of the track–fitting algorithm to yield a particle trajectory. (See Section 2.7.1 for multiple scattering and Section 3.1 for the tracking algorithm.) Also at low energies, higher dE/dx results in better detection efficiency for individual drift cells. The lower efficiency from multiple scattering competes with the higher efficiency from dE/dx, but the relative contribution from multiple scattering drops off by ~500–700 MeV. Finally, at higher energies, the drift path corrections are determined better than at lower energies, resulting in better position resolution and higher track–fitting efficiency. (See Section 3.1.)

To calculate the energy–dependent detection efficiency used in this analysis, we normalize the raw proton spectrum obtained from the data set described at the end of Chapter 3 to the proton spectrum calculated by the University of Siegen collaborators and corrected for

the efficiency described above. These spectra were calculated at the instrument. The final, total efficiency of the selection criteria described in Chapter 3 is shown in Figure 4.3.

The features in the resulting total efficiency arise from a number of factors: The slightly higher efficiency at ~2.6 GeV arises from the switch to the Cherenkov–Rigidity technique above the aerogel Cherenkov threshold energy. In contrast, the Siegen analysis used only rigidity to calculate energy, assuming the bulk of the Z=1 particles were protons (with lower mass selection efficiency via dE/dx vs. deflection). At significantly higher energies (e.g. >3.2 GeV), in this analysis, all Z=1 particles were assumed to be protons, and their energies were determined solely from their measured rigidities. These particles, however, do not enter into the final analysis, and their inclusion in Figure 4.3 was solely for illustration. Furthermore, at high energies, the increased detection efficiency resulting from this analysis, relative to the Siegen DC–only analysis, arises in large part due to the inclusion of MWPC data in the track fitting algorithm. Finally, the decrease at low energies in detection efficiency relative to the Siegen calculation is due mostly to the stricter selection criteria, as described in Chapter 3.

When this energy–dependent detection efficiency (which averages ~51–52%) is compared with the estimated total intrinsic selection efficiency (58.8%) discussed in Section 3.6 — and taking into account that that estimated selection efficiency does not include the IFAIL=0 efficiency — an estimated systematic uncertainty of 5% may be adopted for the detection efficiency.

4.3 Instrumental and Atmospheric Background

The raw proton and antiproton counts at the end of Chapter 3 are not directly comparable to theory or to other experiments. Both the proton and the antiproton counts must be corrected to the top of the atmosphere, taking into account not only the efficiencies described in Section 4.2 but also losses due to interactions (e.g. antiproton annihilations) in the instrument and atmosphere as well as production of secondary protons and antiprotons.

4.3.1 Corrections to the Top of the Atmosphere for Protons

At the energies in consideration for IMAX data, a primary source of proton loss will be due to nuclear inelastic scattering in the IMAX materials. (See Appendix B for a listing of the IMAX materials.) Interaction lengths are calculated from cross sections by

$$\lambda_I(E) = \frac{A}{N\sigma_I(E)} g/cm^2 \tag{4.3.1}$$

where A is the mass number for the target nucleus, and N is Avogadro's number. For the calculation of proton–nucleus inelastic interaction lengths (λ_I), the cross section (σ_I) energy–dependence parametrization of Silberberg and Tsao (1990) was employed. The high energy (energy–independent) values were scaled for the various IMAX materials with values from the Particle Data Group (1992), in order to eliminate the quasi–elastic contribution which is left in the Silberberg and Tsao parametrization (Krizmanic 1995). The resulting interaction lengths agree with those of the Particle Data Group to within ~2% for the available data. For proton–proton inelastic scattering, fits were made to the CERN measurements of Flaminio et al. (1984).

The transmission factor for proton–nucleus inelastic scattering, T_I, is calculated by

$$T_I = e^{-x/\lambda_I} \tag{4.3.2}$$

where x is the thickness of the material. Figure 4.4 shows the resulting attenuation factor for proton–nucleus inelastic scattering through all IMAX materials from the top of the IMAX dome through the bottom TOF paddle, assuming vertical incidence. The correction factor for losses due to proton–nucleus inelastic scattering is approximated by the inverse of the transmission factor. Strictly speaking, this correction factor will be an upper limit, because not all inelastic scattering events will be detected and rejected by the instrument or the analysis. However, most inelastic scattering events should be rejected. Inelastic scattering events in the tracking

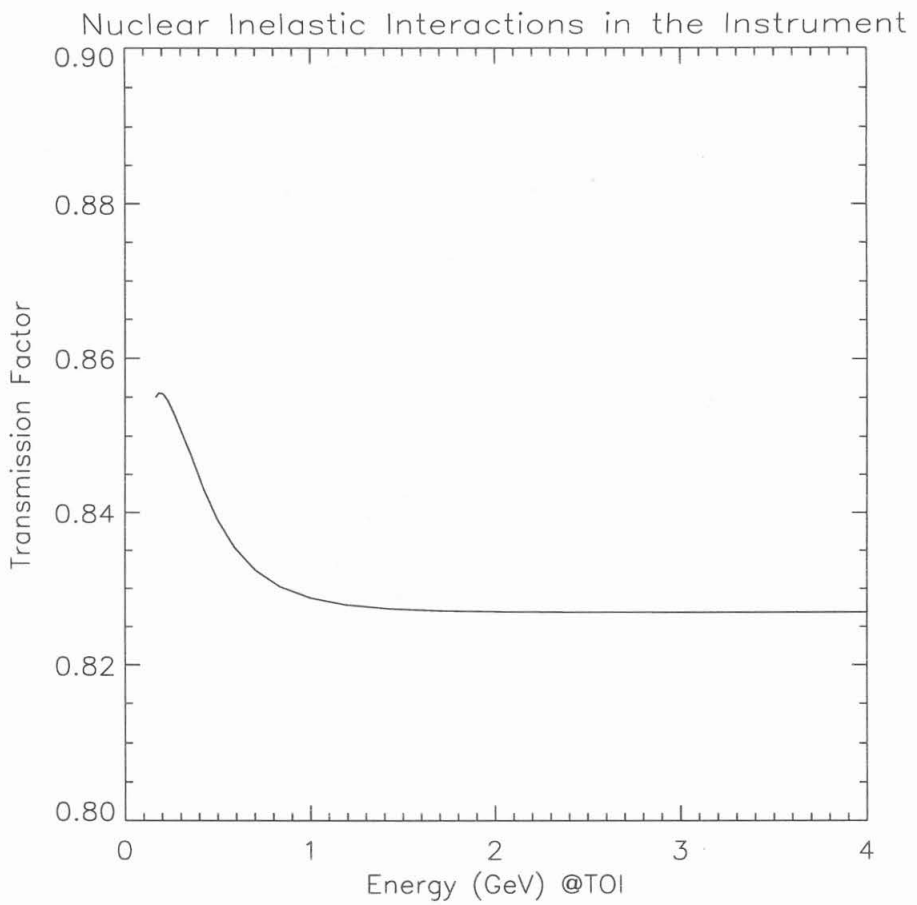

Figure 4.4: Transmission factor for nuclear inelastic interactions of protons in the instrument, as a function of energy at the top of the instrument.

system should be rejected as hard scattering events by the tracking quality selection criteria (Section 3.1). Inelastic scattering events in one of the scintillators will likely produce anomalous scintillator signals which will be rejected by the tightness of the charge selection criteria (Section 3.2), as will any scattering event between scintillators which will produce a large loss of energy. Finally, almost all production of secondary particles (including protons and antiprotons) from inelastic interactions in the instrument will be detected and rejected by tracking quality cuts, charge selection criteria, and possibly by some aerogel Cherenkov selection criteria, particularly given the net forward momenta in the secondary products.

Therefore, the proton–nuclear inelastic scattering correction factor obtained directly from the calculated transmission factor is adopted for this analysis. The resulting transmission factors and attenuation factors, averaged over the three selected energy ranges for IMAX (Section 3.8), are given in Table 4.2.

Table 4.2: Proton–nucleus Inelastic Scattering Transmission and Correction Factors for IMAX

Energy (GeV) at the Top of the Instrument	Transmission Factor	Correction Factor, C_1
0.23 — 0.99	0.8376	1.1939
0.99 — ~2.60	0.8273	1.2087
~2.60 — ~3.10	0.8271	1.2091

Krizmanic (1995) estimates systematic uncertainties of 6% below 1 GeV and 3.5% above 1 GeV for the attenuation factors, which corresponds to uncertainties of ~1% in transmission. These uncertainties arise from uncertainties in the fit by Silberberg and Tsao as well as the uncertainties in the cross section data.

A similar calculation for proton–nuclear inelastic scattering in the atmosphere is shown in Figure 4.5, and the resulting transmission and correction factors are given in Table 4.3.

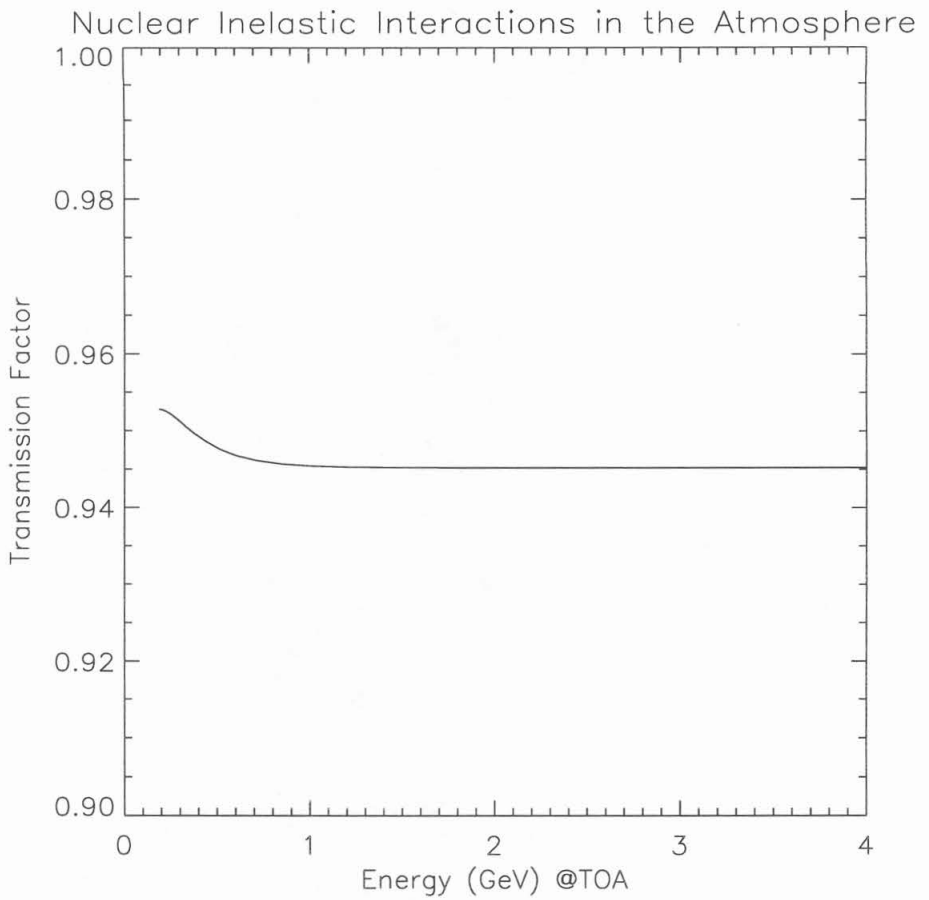

Figure 4.5: Transmission factor for nuclear inelastic interactions of protons in the atmosphere, as a function of energy at the top of the atmosphere. Applying this factor corrects for protons which are not lost but which are also counted (and subtracted in this analysis) as secondary atmospheric protons by Papini et al. (1993).

Although some primary protons are not lost during inelastic interactions in the atmosphere (i.e. they lose energy but still reach the instrument), such protons counted as secondaries in the calculation of secondary atmospheric protons by Papini et al. (1993), even though they contribute to the total proton flux at the top of the atmosphere. Because the present analysis subtracts all secondary atmospheric protons, application of the inelastic interaction correction factor will restore primary protons which have undergone inelastic energy loss. Systematic uncertainties in the cross section fits and measurements, as described above, result in systematic uncertainties of ~0.3–0.6% in atmospheric transmission factors.

Table 4.3: Proton–nucleus Inelastic Scattering Transmission and Correction Factors for 5 g/cm^2 of residual atmosphere

Energy (GeV) at the Top of the Atmosphere	Transmission Factor	Correction Factor, C_3
0.25 — 1.00	0.9474	1.0555
1.00 — ~2.61	0.9506	1.0519
~2.61 — ~3.11	0.9454	1.0578

Nuclear elastic scattering occurs as multiple Coulomb scattering in the payload. (See Section 2.7.1.) Except for hard scattering events, particles which undergo nuclear elastic scattering are not likely to be lost to the data analysis, and those which are lost are primarily accounted for in the efficiency calculations. Krizmanic (1995) has estimated via GEANT simulations that losses due to nuclear elastic scattering are negligible.

Proton counts corrected to the top of the instrument include both primary cosmic ray protons as well as secondary protons produced by interactions in the atmosphere. The contributions from secondary atmospheric protons must be subtracted. Papini et al. (1993) have calculated the secondary atmospheric proton abundances due to cosmic ray interactions in the atmosphere for solar minimum and maximum. (Note that any proton which interacts

inelastically in the atmosphere is counted as a secondary proton in their calculation.) However, the Papini et al. calculation is based on primary proton fluxes of Webber (1973), which underestimates the integrated, high–energy proton flux from IMAX by ~10%. Prior to the availability of IMAX proton fluxes, comparisons were also made with Webber and Potgieter (1989) proton flux, which is also higher than that of Webber (1973).

The Papini et al. calculation is nontrivial, and it was beyond the scope of the IMAX collaboration to reproduce their calculation to levels appropriate for IMAX analysis. Therefore, the Papini et al. calculations of secondary atmospheric proton flux at 5 g/cm^2 were scaled to appropriate values. The scaling factor was calculated as the ratio of the IMAX top–of–the–atmosphere (TOA) proton flux to the Webber (1973) proton flux, both integrated from 10 to 100 GeV under the assumption that the total secondary proton flux scales linearly with the integrated TOA proton flux. Because the calculated IMAX TOA flux is depends on the calculated secondary flux, the scaling calculations had to be carried out through several iterations.

The results of the iterations are shown in the following figures. Figure 4.6 shows the original Webber (1973) proton fluxes for solar minimum and solar maximum, the Webber and Potgieter (1989) proton flux solar modulated to 1992 levels, and the IMAX top of the atmosphere proton flux. Figure 4.7 shows the Papini et al. (1993) secondary atmospheric proton fluxes at 5 g/cm^2 residual atmosphere, for solar minimum and solar maximum and scaled upward by 9%, as well as the interpolated secondary atmospheric proton flux for 1992. Figure 4.8 shows the Papini et al. (1993) secondary/primary proton ratios at 5 g/cm^2 residual atmosphere for solar minimum and solar maximum, as well as the scaled secondary/primary proton ratio used for this analysis.

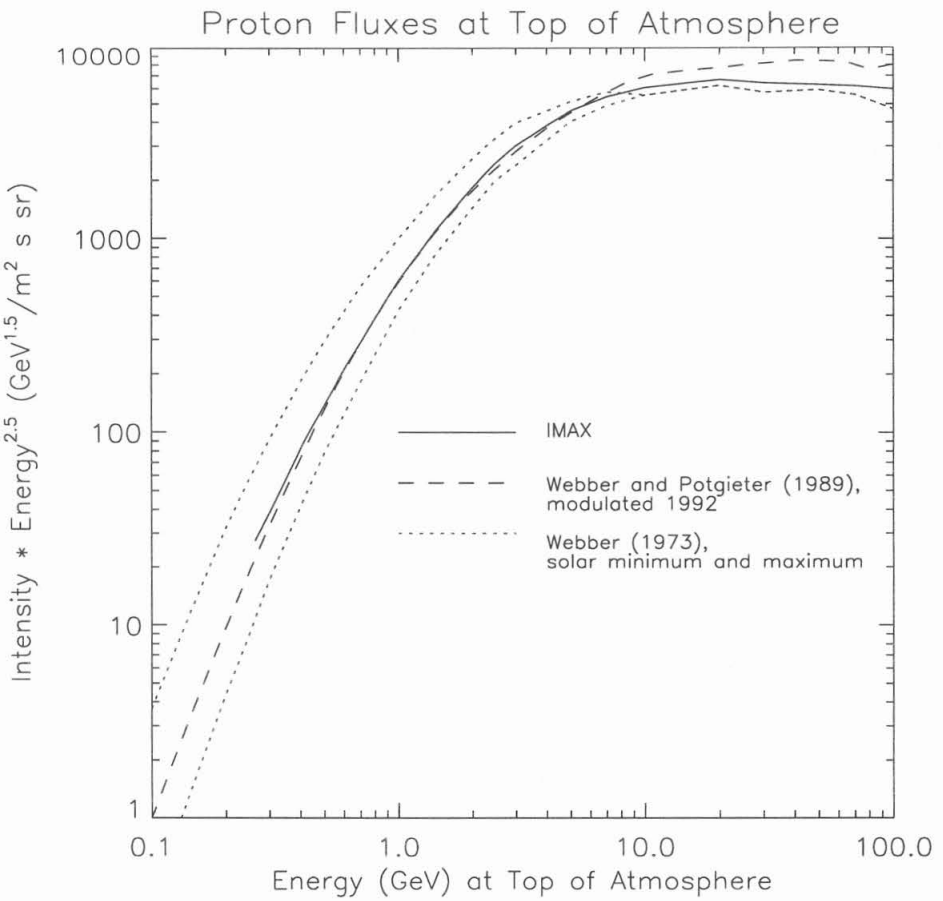

Figure 4.6: The Webber (1973) proton spectra for solar minimum and solar maximum, the Webber and Potgieter (1989) proton spectrum solar modulated to 1992 levels, and the IMAX top of the atmosphere proton spectrum.

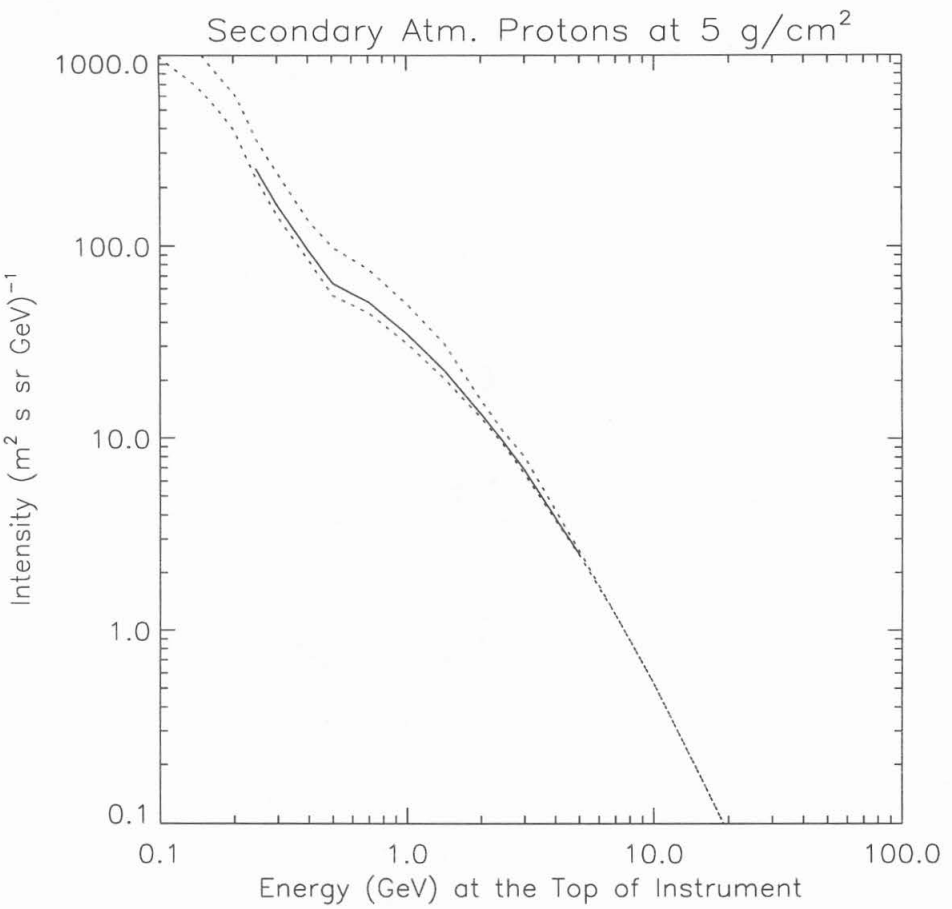

Figure 4.7: The Papini et al. (1993) secondary atmospheric proton spectra (dotted lines) at 5 g/cm^2 residual atmosphere, for solar minimum and solar maximum, scaled upward by 9%. Also shown is the interpolated secondary atmospheric proton spectrum (solid line) for 1992.

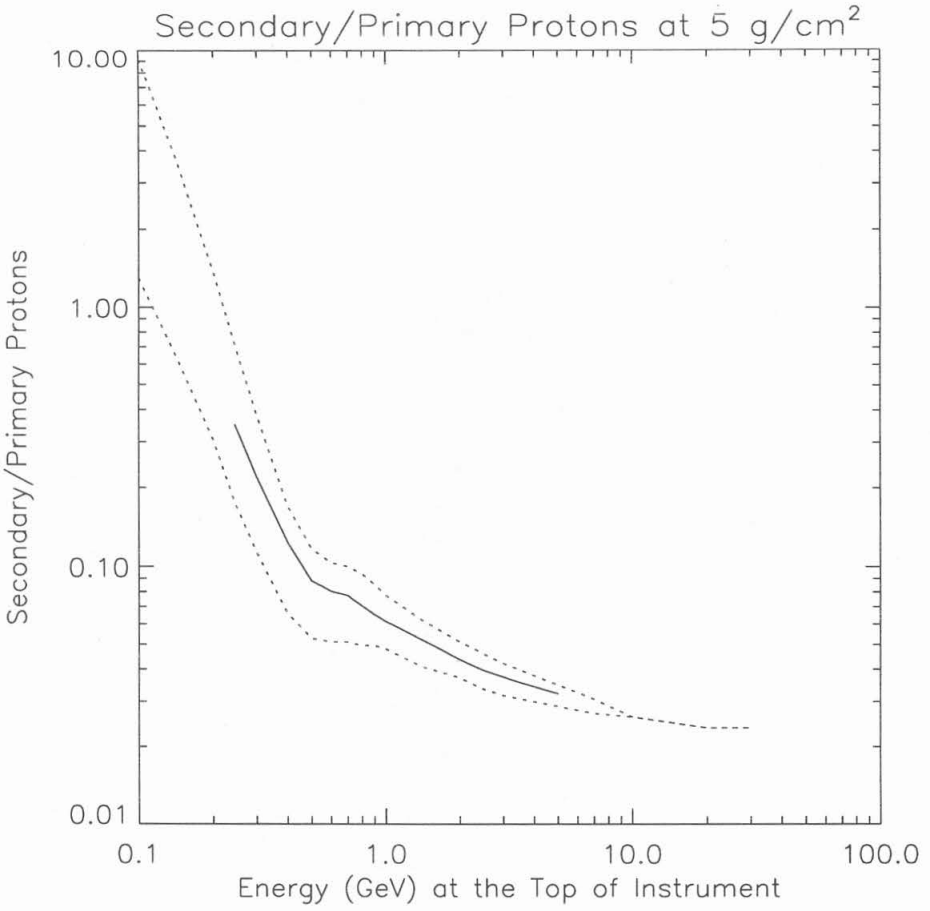

Figure 4.8: The Papini et al. (1993) secondary/primary proton ratios at 5 g/cm^2 residual atmosphere for solar minimum and solar maximum, and the interpolated secondary/primary proton ratio used for this analysis.

The estimated primary proton abundance at 5 g/cm^2 can be calculated from the total abundance, J_{tot}, by

$$J_{prim}(E) = \frac{J_{tot}(E)}{1+(s/p)} \tag{4.3.3}$$

where s/p is the secondary/primary ratio (as a function of energy). With the IMAX proton data, this expression yields the same result as subtracting the secondary contribution from the total abundance, when detector efficiency is taken into account. With the application of this expression, one may obtain a primary proton flux at 5 g/cm^2, and with the application of the atmospheric attenuation correction factors (see above), the top of the atmosphere proton abundance may be obtained.

Table 4.4 shows the secondary/primary proton ratios for each energy bin for the iterations used in this analysis. The ratios are given in averages weighted by the measured proton fluxes.

Table 4.4: Convergence of Secondary/Primary Proton Ratios

Energy (GeV) at Top of Instrument	1st Iteration	2nd	3rd	4th
0.20 — 1.00	0.1418	0.1338	0.1332	0.1324
1.00 — ~2.60	0.0595	0.0501	0.0499	0.0497
~2.60 — ~3.20	0.0488	0.0382	0.0380	0.0379

As a historical matter, these numbers do not correspond to the final energy bins at the top of the instrument, since they were calculated before the final energy bins were selected. The final iteration, re–averaged over the proper top-of-the-instrument energy bins, is given in Table 4.5.

Table 4.5: Final Secondary/Primary Proton Ratios for the IMAX Energy Bins

Energy (GeV) at Top of Instrument	Secondary/Primary Protons (4th Iteration)
0.23 — 0.99	0.1158
0.99 — ~2.60	0.0499
~2.60 — ~3.10	0.0383

An estimated systematic uncertainty of ~30% in the secondary atmospheric proton flux is adopted for this analysis.

4.3.2 Corrections to the Top of the Atmosphere for Antiprotons

With far fewer antiprotons than protons in the final IMAX flight data set, the antiproton count is far more susceptible to instrumental background than the proton count. In particular, IMAX Monte Carlo calculations show that, of the 5 antiproton candidates in the Cherenkov–Rigidity energy range, approximately 0.5±0.5 of these candidates may be accounted for by electrons or light mesons with Cherenkov light yield fluctuations down to the $\overline{f_{2+3}}$=0.16 – 0.36 range. Such contribution is relatively negligible for protons in the same Cherenkov range, and for antiprotons and protons below the effective Cherenkov threshold (C2+C3 Map–Normalized < 0.16), the combination of Cherenkov and TOF rejection makes the contribution from muon fluctuation negligible.

The next major sources of antiproton loss will be annihilation and non–annihilating inelastic interactions in the instrument. The non–annihilating inelastic interaction losses should be roughly the same for protons and antiprotons, with the exception of very low energy interactions where Coulomb effects begin to dominate. Systematic measurements of antiproton annihilation cross sections on a variety of targets and at energies useful in this analysis have recently been reported by Kuzichev et al. (1994). In their paper, they report antiproton annihilation cross section measurements on targets ranging from A=9 (^{9}Be) to A=207 (^{207}Pb) and

for antiproton momenta in the range p = 0.7 – 2.5 GeV/c (or kinetic E = 0.23 – 1.73 GeV). Stephens and Golden (1987) have shown that proton–antiproton annihilation cross sections (Flaminio et al. 1984) can be fitted with an energy–dependent function of the form

$$\sigma_{\bar{p}p,ann} = 42.0\left[E_{kinetic}^{-0.43} - 0.0476\right] \quad \text{mb} \tag{4.3.4}$$

It turns out that the Kuzichev et al. data may be fitted with an energy and target mass (A) function of a similar form,

$$\sigma_{pbar-Ann}(A,E) = \pi\left(a_0 + rA^{1/3}\right)^2\left[E^{-\gamma} + \delta_0\right] \tag{4.3.5}$$

where A is the target mass number, E is the antiproton kinetic energy, and a_0, r, γ, and δ_0 are the fittable parameters. The first part of Equation 4.3.5 gives a hard–sphere scaling for the cross section, while the second part follows the energy–parametrization of Stephens and Golden. The results of a least squares fit of this function to the Kuzichev et al. data are given in Table 4.6. Figure 4.9 shows representative plots of the Kuzichev et al. (1994) measurements along with the results of the fits to their data.

Table 4.6: Results of Least Squares Fit of Equation 4.3.5 to the Antiproton–Nucleus Annihilation Cross Section Measurements of Kuzichev et al. (1994)

A	a_0	r	γ	δ_0
9	1.65	1.79	0.24	2.41
12	1.51	1.66	0.50	2.90
27	0.34	1.11	1.26	12.58
56	0.78	1.20	0.83	9.73
64	0.40	1.10	1.05	13.21
112	0.34	1.07	1.03	14.79
207	1.46	1.25	1.20	8.11

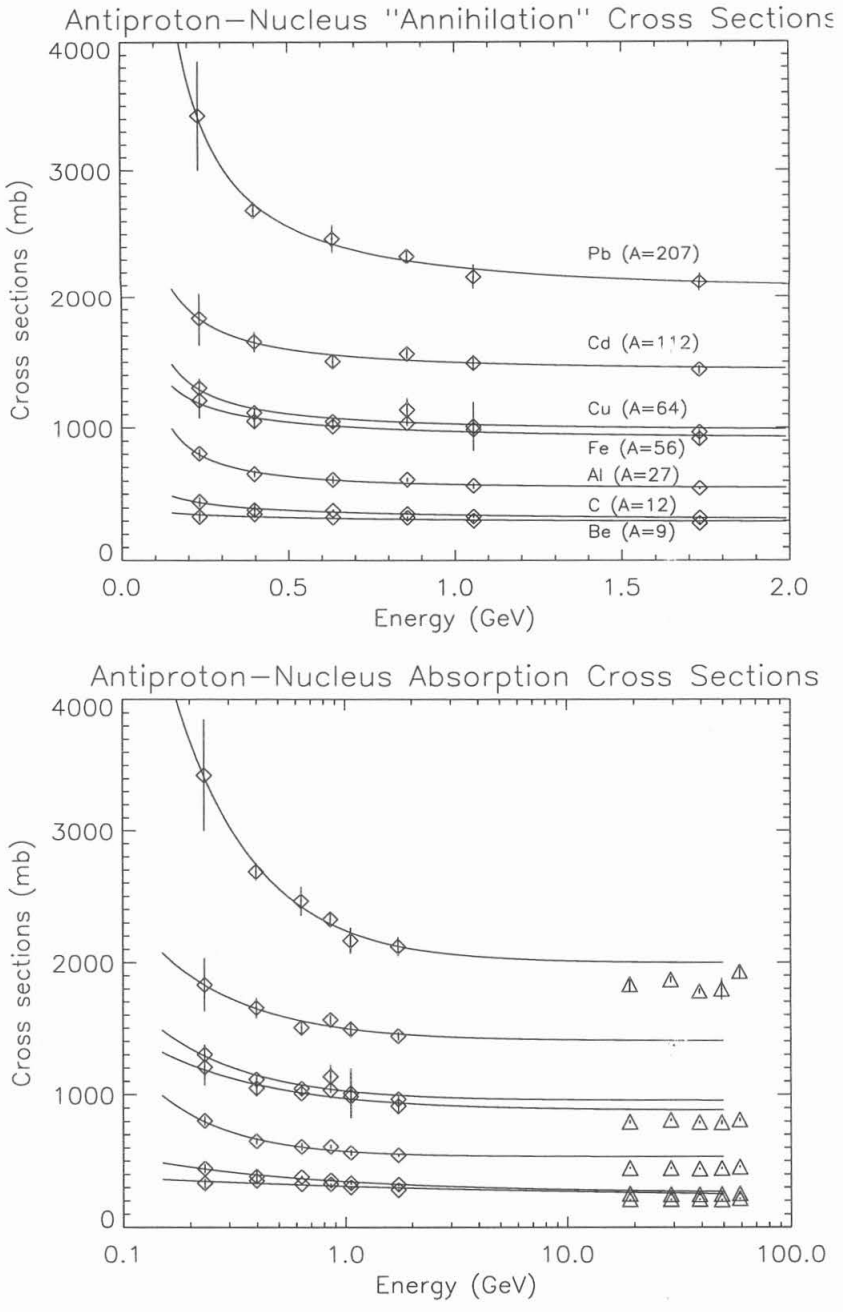

Figure 4.9: Antiproton annihilation cross section measurements by Kuzichev et al. (1994, open diamonds) and Denisov et al. (1973, open triangles) for various target nuclei, and fits to the Kuzichev et al. measurements.

It is important to note that the experimental apparatus used by Kuzichev et al. does not identify the products of the annihilation interactions. The apparatus is an array of Cherenkov counters and scintillators surrounding the target material. No particle trajectories are measured to determine reaction product identities. Therefore, their apparatus does not directly distinguish between annihilation interactions and other non–annihilating inelastic interactions. Although their work attempts to correct for background from non–annihilating interactions via Monte Carlo simulations, it remains possible that significant contamination may remain. This assumption is partially born out in comparison with data from Denisov et al. (1973). The Denisov et al. antiproton absorption cross sections on nuclei are defined as the difference between the total cross section and the elastic cross section — a difference which implicitly combines annihilation and non–annihilating inelastic interactions. Because the fits to the Kuzichev et al. data are roughly consistent with the higher energy Denisov et al. data (see Figure 4.9), the fits to the Kuzichev et al. data are treated as combining annihilation and non–annihilating inelastic interactions in this analysis.

Thus, the total transmission and correction factors for annihilation and non–annihilating inelastic interactions are given in Tables 4.7 and 4.8. The tables use column densities of 18.76 g/cm^2 for the IMAX payload material (top of the spreader bar through the bottom TOF; see Appendix B), and 5 g/cm^2 of residual atmosphere, . The interaction lengths are calculated according to Equation 4.3.1 from the fitted cross sections. The transmission factors are calculated as with Equation 4.3.2 with unweighted averages over each energy bin. The measurement uncertainties of the Kuzichev et al. cross sections range from 8 mb to 34 mb, while the fits to the Kuzichev et al. cross sections generally lie within 26 mb of the measurements. The total uncertainties in the fitted cross sections average 22.1 mb (4%) and 26.4 mb (7%) for carbon and aluminum targets, respectively. These uncertainties yield systematic uncertainties in the correction factors of about 2%.

Table 4.7: Annihilation and Inelastic Interaction Transmission Factors and Correction Factors through 18.76 g/cm^2 of IMAX Payload and Detector Material

Energy (GeV) at Top of Instrument	Transmission Factor	Correction Factor
0.23 – 0.99	0.7291	1.3716
0.99 – ~2.61	0.7650	1.3072
~2.61 – ~3.11	0.7733	1.2932

Table 4.8: Annihilation and Inelastic Interaction Transmission Factors and Correction Factors through 5 g/cm^2 of Residual Atmosphere

Energy (GeV) at Top of Atmosphere	Transmission Factor	Correction Factor
0.25 – 1.00	0.9163	1.0914
1.00 – ~2.61	0.9268	1.0790
~2.61 – ~3.11	0.9294	1.0760

An additional effect of antiproton annihilation has been suggested by Buffington (private communication 1995). In addition to possible annihilation in the instrument, an antiproton may annihilate in the payload material below the bottom TOF. In such an annihilation, some annihilation products may proceed back into the detector stack and contaminate what would otherwise have been a clean measurement. A GEANT simulation has been run to simulate this effect with the known IMAX payload materials below the bottom TOF (Krizmanic 1995) simulated as 11 g/cm^2 of aluminum, and the resulting correction factors are given in Table 4.9.

Table 4.9: Annihilation Backscatter Corrections for IMAX

Energy (GeV) at the Top of the Instrument	Annihilation Backscatter Correction Factor
0.23 – 0.999	1.1163
0.99 – ~2.60	1.0619
~2.60 – ~3.10	1.0522

Finally, as is the case with secondary atmospheric protons, the measured 16 antiproton candidates must include some secondary antiprotons produced by interactions of cosmic rays in the atmosphere. (Secondary antiprotons produced in the instrument will be accompanied by secondary protons and other particles, and with net forward momentum accompanying such production interactions, these multiple secondaries will be rejected by the instrument and selection criteria.) Stephens (1993) has calculated the flux of secondary atmospheric antiprotons for various atmospheric depths. As with Papini et al. (1993), the antiproton calculation makes use of the Webber (1973) proton flux data, although the effect of solar modulation is negligible because the 6 GeV threshold for antiproton production is above the region where solar modulation has greatest effect. Therefore, for this analysis, the Stephens (1993) secondary atmospheric antiproton flux for 5 g/cm^2 residual atmosphere is scaled upward in the same way that the Papini et al. (1993) atmospheric proton fluxes were scaled. (See Section 4.3.1.) The original and the scaled fluxes are shown in Figure 4.10. The scaled flux is integrated over the three IMAX energy bins and multiplied by the energy–dependent geometry factor (Section 4.2.1), the 74% livetime (Section 4.2.2), the energy–dependent IMAX detection efficiencies (Section 4.2.3), and the 14.78 hour duration of the IMAX data set. The estimated number of secondary atmospheric antiprotons at the spectrometer (for comparison with the 16 candidate antiprotons) and at the top of the instrument are given in Table 4.10.

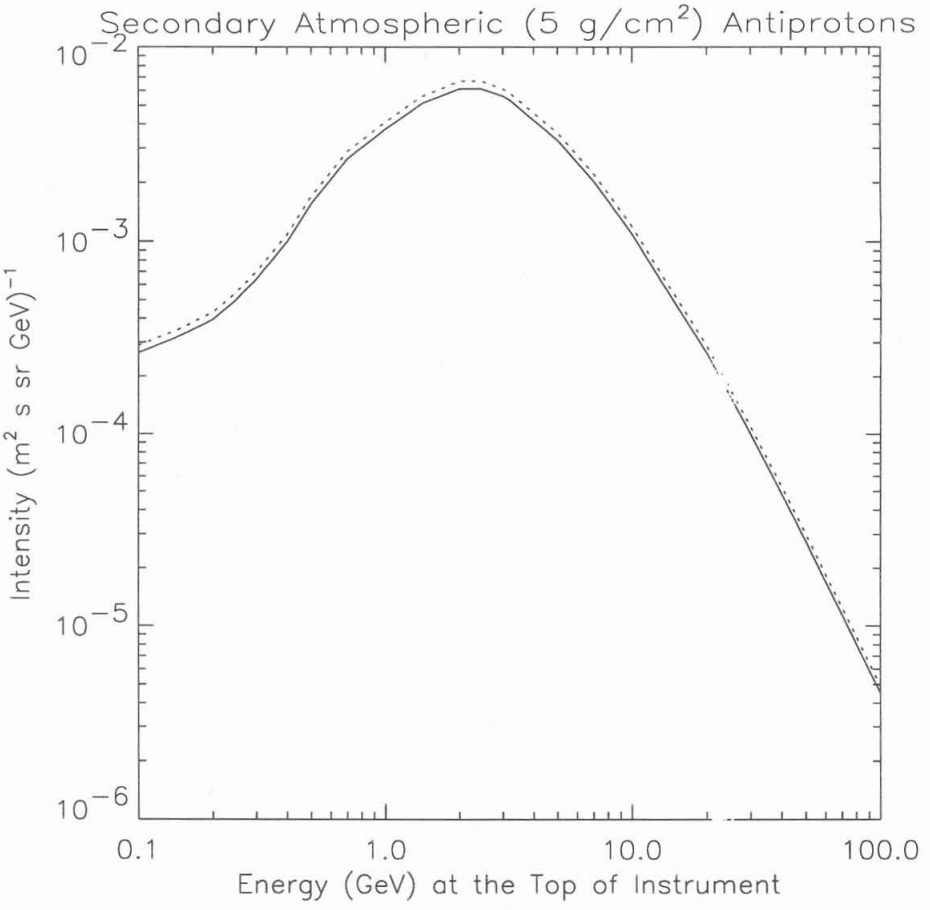

Figure 4.10: Secondary atmospheric antiproton flux at 5 g/cm^2 residual atmosphere, as calculated by Stephens (1993, solid line) and as scaled for this analysis (dotted line).

Table 4.10: Corrections for Secondary Atmospheric Antiprotons

Energy (GeV) at Spectrometer	# Secondary Atm. Antiprotons at Spectrometer	Energy (GeV), Top of the Instrument	# Secondary Atm. Antiprotons, Top of the Instrument
0.19 – 0.97	**0.30**	0.23 — 0.99	0.46
0.97 – ~2.58	**1.89**	0.99 — ~2.60	2.62
~2.58 – ~3.08	**0.62**	~2.60 — ~3.10	0.84

The numbers for the spectrometer may be subtracted from the original 16 candidate antiprotons, or the numbers at the top of the instrument (5 g/cm^2 residual atmosphere) may be subtracted from the numbers corrected to the top of the instrument.

Pfeifer et al. (1996) recently calculated upper and lower limits to the atmospheric antiproton flux using the Webber et al. (1987) and Seo et al. (1991) proton fluxes, respectively. Above 2 GeV, the Pfeifer et al. upper limit exceeds the Stephens result by a few percent to as much as 60%, but the Pfeifer et al. lower limit closely follows the Stephens result (Figure 4.11). Below a few hundred MeV, the Pfeifer et al. limits both exceed the Stephens result, attributed to newer p–nucleus and nucleus–nucleus interaction cross sections. Webber (private communication, 1995) has suggested that the Seo et al. (1991) proton fluxes are too low because of errors in the calculation of instrumental detection efficiency, implying that the Pfeifer et al. atmospheric antiproton flux lower bound is also too low. We may, instead, adopt the Pfeifer et al. upper bound for secondary atmospheric antiprotons.

Thus, if the Pfeifer et al. upper limit is adopted, then, out of the 16 antiprotons detected by IMAX, a total of 2.95 antiprotons would be attributed to atmospheric background — compared with 2.84 using the Stephens (1993) calculation, scaled upward by 9% for this analysis (Sections 4.3.1 and 4.3.2). However, the 9% scaling of the Stephens (1993) calculation is the scaling necessary to compare with the IMAX proton data (Figure 4.6). If the Stephens

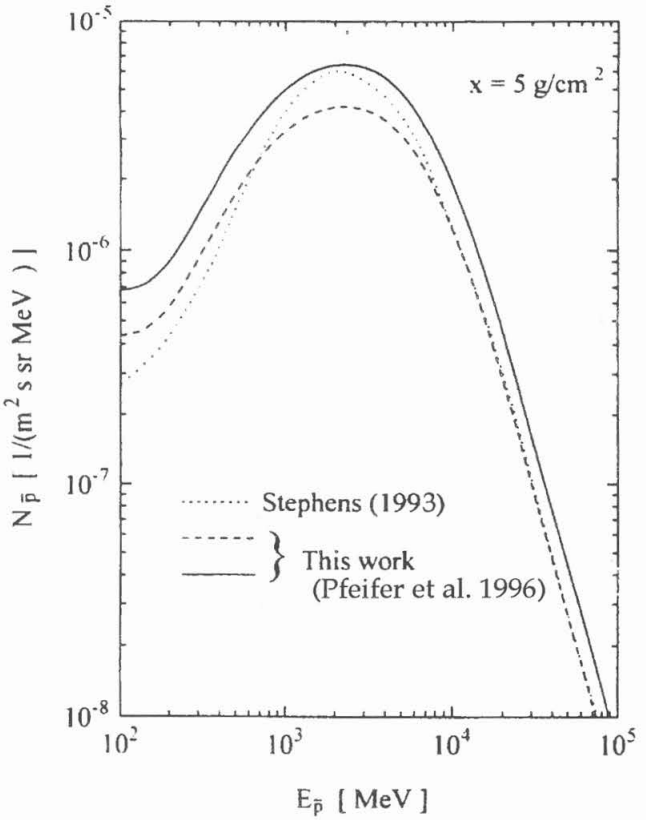

Figure 4.11: Secondary atmospheric antiproton fluxes calculated by Pfeifer et al. (1996), compared with a similar calculation by Stephens (1993). The solid and dashed curves are upper and lower limits calculated by Pfeifer et al. using different proton spectra at the top of the atmosphere. Figure taken from Pfeifer et al. (1996). Note that the Stephens (1993) calculation, as shown in the Figure, has not been scaled upward by 9%, as has been described in Sections 4.3.1 and 4.3.2 for the present analysis. A better comparison would scale the Stephens (1993) calculation upward by 20%, in order to scale from the input proton spectrum used by Stephens (Webber 1973) to that used by Pfeifer et al. (Webber et al. 1987).

(1993) calculations were scaled to the Webber et al. (1987) proton data, the scaling increase would be 20%. Thus, the comparably scaled Stephens (1993) result would be 3.13 atmospheric antiprotons in the IMAX energy range 0.25–3.11 GeV. In the lowest energy bin, the Pfeifer et al. calculation yields 0.43 atmospheric antiprotons, while the comparably scaled Stephens (1993) calculation yields 0.33 atmospheric antiprotons. (Compare this with the 0.30 atmospheric antiprotons scaled for the IMAX analysis.) The difference implies a systematic uncertainty of about 45% in the lowest energy correction factor. Since the higher energy corrections show less relative difference, a conservative systematic uncertainty of 30% is adopted at higher energies. Because a similar calculation by Pfeifer et al. for atmospheric protons is unavailable, it is unclear what the effect would be for the antiproton/proton ratio.

Finally, because the Stephens (1993) calculation is methodologically consistent with the Papini et al. (1993) calculation, and because the Pfeifer et al. (1996) calculation was unavailable until just before this work was completed, the Stephens (1993) result is adopted for this analysis.

4.4 Antiproton/Proton Ratio at the Top of the Atmosphere

In making corrections to the top of the atmosphere for the antiproton/proton ratio measurements, one need not take into account factors which affect protons and antiprotons equally (e.g. geometry factor, detection efficiency, and livetime). For this analysis, only the raw proton and antiproton counts, the Cherenkov light yield fluctuation corrections for antiprotons, the secondary atmospheric background corrections, and annihilation correction factors are required. Inelastic scattering corrections are applied for protons, but inelastic scattering of antiprotons is assumed to be incorporated into the "annihilation" correction factors. (See Section 4.3.)

The corrections to the top of the atmosphere for raw protons (not including livetime, geometry factor, efficiencies) follow the equation

$$p_{TOA,raw} = \left[p_{spect,raw}\right]\left[\frac{1}{T_{inst}}\right]\left[\frac{1}{1+\frac{s}{p}}\right]\left[\frac{1}{T_{atm}}\right] \tag{4.4.1}$$

where T_{inst} and T_{atm} are the nuclear inelastic interaction transmission factors for the instrument and atmosphere, and s/p is the secondary/primary proton ratio at 5 g/cm^2 residual atmosphere (Section 4.3.1). Table 4.11 summarizes the raw proton results from the spectrometer to the top of the atmosphere, without corrections for efficiency, geometry factor, or livetime.

Table 4.11: Raw Proton Results to the Top of the Atmosphere

Energy (GeV) at TOI	Energy (GeV) at TOA	Protons at the Spectrometer	Total Protons at TOI	Primary Protons, TOI	Primary Protons, TOA
0.23 — 0.99	0.25–1.00	124405	148532	133112	140500
0.99 — ~2.60	1.00–~2.61	140617	169963	161892	170300
~2.60 — ~3.10	~2.61–~3.11	22524	27234	26229	27745

Similarly, the raw antiproton counts at the spectrometer can be corrected to the top of the atmosphere by the equation

$$\bar{p}_{TOA,raw} = \left[\left(\bar{p}_{spect,raw} - \mu_{fluct}\right)C_{inst}^{ann+inel}C_{backscatter} - \bar{s}\right]C_{atm}^{ann+inel} \tag{4.4.2}$$

where $\bar{p}_{spect,raw}$ is the raw antiproton count (Section 3.8), μ_{fluct} is the number of Cherenkov fluctuated electrons or light mesons that simulate antiprotons, $\bar{s}$ is the number of secondary atmospheric antiprotons at the top of the instrument (5 g/cm^2 residual atmosphere), $C_{inst}^{ann+inel}$ and $C_{atm}^{ann+inel}$ are the correction factors (1/transmission factor) for annihilation and non–

annihilating inelastic interactions in the instrument and atmosphere, and $C_{backscatter}$ is the correction for annihilation backscatter. See Section 4.3.2 for a description of the correction factors. The raw antiproton results from the spectrometer to the top of the atmosphere, without corrections for efficiency, geometry factor, or livetime, are summarized in Table 4.12.

Table 4.12: Raw Antiproton Results to the Top of the Atmosphere with Statistical Uncertainties

Energy (GeV), TOI	Energy (GeV), TOA	Antiprotons at the Spectrometer	Total Antiprotons, TOI	Primary Antiprotons, TOI	Primary Antiprotons, TOA
0.23 — 0.99	0.25–1.00	3 (+2.9, -1.7)	4.6 (+4.5, -2.5)	4.1 (+4.5, -2.5)	4.5 (+4.9, -2.8)
0.99 — ~2.60	1.00–~2.61	8 (+4.0, -2.8)	11.1 (+5.5, -3.9)	8.5 (+5.5, -3.9)	9.2 (+5.9, -4.2)
~2.60 — ~3.10	~2.61–~3.11	5 (+3.4, -2.2)	6.1 (+4.6, -3.0)	5.3 (+4.6, -3.0)	5.7 (+5.0, -3.2)

The statistical uncertainties for antiprotons dominate the antiproton/proton ratio. In this case, the uncertainties are calculated according to counting statistics of small numbers, with

$$\sigma_n^+ = \sqrt{n + 0.75} + 1$$
$$\sigma_n^- = \sqrt{n - 0.25} \qquad (4.4.3)$$

where n is small (Israel 1979). The error bars on a logarithmic scale appear equal. In this formulation, each error bar gives an 84.13% confidence limit, and the two limits together approximate a 68% confidence interval. The resulting antiproton/proton ratios for the top of the atmosphere are given in Table 4.13. These results are also shown in Figure 4.12. Comparison with theoretical models will follow in Section 5.3, following the discussion of solar modulation in Section 5.2.

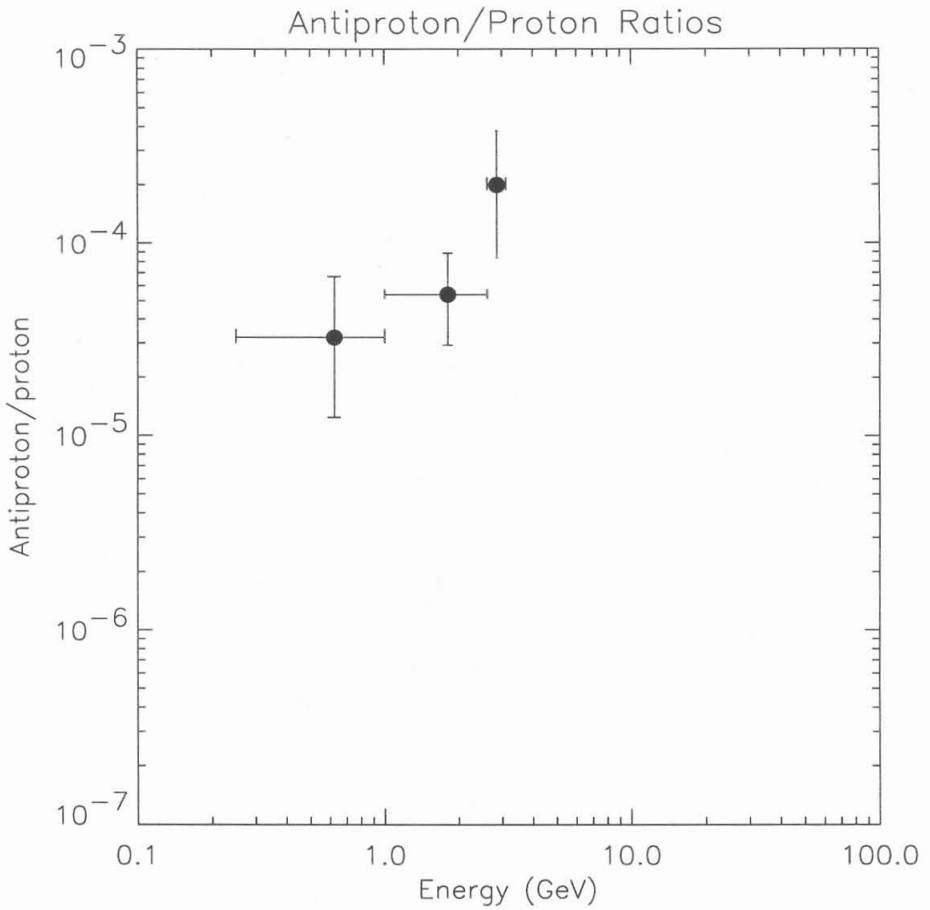

Figure 4.12: The IMAX antiproton/proton ratios at the top of the atmosphere.

Table 4.13: IMAX Antiproton/Proton Ratios at the Top of the Atmosphere

Energy (GeV), Top of the Atmosphere	Antiproton/Proton Ratio
0.25–1.00	$3.21\ (+3.49, -1.97) \times 10^{-5}$
1.00–~2.61	$5.38\ (+3.48, -2.45) \times 10^{-5}$
~2.61–~3.11	$2.05\ (+1.79, -1.15) \times 10^{-4}$

The total systematic uncertainties are 8%, 11%, and 15% for antiprotons and 5%, 5%, and 6% for protons, in these energy ranges. Both total uncertainties arise in part from the 5% systematic uncertainty adopted for the detection efficiency (Section 4.2.3), livetime, and telemetry. For antiprotons, there are additional systematic uncertainties of 30–45% arising from secondary atmospheric antiproton corrections, ~2% for annihilation corrections, and ≤2% for backscatter annihilation (Section 4.3.2). The uncertainty in the 0.5 false antiproton background in the Cherenkov–Rigidity range is set at ±0.5 (Section 3.7.1). For protons, the additional systematic uncertainties are ~30% in the secondary atmospheric proton corrections and ~1% for atmospheric and instrumental attenuation (Section 4.3.1). (These individual systematic uncertainties have been propagated through Equations 4.4.1 and 4.4.2 to derive the total systematic uncertainties.)

4.5 Antiproton Flux at the Top of the Atmosphere

As is demonstrated in Section 5.2.1, the measure of the antiproton flux at the top of the atmosphere is a better test of theoretical models for cosmic ray protons below ~3 GeV than is the antiproton/proton ratio. To calculate the antiproton flux at the top of the atmosphere, one must take into account the detection efficiency of the payload (Section 4.2.3), the payload geometry factor (Section 4.2.1), the livetime fraction (Section 4.2.2), and the exposure time of the payload (Section 2.8), in addition to the corrections for losses and background (Section 4.4). The resulting top of the atmosphere flux can be calculated according to the formula

$$J_{\bar{p}}(E) = \frac{\bar{p}_{TOA,raw}(E)}{[A\Omega(E)][f_{livetime} f_{telemetry} T][\Delta E][\varepsilon(E)]} \quad (4.5.1)$$

where $\bar{p}_{TOA,raw}(E)$ is the raw antiproton count corrected to the top of the atmosphere (Equation 4.4.2), $A\Omega$ is the energy–dependent geometry factor (Equation 4.2.1), T is the exposure time (14.78 hours; Section 2.9), $f_{livetime}$ is fractional livetime (Section 4.2.2), $f_{telemetry}$ is the telemetry efficiency (92.8%; Section 4.2.3), ΔE is the energy bin size, and ε is the energy–dependent detection efficiency (Section 4.2.3). Table 4.14 summarizes the calculation of the antiproton flux at the top of the atmosphere. The uncertainties in the intensity are statistical only (not systematic), derived from Equation 4.4.1. The antiproton fluxes are also shown in Figure 4.13. Comparison with theoretical models and a discussion of solar modulation effects will follow in Chapter 5.

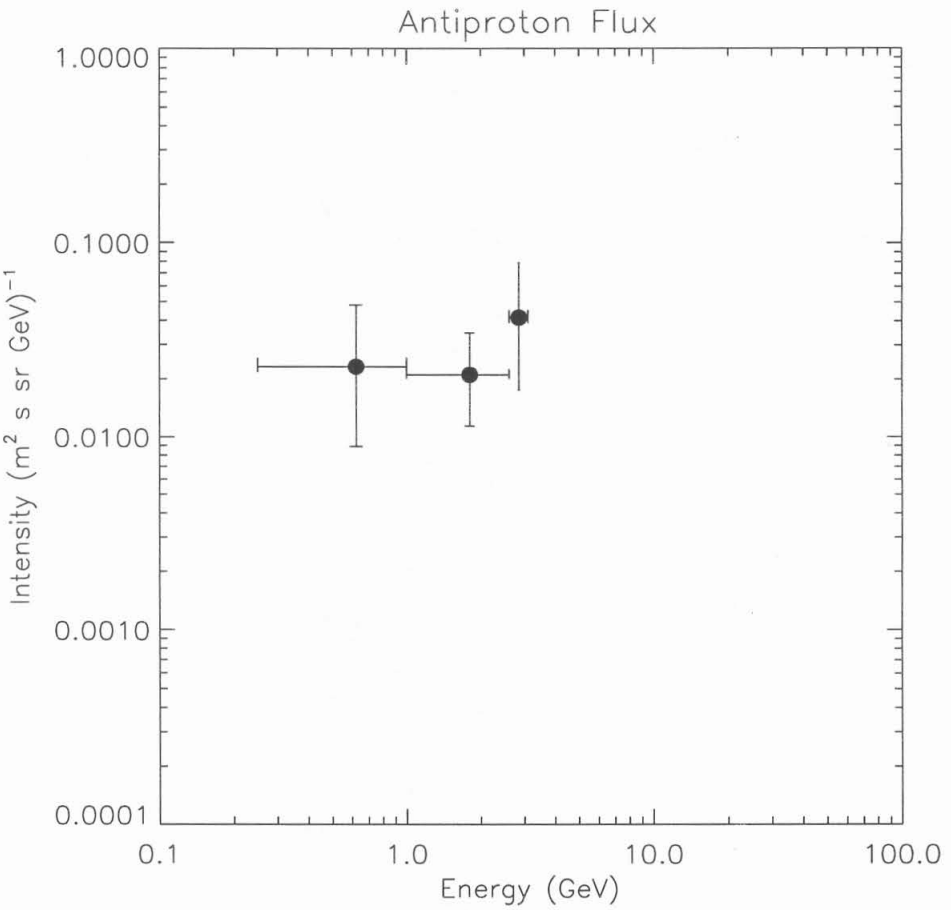

Figure 4.13: The IMAX antiproton fluxes at the top of the atmosphere.

Table 4.14: Calculation of IMAX Antiproton Flux at Top of the Atmosphere, for 14.78 hours of float time, with 74% livetime fraction and 92.8% telemetry efficiency. The exposure time is 14.78 hr x 0.74 x 0.928 = 36539 sec. (See Equation 4.5.1.)

Energy (GeV), TOA	Antiprotons, TOA	Ave. Acceptance $A\Omega$ (m^2 sr)	Energy bin size, ΔE (GeV)	Detection Efficiency, ε	Intensity (m^2 s sr GeV)$^{-1}$
0.25–1.00	4.5 (+4.9, -2.8)	0.0140	0.75	0.51	2.3 (+2.5, -1.4) x10^{-2}
1.00–2.61	9.2 (+5.9, -4.2)	0.0142	1.61	0.52	2.1 (+1.4, -1.0) x 10^{-2}
2.61–3.11	5.7 (+5.0, -3.2)	0.0142	0.50	0.51	4.3 (+3.7, -2.4) x 10^{-2}

5. Comparison with Theory and Discussion

The discussion in this chapter will focus on interpretation of the IMAX antiproton fluxes and antiproton/proton ratios at the top of the atmosphere. In order to compare measurements at the top of the atmosphere with theoretical models which generally predict the spectrum of antiprotons in the interstellar medium, and with the results of other experiments, the effects of solar modulation must be taken into account, particularly at low energies. These effects are further complicated by uncertainties in the interstellar cosmic ray proton and antiproton intensities. After solar modulation is taken into account, the antiproton fluxes and antiproton/proton ratios will be compared with recent calculations of the Standard Leaky Box Model, with implications drawn for galactic dark matter and the antiproton lifetime.

5.1 Selection of Theoretical Model for Comparison

Given its broad, general acceptance, the Standard Leaky Box Model (in its various calculations) will be the standard to which cosmic ray antiproton data will be compared in this analysis. (See Section 1.3.) A comparison of various Standard Leaky Box Model (SLBM) calculations for cosmic ray antiprotons bears some discussion, and although SLBM calculations were made prior to the actual detection of cosmic ray antiprotons (e.g. Gaisser and Maurer 1973), this discussion will be restricted to several calculations which were published after the Buffington et al. (1981) measurement. Three factors will be considered which have a strong influence on the evolution of the models: The assumed interstellar proton spectrum, the escape pathlength for cosmic ray interactions in the Galaxy, and the nuclear enhancement factor, ε. These three factors combine in Equation 1.1.8 to yield the antiproton production spectrum:

$$\frac{dN_{\bar{p}}}{dE} = 2\frac{\langle\lambda\rangle}{m_p}\varepsilon \int_{E_{threshold}}^{\infty} \frac{d\sigma_{pp\rightarrow\bar{p}}}{dE}\frac{dN_p}{dE_p}dE_p \qquad (1.1.8)$$

The antiproton production cross sections are less uncertain than the other factors because of the abundance of accelerator data. (See Section 1.1 for an explanation of this expression.)

The interstellar proton flux is characterized primarily by spectral index and by normalization, and measured spectral indices vary from ~2.65 to ~2.75 at ~10 to ~100 GeV (see Gaisser and Schaefer 1992). Of the available proton spectrum measurements, the highest fluxes (Webber, Golden, and Stephens 1987) and lowest (Seo et al. 1991) vary by as much as a factor of ~2 at energies above 10 GeV, where antiproton production occurs. The calculations of the antiproton spectrum by Gaisser and Schaefer (1992) make use of both of these spectra, to provide upper and lower limits.

Note that the purpose of the Gaisser and Schaefer (1992) calculation was to investigate uncertainties in the SLBM in order to yield extreme outer limits for the theoretical interstellar antiproton flux and antiproton/proton ratio at high energies. (See Figures 1.3, 1.4, and 1.6.) Because the focus is on high energy antiprotons (energy greater than 2 GeV), their calculation neglects the effects of inelastic scattering, which is important below 1 GeV. When the various uncertainties are combined in the calculation of the interstellar antiproton spectra, they find that the antiproton fluxes may be uncertain by as much as a factor of five (or more than a factor of two from the geometric mean). When their calculations are restricted to the best–known or best understood input parameters, the actual uncertainties will be smaller. For example, Webber (private communication, 1995) has suggested that errors in the calculation of instrument detection efficiency have caused the proton fluxes reported by Seo et al. (1991) to be low, particularly at energies above 10 GeV. If the Seo et al. (1991) proton fluxes are neglected, then estimated uncertainties in proton fluxes used by Gaisser and Schaefer (1992) can be reduced by about one third, with the proton spectrum lower bound raised accordingly.

Note that while most proton spectra employed by recent antiproton SLBM calculations (e.g. Protheroe 1981; Stephens 1981; Stephens and Golden 1987) lie close to the median of the Gaisser and Schaefer (1992) outer limits, the Webber and Potgieter (1989) calculation makes use

of the highest available proton spectrum measurements (Webber, Golden, and Stephens 1987), so that all other factors being equal, we may expect the Webber and Potgieter theoretical antiproton flux to be higher as well. The other factors also contribute to higher fluxes from the Webber and Potgieter calculation, as will be discussed below. Hereinafter, Webber and Potgieter (1989) will be referred to as W&P, and Gaisser and Schaefer (1992) will be referred to as G&S.

With better boron production cross section measurements and cosmic ray B/C ratio measurements than previously available (e.g. Gupta and Webber 1989), W&P estimate a greater cosmic ray escape pathlength than previously estimated. (See Equation 1.1.7 for the W&P pathlength.) Protheroe (1981) used a constant pathlength of 7 g/cm^2 up to 4 GV, decreasing with a spectral index of -0.4 above 4 GV, and Stephens (1981) and Stephens and Golden (1987) used constant pathlengths of 5 and 7.91 g/cm^2 respectively. Earlier estimates generally put the pathlength around 5 g/cm^2 (e.g. Gaisser and Maurer 1973). As with the proton fluxes, G&S employ rigidity–dependent bounds for the escape pathlength, derived by Garcia–Muñoz et al. (1987) and showing a maximal systematic uncertainty of ±35% (Figure 1.4; see also Engelmann et al. 1990, Heinbach and Simon 1990). For energies above 3 GV, the W&P pathlength lies near the median of the G&S outer limits. The higher proton fluxes and the increased pathlength results in more interactions of high energy protons with the interstellar medium, resulting in greater antiproton production.

Another contribution to the higher W&P antiproton fluxes is a higher nuclear enhancement factor, ε (Equation 1.1.8). Basic leaky box calculations of antiproton spectra take the primary cosmic rays and the interstellar medium to be protons, and the contributions of heavier nuclei — as target nuclei as well as primary cosmic rays — are included as a nuclear enhancement factor multiplying the proton contributions. The nuclear enhancement factor is influenced by several factors: the relative abundance of heavier nuclei in the interstellar medium, the relative abundance of heavier nuclei in primary cosmic rays, and the contributions of the various nucleons to antiproton production during collisions.

The W&P and G&S calculations also use two of the most widely divergent values for ε. W&P use ε=1.59, whereas G&S use ε=1.20. Other authors (e.g. Stephens and Golden 1987, Orth and Buffington 1976, and Szabelski et al. 1980) use ε=~1.25–~1.34. One of the primary differences between the nuclear enhancement factor of W&P and that of G&S is that the former use the relative abundances of heavy cosmic rays obtained by Lund (1984), whereas the latter use the relative abundances from the review by Simpson (1983) (and Webber, Golden, and Stephens 1987, for the helium abundance). These differences arise in large part because most experiments do not simultaneously measure cosmic ray abundances of $Z \leq 2$ elements and $Z > 2$ elements, so that normalization to hydrogen abundance is inherently uncertain.

The result is that the ε of W&P arises from a larger assumed relative abundance of heavy cosmic rays. Notably, the ratio of helium to hydrogen used by W&P is 0.05, whereas the ratio used by G&S is 0.042. Similarly, the ratio of C, N, and O to H used by W&P is 3×10^{-3}, and the ratio used by G&S is $\sim 2.5 \times 10^{-3}$. However, while G&S tabulate the relative abundances by element, W&P tabulate by charge groups, making more detailed comparison somewhat difficult. Nevertheless, none of the heavier nuclear cosmic rays contribute more than $\sim 3 \times 10^{-3}$ relative to hydrogen, and the relative abundances used by W&P are systematically higher than those used by G&S.

A more significant difference between the nuclear enhancement factors of the two papers is in their treatment of the nuclear multiplicity, which is directly related to the number of participating nucleons in the antiproton production interaction. W&P make use of the multiplicities calculated by Orth and Buffington (1976), who made Monte Carlo estimates of the number of nucleons participating in an antiproton production interaction as well as their contribution relative to pure proton–proton interactions. Parameters from their models were fit to nuclear emulsion data (e.g. Apparao et al. 1956). The difference between W&P's nuclear enhancement factor (1.59) and that of Orth and Buffington (1.34) can be attributed primarily to the difference between the relative abundances of heavy nuclei; W&P use more heavy nuclei (e.g. a helium to hydrogen ratio of 0.05, compared to a ratio of 0.039).

On the other hand, the difference between the results of Orth and Buffington (1976) and G&S can be attributed to the relative contribution of participating nucleons. G&S assume that each participating ("wounded") nucleon in an antiproton production interaction contributes half the yield of a pure proton–proton interaction (e.g. each proton in a proton–proton interaction contributes half). The wounded nucleon model employed by G&S is by Bialas et al. (1976). Orth and Buffington assume that each participating nucleon contributes four–fifths that of a proton in a proton–proton interaction. This and the differences in relative nuclear abundances are the primary differences between the Orth and Buffington and G&S multiplicities.

However, because their multiplicity calculations are significantly dissimilar, it is difficult to determine which is the more accurate calculation. It is unclear how the Orth and Buffington multiplicities are normalized to pure proton–proton interactions; clearly, each proton in the interaction will contribute half of the interaction. The "wounded nucleon" model (Bialas et al. 1976) has been shown to predict pion and kaon production multiplicities in proton–nucleus and helium–helium interactions (e.g. Brick et al. 1989, and Faessler 1984), and it has recently been shown to be in good agreement with very high energy (200 GeV) nucleus–nucleus and nucleon–nucleus interactions which produce antiprotons (Kadija et al. 1996). Thus, given its agreement with recent accelerator data vs. Orth and Buffington's use of older nuclear emulsion data, it is reasonable to assume that the wounded nucleon model is probably more correct in application to antiproton production.

In light of the preceding discussion, future calculations of the SLBM might include the "wounded nucleon" model implemented by G&S and the pathlengths and cosmic ray elemental abundances used by W&P. For the following solar modulation calculations, we may consider the interstellar proton and antiproton spectra by W&P and G&S. However, because G&S focus on high energies and neglect inelastic scattering (which strongly affects low energy spectra), and because G&S do not provide proton spectrum bounds below 7 GeV, their spectra are less applicable to the discussion of solar modulation in Section 5.2 and to comparison with our IMAX data. Thus, to investigate the effects of solar modulation we use as a reference the recent

interstellar antiproton spectrum by W&P (Webber and Potgieter 1989). For consistency, we also use the interstellar proton spectrum from W&P.

5.2 Solar Modulation

Cosmic ray antiproton investigations have traditionally expressed their results in terms of the antiproton/proton ratio, which is somewhat easier to obtain than proton and antiproton flux measurements. In order to compare the IMAX results with theoretical predictions at 1 AU, one must take into account the effects of solar modulation on both the primary proton spectrum and the secondary antiproton spectrum. Although previously published antiproton measurements (with the exception of the work by Golden et al. 1984 and Hof et al. 1995) have been at energies below ~5 GeV/nuc, most reports prior to this analysis have not taken solar modulation effects into account in a systematic fashion.

The effects of solar modulation may be calculated using the standard spherically symmetric approach of Fisk (1971), including the effects of diffusion, convection, and adiabatic deceleration. In this calculation, the propagation of cosmic rays into the solar system is described by the Fokker–Planck equation:

$$\frac{1}{r}\frac{\partial}{\partial r}\left(r^2 VU\right) - \frac{1}{3}\left[\frac{1}{r^2}\frac{\partial}{\partial r}\left(r^2 V\right)\right]\left[\frac{\partial}{\partial T}(\alpha TU)\right] - \frac{1}{r^2}\frac{\partial}{\partial r}\left(r^2 \kappa \frac{\partial U}{\partial r}\right) = 0 \qquad (5.2.1)$$

where U is the cosmic ray density, V is the solar wind velocity, T is kinetic energy, and r is radial distance from the Sun. A velocity V of 400 km/sec is adopted for this calculation, and the diffusion coefficient takes the form

$$\kappa = k\beta R \qquad (5.2.2)$$

where k is a constant (i.e. independent of radius), and R is rigidity. The diffusion coefficient multiplier constant (or the "radial part of the diffusion coefficient"), k, may be used to

calculate the modulation strength parameter of Gleeson and Axford (1968):

$$\phi = \frac{1}{3}\int_{r=1AU}^{D} \frac{V(r)}{\kappa(r)}dr = \frac{V(D-1)}{3k} \tag{5.2.3}$$

where the "modulation boundary", D, is taken to be 100 AU. Given that the constant k may be varied to give the desired modulation strength ϕ for any value of D ($\neq$1), the exact value of D is unimportant for the purpose of this analysis.

5.2.1 Solar Modulation of Protons and Antiprotons

To obtain estimates of proton and antiproton fluxes at 1 AU for comparison with IMAX data, we modulate the W&P interstellar spectra. The strength of solar modulation is adjusted to fit proton fluxes measured at 1 AU for 1992 (the year of the IMAX flight) as well as in a series of reference years (1979, 1980, 1985, 1986, 1987, 1991, and 1993), when other antiproton observations are available. (See Table 5.1.) To include the widest range of solar modulation, this analysis also includes the years of minimum and maximum modulation (1977 and 1990) over the past three solar cycles. The proton spectra were modulated to coincide with IMP–8 proton flux measurements at 131–230 MeV (McGuire et al. 1995), which are available in the form of 26 day averages from November 1973 to the present. While corresponding proton spectrum measurements over a broader energy interval are generally unavailable for all of the antiproton measurements to date, the IMP–8 data are consistent with other proton flux measurements at various times in the solar cycle (e.g. Evenson et al. 1983 and 1985). Therefore, this calculation takes the IMP–8 measurements at the time of the various antiproton measurements as reference proton measurements. Finally, we ignore the effects of drifts (e.g., Kóta and Jokipii 1983, Burger and Potgieter 1989, and W&P), thereby obtaining a lower limit to possible solar cycle effects on the antiproton/proton ratio. Thus, we modulate the antiproton spectra with the same modulation parameters used for protons for the reference years.

Figures 5.1 and 5.2 illustrate the effects of solar modulation on two artificially

constructed interstellar spectra. The figures (modeled after similar figures from Goldstein, Fisk, and Ramaty 1970) show Gaussian "interstellar" proton and antiproton fluxes centered at 0.1, 0.2, 0.5, 1, 2, 5, 10, 20, and 50 GeV. The amplitudes of the peaks correspond to the proton and antiproton fluxes calculated by Webber and Potgieter for these energies. Also shown (dashed lines) are the same fluxes modulated to 1 AU with a modulation parameter ϕ=750 MV, which corresponds to an intermediate level of modulation. As can be seen in the figures, the effect of modulation is not only to reduce the amplitude of the peaks and spread them out in energy but also to shift fluxes lower in energy, through adiabatic energy loss. The resulting flux at 1 AU is dependent both on the strength of the modulation as well as the interstellar spectrum.

Note that this approach differs from that of Perko (1992), who obtains modulation parameters for protons and antiprotons (electrons) separately, and then "demodulates" the 1 AU measurements via the force field approximation and presents results for the local interstellar medium. The present results have the advantage that they are directly comparable to available measurements. Furthermore, the demodulation process assumes a one–to–one correspondence between points on the modulated flux curve and the interstellar flux curve which is not borne out by calculations such as those given in Figures 5.1 and 5.2. From Figure 5.1, where the amplitudes of the peaks correspond to the Webber and Potgieter interstellar proton flux, the modulated flux level at ~0.2 GeV has roughly equal contributions from the interstellar 0.5 and 1 GeV peaks and negligible contribution from 0.2 GeV itself. However, the modulated antiproton spectra in Figure 5.2 show a significantly different mix of contributions at ~0.2 GeV. It is clear from these figures that one cannot reliably "demodulate" low energy measurements of the antiproton/proton ratio. This conclusion was known as early as 1970 (e.g. Gleeson and Urch 1970).

Table 5.1: Dates of Antiproton Observations and Modulation Parameters Used in This Analysis

References	Date of Flight	ϕ, MV
IMAX (this analysis)	July 16, 1992	726
Golden et al. 1984	June 21–22, 1979	613
Bogomolov et al. 1987	1984–1985	673
Bogomolov et al. 1990	1986-1988	540
Buffington et al. 1981	June 18, 1980	770
Salamon et al. 1990	August 13, 1987	493
Moats et al. 1990, Stochaj 1990	August 21, 1987	493
Hof et al. 1995	September 1991	981
Yoshimura et al. 1995	July 26, 1993	565

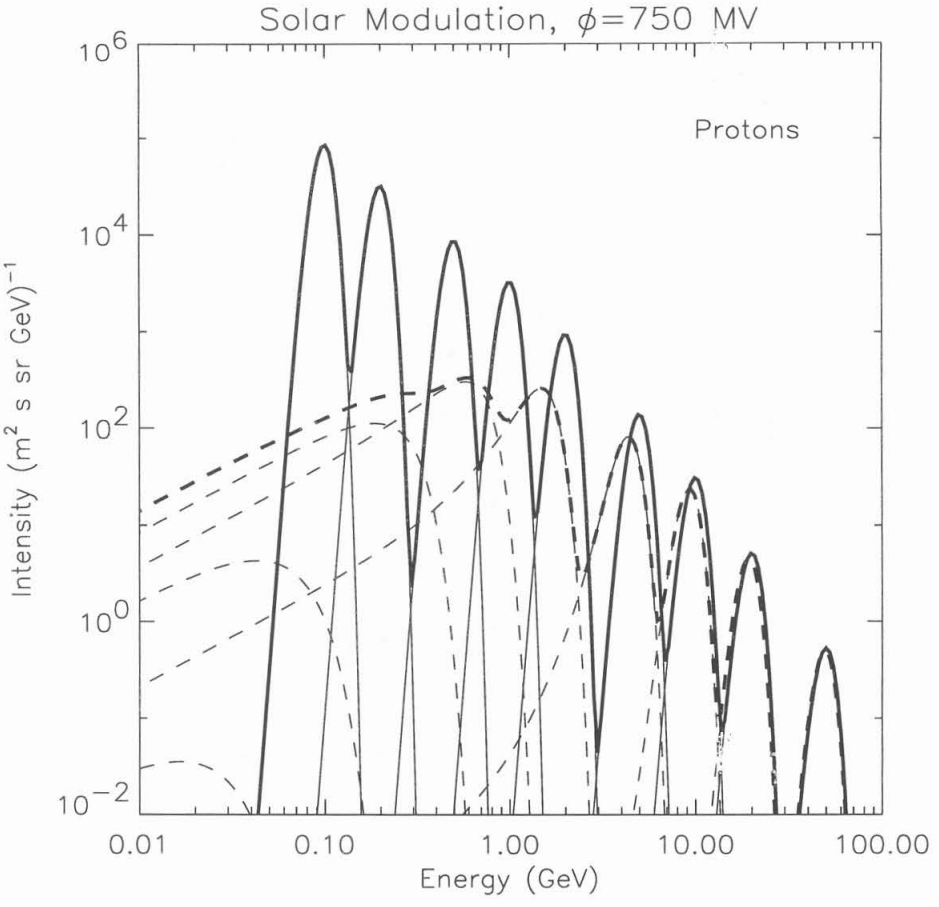

Figure 5.1: Gaussian "interstellar" proton fluxes at 0.1, 0.2, 0.5, 1, 2, 5, 10, 20, and 50 GeV, modulated to 1 AU with a modulation strength of 750 MV. The peak amplitudes correspond to proton fluxes adopted by W&P for the interstellar medium.

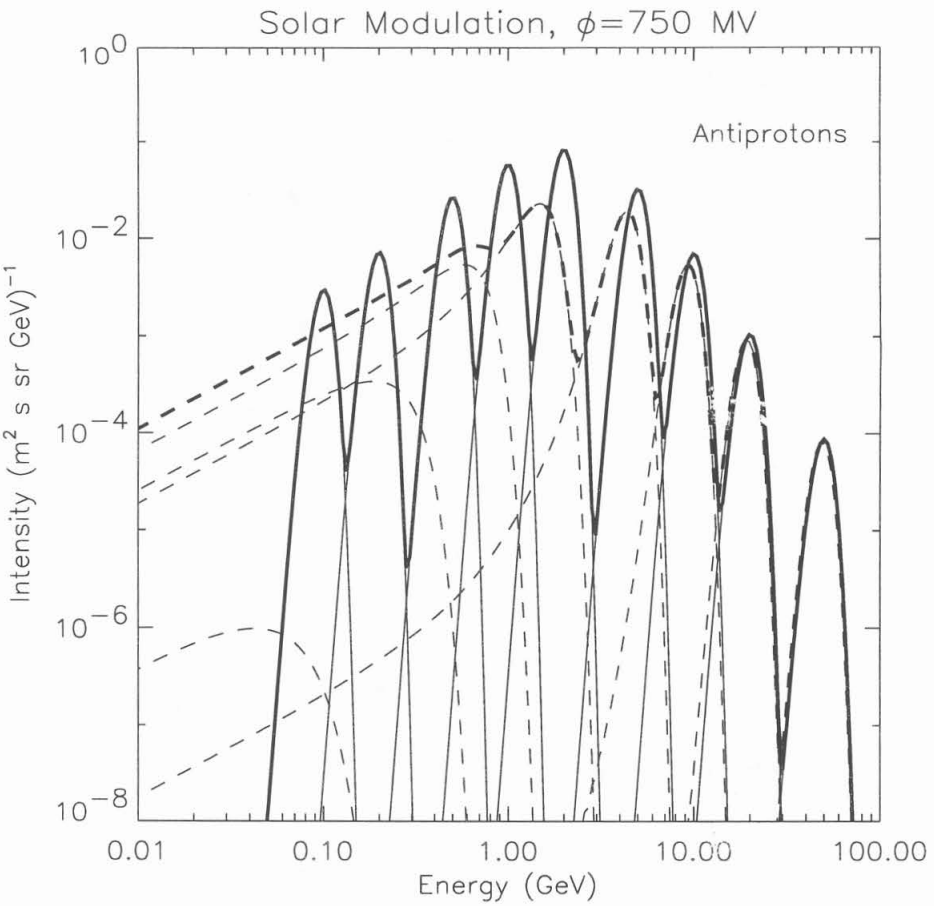

Figure 5.2: Gaussian "interstellar" antiproton fluxes at 0.1, 0.2, 0.5, 1, 2, 5, 10, 20, and 50 GeV, modulated to 1 AU with a modulation strength of 750 MV. The peak amplitudes correspond to interstellar antiproton fluxes calculated by W&P for a leaky box model.

Figure 5.3 shows modulated proton spectra for the case of near solar minimum (top, 1987), near solar maximum (bottom, 1991), and intermediate levels of modulation, with the 1992 (IMAX flight year) shown in bold. Note that for each interstellar proton spectrum it is possible to obtain a reasonable fit to the measured intensity levels over the solar cycle simply by varying the magnitude of the diffusion coefficient. Although it is possible that the rigidity dependence of the diffusion coefficient also varies over the solar cycle and that the diffusion coefficient varies with radius in the heliosphere (e.g. Palmer 1982, Bieber et al. 1994), such possibilities are neglected in favor of the simplest possible solar cycle variations in order to illustrate their effect.

Figure 5.4 shows the modulated antiproton spectra at 1 AU for these same cases. Again, the curve appropriate for comparison with IMAX data is shown in bold. Antiprotons observed at 1 AU with energies ≤1 GeV are primarily the result of adiabatic deceleration of higher energy antiprotons. (See Figure 5.2). As a result, the low energy antiproton flux varies much less over the solar cycle than does the flux of low energy protons (Figure 5.3), because most of the antiprotons originate in the interstellar medium at ~1–2 GeV, where the effects of solar modulation are much less.

Figure 5.5 shows the resulting antiproton/proton ratio, with the 1992 curve for comparison with IMAX shown in bold. Note that the ratio at several hundred MeV varies by almost one order of magnitude over the solar cycle. Inspection of Figures 3 and 4 indicates that these variations in the antiproton/proton ratio are due mainly to variations in the 1 AU proton flux rather than to variations in the antiproton flux. Figure 5.6 shows the proton flux at 131–230 MeV as measured by IMP–8 (McGuire et al. 1995) between 1973 and 1995 as well as the estimated antiproton flux at roughly the same energy. From these solar modulation calculations, it is apparent that, while the low energy proton flux can vary by as much as one order of magnitude over the solar cycle, the low energy antiproton flux varies by less than a factor of 2. Therefore, it should be more useful to compare low energy antiproton measurements

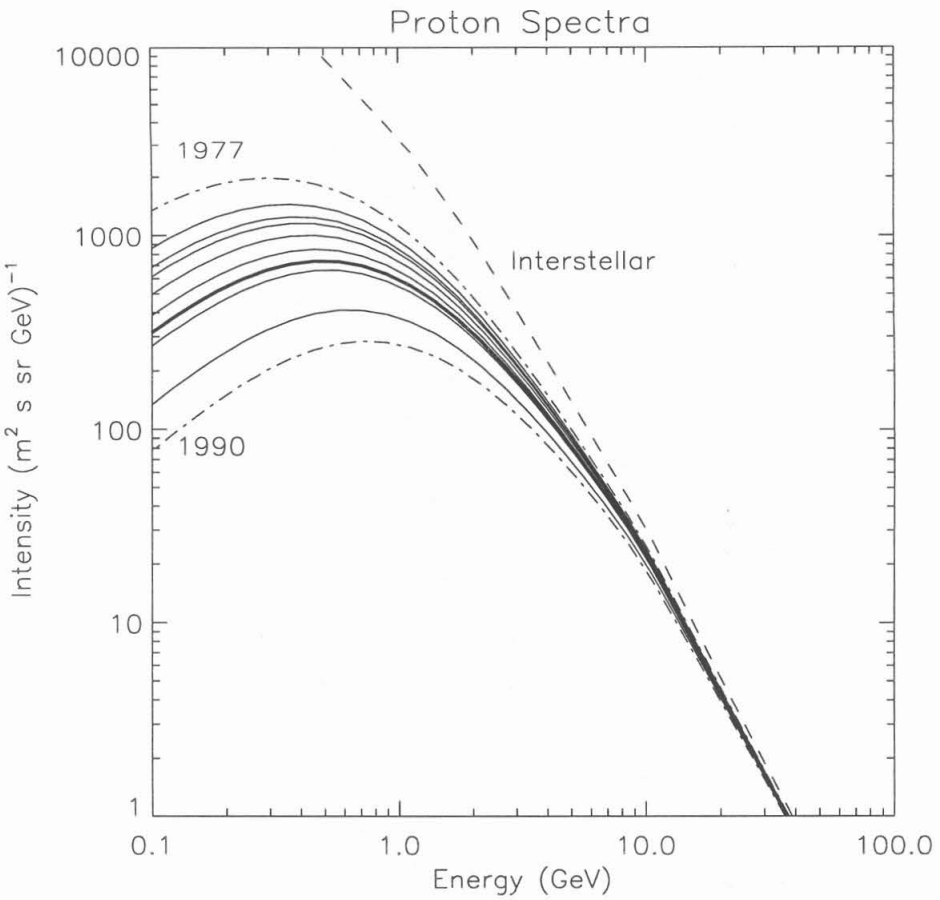

Figure 5.3: The interstellar proton spectrum of W&P, modulated to agree with measured proton flux levels at 1 AU for years when cosmic ray antiproton measurements are available. The reference years are (solid lines, from top to bottom) 1987, 1986, 1993, 1979, 1985, 1992, 1980, and 1991. The 1992 flux is highlighted in bold for comparison with IMAX data. The dotted–dashed lines represent the 1977 solar minimum and 1990 solar maximum fluxes.

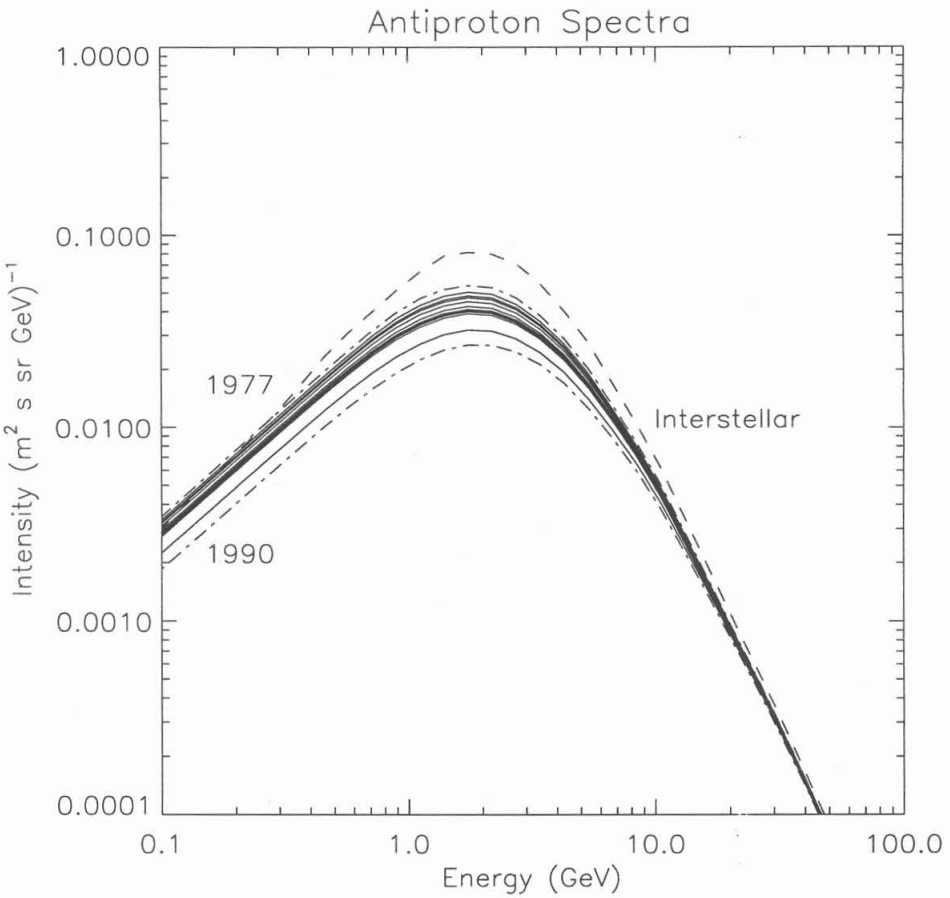

Figure 5.4: The interstellar antiproton flux of W&P, modulated with the same parameters used for the spectra in Figure 5.3, to produce expected spectra at 1 AU for the same years (1987, 1986, 1993, 1979, 1985, 1992, 1980, and 1991, solid lines from top to bottom). The 1992 flux is highlighted in bold for comparison with IMAX data. The dotted–dashed lines represent the 1977 solar minimum and 1990 solar maximum fluxes.

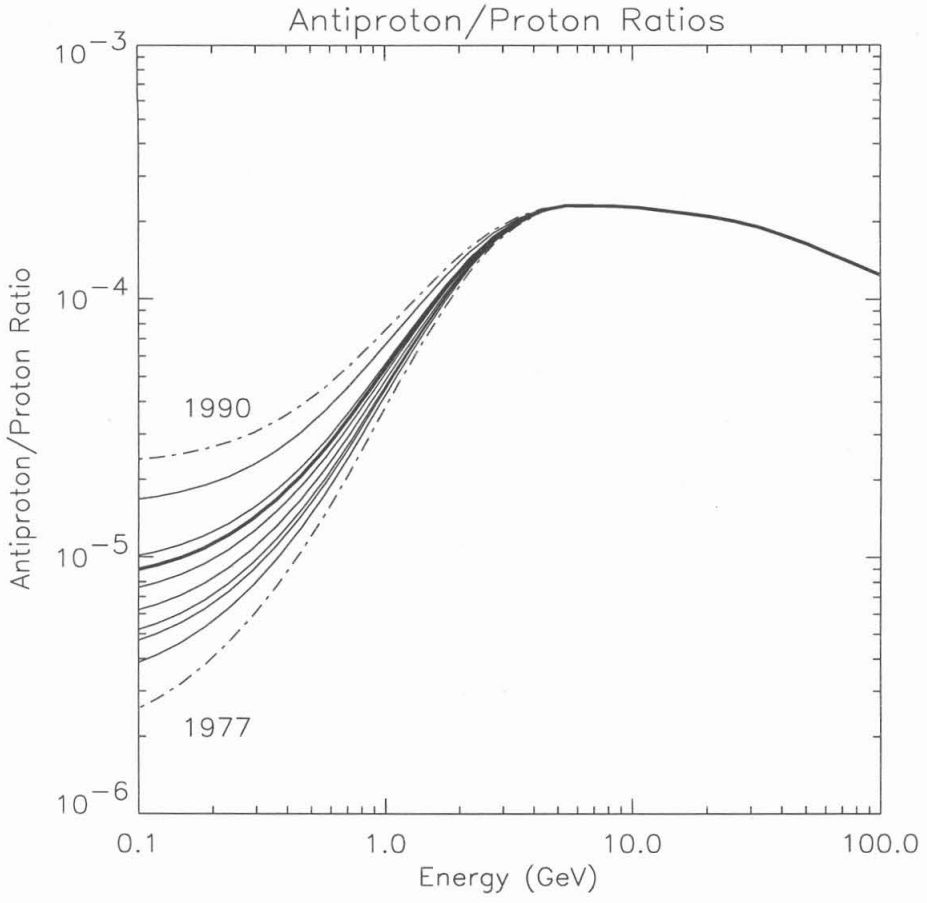

Figure 5.5: The antiproton/proton ratio at 1 AU, derived from the modulated spectra in Figures 5.3 and 5.4 for the years 1987, 1986, 1993, 1979, 1985, 1992, 1980, and 1991 (solid lines, from bottom to top). The 1992 flux is highlighted in bold for comparison with IMAX data. The dotted–dashed lines represent the 1977 solar minimum and 1990 solar maximum ratios.

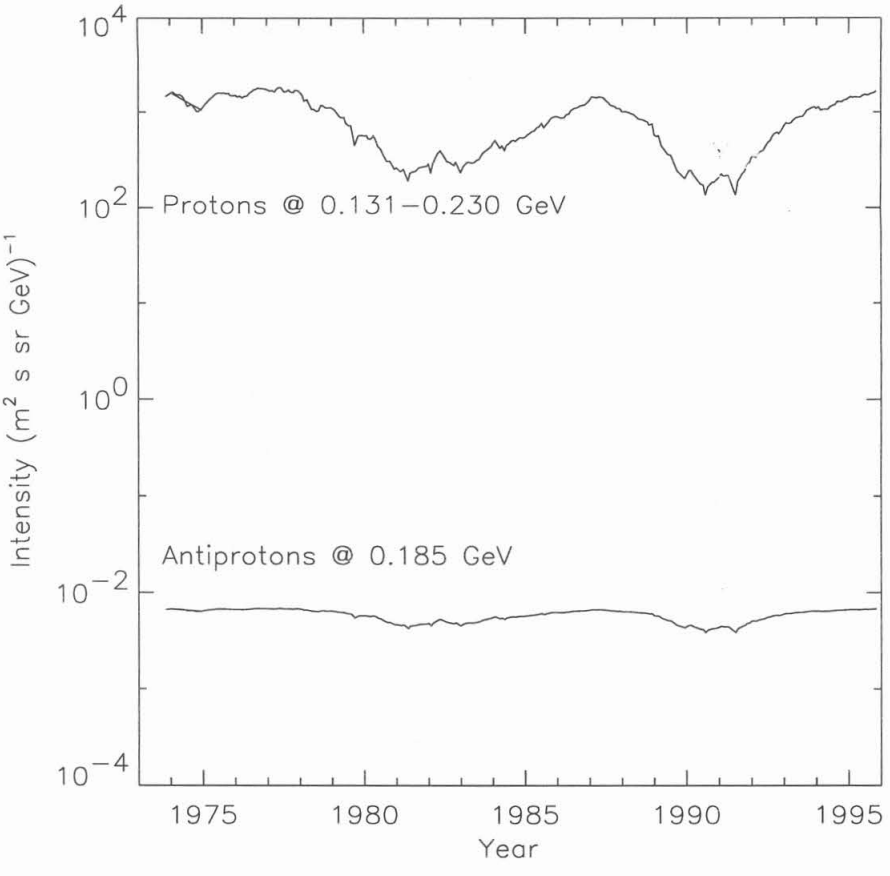

Figure 5.6: Proton fluxes measured by IMP–8 (McGuire et al. 1995) at 131–230 MeV/nuc from 1973 to 1995. The antiproton flux at 0.185 GeV is calculated by modulating the W&P interstellar antiproton flux, using the same modulation parameters which fit the low energy proton measurements.

to the expected antiproton spectrum rather than to the antiproton/proton ratio which has traditionally been considered.

If cosmic ray antiprotons are of "secondary" origin, produced by interactions of "primary" protons with the interstellar medium, they are daughters of cosmic rays with energies > 6 GeV/nuc. Note in Figure 5.5 that the expected antiproton/proton ratio at energies >~3 GeV is very insensitive to the effects of solar modulation, and it is therefore a useful diagnostic of cosmic ray transport in the Galaxy. However, at lower energies (e.g., <1 GeV), the expected antiproton/proton ratio is much more uncertain because of solar cycle variations and uncertainties in the interstellar spectra. With few exceptions, most discussions of the antiproton/proton ratio have not taken these uncertainties into account.

In addition to the effects of solar modulation, there are also additional uncertainties in the interstellar spectra. For example, the assumed interstellar spectra adopted by G&S differ from those of W&P. However, because the G&S calculation concentrates on the high energy antiproton flux and antiproton/proton ratio, effects such as inelastic scattering during propagation are explicitly neglected. The result is that their low energy interstellar antiproton spectrum has a steeper slope below 2 GeV and underestimates the antiproton flux from 0.1 to 1 GeV. As a result, their antiproton flux is more sensitive to adiabatic energy loss, and the resulting antiproton/proton ratios varies more over the solar cycle than those based on the Webber and Potgieter curves. However, because the Webber and Potgieter calculations include inelastic scattering, the results of solar modulation on the Webber and Potgieter curves are probably more correct at low energies.

The effect of uncertainties in the low energy interstellar proton spectrum can be demonstrated by a slight modification of the Webber and Potgieter proton flux: We may extend their proton flux to low energies with the same spectral index as at energies above 5 GeV, in effect eliminating much of the low–rigidity turnover. The result is a higher interstellar proton flux at low energies, which requires more solar modulation to match the observations. Because antiprotons are produced by cosmic rays with energies above ~6 GeV/nuc, the Webber and

Potgieter interstellar antiproton flux remains unchanged. The solar modulation calculations are repeated, with smaller diffusion coefficients needed to fit the interstellar proton fluxes to the IMP–8 data. Figures 5.7 and 5.8 show the modified and original 1992 proton and antiproton fluxes for possible comparison with IMAX data, using the modified Webber and Potgieter interstellar proton fluxes. The Figures also show the new solar minimum and solar maximum proton and antiproton spectra. Figure 5.9 shows that the new antiproton/proton ratios give slightly lower variation over the solar cycle, as well as lower overall ratios in comparison to the previous calculation.

It should be pointed out that these calculations of the effects of solar modulation do not include the effects of gradient and curvature drifts in the large scale interplanetary magnetic field, which may lead to solar–cycle dependent differences in the relative modulation of positively and negatively charged particles with the same rigidity. To incorporate these effects would require a more sophisticated solar modulation code than is generally available (e.g., Kóta and Jokipii 1983). During even-numbered solar cycles (e.g., the 1970's and 1990's) positive particles drift from the poles of the heliosphere towards the equator and then out along the current sheet, while during the odd-numbered solar cycles the direction of drift is reversed. Negative particles always drift in the opposite direction as positively charged particles. The result is a 22-year solar modulation cycle. For observations made in the ecliptic plane, we might expect low-energy protons to be favored during the 1970's and 1990's, with antiprotons favored during the 1980's.

While there is some evidence for charge–sign dependent effects on the modulation of electrons and He of the same rigidity (Evenson et al. 1995), the magnitude of such effects is not well established experimentally. W&P have estimated that drift effects might vary the antiproton/proton ratio by as much as a factor of 2 at 200 MeV, depending on the tilt of the current sheets, but the magnitude of these effects is very model–dependent. In any case, the variations shown in this calculation should be regarded as a lower limit to the effects that

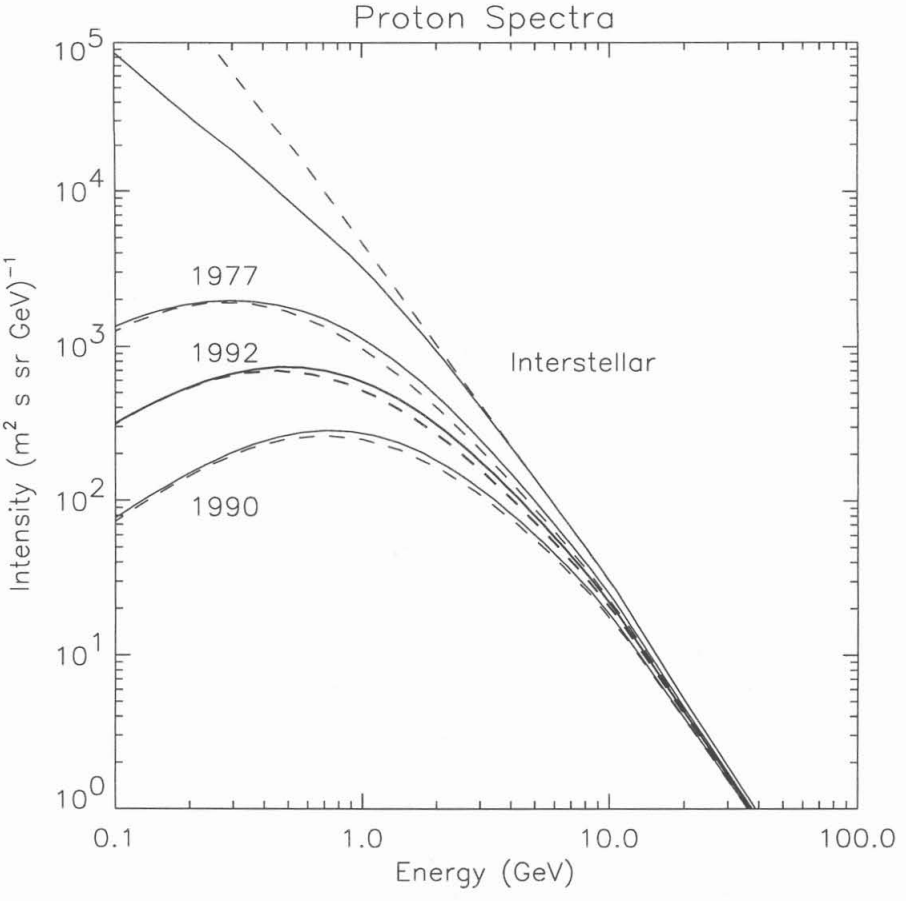

Figure 5.7: Illustration of the effects of solar modulation on a modified interstellar proton spectrum that includes additional low energy flux. The solid lines are the original W&P interstellar flux and modulated curves from Figure 5.3, and the dashed lines are the modified flux curves. The 1992 calculation appropriate for comparison with IMAX data is shown as bold solid and dashed lines. Results are also shown for the 1977 solar minimum and 1990 solar maximum.

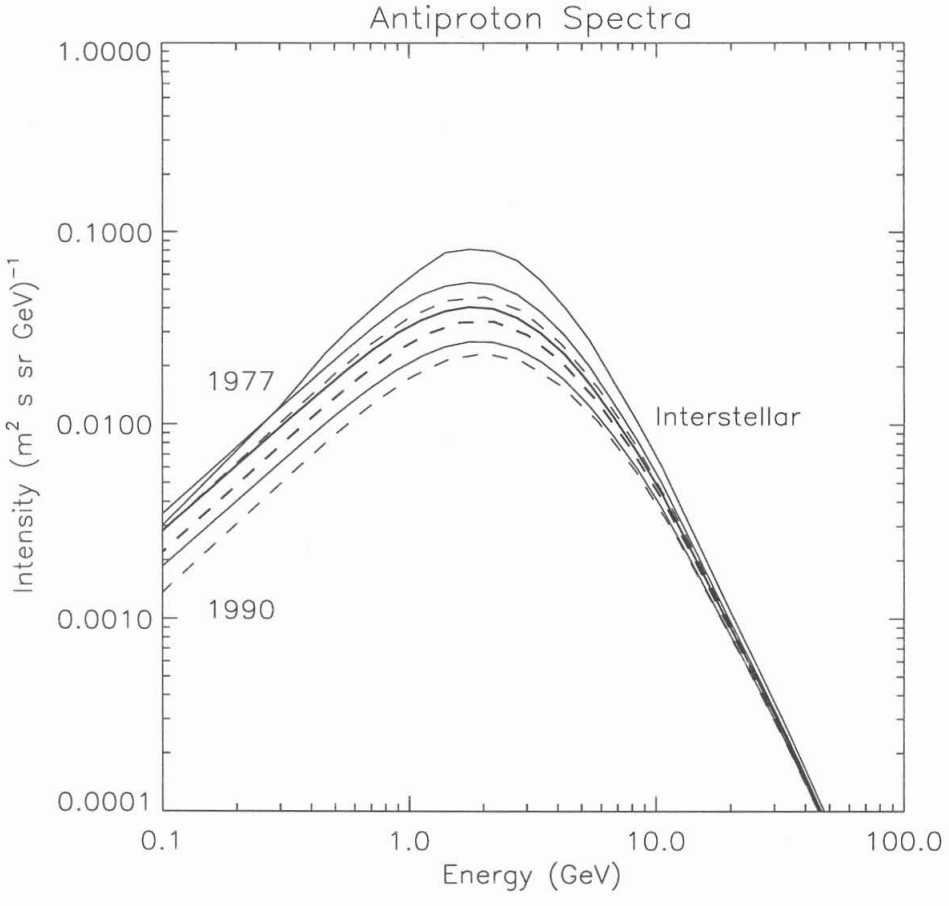

Figure 5.8: The interstellar antiproton flux of W&P, modulated with the same parameters employed for Figure 5.7 (dashed lines). The 1992 calculation appropriate for comparison with IMAX data is shown as bold solid and dashed lines. The solid lines are the original W&P interstellar flux and the modulated curves from Figure 5.4.

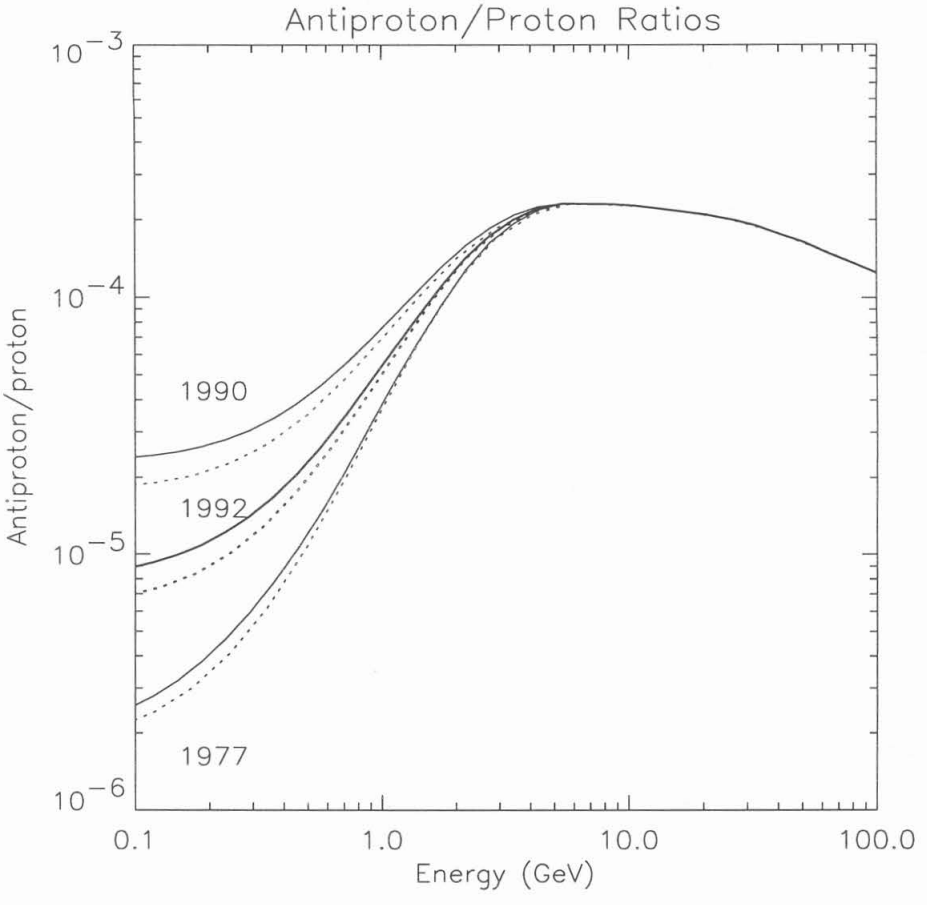

Figure 5.9: Illustration of the effect of uncertainties in the low energy interstellar proton spectrum on the antiproton/proton ratio at 1 AU. The solid curves are from Figure 5.5 for the nominal W&P interstellar spectra. The dashed curves are the ratios calculated from the modified fluxes of Figures 5.8 and 5.9. The 1992 calculation appropriate for comparison with IMAX data is shown as bold solid and dashed lines.

solar modulation processes can have on the antiproton/proton ratio over the course of the solar cycle.

5.3 Comparison with Leaky Box Models

Figure 5.10 gives the IMAX antiproton/proton ratios, along with the modulated 1992 curve based on the W&P interstellar proton and antiproton fluxes, and Figure 5.11 compares the IMAX antiproton flux measurements with the modulated 1992 W&P antiproton spectrum. From the Figures, one may see that the IMAX data compare well with the theoretical prediction based on the W&P spectra. If we divide the measured ratios with the ratios predicted by theory and average over the three IMAX measurements, we get a weighted average of the measured–to–predicted ratio of 0.64(+0.31,-0.21), implying consistency with the W&P prediction. (An exact agreement would put the measured–to–predicted ratio at 1.00.) If we calculate the weighted average in logarithm–space — in order to calculate weights by relative uncertainties rather than absolute uncertainties — the average becomes 0.76(+0.31,-0.27). Finally, if we calculate the ratio of the IMAX fluxes to the modulated 1992 W&P antiproton spectrum, we get a weighted average of 0.67(+0.33,-0.23) (or 0.83(+0.31,-0.27) in logarithm–space). Thus, the IMAX antiproton/proton and antiproton flux data are consistent with the standard model in which cosmic ray antiprotons arise solely as the secondary products of high energy cosmic ray interactions with the interstellar medium.

Two additional cosmic ray antiproton measurements have recently been reported. The BESS experiment was a large area (acceptance=0.4 m^2sr) magnet spectrometer which reported four antiprotons in the energy range 300-500 MeV and an antiproton/proton ratio of $1.2(+1.0,-0.65)\times10^{-5}$ (Yoshimura et al. 1995). It used a combination of time–of-flight measurements and a JET chamber for tracking to identify particles by the TOF–Rigidity technique. This instrument is particularly important because it has had further flights from Lynn Lake in 1994 and 1995, although these results have not yet been reported. It is expected to fly again in the future with

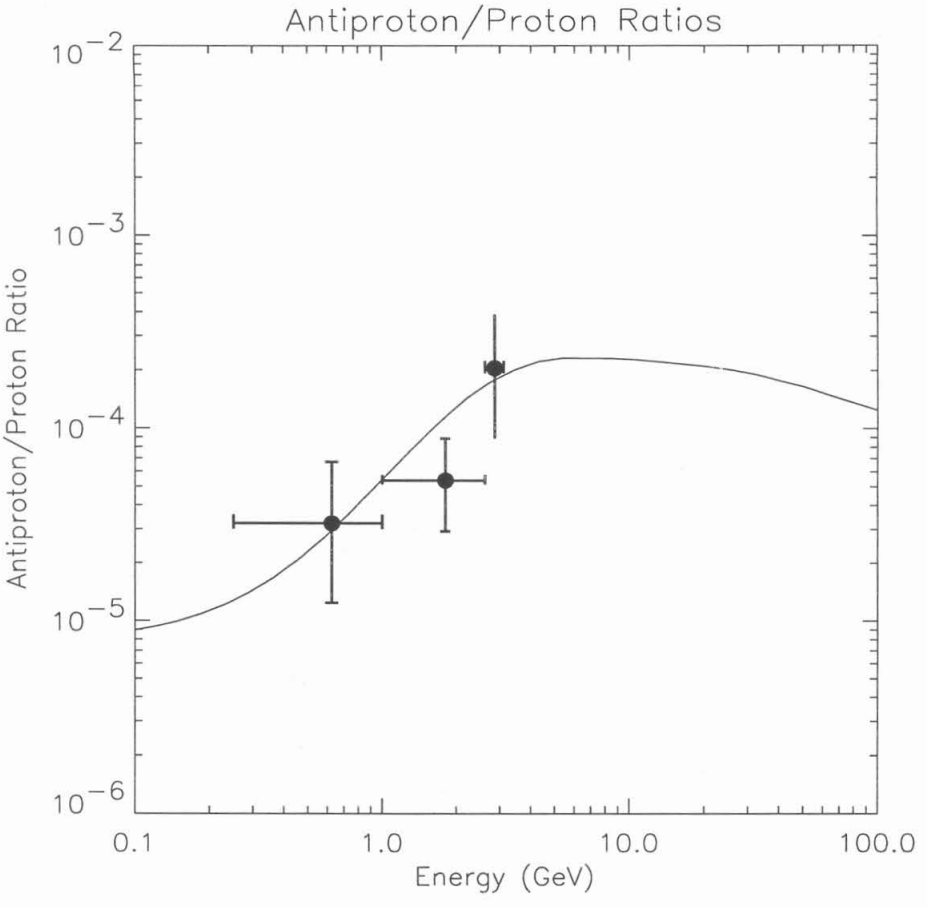

Figure 5.10: The IMAX antiproton/proton ratios, compared with the Webber and Potgieter (1989) antiproton/proton ratio modulated to 1992 levels. Calculations by Gaisser and Schaefer (1992) imply that the antiproton/proton ratio is uncertain by more than a factor of ~2 at high energies.

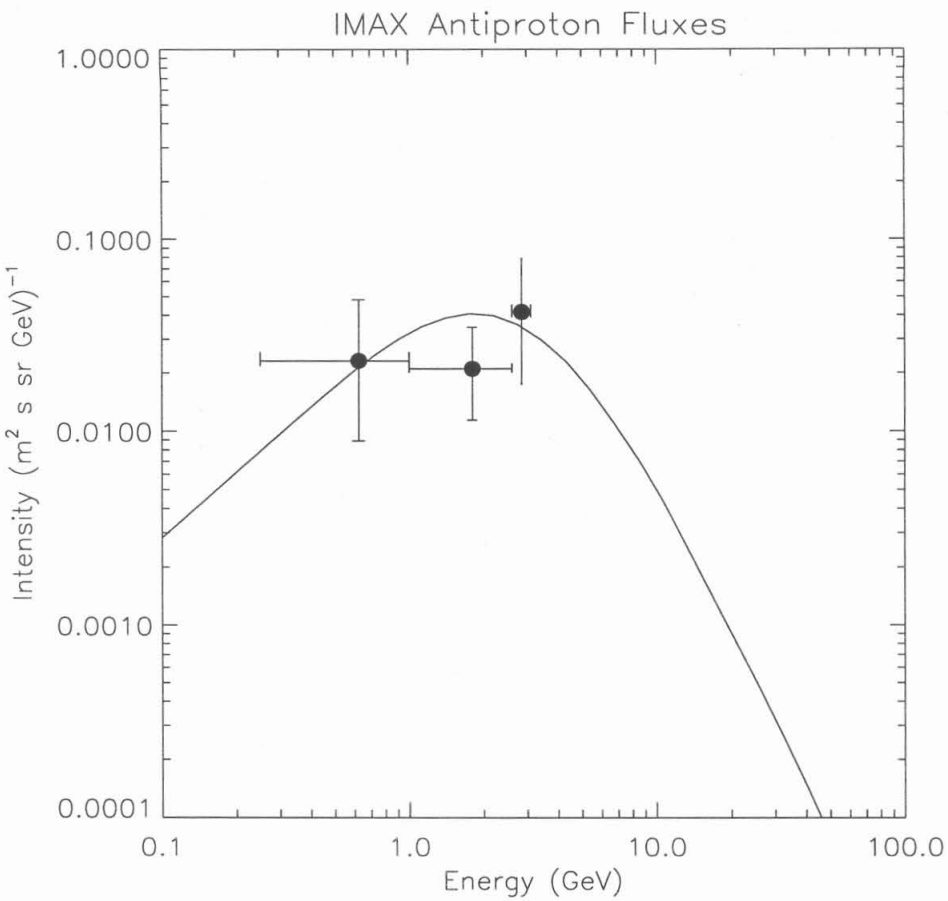

Figure 5.11: The IMAX antiproton fluxes, compared with the Webber and Potgieter (1989) antiproton flux modulated to 1992 levels. Calculations by Gaisser and Schaefer (1992) imply that the antiproton spectrum is uncertain by more than a factor of ~2 at high energies.

increased energy range. The BESS measurement is shown in Figure 5.12, along with other measurements.

The recent MASS2 experiment (also called MASS91) was based on the BBMF framework used by Golden et al. (1984), with the addition of drift chambers from the University of Siegen for much–improved rigidity resolution. They recently reported detecting 9 antiprotons in the energy range 4–19 GeV, with an antiproton/proton ratio of $1.52\pm0.52\times10^{-4}$ (Hof et al. 1995). The understanding of instrument efficiencies has also been refined since the Golden et al. (1984) measurement. This experiment is particularly important because it is the only experiment to date to repeat measurements in the same energy range as the original Golden et al. (1979, 1984) measurement. The much lower antiproton/proton measurement can be attributed to improvements in the detector technology as well as to improved understanding of instrumental and atmospheric background (Hof et al. 1995). The MASS2 measurement is shown in Figure 5.12.[1]

Figure 5.13 show the ratio of measured antiproton/proton ratios to the antiproton/proton ratios predicted by W&P and modulated for the years of the measurements. If we average the recent Hof et al. (1995) and Yoshimura et al. (1995) measured–to–predicted ratios for 1991 and 1993 with the IMAX ratios, the resulting measured–to–predicted ratio for these three most recent measurements is 0.67(+0.18,-0.15). If the average is calculated in logarithm–space, in order to calculate weights by relative uncertainties rather than absolute uncertainties, then the average is 0.72(+0.17,-0.18). Thus, the IMAX antiproton/proton ratios and recent measurements (MASS2 and BESS) are generally consistent with to within ~2σ of a cosmic ray antiproton/proton ratio calculation in which cosmic ray antiprotons arise solely from interactions of primary cosmic rays with the interstellar medium. The averages being lower than 1.0 is also consistent with the idea that the nuclear enhancement factor used by W&P (Webber and Potgieter 1989) may be high by ~20-30% (Section 5.1).

---

[1]After this thesis was originally completed, revised MASS91 results by Hof et al. were made available (*Astrophysical Journal*, **467**, L33, 1996).

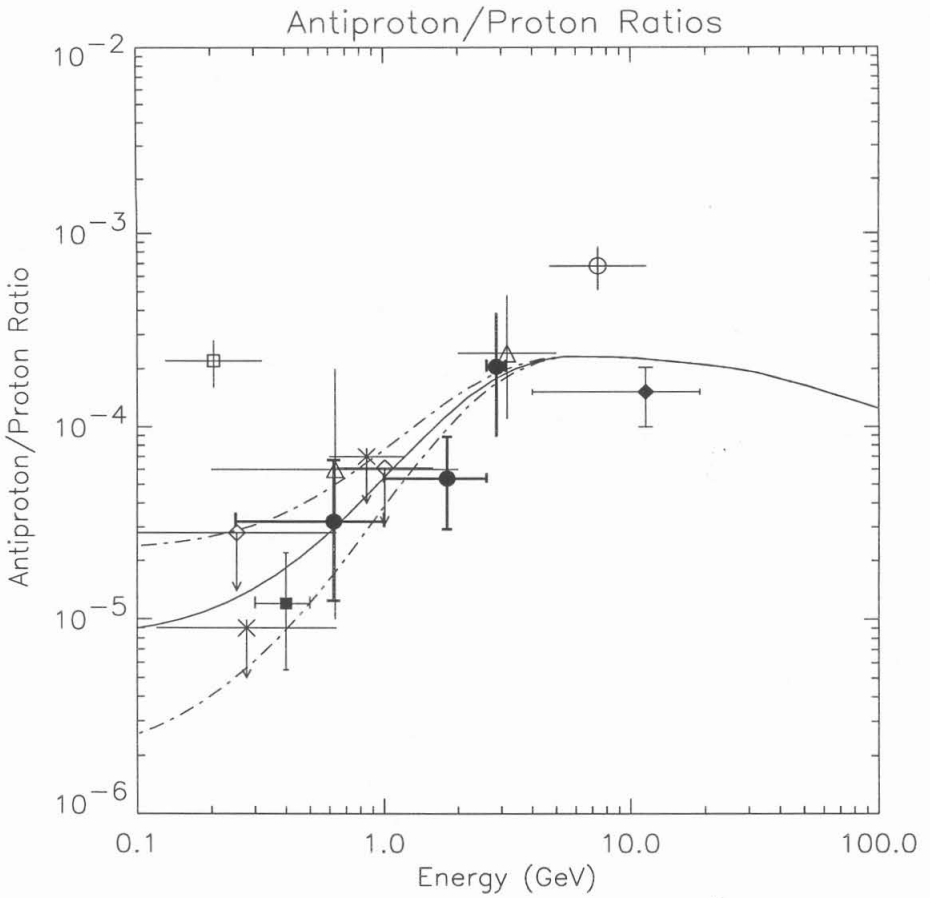

Figure 5.12: Summary of antiproton/proton measurements to date. The antiproton/proton results for this (IMAX) analysis are the closed circles with bold error bars, and the solid line is the 1992 antiproton/proton ratio calculated from the Webber and Potgieter (1989) interstellar spectra. Other points are from Golden et al. (1984, open circle), Bogomolov et al. (1987 and 1990, open triangle), Buffington et al. (1981, open square), Salamon et al. (1990, open diamond), Stochaj (1990) and Moats et al. (1990, asterisk), Hof et al. (1995, closed diamond), and Yoshimura et al. (1995, closed square). The dashed curves are for the 1977 solar minimum and 1990 solar maximum.

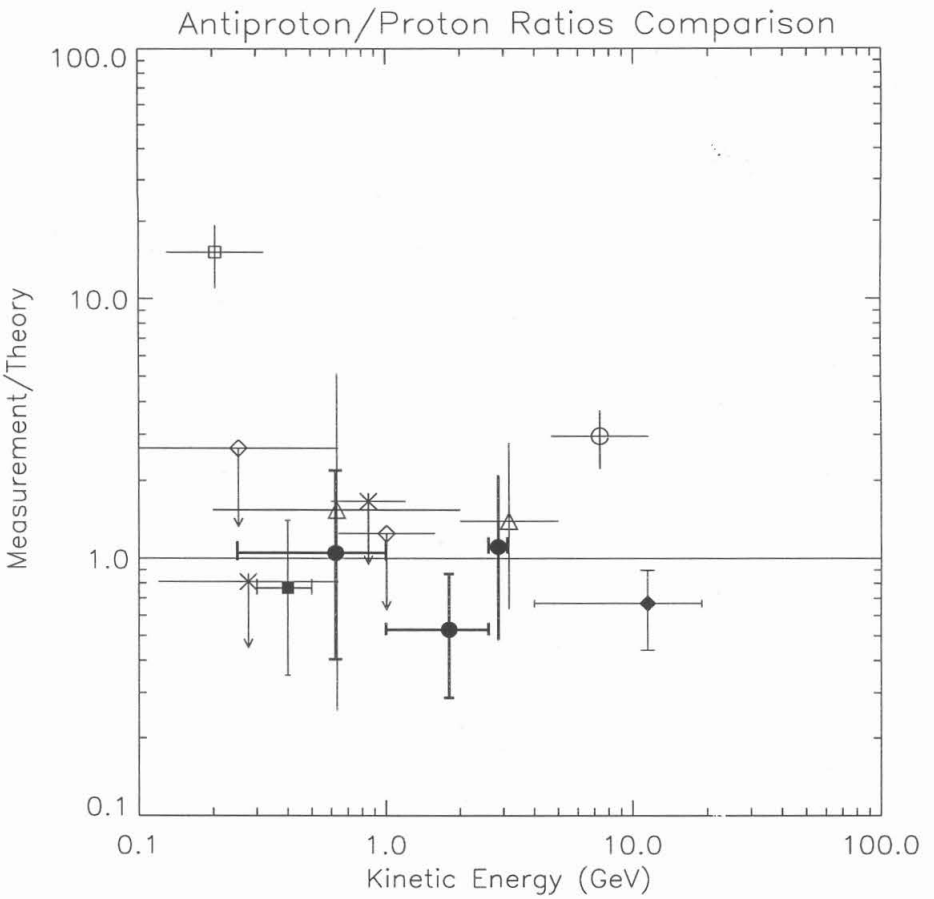

Figure 5.13: Ratio of the measured antiproton/proton ratios to the theoretical values calculated from solar modulation on the Webber and Potgieter (1989) interstellar fluxes. The points are from the present IMAX analysis (closed circles), Golden et al. (1984, open circle), Bogomolov et al. (1987 and 1990, open triangle), Buffington et al. (1981, open square), Salamon et al. (1990, open diamond), Stochaj (1990) and Moats et al. (1990, asterisk), Hof et al. (1995, closed diamond), and Yoshimura et al. (1995, closed square).

5.4 Implications for Galactic Dark Matter

Several authors (e.g. Rudaz and Stecker 1988) have suggested that dark matter candidates such as 15 GeV higgsinos may decay and produce low energy antiprotons. (See Figure 1.9.) Such dark matter decays might result in low energy antiproton abundances and antiproton/proton ratios above those expected from Standard Leaky Box Model calculations.

Diehl et al. (1995) have calculated that if the dark matter candidate is the lightest supersymmetric partner (LSP, e.g. a neutralino of mass ~23 GeV), then decays of the LSP will increase the measured cosmic ray antiproton abundance by as much as 60% in the energy range 100–200 MeV at 1 AU. If the LSP is significantly more massive, then constraints on galactic dark matter density would reduce the abundance of such particles and correspondingly reduce the number of decays which produce antiprotons. Thus, if galactic dark matter is dominated by 80 GeV neutralinos, Diehl et al. (1995) calculate that their corresponding addition to cosmic ray antiproton abundance would only be a fraction of a percent over that expected from Standard Leaky Box Model (SLBM) calculations.

Such dark matter signatures in the cosmic ray antiproton flux and antiproton/proton ratios are complicated by solar modulation and uncertainties in the theoretical interstellar proton and antiproton fluxes. As shown in Figure 5.4, the low energy antiproton flux can vary by as much as a factor of 2 from solar modulation alone, and Figure 5.5 shows that the antiproton/proton ratio can vary by as much as an order of magnitude. These variations are for solar modulation alone and do not include uncertainties in the interstellar proton and antiproton intensities. When the low energy interstellar proton flux is varied as discussed in Section 5.2, there is an additional uncertainty of as much as 50% in the low energy antiproton flux and antiproton/proton ratio expected at 1 AU from the SLBM. (See Figures 5.8 and 5.9.)

Thus, any measurement of antiproton flux and antiproton/proton ratio at 1 AU must take into account current uncertainties in theoretical SLBM spectra and solar modulation variations which can be comparable to or significantly larger than any additional contribution

due to dark matter decay. As stated in the previous section, the IMAX antiproton intensity and antiproton/proton ratios are consistent with SLBM calculations, in which antiprotons arise solely as the product of cosmic ray interactions in the interstellar medium. The statistical uncertainties of these measurements are such that it is not possible to detect any contribution to dark matter decay from even the lightest possible LSP.

5.5 Implications for Antiproton Lifetime

Direct searches of antihelium abundance in cosmic rays (Buffington et al. 1981) as well as indirect arguments suggest (e.g. Steigman 1976) that the antimatter/matter ratio is less than $\sim 10^{-4}$. Direct searches for Z>2 antimatter place the heavier antimatter/matter ratio around 10^{-4} (Smoot, Buffington, and Orth 1975). At the scale of large galaxy clusters, gamma ray measurements imply a mixing of antimatter and matter on the order of $\bar{p}/p \leq 10^{-6}$ (Peebles 1993). One possible explanation for the apparent imbalance between matter and antimatter in the universe is the possibility of antiproton decay. However, one consequence of CPT invariance (symmetry under charge, parity, and time reversal) is that particles and their antiparticles must have the same mass and lifetime, and the proton appears to be stable. Measurements of the proton mean lifetime place a lower limit at 1.6×10^{25} yr, whereas the best direct measurement of the antiproton lifetime sets a lower limit at 1848 yr (Montanet et al. 1994), based on laboratory antiproton storage.

Steigman (1977) first suggested that measurements of the cosmic ray antiproton/proton ratio could be used to place a lower limit on the antiproton lifetime. Measurements of the abundance of ^{10}Be (a cosmic ray clock, with a half–life of 1.5×10^6 yr) in cosmic rays implies a storage lifetime in the containment volume of $\sim 10^7$ yr (e.g. Garcia–Muñoz and Simpson 1988). If the lifetime of antiprotons is substantially less than the storage lifetime of cosmic rays, then the antiproton fluxes would be lower in overall intensity than has been calculated with the Standard Leaky Box Model assuming stable antiprotons.

Given that the IMAX antiproton flux and antiproton/proton ratio measurements, and in

addition the BESS and MASS2 antiproton/proton measurements, are consistent with models in which cosmic ray antiprotons arise solely as secondary cosmic rays and propagate according to the Standard Leaky Box Model, these measurements imply that the antiproton lifetime must be greater than or equal to the ~10^7 yr storage lifetime in the Galaxy.

5.6 Summary

Previous measurements of cosmic ray antiproton abundances were found to exceed early theoretical predictions in which cosmic ray antiprotons originate from interactions of high energy cosmic rays with the interstellar medium. The Isotope Matter Antimatter Experiment (IMAX) was a superconducting magnet spectrometer designed to measure the cosmic ray abundances of protons, antiprotons, and the light isotopes. It employed redundant measurements of magnetic rigidity, charge, and velocity to identify particles by charge and mass via the Cherenkov–Rigidity and TOF–Rigidity techniques. It was successfully flown from Lynn Lake, Manitoba, Canada on July 16, 1992. A total of 16 antiprotons are reported in this analysis of IMAX flight data. A total of ~3.2 of these are attributed to atmospheric secondaries and instrumental background, and the remaining are interpreted as antiprotons coming from the galaxy. These are used to derive the antiproton flux and antiproton/proton ratio.

A study of the solar modulation of protons and antiprotons shows that the antiproton/proton ratio below 2 GeV is expected to vary over the solar cycle by as much as an order of magnitude, a result which has not been fully appreciated in earlier studies. This analysis also shows that more attention should be given to the antiproton spectrum rather than to the antiproton/proton ratio, since the antiproton spectrum is less sensitive to solar modulation effects. These solar cycle variations have been taken into account in the present analysis, so that the IMAX results are compared with predictions appropriate for the 1992 flight.

The IMAX antiproton/proton ratios and antiproton energy spectrum are consistent with

more recent calculations of the Standard Leaky Box Model (SLBM) and with expected solar modulation results, over the energy range 0.25–3.1 GeV. Because the SLBM assumes that cosmic ray antiprotons are produced solely as secondaries arising from interactions of cosmic rays with the interstellar medium, the IMAX data show no evidence of antiproton excess arising from dark matter decay, nor do the data show evidence of antiproton decay with a mean lifetime significantly less than the $\sim 10^7$ yr storage lifetime in the galaxy.

Recent measurements from other experiments in somewhat different energy intervals (Hof et al. 1995, Yoshimura et al. 1995) confirm the interpretation of the IMAX data. The ensemble of recent measurements are consistent with the SLBM when solar modulation is taken into account, suggesting that the pioneering antiproton measurements of Golden et al. (1979, 1984) and Buffington et al. (1981), which reported an excess of antiprotons, may have been in error.

Appendix A: Aerogel Preparation

A significant part of the work contributing to this research involved preparation and testing of the aerogel radiators. Significant effort was placed in long–term storage of aerogels, in the techniques for mounting large area aerogels into aluminum frames suitable for balloon flight, in testing aerogels for Cherenkov light yield, and in treating aerogels to increase light yield.

A.1 Aerogel Production

The aerogels used in IMAX were manufactured by the Airglass Company in Sweden and shipped to Caltech. Airglass went out of business in January 1996. Caltech did no on–site aerogel production. The aerogels provided to Caltech had an effective refractive index of 1.043 and dimensions of 58.4 cm x 58.4 cm x 2.86 cm (23" x 23" x 1.125"). Airglass also provided aerogels with refractive index 1.025 and slightly smaller dimensions of about 50.8 cm x 50.8 cm x 2.86 cm (20" x 20" x 1.125"). The aerogels have the appearance of translucent "solid smoke" with a blue or yellow tinge. They are hard but brittle, and they easily chip or crack at the edges.

Chemical manufacture of aerogels is straightforward. (See Poelz (1986) for a review.) The aerogel is prepared through a two–step chemical process, the first step of which is a hydrolysis reaction:

$$Si(OCH_3)_4 + 4H_2O \xrightarrow{\text{Base}} Si(OH)_4 + 4CH_3OH \qquad (A.1)$$

In this reaction, tetramethylorthosilicate (TMOS) is mixed with water in the presence of a base (usually ammonia) acting as catalyst. In principal, the methoxyl groups may be substituted by any similar alkoxyl group (i.e. any $-(OR)_d$) although the methoxyl is most commonly used. Very long chain alkoxyls may affect solubility.

The second reaction proceeds without intervention as a condensation reaction:

$$Si(OH)_4 \xrightarrow{Base} SiO_2 + 2H_2O \qquad (A.2)$$

The catalytic base is the same as that of the first reaction. Since the chemical process proceeds automatically through the two reactions, it may be considered in practice as a one–step process.

The density of the resulting aerogel solid can be controlled closely within a given range by the addition or extraction of methanol to the mixture during the chemical reactions and prior to the final extraction of the methanol (see below). As the resulting aerogel occupies the same volume as the mixture, addition or extraction of methanol decreases or increases the resulting density of the aerogel. The density has a lower limit arising from back reactions of excess methanol and an upper limit arising largely from the stoichiometry of the reactions.

The resulting aerogel is a highly porous structure composed of colloidal silica. After the condensation is complete, the interstitial spaces are still occupied by the methanol and water reaction products. If the water and methanol were removed by simple evaporation, capillary action would collapse the aerogel, increasing the density of the resulting structure. Instead, the aerogel is heated in a pressure vessel to beyond the critical temperature of the methanol, and the resulting vapor is removed and substituted with air upon cooling. Note that the resulting aerogel is hygroscopic, and it should be kept dry and away from solvents or solvent vapors. (See Aerogel Storage and Handling, below.)

Control of the aerogel density is important because the density is related to the index of refraction by the formula

$$n - 1 = 0.21\rho \qquad (A.3)$$

where ρ is the density in grams per cubic centimeter, and n is the index of refraction. By the chemical manufacture alone, aerogels can be produced with n between 1.02 and 1.06. Further

sintering of the aerogel (at temperatures well above those needed to remove residual methanol) can produce refractive indices from 1.06 to about 1.25 (Rasmussen 1988). Control of the refractive indices in manufacture makes aerogels very useful as Cherenkov radiators in astrophysics and high energy physics experiments.

Although the ammonia is used as a chemical catalyst and not as a reactant, there may be some evidence that the concentration of ammonia affects the amount of residual methanol in the resulting aerogels and, thus, the "quality" (light production, transmission coefficients) of the aerogels. The reasoning is unclear and does not proceed from the chemical equations. However, two possibly related effects are documented: 1) Gelling speed increases with increasing TMOS concentration (which also increases the index of refraction), and 2) the transmission coefficient increases with increasing gelling time. Test results with aerogels produced with strictly controlled ammonia concentration at Airglass have been inconclusive (Airglass, private communication).

A.2 Aerogel Storage and Handling

As noted above, aerogels are hygroscopic, and absorption of water or other solvents by the aerogel can result in chemical breakdown of the aerogel, alteration of its refractive index, or a degradation of its optical characteristics. Aerogels are particularly hydrophilic after baking to remove residual methanol. (See section A.3)

In order to keep them dry prior to flight, the aerogels were stored in separate aluminum trays, lined with dried Kimwipe paper and mounted in Plexiglas cabinets. Prior to being put to use as storage facilities, the cabinets were dried for 7 to 10 days under a 15 cubic ft/hour dry nitrogen gas flow and heated to approximately 35°C. The aluminum trays were also cleaned and dried. Once in use, the cabinets were kept sealed and dry with a nitrogen gas flow of 8 to 10 cubic ft/hour (except when opened for access to the aerogels). The relative humidity in each cabinet was monitored, and the gas flow is adjusted to keep the humidity below 15%.

Further precautions were taken to assure that water or other solvents are kept far from the cabinets. Any solvents used within the lab were stored and used under a ventilation hood, with a ventilation rate of 143 (cubic) ft/min when turned on.

When moving aerogels from the cabinet, handlers wore dry, clean rubber gloves. (Polyethylene gloves may also be used, but they provide a less secure grip than do the surgical rubber gloves. Rubber gloves which are lubricated with powder were avoided.) Care was taken to avoid spitting or breathing on the aerogels. Care was also taken to avoid any physical shocks to the aerogels, as they are brittle. Furthermore, aerogel dust can cause lung damage, so prolonged exposure to aerogel dust was avoided.

A.3 Aerogel Baking Procedure

None of the aerogels received from Airglass produced enough light initially to meet the scientific objectives of IMAX. After a long series of tests which studied the characteristics of the Cherenkov counters as well as the aerogels, it was determined that baking the aerogels to remove all residual methanol improved the light yield enough to meet the scientific objectives of IMAX with a full complement of n=1.043 aerogels. (See Section 2.1.3.)

The reasoning is straightforward: Residual methanol may not be completely removed during the manufacturing process. This methanol absorbs Cherenkov light, which increases reabsorption of light produced in the aerogel. The solution is to remove as much of the residual methanol as possible by oxidizing the methanol to formaldehyde and formic acid vapor, which easily diffuses from the aerogel. The technique suggested by Rasmussen (1991) involves baking the aerogel in air at a temperature high enough to oxidize the methanol without sintering the aerogel. The change in refractive index is not expected to be larger than ±0.001.

The procedure benefits from the use of a microprocessor–controlled oven. An aerogel was placed carefully in the oven, and the oven was then programmed to raise the temperature linearly to 932 °F (500 °C) over a period of 14 hours, to hold the 932 °F temperature for 1 hour, and then to lower the temperature linearly back to room temperature over a period of 14 more

hours. Depending on the amount of residual methanol in the block, the smell of formaldehyde and formic acid can be quite strong during temperature ramp–up.

The visual results can be quite spectacular. If the original, unbaked aerogel had a yellow tinge, the baked aerogel has a clearer, blue tinge. Figure A.1 shows curves of transmission vs. wavelength for baked and unbaked aerogel samples, with a clear overall improvement in transmission after baking. (See also Section A.6.)

A.4 Aerogel Cutting Procedure

The raw n=1.043 aerogels were too large to be mounted in the IMAX counters directly, so they were cut to the appropriate size of approximately 52.6 cm x 52.6 cm x 2.86 cm (20.7" x 20.7" x 1.125"). Cutting may take place before or after baking with no significant difference in the quality of the cut.

Because the aerogels are essentially expanded glass, the cutting process presents special problems arising from glass dust and from the brittle nature of the aerogel. Cutting must be done with a diamond–impregnated wire blade saw, with a blade of 15 mil diameter. The aerogel was mounted and fixed to a slowly moving platform which drew the aerogel past the moving blade at a rate of approximately 0.25 inch/minute. The first and last half–inch of each edge were cut at slower speeds. Significantly faster speeds could break the blade and damage the aerogel, and experience showed that the blades remain useful for cutting no more than two edges of an aerogel. The process of cutting four edges of a raw aerogel could take two afternoons or one full work day.

Safety concerns were important for the saw operator, because the aerogel dust arising from the cutting process can lead to lung damage after prolonged exposure. The cutting region of the saw was encased in a Plexiglas box which was continually evacuated by a vacuum cleaner during the cutting process. The surfaces of the saw and work area were periodically vacuumed free of stray aerogel dust. Dust masks (filters, respirators, etc.) were also useful.

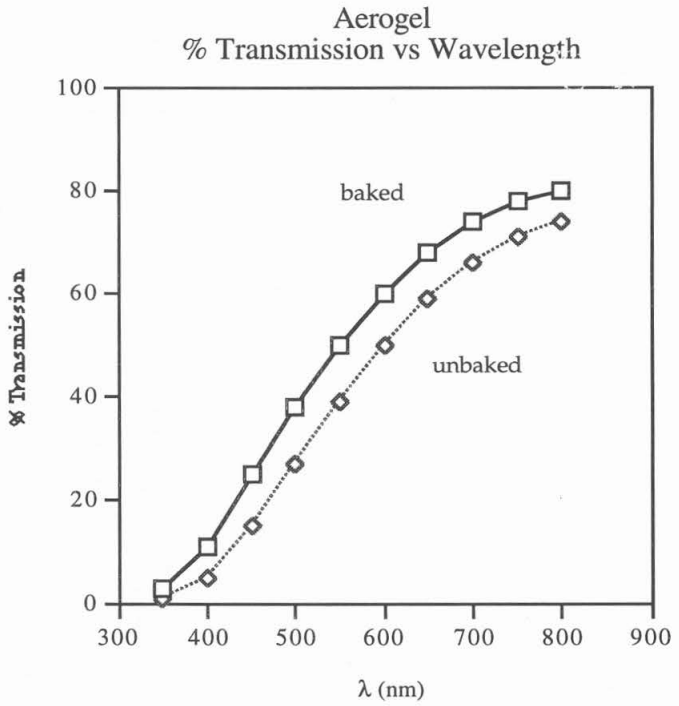

Figure A.1: % Transmission vs. Wavelength for baked and unbaked aerogel (n=1.043) samples.

A.5 Aerogel Mounting Procedure

Once cut to appropriate size, the aerogels were then mounted in aluminum frames appropriate for bolting onto the light collection boxes of the Cherenkov counters. The C2 and C3 counters for IMAX were designed to allow stacking of mounted aerogels above each light collection box, up to the limits imposed by space restrictions on the payload.

The aluminum mounting frames were made of four 6061 aluminum channels, 4.13 cm (1.625 inches) wide, welded into a square frame with interior dimensions of 53.3 cm x 53.3 cm x 4.13 cm (21" x 21" x 1.625"). After welding, the top and bottom faces of the frames were ground flat and parallel. These frames were manufactured at Caltech Central Engineering.

Five holes were drilled and tapped along each side of a frame, allowing for a total of 20 nut, washer, and screw assemblies to be inserted into the frame to hold an aerogel in place for potting. The aerogel was held in place as the screws were slowly advanced. The screws were not allowed to come into direct contact with the aerogel; rather, they pressed against small Sylgard 184 pads, placed between the screw and the aerogel to protect the aerogel edge from further damage. The pressure on each screw was adjusted to provide just enough friction to hold the aerogel in place for potting but not so much pressure as to crack the aerogel. The screws were also adjusted to center the aerogel within the frame.

Once the aerogel was secured, the frame–plus–aerogel assembly was placed upright on one edge and secured to prevent falling. Strips of aluminum sheet metal were bolted along the sides of the bottom edge to provide a well between the frame and the aerogel, and the well was made deep enough to extend above the edge of the aerogel. (See Figure A.4.)

The aerogel potting material was Sylgard 184, a clear silicone elastomer manufactured by Dow Corning. The elastomer comes in two components with instructions for mixing. Its specific gravity is 1.05. Apart from some small surface damage at the aerogel–Sylgard interface caused by the drying of the elastomer, Sylgard 184 was not found to harm aerogels.

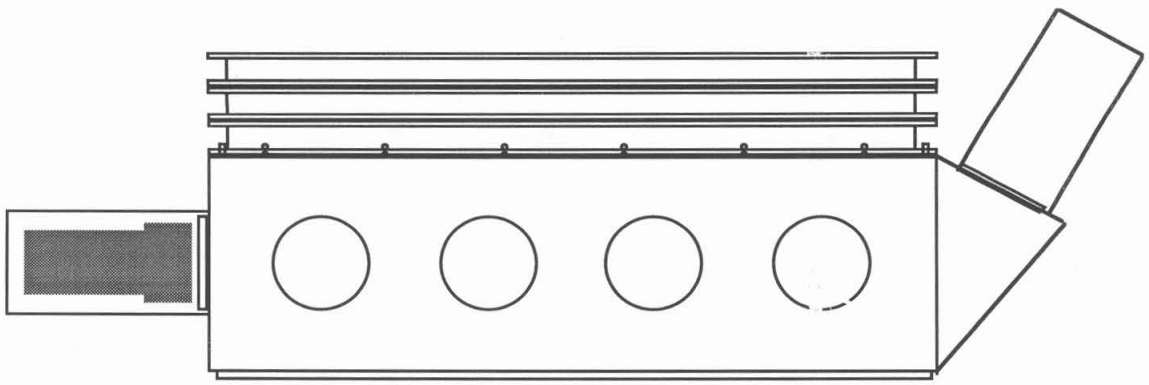

Figure A.2: C3 with Triple Aerogel Stack

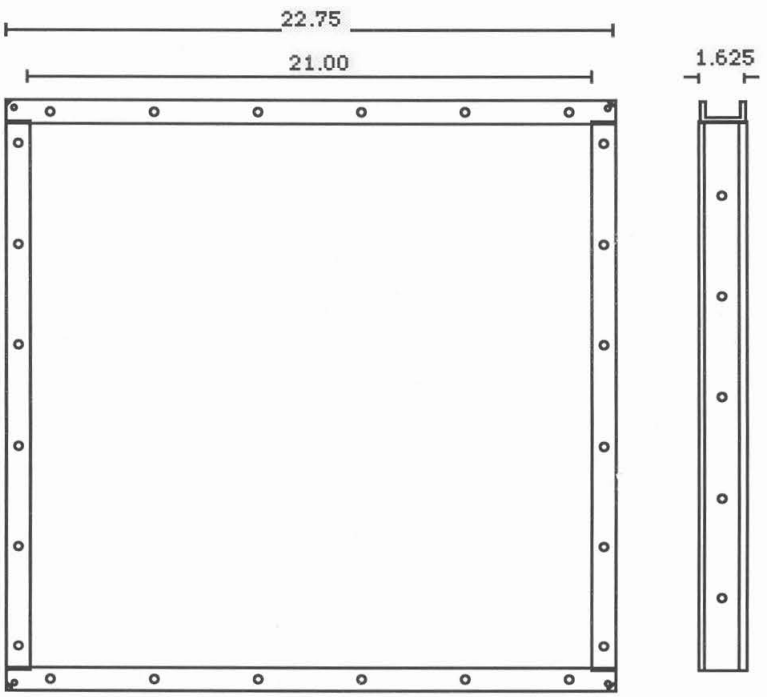

Figure A.3: Standard Aerogel Mounting Frame. Dimensions are in inches.

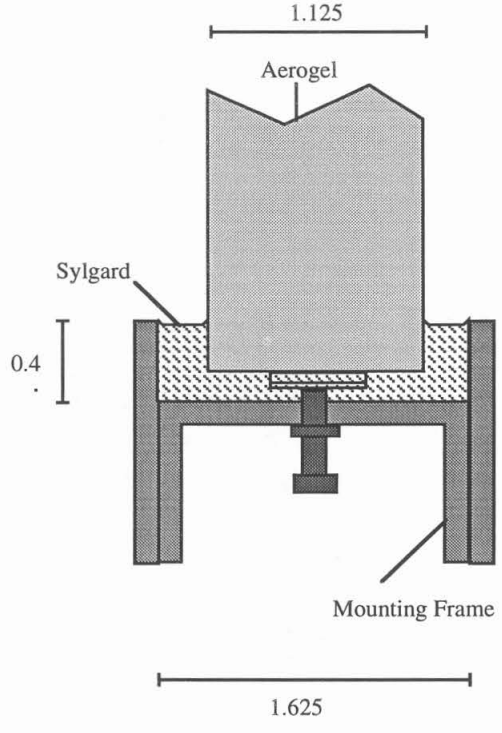

Figure A.4: Aerogel potting cross section. Dimensions are in inches.

The Sylgard 184 was prepared and mixed according to the instructions provided by Dow Corning. Once mixed, it was pumped in a small vacuum oven, repeatedly depressurized and repressurized, in order to remove trapped air bubbles. Then the Sylgard 184 was injected with a large syringe into the potting well until it extended over the edge of the aerogel. The transparency of the Sylgard 184 and the translucence of the aerogel made potting somewhat difficult, and care was taken to minimize the amount of stray Sylgard 184 on the aerogel.

It took slightly less than 200 grams of mixed Sylgard 184 to pot one aerogel side completely. Once a side is potted, the Sylgard 184 was allowed to dry overnight in the presence of a dry nitrogen flow. In practice, it took up to one week for Sylgard 184 to dry completely, but it was sufficiently dry overnight to allow for the potting of other sides. It took four days to pot the four sides.

The Sylgard 184 extended beyond the edge of an aerogel, providing approximately one–quarter inch of overlap. Once the aerogel was potted securely into the frame, the positioning screws are withdrawn slightly. The aerogel was then held securely in the frame by the potting material alone; the Sylgard 184 provided both mounting strength and some shock absorption. This mounting technique was used successfully in the IMAX flight, in which the mounted aerogels were recovered after parachute landing without damage to the frames or the aerogels.

A.6 Aerogel Testing

During the development phase of the aerogel Cherenkov counters, we conducted tests to determine the light yield characteristics of the aerogels and to maximize the light yield of the counters. Laboratory measurements of light yield with muons were made with a particle telescope and Camac system employing the same PMTs, amplifiers, and analog-to-digital converters used in flight. The test particles were relativistic muons produced in the upper atmosphere. Signals from the PMTs were individually digitized. A special mounting

apparatus was implemented to hold uncut, unbaked, and unmounted aerogels in the test counters.

With this system, it was possible to resolve the 0, 1, and, in some cases, 2 photoelectron (pe) signals for individual PMTs, as was also the case with flight data (Section 2.1.1). For a single PMT, the average light yield, in pes, was obtained from histograms of the PMT response and calculated by the "fraction of zeros" equation

$$C = -\ln\left(p_0/p\right) \tag{A.4}$$

where C is the average light yield, p_0 is the number of events with 0 photoelectrons, and p is the total number of events in the histogram. The fraction of zeros equation assumes that the light yield follows a Poisson distribution. The average light yield measured in a single PMT may be determined by counting all of the 0 pe signals as a fraction of all signals measured by the PMT. (See Figure 2.7.) Average light yield for a given counter is obtained by summing Equation A.4 over all the PMTs in the counter.

Initial aerogel tests indicated that the aerogels, as received from Airglass, did not produce enough light to meet the science objectives of IMAX. As is noted in Section A.3, a baking technique was adopted to remove residual methanol and increase light yield. The post-bake improvement in light yield was most striking in the laboratory tests in which multiple aerogel layers were added. If we include attenuation of Cherenkov light by scattering or absorption in the radiator, the total light emitted by a charged particle passing through a radiator can be represented by

$$L(t) = K\lambda\left(1-\frac{1}{n^2}\right)\left(1-e^{-t/\lambda}\right) \tag{A.5}$$

where L(t) is the measured light generated by a Z=1, ß=1 particle passing through a radiator of index n and thickness t, and λ is interpreted as an effective transmission length characteristic of the radiator and the counter geometry. K is a constant.

Curve fits on Figure A.5 show that the baked aerogels have l = 4.7 cm in C3, while the aerogels prior to baking had l = 1.7 cm. While individual results varied from block to block, these results were typical of the aerogels used for flight. From lab tests, we predicted a fraction of zeros average response for Z=1, ß=1 particles of 13 pes in the counter designated C3, and 10 pes in the counter designated C2.

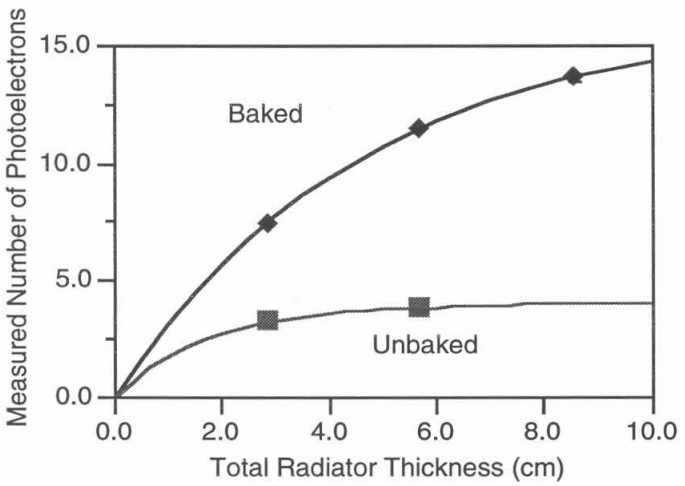

Figure A.5: C3 radiator light yield, in photoelectrons, vs. radiator thickness, for unbaked and baked aerogels. All blocks have an index of refraction of n=~1.043. (Uncertainties are smaller than the plot symbols.)

Appendix B: IMAX Detector Grammages and Energy Shifting

In order to correct for interactions in the instrument (e.g. antiproton annihilation, Section 4.3.2), we must employ an accounting of the atmosphere and the IMAX detector materials and thicknesses.

Table B.1 lists the materials accounted for in this analysis, from the top of the atmosphere to the bottom plate of the IMAX payload. (See Figure 2.1 for a drawing of the payload.) The materials are broken down into major chemical components. The seventh column gives the vertical path length (in g/cm^2), calculated from the material thickness (cm, fifth column) and density (g/cm^3, sixth column).

The atmosphere is approximated as 5 g/cm^2 of mostly nitrogen and oxygen. The spreader bar was an aluminum I–beam which was suspended from the balloon and parachute and from which the payload itself was suspended. The spreader bar contribution is averaged as 0.88 g/cm^2 of aluminum spread over the top of the payload. Gatorfoam covered the payload shell for insulation; it is treated as 1 cm Styrofoam ($C_{11}H_{11}N$).

The plastic scintillator materials (in the TOF paddles, S1, and S2) are treated as polystyrene (CH), and the aerogel Cherenkov radiators are treated as SiO_2, with the material density given by Equation A.3 for n=1.043. The C1 radiator was Teflon (CF). The counter "walls" — i.e. the tops (lids) and bottoms (floors) of S1, S2, C1, C2, and C3 — were combined into single walls for each counter, to simplify the calculations. Because these counter walls were fractions of a centimeter in thickness, separating the walls into top and bottom walls added corrections of only a few MeV, which was negligible in this analysis.

The drift chamber (DC) and multiwire proportional counter (MWPC) material composition was provided by Menn (private communication, 1995). Although the IMAX payload contained a dry nitrogen atmosphere throughout the payload volume (except the DC interiors), it is treated as a single layer at the bottom of Table B.1. The contribution to the dry nitrogen atmosphere is negligible.

Table B.1: IMAX Detector (and other) Grammages

	Material	Composition	A	Density (g/cm^3)	Thickness (cm)	Vertical Path (g/cm^2)
Atmosphere	Air	N	14.01			3.50
		O	16.00			1.50
Spreader bar	Aluminum	Al	26.98	2.70		0.88
Gatorfoam		C_{11}	12.01	0.15	1.00	0.15
		H_{11}	1.00	0.01	1.00	0.01
		N	14.01	0.02	1.00	0.02
Dome	Aluminum	Al	26.98	2.70	0.23	0.62
Top TOF	BC-420	C	12.01	0.95	1.00	0.95
		H	1.00	0.08	1.00	0.08
C1 radiator	Teflon	C	12.01	0.52	2.06	1.07
		F	19.00	1.64	2.06	3.38
C1 walls	Aluminum	Al	26.98	2.70	0.10	0.27
S1 scintillator	BC-400	C	12.01	0.95	1.27	1.21
		H	1.00	0.08	1.27	0.10
S1 walls	Aluminum	Al	26.98	2.70	0.10	0.27
C3 radiator	Aerogel, n=1.043	Si	28.09	0.10	9.00	0.86
		O_2	16.00	0.11	9.00	0.98
C3 walls	Aluminum	Al	26.98	2.70	0.29	0.78
DC Copper	Copper	Cu	63.55	8.96	0.01	0.13
DC Mylar	Mylar (polyester polyethylene terephthalate)	C_{10}	12.01	0.87	0.05	0.04
		H_8	1.00	0.06	0.05	0.00
		O_4	16.00	0.46	0.05	0.02
DC Tungsten	Tungsten	W	183.85	19.30	0.01	0.14
DC CO_2	Carbon Dioxide	C	12.01	5.40×10^{-4}	66.00	3.56×10^{-2}
		O_2	16.00	1.44×10^{-3}	66.00	9.49×10^{-2}
MWPC Mylar	Mylar (polyester polyethylene terephthalate)	C_{10}	12.01	0.87	0.03	0.02
		H_8	1.00	0.06	0.03	0.00
		O_4	16.00	0.46	0.03	0.01
MWPC Steel	Fe	Fe	56.85	7.87	6.56×10^{-3}	0.05
MWPC Argon	Ar	Ar	39.95	1.78×10^{-3}	28.80	5.13×10^{-2}
C2 radiator	Aerogel, n=1.043	Si	28.09	0.10	9.00	0.86
		O_2	16.00	0.11	9.00	0.98
C2 walls	Aluminum	Al	26.98	2.70	0.29	0.78
S2 scintillator	BC-408	C	12.01	0.95	1.78	1.69
		H	1.00	0.08	1.78	0.14
S2 walls	Aluminum	Al	26.98	2.70	0.32	0.86
Bottom TOF	BC-420	C	12.01	0.95	1.00	0.95
		H	1.00	0.08	1.00	0.08
IMAX N_2 Atmosphere	Nitrogen	N_2	14.01	1.25×10^{-3}	132.50	1.66×10^{-1}
IMAX Bottom Plate	Aluminum	Al	26.98			10.67

The total vertical pathlength from the top of the atmosphere to the bottom TOF is 23.76 g/cm^2, of which 18.76 g/cm^2 is the IMAX payload. The "middle" of the instrument is defined as the top of the spectrometer (tracking systems), for the purpose of calculating the average energy of a particle as it travels from the top TOF to the bottom TOF. The total IMAX vertical pathlength from the middle of the instrument to the top is 11.64 g/cm^2.

As a particle travels from the top of the atmosphere through the bottom of the IMAX payload, it gradually loses energy to interactions in the various materials. Table B.2 follows protons of energies 0.25 GeV, 1.00 GeV, 2.61 GeV, and 3.11 GeV from the top of the atmosphere to the bottom of the IMAX payload, in the same order of materials as given in Table B.1 and assuming vertical incidence. The materials are treated as equivalent to equal thicknesses (in g/cm^2) of air and using range–energy losses compiled by Janni (1966).

Table B.2: IMAX Energies vs. Approximate Vertical Depth

	Material	Vertical Path (g/cm^2)	Energies (GeV) at the Top of Each Layer			
Atmosphere	Air	3.50	0.250	1.000	2.610	3.110
		1.50	0.238	0.993	2.604	3.104
Spreader bar	Aluminum	0.88	0.232	0.990	2.601	3.101
Gatorfoam		0.15	0.229	0.988	2.599	3.099
		0.01	0.229	0.988	2.599	3.099
		0.02	0.229	0.988	2.599	3.099
Dome	Aluminum	0.62	0.228	0.988	2.599	3.099
Top TOF	BC-420	0.95	0.226	0.987	2.598	3.098
		0.08	0.223	0.985	2.596	3.096
C1 radiator	Teflon	1.07	0.222	0.985	2.596	3.096
		3.38	0.218	0.983	2.594	3.094
C1 walls	Aluminum	0.27	0.205	0.976	2.588	3.088
S1 scintillator	BC-400	1.21	0.204	0.976	2.587	3.087
		0.10	0.200	0.973	2.585	3.085
S1 walls	Aluminum	0.27	0.199	0.973	2.585	3.085
C3 radiator	Aerogel, n=1.043	0.86	0.198	0.972	2.585	3.084
		0.98	0.195	0.971	2.583	3.083
C3 walls	Aluminum	0.78	0.191	0.969	2.581	3.081
DC Copper	Copper	0.13	0.188	0.967	2.580	3.080
DC Mylar	Mylar (polyester polyethylene terephthalate)	0.04	0.187	0.967	2.580	3.079
		0.00	0.187	0.967	2.579	3.079
		0.02	0.187	0.967	2.579	3.079
DC Tungsten	Tungsten	0.14	0.187	0.967	2.579	3.079
DC CO_2	Carbon Dioxide	3.56×10^{-2}	0.186	0.967	2.579	3.079
		9.49×10^{-2}	0.186	0.967	2.579	3.079
MWPC Mylar	Mylar (polyester polyethylene terephthalate)	0.02	0.186	0.966	2.579	3.079
		0.00	0.186	0.966	2.579	3.079
		0.01	0.186	0.966	2.579	3.079
MWPC Steel	Fe	0.05	0.186	0.966	2.579	3.079
MWPC Argon	Ar	5.13×10^{-2}	0.185	0.966	2.579	3.079
C2 radiator	Aerogel, n=1.043	0.86	0.185	0.966	2.579	3.078
		0.98	0.181	0.964	2.577	3.077
C2 walls	Aluminum	0.78	0.177	0.962	2.575	3.075
S2 scintillator	BC-408	1.69	0.174	0.961	2.574	3.074
		0.14	0.166	0.958	2.571	3.071
S2 walls	Aluminum	0.86	0.166	0.957	2.571	3.070
Bottom TOF	BC-420	0.95	0.162	0.956	2.569	3.069
		0.08	0.158	0.954	2.567	3.067
IMAX N_2 Atmosphere	Nitrogen	1.66×10^{-1}	0.157	0.954	2.567	3.067
IMAX Bottom Plate	Aluminum	10.67	0.156	0.953	2.567	3.067

Appendix C: The Antiproton Data

This Appendix lists all of the IMAX numerical data used in this analysis for the 16 antiproton events. Each event is given two pages of data, with the data grouped into event identifiers (e.g. event #'s), mass and energy calculations, time of flight (TOF) data, Cherenkov data, scintillator data, and tracking data. Also included are plots of the position measurements and fitted trajectories through the IMAX tracking systems.

Some data elements are included in this appendix which were not actually employed in this analysis. For example, the element "distance from C2=C3 (pes)" was an early calculation intended for use in a C2 vs. C3 correlation cut; this cut was replaced by the C2-C3 correlation cut described in Section 3.3.2. Similarly, the "# DC hits" elements were replaced by the "# good positions," and the "C2+C3 Map–Normalized, weighted average" element was replaced with the single counter form, described in Section 3.3. These unused data elements were left in the selection set for historical reasons.

The scintillator data are in arbitrary units (Section 3.2). Deflections are in GV^{-1}, and all position data are in cm and in coordinates defined by the tracking system. The velocity, β, employed for mass calculation was either the Cherenkov velocity or the TOF velocity, depending on whether a given event passed the Cherenkov threshold selection criterion.

The trajectory plots show the x-projection on the left and the y–projection on the right. The rectangles are the DCs, and the MWPCs are shown as lines above, below, and between the DCs. Hits in the DC layers are shown as circles, and hits in the MWPC layers are shown as x's. The final, fitted trajectories are shown.

A final note on Event # 2799013: The Cherenkov signal (C2+C3 Map–Norm, single counter form) for this event defines this event as a below–threshold event, by the criterion described in Section 3.7. The β_{TOF} calculated by the software at Caltech was 1.00085, making its mass incalculable via the TOF–Rigidity method. However, the β_{TOF} calculated at Siegen

was 0.984. This difference was pursued variable–by–variable and bit–by–bit through the software at both NMSU (using VAX/VMS, as at Siegen) and Caltech (using Sparcstations running Unix). The difference was eventually traced to machine–specific differences in the treatment of the least significant bits during early arithmetic operations in the tracking software. The Siegen result was adopted as correct for the mass calculation. This event and event 3680471 also have calculated TOF energies above Cherenkov threshold, although their Cherenkov signals are below threshold. They are assigned to the 1–2.61 GeV energy range, based on their below–threshold Cherenkov signals.

Event:	1556179
Checksum:	0
IFAIL Flag	0
Payload time:	3148 (1 count = 10 sec)

Mass, energy calculation

Rigidity (GV)	-2.468
ßTOF	0.944
Mass (GeV/c^2)	-0.862
Energy (assuming proton mass)	1.906

Time-of-flight

ßTOF	0.944		
TOF Error flag	0	In Paddle Gap flag (tracking)	0
Off Edge Flag (tracking)	0	Off Edge Flag (TDC)	0

	Top	Bottom
TOF Scint. dE/dx (sqrt(E*W PMTs))	0.667	0.884
TOF PMT signal ratio (E/W)	1.577	0.998
Δx (tracking-TDC)	0.306	0.778

C2, C3 (Aerogel Cherenkov counters)

	C2	C3
pe Light yield	-0.091	1.15
Map-Normalized Light yield	-0.008	0.124
Map-Norm light yield, Knock-on corrected	-0.009	0.109
ß (with index maps)	-1	0.96
>5pe flag	0	0
Response Map (pes)	10.949+/-0.002	9.240+/-0.003
Index Map	1.045	1.047
Ratio Function	-0.676	-0.815

C2+C3	
C2+C3 pes	1.059
C2+C3 Map-Normalized, single counter form	0.052
C2+C3 Map-Norm, single counter, Knock-on corrected	0.044
C2+C3 Map-Normalized, weighted average	0.042+/-0.066
ß (C2+C3 MN weighted average, with index maps)	0.958
Distance from C2=C3 (pes)	0.65
Distance from C2=C3 (Map-Norm)	0.009
Cherenkov software Z, best guess	1

Scintillators and C1

S1 dE/dx (mapped)	3.293
S2 dE/dx (mapped)	15.039
C1 light yield	2.582

DC+MWPC (HYBRID)

	x	y
# DC hits	11	7
# measured DC positions > 4cm off fitted track	0	0
# planes with measured positions > 4cm off fitted track	0	0
# good positions (NGx,NGy)	17	10
Chi-square	1.614	1.54
DC1, position at 3rd layer	13.158	19.578
DC2, position at 3rd layer	9.94	11.857
Deflection +/- Sigma Deflection (hybrid, DC+MWPC)	-0.405+/-0.006	
Deflection +/- Sigma Deflection (Upper DC)	-0.464+/-0.053	
Deflection +/- Sigma Deflection (Lower DC)	-0.692+/-0.183	

Positions at detectors, in DC coordinates (x,y)

Counter	x (cm)	y(cm)
Spreader bar	-2.856	-29.428
Top TOF	5.066	-4.244
C1	5.844	-1.769
C3	6.554	0.502
S1	8.135	5.673
C2	16.674	26.663
S2	18.521	30.423
Bottom TOF	21.455	36.439

=====

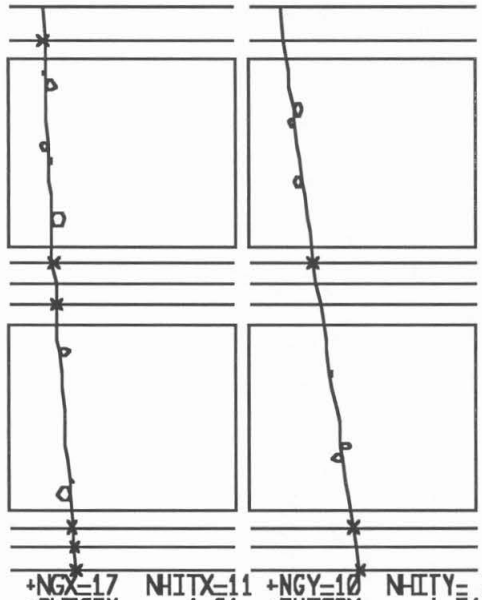

Event:	1836913
Checksum:	0
IFAIL Flag	0
Payload time:	3575 (1 count = 10 sec)

Mass, energy calculation

Rigidity (GV)	-3.618
ß (Cherenkov, assuming n=1.043)	0.969
Mass (GeV/c^2)	-0.925
Energy (assuming proton mass)	2.848

Time-of-flight

ßTOF	0.962		
TOF Error flag	0	In Paddle Gap flag (tracking)	0
Off Edge Flag (tracking)	0	Off Edge Flag (TDC)	0

	Top	Bottom
TOF Scint. dE/dx (sqrt(E*W PMTs))	0.86	0.932
TOF PMT signal ratio (E/W)	1.033	1.037
Δx (tracking-TDC)	0.66	0.264

C2, C3 (Aerogel Cherenkov counters)

	C2	C3
pe Light yield	2.946	2.842
Map-Normalized Light yield	0.275	0.238
Map-Norm light yield, Knock-on corrected	0.267	0.228
ß (with index maps)	0.968	0.966
>5pe flag	0	0
Response Map (pes)	10.717+/-0.002	11.933+/-0.003
Index Map	1.045	1.046
Ratio Function	0.236	-0.009

C2+C3

C2+C3 pes	5.788
C2+C3 Map-Normalized, single counter form	0.256
C2+C3 Map-Norm, single counter, Knock-on corrected	0.247
C2+C3 Map-Normalized, weighted average	0.254+/-0.107
ß (C2+C3 MN weighted average, with index maps)	0.967
Distance from C2=C3 (pes)	0.197
Distance from C2=C3 (Map-Norm)	0.001
Cherenkov software Z, best guess	1

Scintillators and C1

S1 dE/dx (mapped)	2.58
S2 dE/dx (mapped)	18.381
C1 light yield	2.255

DC+MWPC (HYBRID)

	x	y
# DC hits	12	6
# measured DC positions > 4cm off fitted track	0	0
# planes with measured positions > 4cm off fitted track	0	0
# good positions (NGx,NGy)	19	9
Chi-square	0.954	1.227
DC1, position at 3rd layer	30.657	27.127
DC2, position at 3rd layer	34.879	22.049
Deflection +/- Sigma Deflection (hybrid, DC+MWPC)	-0.276+/-0.007	
Deflection +/- Sigma Deflection (Upper DC)	-0.177+/-0.092	
Deflection +/- Sigma Deflection (Lower DC)	-0.171+/-0.166	

Positions at detectors, in DC coordinates (x,y)

Counter	x (cm)	y(cm)
Spreader bar	64.24	-9.733
Top TOF	46.306	9.717
C1	44.544	11.628
C3	42.924	13.382
S1	39.223	17.371
C2	27.492	31.343
S2	25.835	33.554
Bottom TOF	23.176	37.087

=====

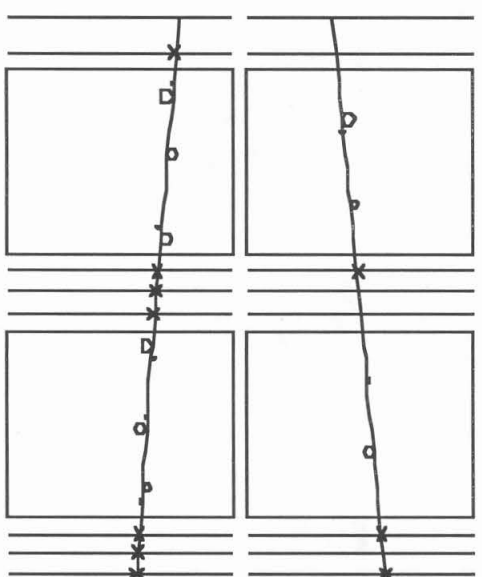

Event:	1919833
Checksum:	0
IFAIL Flag	0
Payload time:	3703 (1 count = 10 sec)

Mass, energy calculation

Rigidity (GV)	-2.69
ßTOF	0.948
Mass (GeV/c^2)	-0.903
Energy (assuming proton mass)	2.008

Time-of-flight

ßTOF 0.948

TOF Error flag	0	In Paddle Gap flag (tracking)	0
Off Edge Flag (tracking)	0	Off Edge Flag (TDC)	0

	Top	Bottom
TOF Scint. dE/dx (sqrt(E*W PMTs))	1.342	0.85
TOF PMT signal ratio (E/W)	0.987	0.889
Δx (tracking-TDC)	1.409	2.655

C2, C3 (Aerogel Cherenkov counters)

	C2	C3
pe Light yield	-0.086	-0.039
Map-Normalized Light yield	-0.009	-0.003
Map-Norm light yield, Knock-on corrected	-0.01	-0.003
ß (with index maps)	-1	-1
>5pe flag	0	0
Response Map (pes)	9.232+/-0.003	12.250+/-0.002
Index Map	1.047	1.047
Ratio Function	1.237	1

C2+C3

C2+C3 pes	-0.124
C2+C3 Map-Normalized, single counter form	-0.006
C2+C3 Map-Norm, single counter, Knock-on corrected	-0.006
C2+C3 Map-Normalized, weighted average	-0.005+/-0.034
ß (C2+C3 MN weighted average, with index maps)	0.955
Distance from C2=C3 (pes)	0.002
Distance from C2=C3 (Map-Norm)	0
Cherenkov software Z, best guess	1

Scintillators and C1

S1 dE/dx (mapped)	4.268
S2 dE/dx (mapped)	10.355
C1 light yield	1.371

DC+MWPC (HYBRID)

	x	y
# DC hits	13	8
# measured DC positions > 4cm off fitted track	0	0
# planes with measured positions > 4cm off fitted track	0	0
# good positions (NGx,NGy)	20	12
Chi-square	0.925	2.281
DC1, position at 3rd layer	34.021	43.428
DC2, position at 3rd layer	26.204	39.971
Deflection +/- Sigma Deflection (hybrid, DC+MWPC)	-0.372+/-0.019	
Deflection +/- Sigma Deflection (Upper DC)	-0.358+/-0.123	
Deflection +/- Sigma Deflection (Lower DC)	-0.685+/-0.153	

Positions at detectors, in DC coordinates (x,y)

Counter	x (cm)	y(cm)
Spreader bar	-17.955	18.796
Top TOF	9.018	31.751
C1	11.669	33.025
C3	14.1	34.193
S1	19.624	36.849
C2	40.982	46.345
S2	44.667	47.877
Bottom TOF	50.555	50.325

=====

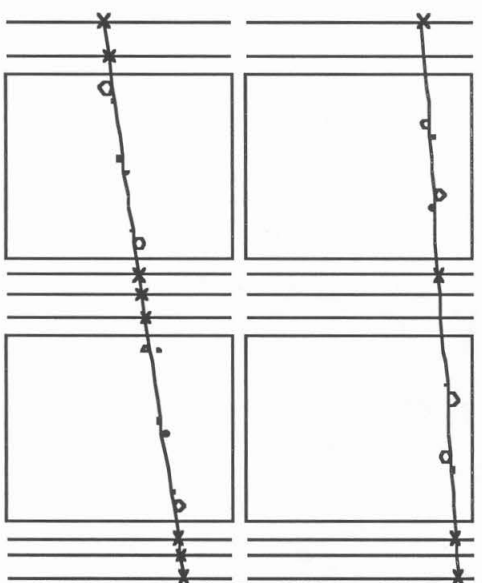

Event:	2088971
Checksum:	0
IFAIL Flag	0
Payload time:	3961 (1 count = 10 sec)

Mass, energy calculation

Rigidity (GV)	-1.167
ßTOF	0.774
Mass (GeV/c^2)	-0.954
Energy (assuming proton mass)	0.544

Time-of-flight

ßTOF	0.774

TOF Error flag	0	In Paddle Gap flag (tracking)	0
Off Edge Flag (tracking)	0	Off Edge Flag (TDC)	0

	Top	Bottom
TOF Scint. dE/dx (sqrt(E*W PMTs))	1.275	1.144
TOF PMT signal ratio (E/W)	1.122	1.006
Δx (tracking-TDC)	1.977	2.238

C2, C3 (Aerogel Cherenkov counters)

	C2	C3
pe Light yield	0.025	0.068
Map-Normalized Light yield	0.002	0.005
Map-Norm light yield, Knock-on corrected	0	0
ß (with index maps)	0.96	0.956
>5pe flag	0	0
Response Map (pes)	11.247+/-0.002	12.496+/-0.002
Index Map	1.042	1.046
Ratio Function	1.355	1.335

C2+C3

C2+C3 pes	0.093
C2+C3 Map-Normalized, single counter form	0.004
C2+C3 Map-Norm, single counter, Knock-on corrected	0
C2+C3 Map-Normalized, weighted average	0.004+/-0.031
ß (C2+C3 MN weighted average, with index maps)	0.96
Distance from C2=C3 (pes)	0.001
Distance from C2=C3 (Map-Norm)	0
Cherenkov software Z, best guess	1

Scintillators and C1

S1 dE/dx (mapped)	4.003
S2 dE/dx (mapped)	19.903
C1 light yield	0.146

DC+MWPC (HYBRID)

	x	y
# DC hits	11	8
# measured DC positions > 4cm off fitted track	0	0
# planes with measured positions > 4cm off fitted track	0	0
# good positions (NGx,NGy)	18	12
Chi-square	0.721	0.71
DC1, position at 3rd layer	29.138	12.609
DC2, position at 3rd layer	25.625	21.035
Deflection +/- Sigma Deflection (hybrid, DC+MWPC)	-0.857+/-0.006	
Deflection +/- Sigma Deflection (Upper DC)	-0.953+/-0.102	
Deflection +/- Sigma Deflection (Lower DC)	-0.866+/-0.048	

Positions at detectors, in DC coordinates (x,y)

Counter	x (cm)	y(cm)
Spreader bar	19.493	71.198
Top TOF	23.292	40.532
C1	23.665	37.518
C3	24.002	34.752
S1	24.733	28.46
C2	34.665	5.327
S2	37.539	1.493
Bottom TOF	42.055	-4.633

=====

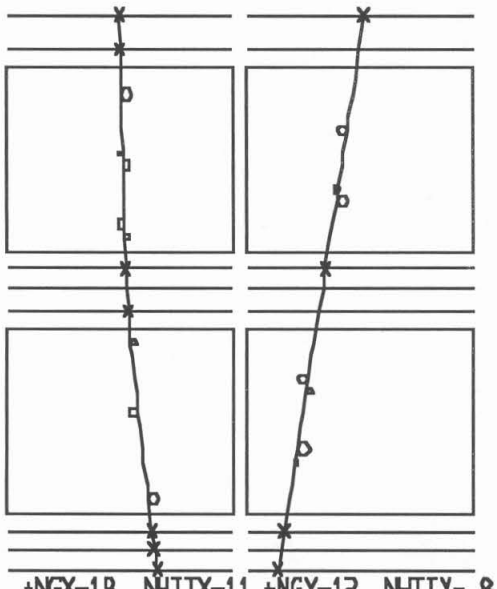

Event:	2581308
Checksum:	0
IFAIL Flag	0
Payload time:	4718 (1 count = 10 sec)

Mass, energy calculation

Rigidity (GV)	-3.433
ß (Cherenkov, assuming n=1.043)	0.969
Mass (GeV/c^2)	-0.876
Energy (assuming proton mass)	2.854

Time-of-flight

ßTOF	0.948

TOF Error flag	0	In Paddle Gap flag (tracking)	0
Off Edge Flag (tracking)	0	Off Edge Flag (TDC)	0

	Top	Bottom
TOF Scint. dE/dx (sqrt(E*W PMTs))	0.691	0.963
TOF PMT signal ratio (E/W)	1.181	1.259
Δx (tracking-TDC)	0.382	0.952

C2, C3 (Aerogel Cherenkov counters)

	C2	C3
pe Light yield	1.728	4.257
Map-Normalized Light yield	0.156	0.352
Map-Norm light yield, Knock-on corrected	0.145	0.347
ß (with index maps)	0.964	0.971
>5pe flag	0	0
Response Map (pes)	11.099+/-0.001	12.086+/-0.002
Index Map	1.044	1.045
Ratio Function	1.088	0.074

C2+C3

C2+C3 pes	5.985
C2+C3 Map-Normalized, single counter form	0.258
C2+C3 Map-Norm, single counter, Knock-on corrected	0.248
C2+C3 Map-Normalized, weighted average	0.220+/-0.118
ß (C2+C3 MN weighted average, with index maps)	0.966
Distance from C2=C3 (pes)	1.954
Distance from C2=C3 (Map-Norm)	0.019
Cherenkov software Z, best guess	1

Scintillators and C1

S1 dE/dx (mapped)	4.004
S2 dE/dx (mapped)	9.094
C1 light yield	0.839

DC+MWPC (HYBRID)

	x	y
# DC hits	11	8
# measured DC positions > 4cm off fitted track	0	0
# planes with measured positions > 4cm off fitted track	0	0
# good positions (NGx,NGy)	14	7
Chi-square	0.859	0.227
DC1, position at 3rd layer	23.348	19.85
DC2, position at 3rd layer	22.928	15.467
Deflection +/- Sigma Deflection (hybrid, DC+MWPC)	-0.291+/-0.005	
Deflection +/- Sigma Deflection (Upper DC)	-0.255+/-0.042	
Deflection +/- Sigma Deflection (Lower DC)	-0.368+/-0.058	

Positions at detectors, in DC coordinates (x,y)

Counter	x (cm)	y(cm)
Spreader bar	26.218	-10.287
Top TOF	24.246	5.45
C1	24.052	6.997
C3	23.871	8.416
S1	23.438	11.645
C2	24.356	23.652
S2	24.889	25.657
Bottom TOF	25.726	28.865

=====

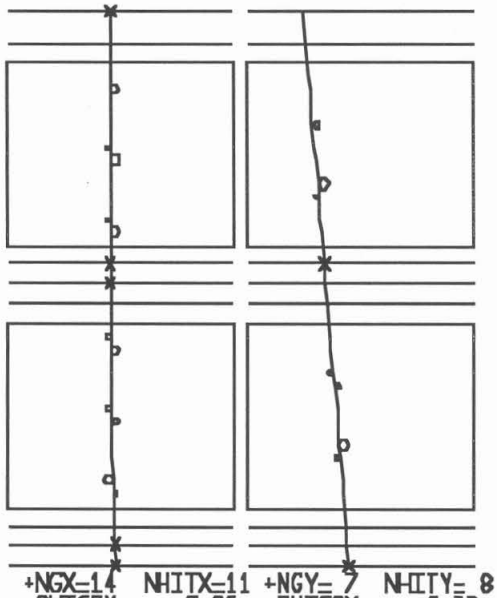

Event:	2610216
Checksum:	0
IFAIL Flag	0
Payload time:	4763 (1 count = 10 sec)

Mass, energy calculation

Rigidity (GV)	-3.138
ß (Cherenkov, assuming n=1.043)	0.968
Mass (GeV/c^2)	-0.815
Energy (assuming proton mass)	2.794

Time-of-flight

ßTOF	0.967

TOF Error flag	0	In Paddle Gap flag (tracking)	0
Off Edge Flag (tracking)	0	Off Edge Flag (TDC)	0

	Top	Bottom
TOF Scint. dE/dx (sqrt(E*W PMTs))	0.989	1.137
TOF PMT signal ratio (E/W)	1.193	1.632
Δx (tracking-TDC)	2.717	1.372

C2, C3 (Aerogel Cherenkov counters)

	C2	C3
pe Light yield	4.476	0.09
Map-Normalized Light yield	0.469	0.009
Map-Norm light yield, Knock-on corrected	0.464	0
ß (with index maps)	0.976	0.956
>5pe flag	0	0
Response Map (pes)	9.541+/-0.003	10.096+/-0.003
Index Map	1.045	1.046
Ratio Function	0.026	1.225

C2+C3

C2+C3 pes	4.566
C2+C3 Map-Normalized, single counter form	0.233
C2+C3 Map-Norm, single counter, Knock-on corrected	0.231
C2+C3 Map-Normalized, weighted average	0.085+/-0.134
ß (C2+C3 MN weighted average, with index maps)	0.96
Distance from C2=C3 (pes)	11.427
Distance from C2=C3 (Map-Norm)	0.106
Cherenkov software Z, best guess	1

Scintillators and C1

S1 dE/dx (mapped)	3.287
S2 dE/dx (mapped)	8.875
C1 light yield	3.568

DC+MWPC (HYBRID)

	x	y
# DC hits	10	7
# measured DC positions > 4cm off fitted track	0	0
# planes with measured positions > 4cm off fitted track	0	0
# good positions (NGx,NGy)	11	10
Chi-square	1.111	0.684
DC1, position at 3rd layer	45.606	11.955
DC2, position at 3rd layer	44.195	9.029
Deflection +/- Sigma Deflection (hybrid, DC+MWPC)	-0.319+/-0.007	
Deflection +/- Sigma Deflection (Upper DC)	-0.329+/-0.177	
Deflection +/- Sigma Deflection (Lower DC)	-0.317+/-0.140	

Positions at detectors, in DC coordinates (x,y)

Counter	x (cm)	y(cm)
Spreader bar	40.16	-14.61
Top TOF	42.72	-0.098
C1	42.972	1.328
C3	43.199	2.637
S1	43.689	5.61
C2	47.371	13.825
S2	48.277	14.78
Bottom TOF	49.705	16.301

=====

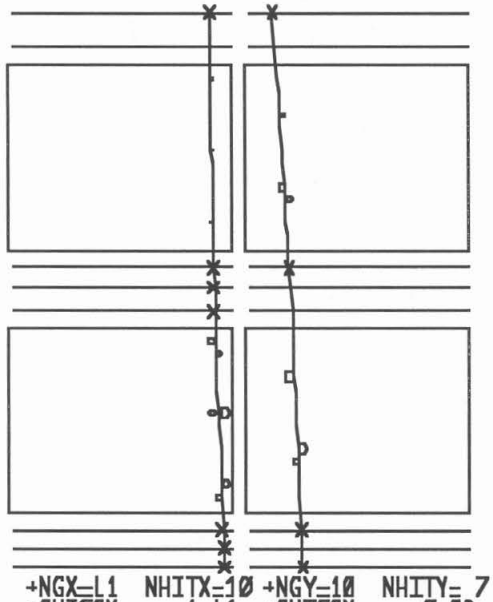

Event:	2799013
Checksum:	0
IFAIL Flag	0
Payload time:	5054 (1 count = 10 sec)

Mass, energy calculation

Rigidity (GV)	-3.92	
ßTOF	*0.984*	
Mass (GeV/c^2)	*-.710*	
Energy (assuming proton mass)	4.33	*

Time-of-flight

ßTOF	1.001		
TOF Error flag	0	In Paddle Gap flag (tracking)	0
Off Edge Flag (tracking)	0	Off Edge Flag (TDC)	0

	Top	Bottom
TOF Scint. dE/dx (sqrt(E*W PMTs))	1.035	0.948
TOF PMT signal ratio (E/W)	0.819	1.146
Δx (tracking-TDC)	3.698	3.111

C2, C3 (Aerogel Cherenkov counters)

	C2	C3
pe Light yield	-0.176	2.274
Map-Normalized Light yield	-0.017	0.234
Map-Norm light yield, Knock-on corrected	-0.018	0.224
ß (with index maps)	-1	0.964
>5pe flag	0	0
Response Map (pes)	10.154+/-0.002	9.697+/-0.003
Index Map	1.046	1.048
Ratio Function	0.794	-0.94

C2+C3	
C2+C3 pes	2.098
C2+C3 Map-Normalized, single counter form	0.106
C2+C3 Map-Norm, single counter, Knock-on corrected	0.097
C2+C3 Map-Normalized, weighted average	0.055+/-0.099
ß (C2+C3 MN weighted average, with index maps)	0.958
Distance from C2=C3 (pes)	2.53
Distance from C2=C3 (Map-Norm)	0.032
Cherenkov software Z, best guess	1

Scintillators and C1

S1 dE/dx (mapped)	2.742
S2 dE/dx (mapped)	35.46
C1 light yield	1.094

DC+MWPC (HYBRID)

	x	y
# DC hits	10	6
# measured DC positions > 4cm off fitted track	0	0
# planes with measured positions > 4cm off fitted track	0	0
# good positions (NGx,NGy)	18	10
Chi-square	2.228	1.976
DC1, position at 3rd layer	31.402	29.509
DC2, position at 3rd layer	19.753	27.639
Deflection +/- Sigma Deflection (hybrid, DC+MWPC)	-0.255+/-0.009	
Deflection +/- Sigma Deflection (Upper DC)	-0.236+/-0.068	
Deflection +/- Sigma Deflection (Lower DC)	-0.212+/-0.084	

Positions at detectors, in DC coordinates (x,y)

Counter	x (cm)	y(cm)
Spreader bar	-47.271	16.45
Top TOF	-6.289	23.29
C1	-2.261	23.962
C3	1.433	24.579
S1	9.826	25.982
C2	41.711	31.112
S2	47.149	31.957
Bottom TOF	55.834	33.307

=====

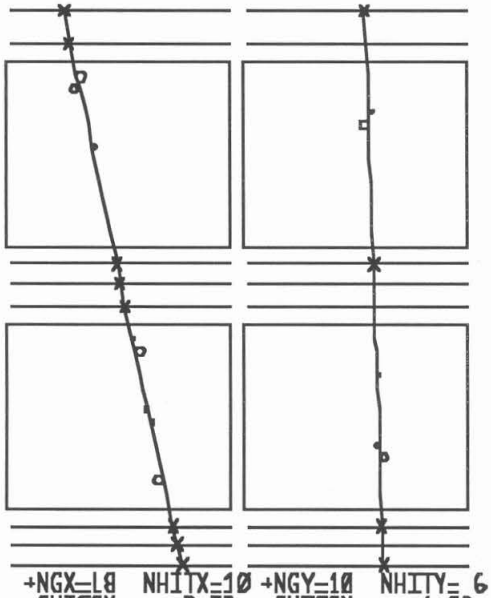

Event:	2896509
Checksum:	0
IFAIL Flag	0
Payload time:	5206 (1 count = 10 sec)

Mass, energy calculation

Rigidity (GV)	-3.896
ß (Cherenkov, assuming n=1.043)	0.971
Mass (GeV/c^2)	-0.956
Energy (assuming proton mass)	2.998

Time-of-flight

ßTOF	0.979

TOF Error flag	0	In Paddle Gap flag (tracking)	0
Off Edge Flag (tracking)	0	Off Edge Flag (TDC)	0

	Top	Bottom
TOF Scint. dE/dx (sqrt(E*W PMTs))	0.626	0.958
TOF PMT signal ratio (E/W)	1.395	1.451
Δx (tracking-TDC)	0.49	2.31

C2, C3 (Aerogel Cherenkov counters)

	C2	C3
pe Light yield	3.8	2.702
Map-Normalized Light yield	0.344	0.281
Map-Norm light yield, Knock-on corrected	0.337	0.272
ß (with index maps)	0.972	0.967
>5pe flag	0	0
Response Map (pes)	11.044+/-0.002	9.628+/-0.003
Index Map	1.044	1.047
Ratio Function	-0.459	-0.043

C2+C3

C2+C3 pes	6.503
C2+C3 Map-Normalized, single counter form	0.315
C2+C3 Map-Norm, single counter, Knock-on corrected	0.308
C2+C3 Map-Normalized, weighted average	0.311+/-0.125
ß (C2+C3 MN weighted average, with index maps)	0.97
Distance from C2=C3 (pes)	1.415
Distance from C2=C3 (Map-Norm)	0.002
Cherenkov software Z, best guess	1

Scintillators and C1

S1 dE/dx (mapped)	2.964
S2 dE/dx (mapped)	10.338
C1 light yield	1.979

DC+MWPC (HYBRID)

	x	y
# DC hits	12	8
# measured DC positions > 4cm off fitted track	0	0
# planes with measured positions > 4cm off fitted track	0	0
# good positions (NGx,NGy)	19	11
Chi-square	2.037	0.431
DC1, position at 3rd layer	23.907	15.84
DC2, position at 3rd layer	16.812	10.34
Deflection +/- Sigma Deflection (hybrid, DC+MWPC)	-0.257+/-0.003	
Deflection +/- Sigma Deflection (Upper DC)	-0.240+/-0.030	
Deflection +/- Sigma Deflection (Lower DC)	-0.094+/-0.063	

Positions at detectors, in DC coordinates (x,y)

Counter	x (cm)	y(cm)
Spreader bar	-19.836	-21.053
Top TOF	2.634	-1.876
C1	4.842	0.009
C3	6.866	1.739
S1	11.447	5.674
C2	30.679	20.709
S2	34.238	23.281
Bottom TOF	39.913	27.395

=====

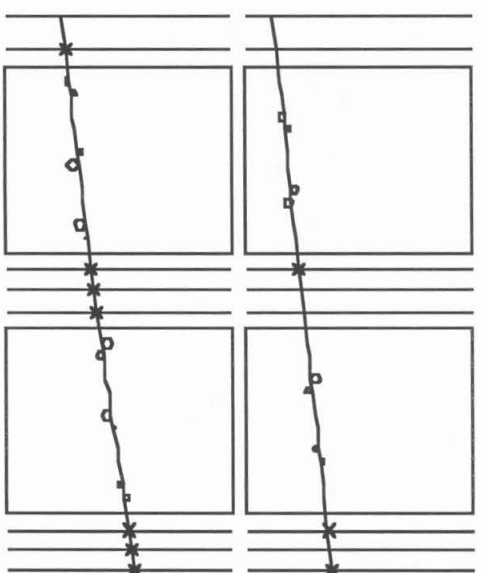

Event:	3310618
Checksum:	0
IFAIL Flag	0
Payload time:	5856 (1 count = 10 sec)

Mass, energy calculation

Rigidity (GV)	-4.045
ß (Cherenkov, assuming n=1.043)	0.972
Mass (GeV/c^2)	-0.976
Energy (assuming proton mass)	3.063

Time-of-flight

ßTOF	0.975

TOF Error flag	0	In Paddle Gap flag (tracking)	0
Off Edge Flag (tracking)	0	Off Edge Flag (TDC)	0

	Top	Bottom
TOF Scint. dE/dx (sqrt(E*W PMTs))	0.84	0.622
TOF PMT signal ratio (E/W)	0.675	0.846
Δx (tracking-TDC)	0.929	1.906

C2, C3 (Aerogel Cherenkov counters)

	C2	C3
pe Light yield	3.987	3.781
Map-Normalized Light yield	0.381	0.302
Map-Norm light yield, Knock-on corrected	0.374	0.294
ß (with index maps)	0.972	0.969
>5pe flag	0	0
Response Map (pes)	10.458+/-0.002	12.531+/-0.002
Index Map	1.046	1.046
Ratio Function	0.009	0.961

C2+C3

C2+C3 pes	7.767
C2+C3 Map-Normalized, single counter form	0.338
C2+C3 Map-Norm, single counter, Knock-on corrected	0.332
C2+C3 Map-Normalized, weighted average	0.333+/-0.123
ß (C2+C3 MN weighted average, with index maps)	0.97
Distance from C2=C3 (pes)	0.412
Distance from C2=C3 (Map-Norm)	0.003
Cherenkov software Z, best guess	1

Scintillators and C1

S1 dE/dx (mapped)	2.603
S2 dE/dx (mapped)	10.9
C1 light yield	0.426

DC+MWPC (HYBRID)

	x	y
# DC hits	12	8
# measured DC positions > 4cm off fitted track	0	0
# planes with measured positions > 4cm off fitted track	0	0
# good positions (NGx,NGy)	18	9
Chi-square	0.275	0.35
DC1, position at 3rd layer	27.349	33.983
DC2, position at 3rd layer	21.908	31.071
Deflection +/- Sigma Deflection (hybrid, DC+MWPC)	-0.247+/-0.007	
Deflection +/- Sigma Deflection (Upper DC)	-0.277+/-0.077	
Deflection +/- Sigma Deflection (Lower DC)	-0.206+/-0.092	

Positions at detectors, in DC coordinates (x,y)

Counter	x (cm)	y(cm)
Spreader bar	-8.263	13.628
Top TOF	10.179	24.291
C1	11.991	25.338
C3	13.653	26.3
S1	17.424	28.488
C2	32.278	36.477
S2	34.886	37.791
Bottom TOF	39.049	39.891

=====

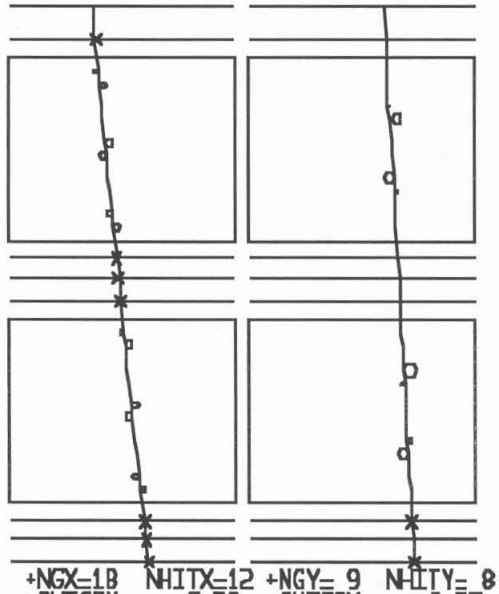

Event:	3454056
Checksum:	0
IFAIL Flag	0
Payload time:	6085 (1 count = 10 sec)

Mass, energy calculation

Rigidity (GV)	-1.202
ßTOF	0.789
Mass (GeV/c^2)	-0.936
Energy (assuming proton mass)	0.589

Time-of-flight

ßTOF	0.789

TOF Error flag	0	In Paddle Gap flag (tracking)	0
Off Edge Flag (tracking)	0	Off Edge Flag (TDC)	0

	Top	Bottom
TOF Scint. dE/dx (sqrt(E*W PMTs))	1.369	0.944
TOF PMT signal ratio (E/W)	0.811	1.313
Δx (tracking-TDC)	1.113	2.036

C2, C3 (Aerogel Cherenkov counters)

	C2	C3
pe Light yield	-0.008	-0.103
Map-Normalized Light yield	-0.001	-0.008
Map-Norm light yield, Knock-on corrected	-0.001	-0.009
ß (with index maps)	-1	-1
>5pe flag	0	0
Response Map (pes)	11.121+/-0.002	12.107+/-0.002
Index Map	1.043	1.046
Ratio Function	1000000	-0.589

C2+C3

C2+C3 pes	-0.111
C2+C3 Map-Normalized, single counter form	-0.005
C2+C3 Map-Norm, single counter, Knock-on corrected	-0.005
C2+C3 Map-Normalized, weighted average	-0.005+/-0.029
ß (C2+C3 MN weighted average, with index maps)	0.956
Distance from C2=C3 (pes)	0.004
Distance from C2=C3 (Map-Norm)	0
Cherenkov software Z, best guess	1

Scintillators and C1

S1 dE/dx (mapped)	4.723
S2 dE/dx (mapped)	13.236
C1 light yield	-0.036

DC+MWPC (HYBRID)

	x	y
# DC hits	11	7
# measured DC positions > 4cm off fitted track	0	0
# planes with measured positions > 4cm off fitted track	0	0
# good positions (NGx,NGy)	18	8
Chi-square	0.467	1.282
DC1, position at 3rd layer	25.977	19.451
DC2, position at 3rd layer	31.104	21.614
Deflection +/- Sigma Deflection (hybrid, DC+MWPC)	-0.832+/-0.008	
Deflection +/- Sigma Deflection (Upper DC)	-0.742+/-0.064	
Deflection +/- Sigma Deflection (Lower DC)	-0.831+/-0.066	

Positions at detectors, in DC coordinates (x,y)

Counter	x (cm)	y(cm)
Spreader bar	75.205	33.456
Top TOF	48.289	26.232
C1	45.644	25.522
C3	43.209	24.871
S1	37.633	23.386
C2	23.429	17.459
S2	22.102	16.401
Bottom TOF	19.93	14.708

=====

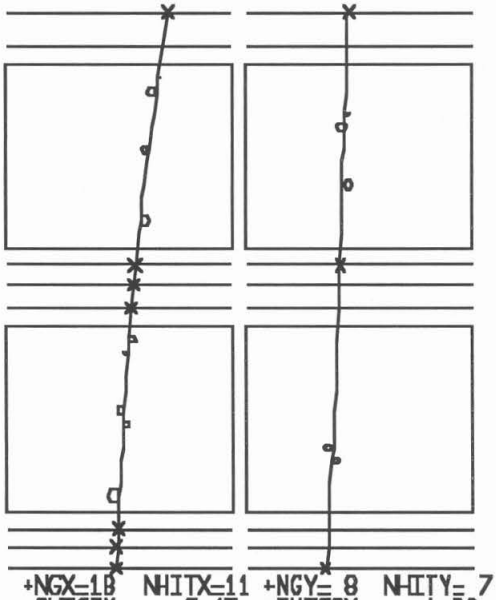

Event:	3680471
Checksum:	0
IFAIL Flag	0
Payload time:	6449 (1 count = 10 sec)

Mass, energy calculation

Rigidity (GV)	-3.346	
ßTOF	0.973	
Mass (GeV/c^2)	-0.79	
Energy (assuming proton mass)	3.142	*

Time-of-flight

ßTOF	0.973		
TOF Error flag	0	In Paddle Gap flag (tracking)	0
Off Edge Flag (tracking)	0	Off Edge Flag (TDC)	0

	Top	Bottom
TOF Scint. dE/dx (sqrt(E*W PMTs))	0.781	1.118
TOF PMT signal ratio (E/W)	1.251	1.068
Δx (tracking-TDC)	1.1	0.657

C2, C3 (Aerogel Cherenkov counters)

	C2	C3
pe Light yield	1.478	0.874
Map-Normalized Light yield	0.129	0.07
Map-Norm light yield, Knock-on corrected	0.118	0.051
ß (with index maps)	0.964	0.96
>5pe flag	0	0
Response Map (pes)	11.423+/-0.002	12.457+/-0.002
Index Map	1.043	1.045
Ratio Function	-0.999	-0.977

C2+C3

C2+C3 pes	2.351
C2+C3 Map-Normalized, single counter form	0.098
C2+C3 Map-Norm, single counter, Knock-on corrected	0.084
C2+C3 Map-Normalized, weighted average	0.092+/-0.068
ß (C2+C3 MN weighted average, with index maps)	0.962
Distance from C2=C3 (pes)	0.332
Distance from C2=C3 (Map-Norm)	0.002
Cherenkov software Z, best guess	1

Scintillators and C1

S1 dE/dx (mapped)	3.023
S2 dE/dx (mapped)	10.41
C1 light yield	1.329

DC+MWPC (HYBRID)

	x	y
# DC hits	10	8
# measured DC positions > 4cm off fitted track	0	0
# planes with measured positions > 4cm off fitted track	0	0
# good positions (NGx,NGy)	15	10
Chi-square	0.331	0.958
DC1, position at 3rd layer	23.50c	11.06
DC2, position at 3rd layer	25.979	10.949
Deflection +/- Sigma Deflection (hybrid, DC+MWPC)	-0.299+/-0.004	
Deflection +/- Sigma Deflection (Upper DC)	-0.292+/-0.089	
Deflection +/- Sigma Deflection (Lower DC)	-0.355+/-0.052	

Positions at detectors, in DC coordinates (x,y)

Counter	x (cm)	y(cm)
Spreader bar	48.66	10.697
Top TOF	34.852	10.847
C1	33.495	10.861
C3	32.246	10.875
S1	29.383	10.906
C2	22.397	11.202
S2	21.796	11.28
Bottom TOF	20.813	11.405

=====

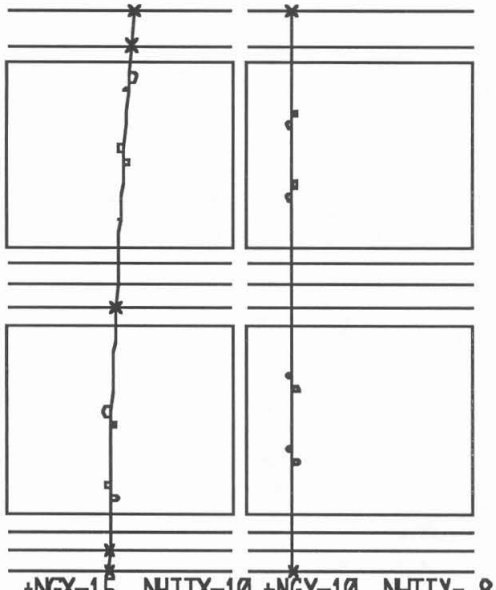

Event:	3837134
Checksum:	0
IFAIL Flag	0
Payload time:	6703 (1 count = 10 sec)

Mass, energy calculation

Rigidity (GV)	-1.979
ßTOF	0.903
Mass (GeV/c^2)	-0.943
Energy (assuming proton mass)	1.243

Time-of-flight

ßTOF 0.903

TOF Error flag	0	In Paddle Gap flag (tracking)	0
Off Edge Flag (tracking)	0	Off Edge Flag (TDC)	0

	Top	Bottom
TOF Scint. dE/dx (sqrt(E*W PMTs))	1.369	0.894
TOF PMT signal ratio (E/W)	0.892	1.296
Δx (tracking-TDC)	0.246	0.092

C2, C3 (Aerogel Cherenkov counters)

	C2	C3
pe Light yield	0.013	-0.058
Map-Normalized Light yield	0.001	-0.005
Map-Norm light yield, Knock-on corrected	0	-0.005
ß (with index maps)	0.958	-1
>5pe flag	0	0
Response Map (pes)	10.971+/-0.002	12.691+/-0.002
Index Map	1.044	1.045
Ratio Function	1.411	-0.561

C2+C3	
C2+C3 pes	-0.045
C2+C3 Map-Normalized, single counter form	-0.002
C2+C3 Map-Norm, single counter, Knock-on corrected	-0.003
C2+C3 Map-Normalized, weighted average	-0.002+/-0.030
ß (C2+C3 MN weighted average, with index maps)	0.957
Distance from C2=C3 (pes)	0.002
Distance from C2=C3 (Map-Norm)	0
Cherenkov software Z, best guess	1

Scintillators and C1

S1 dE/dx (mapped)	3.993
S2 dE/dx (mapped)	12.677
C1 light yield	1.583

DC+MWPC (HYBRID)

	x	y
# DC hits	10	5
# measured DC positions > 4cm off fitted track	0	0
# planes with measured positions > 4cm off fitted track	0	0
# good positions (NGx,NGy)	17	9
Chi-square	0.64	0.162
DC1, position at 3rd layer	31.797	21.27
DC2, position at 3rd layer	32.441	21.306
Deflection +/- Sigma Deflection (hybrid, DC+MWPC)	-0.505+/-0.009	
Deflection +/- Sigma Deflection (Upper DC)	-0.573+/-0.057	
Deflection +/- Sigma Deflection (Lower DC)	-0.741+/-0.105	

Positions at detectors, in DC coordinates (x,y)

Counter	x (cm)	y(cm)
Spreader bar	43.946	19.615
Top TOF	36.942	20.677
C1	36.254	20.781
C3	35.618	20.877
S1	34.146	21.091
C2	32.222	21.022
S2	32.456	20.877
Bottom TOF	32.804	20.64

=====

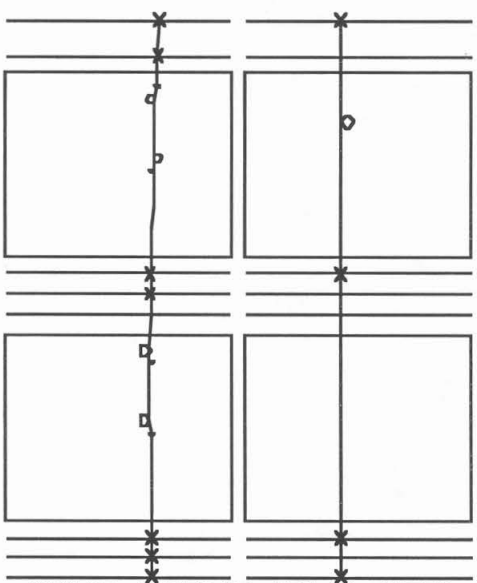

Event:	4339971
Checksum:	0
IFAIL Flag	0
Payload time:	7529 (1 count = 10 sec)

Mass, energy calculation

Rigidity (GV)	-2.723
ßTOF	0.939
Mass (GeV/c^2)	-0.993
Energy (assuming proton mass)	1.8

Time-of-flight

ßTOF	0.939		
TOF Error flag	0	In Paddle Gap flag (tracking)	0
Off Edge Flag (tracking)	0	Off Edge Flag (TDC)	0

	Top	Bottom
TOF Scint. dE/dx (sqrt(E*W PMTs))	1.033	0.828
TOF PMT signal ratio (E/W)	0.858	0.822
Δx (tracking-TDC)	2.797	1.116

C2, C3 (Aerogel Cherenkov counters)

	C2	C3
pe Light yield	0.667	0.043
Map-Normalized Light yield	0.068	0.003
Map-Norm light yield, Knock-on corrected	0.055	0
ß (with index maps)	0.959	0.956
>5pe flag	0	0
Response Map (pes)	9.831+/-0.002	12.600+/-0.002
Index Map	1.046	1.047
Ratio Function	0.82	1.349

C2+C3	
C2+C3 pes	0.71
C2+C3 Map-Normalized, single counter form	0.032
C2+C3 Map-Norm, single counter, Knock-on corrected	0.025
C2+C3 Map-Normalized, weighted average	0.028+/-0.049
ß (C2+C3 MN weighted average, with index maps)	0.957
Distance from C2=C3 (pes)	0.235
Distance from C2=C3 (Map-Norm)	0.002
Cherenkov software Z, best guess	1

Scintillators and C1

S1 dE/dx (mapped)	3.173
S2 dE/dx (mapped)	12.065
C1 light yield	1.154

DC+MWPC (HYBRID)

	x	y
# DC hits	10	6
# measured DC positions > 4cm off fitted track	0	0
# planes with measured positions > 4cm off fitted track	0	0
# good positions (NGx,NGy)	15	7
Chi-square	0.391	0.903
DC1, position at 3rd layer	33.574	40.315
DC2, position at 3rd layer	30.759	36.413
Deflection +/- Sigma Deflection (hybrid, DC+MWPC)	-0.367+/-0.011	
Deflection +/- Sigma Deflection (Upper DC)	-0.530+/-0.184	
Deflection +/- Sigma Deflection (Lower DC)	-0.294+/-0.227	

Positions at detectors, in DC coordinates (x,y)

Counter	x (cm)	y(cm)
Spreader bar	16.967	12.262
Top TOF	25.38	27.044
C1	26.207	28.497
C3	26.963	29.83
S1	28.676	32.86
C2	36.295	43.584
S2	37.747	45.299
Bottom TOF	40.064	48.038

=====

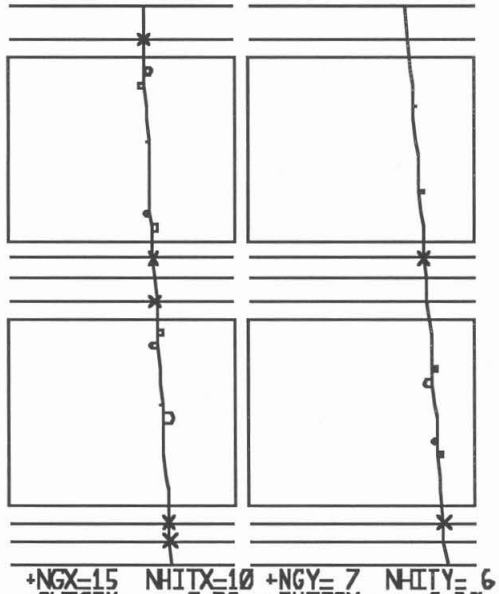

Event:	4377456
Checksum:	0
IFAIL Flag	0
Payload time:	7591 (1 count = 10 sec)

Mass, energy calculation

Rigidity (GV)	-2.555
ßTOF	0.946
Mass (GeV/c^2)	-0.876
Energy (assuming proton mass)	1.953

Time-of-flight

ßTOF 0.946

TOF Error flag	0	In Paddle Gap flag (tracking)	0
Off Edge Flag (tracking)	0	Off Edge Flag (TDC)	0

	Top	Bottom
TOF Scint. dE/dx (sqrt(E*W PMTs))	0.917	1.018
TOF PMT signal ratio (E/W)	0.68	1.519
Δx (tracking-TDC)	0.039	0.301

C2, C3 (Aerogel Cherenkov counters)

	C2	C3
pe Light yield	-0.135	-0.552
Map-Normalized Light yield	-0.013	-0.046
Map-Norm light yield, Knock-on corrected	-0.013	-0.05
ß (with index maps)	-1	-1
>5pe flag	0	0
Response Map (pes)	10.736+/-0.002	11.962+/-0.002
Index Map	1.045	1.046
Ratio Function	-0.438	-0.557

C2+C3

C2+C3 pes	-0.687
C2+C3 Map-Normalized, single counter form	-0.03
C2+C3 Map-Norm, single counter, Knock-on corrected	-0.032
C2+C3 Map-Normalized, weighted average	-0.031+/-0.024
ß (C2+C3 MN weighted average, with index maps)	0.955
Distance from C2=C3 (pes)	0.063
Distance from C2=C3 (Map-Norm)	0.001
Cherenkov software Z, best guess	1

Scintillators and C1

S1 dE/dx (mapped)	2.702
S2 dE/dx (mapped)	16.724
C1 light yield	0.734

DC+MWPC (HYBRID)

	x	y
# DC hits	11	7
# measured DC positions > 4cm off fitted track	0	0
# planes with measured positions > 4cm off fitted track	0	0
# good positions (NGx,NGy)	16	9
Chi-square	1.88	3.803
DC1, position at 3rd layer	25.849	27.443
DC2, position at 3rd layer	18.344	27.091
Deflection +/- Sigma Deflection (hybrid, DC+MWPC)	-0.391+/-0.009	
Deflection +/- Sigma Deflection (Upper DC)	-0.513+/-0.077	
Deflection +/- Sigma Deflection (Lower DC)	-0.346+/-0.085	

Positions at detectors, in DC coordinates (x,y)

Counter	x (cm)	y(cm)
Spreader bar	-22.121	25.658
Top TOF	2.625	26.521
C1	5.057	26.606
C3	7.286	26.684
S1	12.342	26.863
C2	32.861	27.821
S2	36.569	28.027
Bottom TOF	42.484	28.358

=====

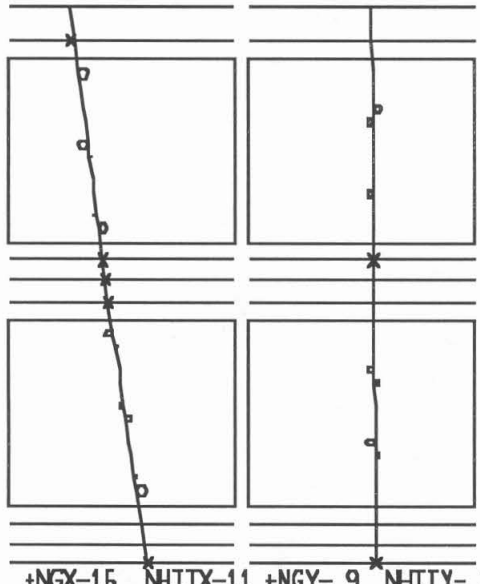

Event:	4800072
Checksum:	0
IFAIL Flag	0
Payload time:	8300 (1 count = 10 sec)

Mass, energy calculation

Rigidity (GV)	-3.006
ßTOF	0.926
Mass (GeV/c^2)	-1.223
Energy (assuming proton mass)	1.551

Time-of-flight

ßTOF 0.926

TOF Error flag	0	In Paddle Gap flag (tracking)	0
Off Edge Flag (tracking)	0	Off Edge Flag (TDC)	0

	Top	Bottom
TOF Scint. dE/dx (sqrt(E*W PMTs))	0.905	0.748
TOF PMT signal ratio (E/W)	0.815	0.919
Δx (tracking-TDC)	1.204	1.674

C2, C3 (Aerogel Cherenkov counters)

	C2	C3
pe Light yield	0.109	-0.121
Map-Normalized Light yield	0.01	-0.01
Map-Norm light yield, Knock-on corrected	0.001	-0.01
ß (with index maps)	0.959	-1
>5pe flag	0	0
Response Map (pes)	11.253+/-0.002	12.606+/-0.002
Index Map	1.043	1.045
Ratio Function	1.049	-0.828

C2+C3

C2+C3 pes	-0.012
C2+C3 Map-Normalized, single counter form	-0.001
C2+C3 Map-Norm, single counter, Knock-on corrected	-0.005
C2+C3 Map-Normalized, weighted average	-0.001+/-0.031
ß (C2+C3 MN weighted average, with index maps)	0.957
Distance from C2=C3 (pes)	0.026
Distance from C2=C3 (Map-Norm)	0
Cherenkov software Z, best guess	1

Scintillators and C1

S1 dE/dx (mapped)	3.794
S2 dE/dx (mapped)	11.144
C1 light yield	2.605

DC+MWPC (HYBRID)

	x	y
# DC hits	9	8
# measured DC positions > 4cm off fitted track	0	0
# planes with measured positions > 4cm off fitted track	0	0
# good positions (NGx,NGy)	14	8
Chi-square	1.65	1.088
DC1, position at 3rd layer	17.75	13.699
DC2, position at 3rd layer	18.184	14.198
Deflection +/- Sigma Deflection (hybrid, DC+MWPC)	-0.333+/-0.007	
Deflection +/- Sigma Deflection (Upper DC)	-0.233+/-0.078	
Deflection +/- Sigma Deflection (Lower DC)	-0.268+/-0.050	

Positions at detectors, in DC coordinates (x,y)

Counter	x (cm)	y(cm)
Spreader bar	27.597	19.718
Top TOF	21.891	16.313
C1	21.33	15.978
C3	20.812	15.671
S1	19.613	14.975
C2	18.268	13.57
S2	18.53	13.519
Bottom TOF	18.925	13.439

=====

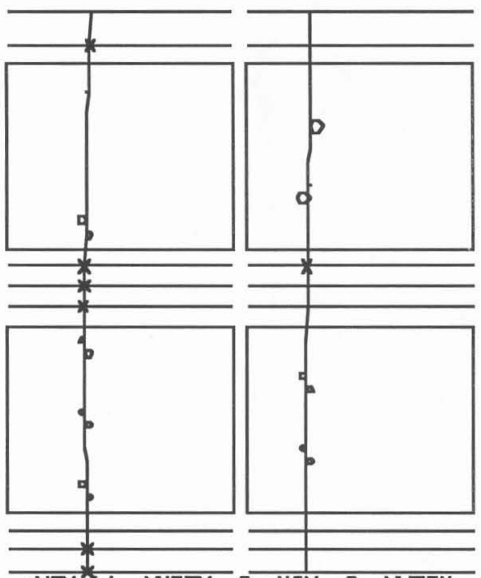

Event:	4918744
Checksum:	0
IFAIL Flag	0
Payload time:	8499 (1 count = 10 sec)

Mass, energy calculation

Rigidity (GV)	-1.397
ßTOF	0.838
Mass (GeV/c^2)	-0.909
Energy (assuming proton mass)	0.783

Time-of-flight

ßTOF	0.838

TOF Error flag	0	In Paddle Gap flag (tracking)	0
Off Edge Flag (tracking)	0	Off Edge Flag (TDC)	0

	Top	Bottom
TOF Scint. dE/dx (sqrt(E*W PMTs))	1.173	1.156
TOF PMT signal ratio (E/W)	0.677	1.217
Δx (tracking-TDC)	3.286	1.653

C2, C3 (Aerogel Cherenkov counters)

	C2	C3
pe Light yield	-0.404	-0.426
Map-Normalized Light yield	-0.037	-0.037
Map-Norm light yield, Knock-on corrected	-0.038	-0.04
ß (with index maps)	-1	-1
>5pe flag	0	0
Response Map (pes)	11.065+/-0.002	11.624+/-0.002
Index Map	1.044	1.045
Ratio Function	-0.766	0.047

C2+C3	
C2+C3 pes	-0.83
C2+C3 Map-Normalized, single counter form	-0.037
C2+C3 Map-Norm, single counter, Knock-on corrected	-0.039
C2+C3 Map-Normalized, weighted average	-0.037+/-0.018
ß (C2+C3 MN weighted average, with index maps)	0.956
Distance from C2=C3 (pes)	0.001
Distance from C2=C3 (Map-Norm)	0
Cherenkov software Z, best guess	1

Scintillators and C1

S1 dE/dx (mapped)	5.648
S2 dE/dx (mapped)	18.949
C1 light yield	0.892

DC+MWPC (HYBRID)

	x	y
# DC hits	9	6
# measured DC positions > 4cm off fitted track	0	0
# planes with measured positions > 4cm off fitted track	0	0
# good positions (NGx,NGy)	13	7
Chi-square	0.8	0.378
DC1, position at 3rd layer	31.935	22.212
DC2, position at 3rd layer	35.894	22.468
Deflection +/- Sigma Deflection (hybrid, DC+MWPC)	-0.715+/-0.008	
Deflection +/- Sigma Deflection (Upper DC)	-0.340+/-0.175	
Deflection +/- Sigma Deflection (Lower DC)	-0.669+/-0.146	

Positions at detectors, in DC coordinates (x,y)

Counter	x (cm)	y(cm)
Spreader bar	69.635	20.857
Top TOF	49.047	21.889
C1	47.024	21.991
C3	45.161	22.083
S1	40.89	22.289
C2	29.874	21.626
S2	28.807	21.29
Bottom TOF	27.066	20.746

=====

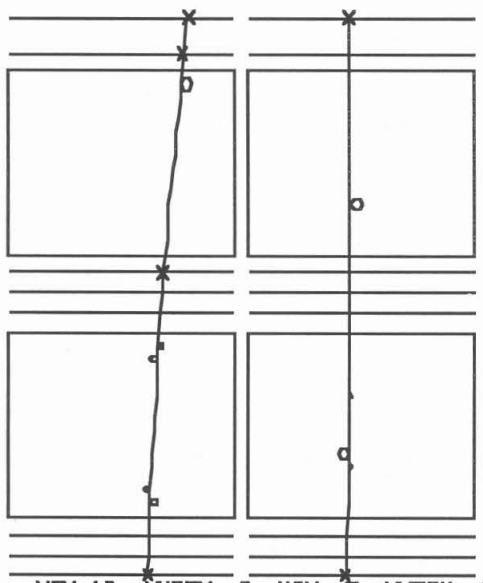

References

Ahlen, S.P., Barwick, S., Beatty, J.J., Bower, C.R., Gerbier, G., Heinz, R.M., Lowder, D., McKee, S., Mufson, S., Musser, J.A., Price, P.B., Salamon, M.H., Tarlé, G., Tomasch, A., and Zhou, B., *Physical Review Letters*, **61**, 145 (1988).

Anders, E. and Grevesse, N., *Geochimica et Cosmochimica Acta*, **53**, 197 (1989).

Apparao, M.V.K., Daniel, R.R., and Neelakantan, K.A., *Proc. Indian Academy of Sciences*, **43A**, 181 (1956).

Badhwar, G.D. et al., *Proc. 15th International Cosmic Ray Conference, Plovdiv*, **1**, 204 (1977).

Barwick, S.W., Ahlen, S.P., Beatty, J.J., Bower, C.R., Heinz, R.M., Lowder, D.M., McKee, S., Miller, J.L., Mufson, S.L., Musser, J.A., Price, P.B., Salamon, M.H., Tarlé, G., Tomasch, A., Zhou, B., *Proc. 21st International Cosmic Ray Conference, Adelaide*, **3**, 273 (1990).

Bell, A.R., *Monthly Notices of the Royal Astronomical Society*, **182**, 147 (1978).

Berezinskii, V.S., Bulanov, S.V., Dogiel, V.A., Ginzburg, V.L., and Ptuskin, V.S., *Astrophysics of Cosmic Rays*, North–Holland, Elsevier Science Publishers B.V., Amsterdam (1990).

Bialas, A., Bleszynski, M., and Czyz, W., *Nuclear Physics B*, **111**, 461 (1976).

Bieber, J. W., et al., *Astrophysical Journal*, **420**, 294 (1994).

Blandford, R.D and Ostriker, J.P., *Astrophysical Journal*, **221**, L29 (1978).

Blum, W., and Rolandi, L., *Particle Detection with Drift Chambers*, Springer–Verlag, New York, 1993.

Bogomolov, E.A., Lubyanaya, N.D., and Romanov, V.A., *Proc. 12th International Cosmic Ray Conference, Hobart*, **5**, 1730 (1971).

Bogomolov, E.A., Lubyanaya, N.D., Romanov, V.A., Stepanov, S.V., and Shulkova, M.S., *Proc. 16th International Cosmic Ray Conference, Kyoto*, **1**, 330 (1979).

Bogomolov, E.A, et al., *Proc. 17th International Cosmic Ray Conference, Paris*, **9**, 146 (1981).

Bogomolov, E.A., Vasilyev, G.I., Krut'kov, S.Yu., Lubyanaya, N.D., Romanov, V.A., Stepanov, S.V., and Shulakova, M.S., *Proc. 20th International Cosmic Ray Conference, Moscow*, **2**, 72 (1987).

Bogomolov, E.A., Vasilyev, G.I., Krut'kov, S.Yu., Lubyanaya, N.D., Romanov, V.A., Stepanov, S.V., and Shulakova, M.S., *Proc. 21st International Cosmic Ray Conference, Adelaide*, **3**, 288 (1990).

Brick, D.H., et al., *Physical Review D*, **39**, 2484 (1989).

Buffington, A. Private communication (1995).

Buffington, A., Schindler, S.M., and Pennypacker, C.R., *Astrophysical Journal*, **248**, 1179 (1981).

Burger, R. A., & Potgieter, M. S., *Astrophysical Journal*, **339**, 501 (1989).

Chamberlain, O., Sarge, E., Wiegand, C., and Ypsilantis, T., *Physical Review*, **100**, 947 (1955).

Clem, J.M., Clements, D., Constantin, C., Esposito, J., Evenson, P.A., Huber, D., and L'Heureux, J., *Proc. 24th International Cosmic Ray Conference, Rome*, **3**, 5 (1995).

Cowsik, R. and Gaisser, T.K., *Proc. 17th International Cosmic Ray Conference, Paris*, **2**, 218 (1981).

Davis, A.J. Private communication (1994). (MAGSPEC Version 2.1.)

Davis, A.J., Menn, W., Barbier, L.M., Christian, E.R., Golden, R.L., Hof, M., Krombel, K.E., Labrador, A.W., Mewaldt, R.A., Mitchell, J.W., Ormes, J.F., Rasmussen, I.L., Reimer, O., Schindler, S.M., Simon, M., Stochaj, S.J., Streitmatter, R.E., Webber, W.R., *Proc. 24th International Cosmic Ray Conference, Rome*, **2**, 622 (1995).

Denisov, S.P., Donskov, S.V., Gorin, Yu.P., Krasnokutsky, R.N., Petrukhin, A.I., Prokoshkin, Yu.D., and Stoyanova, D.A., *Nuclear Physics*, **B61**, 62 (1973).

Diehl, E., Kane, G.L., Kolda, C., Wells, J.D., *Physical Review D*, **52**, 4223 (1995).

Engelmann, J.J., Ferrando, P., Soutoul, A., Goret, P., Juliusson, E., Koch-Miramond, L., Lund, N., Masse, P., Peters, B., Petrou, N., and Rasmussen, I.L, *Astronomy and Astrophysics*, **233**, 96 (1990).

Evenson, P., et al., *Astrophysical Journal*, **275**, L15 (1983).

Evenson, P., et al., Proc. 19th International Cosmic Ray Conference, La Jolla, 2, 60 (1985).

Faessler, M.A., Physics Reports, **115**, 1 (1984).

Fisk, L.A., *Journal of Geophysical Research*, **76**, 221 (1971).

Flaminio, V., et al. *Compilation of Cross Sections III: p and pbar Induced Reactions*, CERN–HERA 84-01 (1984).

Gaisser, T.K., and Maurer, R.H., *Physical Review Letters*, **30**, 1264 (1973).

Gaisser, T.K., and Schaefer, R.K., *Astrophysical Journal*, **394**, 174 (1992).

Garcia–Muñoz, M., and Simpson, J.A., *Space Science Reviews*, **46**, 205 (1988).

Garcia–Muñoz, M., Simpson, J.A., Guzik, T.G., Wefel, J.P., Margolis, S.H., *Astrophysical Journal Supplement*, **64**, 269 (1987).

Gibner, P.S., Ph.D. Thesis, California Institute of Technology, 1992. (Unpublished)

Ginzburg, V.L, and Syrovatskii, S.I. *The Origin of Cosmic Rays* (Pergamon Press: New York, 1964).

Gleeson, L. J., and Axford, W. I., *Astrophysical Journal*, **154**, 1011 (1968).

Gleeson, L.J., and Urch, I.H., *Astrophysics and Space Science*, **11**, 288 (1971).

Gluckstern, R.L., *Nuclear Instruments and Methods in Physics Research*, **24**, 381 (1963).

Golden, R.L., Horan, S., Mauger, B.G., Badhwar, G.D., Lacy, J.L., Stephens, S.A., Daniel, R.R., and Zipse, J.E., *Physical Review Letters*, **43**, 1196 (1979).

Golden, R.L., Mauger, B.G., Nunn, S., and Horan, S., *Astrophysical Letters*, **24**, 75 (1984).

Golden, R.L., et al., *Nuclear Instruments and Methods in Physics Research*, **A306**, 366 (1991).

Golden, R.L., et al., *Astrophysical Journal*, **436**, 769 (1994).

Goldstein, M. L., Fisk, L. A., & Ramaty, R., *Physical Review Letters*, **25**, 832 (1970).

Grove, J.E., Ph.D. Thesis, California Institute of Technology (1989).

Grove, J.E., and Mewaldt, R.A. *Nuclear Instruments and Methods in Physics Research*, **A314**, 495 (1992).

Gupta, M., and Webber, W.R., *Astrophysical Journal*, **340**, 1124 (1989).

Hawking, S.W., *Nature*, **248**, 30 (1974).

Heinbach, U. and Simon, M., *Proc. 21st International Cosmic Ray Conf., Adelaide*, **3**, 361 (1990).

Heinbach, U. and Simon, M., *Astrophysical Journal*, **441**, 209 (1995).

Henning, S. and Svensson, L., *Physica Scripta*, **23**, 697 (1981).

Hess, V. K., *Physik Z.* , **13**, 1084 (1912).

Hof, M., Bremerich, M., Menn, W., Mitchell, J.W., Reimer, O., and Simon, M., *Proc. of the 23rd International Cosmic Ray Conference, Calgary*, **2**, 544 (1993).

Hof, M., Bremerich, M., Menn, W., Pfeifer, C., Reimer, O., Simon, M., Mitchell, J.W., Barbier, L.M., Christian, E.R., Ormes, J.F., Streitmatter, R.E., and Stochaj, S.J., *Nuclear Instruments and Methods in Physics Research*, **A345**, 561 (1994).

Hof, M., et al., *Proc. 24th International Cosmic Ray Conference, Rome*, 3, 60 (1995).

Israel, M. SRL Internal Report #4 (1968).

Jackson, J.D., *Classical Electrodynamics, 2nd Ed.*, John Wiley & Sons, New York (1975).

Janni, J.F., Air Force Weapons Laboratory, Technical Report 65-150 (1966).

Kadija, K., Schmitz, N., and Seyboth, P., *Zeitschrift Für Physik C*, **71**, 239 (1996).

Knoll, G.F., *Radiation Detection and Measurement, 2nd Ed.* John Wiley & Sons, New York (1989).

Kóta, J. & Jokipii, J. R., *Astrophysical Journal*, **265**, 573 (1983).

Koyama, K., Petre, R., Gotthelf, E.V., Hwang, U., Matsuura, M., Ozaki, M., and Holt, S.S., *Nature*, **378**, 255 (1995).

Krombel, K.E., and Wiedenbeck, M.E., *Astrophysical Journal*, **328**, 940 (1988).

Krizmanic, J.F. Private communication (1995).

Kuzichev, V.F., Lepikhin, Yu.B., and Smirnitsky, V.A., *Nuclear Physics* , A**576**, 581 (1994).

Labrador, A.W., Mewaldt, R.A., Schindler, S.M., Stone, E.C., Barbier, L.M., Christian, E.R., Mitchell, J.W., Streitmatter, R.E., Stochaj, S.J., and Rasmussen, I.L., *Proc. 23rd International Cosmic Ray Conference, Calgary*, **2**, 524 (1993).

Labrador, A. W., and Mewaldt, R. A. , *Proc. 24th International Cosmic Ray Conference, Rome*, **3**, 68 (1995).

Lacy, J.L., and Lindsey, R.S., *Nuclear Instruments and Methods in Physics Research*, **119**, 483 (1974).

Lagage, P.O. and Cesarsky, C.J., *Astronomy and Astrophysics*, **147**, 127 (1985).

Lezniak, J.A. *Nuclear Instruments and Methods in Physics Research*, **136**, 299 (1976).

Lukasiak, A., Ferrando, P., McDonald, F.B., and Webber, W.R., *Ap. J.* **423**, 426 (1994).

Lund, N., *Advances in Space Research*, **4**, 5 (1984).

McGuire, P.C., Ph. D. Thesis, University of Arizona (1994). Unpublished.

McGuire, W., Schuster, P., & McDonald, F. Private communication (1995).

Menn, W., Barbier, L.M., Christian, E.R, Hof, M., Mitchell, J.W., Ormes, J.F., Pfeifer, C., Simon, M. Stochaj, S.J., and Streitmatter, R.E., Proc. of the 23rd International Cosmic Ray Conference, Calgary, **2**, 548 (1993).

Menn, W. Private communication (1994).

Menn, W. Private communication (1995).

Millikan, R. A., and Cameron, G. H., *Physical Review*, **28**, 851 (1926).

Mitchell, J.W., Barbier, L.M., Christian, E.R., Golden, R.L., Hof, M., Labrador, A.W., Menn, W., Mewaldt, R.A., Ormes, J.F., Rasmussen, I.L., Reimer, O., Schindler, S.M., Simon, M., Stochaj, S.J., Streitmatter, R.E., and Webber, W.R., *Proc. 23rd International Cosmic Ray Conference, Calgary*, **1**, 519 (1993a).

Mitchell, J.W., Barbier, L.M., Christian, E.R., Hof, M., Holder, S.F., Labrador, A.W., Menn, W., Ormes, J.F., Reimer, O., Righter, D.L., Simon, M., Stochaj, S.J., and Streitmatter, R.E., *Proc. 23rd International Cosmic Ray Conference, Calgary*, **2**, 627 (1993b).

Moats, A., Bowen, T., Streitmatter, R.E., Stochaj, S.J., Ormes, J.F., Barbier, L., Golden, R.L., Stephens, S.A., and Evans, J.L., *Proc. 21st International Cosmic Ray Conference, Adelaide*, **3**, 284 (1990).

Montanet, L. et al., *Physical Review*, **D50**, 1173 (1994).

Orth, C.D., and Buffington, A., *Astrophysical Journal*, **206**, 312 (1976).

Palmer, I. D., *Revews of Geophysics and Space Physics*, **20**, 335 (1982).

Pantuev, V.S., Filippov, S.N., and Kurepin, A.B., *Nuclear Physics A*, **585**, 13c (1995).

Papini, P., Grimani, C., and Stephens, S.A., *Proc. 23rd International Cosmic Ray Conference, Calgary*, **3**, 761 (1993).

Particle Data Group, *Particle Properties Data Booklet*, AIP, June 1992.

Peebles, P.J.E., *Principles of Physical Cosmology.*, Princeton University Press, Princeton (1993).

Perko, J. S., *Astrophysical Journal*, **397**, 153 (1992).

Peters, B., and Westergaard, N.J., *Ap. Space Sci.*, **48**, 21 (1977).

Pfeifer, Ch., Rösler, St., and Simon, M., *Physical Review C*, **54**, 882 (1996).

Poelz, G. "Aerogel in High Energy Physics", Aerogels., Ed. J. Fricke. (Springer–Verlag, Berlin, 1986) p. 176.

Poelz, G., *Nuclear Instruments and Methods in Physics Research*, **248**, 118 (1986a).

Poelz, G. and Riethmüller, R., *Nuclear Instruments and Methods in Physics Research*, **195**, 491 (1982).

Press, W.H., Flannery, B.P., Teukolsky, S.A., and Vetterling, W.T., *Numerical Recipes in C: The Art of Scientific Computing*, Cambridge University Press, New York (1988).

Protheroe, R.J., *Astrophysical Journal*, **251**, 387 (1981).

Rasmussen, I.L., *Proc. 2nd International Symposium on Aerogels, Montpellier France (1988)*, Published in *Revue de Physique Appliquée*, C4, 221 (1989).

Rasmussen, I.L. Private communication (1991).

Reimer, O. Private communication (1994).

Reimer, O., Barbier, L.M., Christian, E.R.Davis, A.J., Golden, R.L., Hof, M., Krombel, K.E., Labrador, A.W., Menn, W., Mewaldt, R.A., Mitchell, J.W., Ormes, J.F., Rasmussen, I.L., Schindler, S.M., Simon, M., Stochaj, S.J., Streitmatter, R.E., Webber, W.R., *Proc. 24th International Cosmic Ray Conference, Rome*, **2**, 618 (1995).

Rossi, B. *High Energy Particles* (Prentice–Hall: New York, 1952).

Rudaz, S., and Stecker, F.W., *Astrophysical Journal*, **325**, 16 (1988).

Ryan, M.J., Ormes, J.F., and Balasubrahmanyan, V.K., *Physical Review Letters*, 28, 985 (1972).

Salamon, M.H., McKee, S., Musser, J.A., Tarlé, G., Tomasch, A., Bower, C.R., Heinz, R.M., Miller, J.L., Mufson, S.L., Barwick, S.W., Gerbier, G., Lowder, D.M., Price, P.B., Zhou, B., Beatty, J.J., and Ahlen, S.P., *Astrophysical Journal*, **349**, 78 (1990).

Seo, E.S., et al., *Astrophysical Journal*, **378**, 763 (1991).

Shea, M.A., and Smart, D.F., *Proc. 18h International Cosmic Ray Conference, Bangalore*, **3**, 415 (1983).

Simon, M., Heinbach, U., and Koch, Ch., *Astrophysical Journal*, **320**, 699 (1987).

Simon, M., and Heinbach, U., *Astrophysical Journal*, **456**, 519 (1996).

Simpson, J.A., *Annual Review of Nuclear and Particle Science*, **33**, 323 (1983).

Simpson, J.A. and Garcia–Muñoz, M. *Space Science Reviews*, **46**, 205 (1988).

Smoot, G.F., Buffington, A., and Orth, C.D., *Phys Rev. Letters*, **35**, 258 (1975).

Stecker, F.W., Rudaz, S., and Wallsh, T.F., *Physical Review Letters*, **55**, 2622 (1985).

Stecker, F.W., and Tylka, A.J, *Astrophysical Journal*, **336**, L51 (1989).

Steigman, G., *Annual Reviews of Astronomy and Astrophysics*, **14**, 339 (1976).

Steigman, G., *Astrophysical Journal*, **L217**, 131 (1977).

Stephens, S.A., *Astrophysics and Space Science*, **76**, 87 (1981).

Stephens, S.A., *Proc. 23rd International Cosmic Ray Conference, Calgary*, **2**, 144 (1993).

Stephens, S.A. and Golden, R.L., *Space Science Reviews*, **46**, 31 (1987).

Stochaj, S.J., Ph. D. Thesis, University of Maryland (1990). Unpublished.

Streitmatter, R.E., Engineering Note I-253 Cosmic Ray Observatory, University of Chicago (1970).

Streitmatter, R.E., Private communication (1992).

Szabelski,J., Wdowczyk, J., and Wolfendale, A.W., *Nature*, **285**, 386 (1980).

Tan, L.C., and Ng, L.K, *J. Phys*, **G9**, 227 (1983a).

Tan, L.C., and Ng, L.K., *Astrophysical Journal*, **269**, 751 (1983b).

Webber, W. R., Private communication (1995).

Webber, W.R., Golden, R.L., and Stephens, S.A., *Proc. 20th International Cosmic Ray Conference, Moscow*, **1**, 325 (1987).

Webber, W.R. and Potgieter, M.S., *Astrophysical Journal*, **344**, 779 (1989).

Yoshimura, K., et al., *Physical Review Letters*, **75**, 3792 (1995).

Yuan, L.C.L., and Wu, C.S. (editors), *Methods of Experimental Physics*, Vol 5A, Academic Press, New York (1961).

"Real artists ship."
— Steve Jobs